Mechanics of Large-Strain Deformation of Particle-Modified Polymers

by

Ethan Moore Parsons

Submitted to the Department of Mechanical Engineering
in partial fulfillment of the requirements for the degree of

Doctor of Philosophy in Mechanical Engineering

at the

MASSACHUSETTS INSTITUTE OF TECHNOLOGY

June 2006

Author .....
Department of Mechanical Engineering
May 25, 2006

Certified by .....
Mary C. Boyce
Professor
Thesis Supervisor

Certified by .....
David M. Parks
Professor
Thesis Supervisor

Accepted by .....
Lallit Anand
Chairman, Department Committee on Graduate Students

Mechanics of Large-Strain Deformation of Particle-Modified Polymers

by

Ethan Moore Parsons

Submitted to the Department of Mechanical Engineering
on May 25, 2006, in partial fulfillment of the
requirements for the degree of
Doctor of Philosophy in Mechanical Engineering

Abstract

Over the past several decades, engineering polymers have become increasingly prevalent in the manufacture of virtually all types of products. Polymers are substantially less dense than metals, easy to machine, and readily formed into quite complex geometries. The properties of polymers may be altered by the introduction of second-phase particles. Typically, soft, rubber particles are added to increase fracture toughness while rigid, mineral particles are added to reduce costs or to increase stiffness, thermostability, or porosity.

The deformation to large strains of particle-modified thermoplastic polymers is investigated. Blends with rubber particles and blends with calcium carbonate particles are considered. A novel experimental technique is utilized to characterize the three-dimensional deformation of polycarbonate blends and high-density polyethylene blends during uniaxial tension tests. True stress, true strain, volumetric strain, and full-field contours of strain are extracted from images of the deforming specimens. The experimental results are used to construct and verify single-particle and multi-particle micromechanical models. In the micromechanical models, the stress triaxiality ratio and the properties of the particles, matrix, and interfaces are varied in order to determine their effects on local and macroscopic deformation. A constitutive model for polymers with perfectly bonded or debonding rigid particles is developed based on the knowledge gained from the experiments and micromechanical models.

Thesis Supervisor: Mary C. Boyce
Title: Professor

Thesis Supervisor: David M. Parks
Title: Professor

Acknowledgments

Thank you Mom, Dad, Kate, and Rachel for your love and support.

Contents

List of Figures

List of Tables

Chapter 1

Introduction

As famously prophesied by Walter Brooke [53] in 1967, over the past several decades, engineering polymers have become increasingly prevalent in the manufacture of virtually all types of products. Automotive and defense components, electronics, packaging, sporting equipment, and household goods are all constructed from polymers. Polymers are substantially less dense than metals, easy to machine, and readily formed into quite complex geometries. The latter characteristic facilitates the mass production process and thus significantly reduces manufacturing costs. The properties of polymers can be infinitely varied and tailored to a particular need by altering the polymer composition on the molecular level. Furthermore, the properties of an existing polymer can be altered by the introduction of second (and third, etc.) phase particles. Typically, rubber particles are added to increase fracture toughness while rigid, inorganic particles are added to increase stiffness, thermostability (heat deflection temperature), and/or porosity. Mineral fillers are much cheaper to procure than polymer resin and are sometimes added simply to lower the costs of raw materials.

Thermoplastic polymers are often divided into two broad categories based on their room temperature deformation: intrinsically brittle polymers, such as polystyrene (PS) and polymethyl methacrylate (PMMA), are brittle under almost all conditions and fail primarily by crazing, while intrinsically ductile polymers, such as polypropylene (PP), polyethylene (PE), polycarbonate (PC), polyvinyl chloride (PVC), and polyamide-6 (PA-6), are ductile at room temperature under moderate loading con-

ditions and usually fail only after extensive plastic deformation. As the deformation to large strains is of importance, the focus of this work was narrowed to two intrinsically ductile polymers: polycarbonate and high-density polyethylene (HDPE). In their neat form, under uniaxial tension, these two polymers cold draw to large strains before failure. While neat polymers and rubber-filled polymers are examined for comparison and the purpose of developing methodologies, the major focus of the thesis is the deformation of rigid particle-modified thermoplastic polymers.

Rigid particle-modified polymers are simple and inexpensive to prepare. The particles may first be surface-treated to enhance adhesion to the polymer and improve dispersion. Then, typically, pellets of the neat polymer are pre-mixed with the particles at room temperature and subsequently mixed in the molten state in an extruder. The volume fraction of filler may vary anywhere from on the order of one percent up to over 50% depending on the application. The characteristic size of the particles may range from nanometers to hundreds of microns. The particles may be perfect spheres (e.g. glass beads) or have very high aspect ratios (e.g. clay platelets). Upon cooling, the extrudates are pelletized and can then be molded by a variety of techniques directly into the shape of a product.

This study concentrates on blends with reasonably spherical particles of sizes on the order of a micron and larger. At this scale, it is assumed that the morphology of the majority of the polymer matrix is unaffected by the presence of the particles. Fairly large volume fractions of particles (10-20%) are considered as it is at these proportions that the effects on deformation become significant.

The tensile deformation of a rigid particle-modified polymer is illustrated schematically in Figure 1-1. The particles in almost all blends will be initially adhered to the polymer matrix by chemical bonding and/or thermal misfit stresses. This state is commonly referred to as "perfect bonding." Thus, at small, elastic strain levels the particles reinforce the matrix, and the stiffness of the blend exceeds that of the homopolymer. The increase in elastic modulus with increasing volume fraction of filler is well established and has been measured experimentally in many common thermoplastics by numerous investigators (Chacko et al. [17], Pukanszky [57], Bartczak et

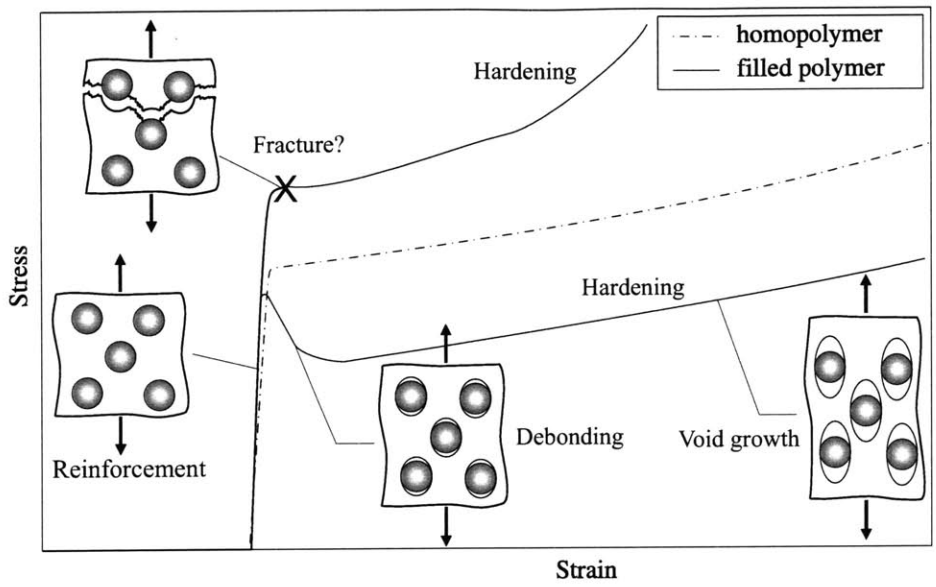

Figure 1-1: Schematic of deformation and stress-strain response of a rigid particle-modified polymer.

al. [8], Wilbrink et al. [79], Thio et al. [71]). At some point, however, usually prior to macroscopic yield, the particles in most blends debond, and the deformation becomes similar to that of a porous material. A sudden change in slope may appear in the stress-strain curve if the particles debond over a sufficiently narrow range of macroscopic strain. When debonding occurs, the effective load-bearing cross-sectional area of the specimen decreases, and the stress-strain curve of the blend drops below that of the homopolymer. The matrix is free to deform around the particles, and plasticity spreads throughout the matrix. A polymer composite with particles that debond in the elastic regime thus exhibits a yield strength lower than that of the homopolymer. A reduction in strength with increasing volume fraction of filler was observed by all of the aforementioned authors. Conversely, if the particles do not debond or debond in the plastic regime, the yield strength of the blend will be superior to that of the homopolymer due to the continued reinforcement provided by the particles. van Hartingsveldt and van Aartsen [75] and Meddad and Fisa [45], for example, increased the yield strength of PA-6 by adding appropriately surface-treated glass beads. In many cases, composites with particles that do not debond prior to macroscopic yield will fracture in a brittle manner due to the high concentrations of tensile stress in

the matrix material near the particles. After debonding (if it occurs), with further deformation, voids form around the particles, and, exacerbated by the "propping open" effect of the particles, large volumetric strains are attained. The large-strain deformation of blends with perfectly bonded or debonded particles has not been sufficiently addressed in the literature. The effect of particles on yield, post-yield strain hardening, and dilatation is therefore examined in this work.

The deformation to large tensile strains of *any* polymer is difficult to measure primarily due to the necking instability that occurs in uniaxial tension. Once the neck forms, the deformation is no longer homogeneous in the axial direction. The addition of second phase particles further complicates matters by introducing a source of substantial volumetric strain. When particles cavitate or debond, due to void growth, the simplifying assumption of incompressible deformation is no longer valid. Thus, the large-strain tensile deformation of particle-modified polymers has not been well characterized in the literature. In order to acquire the necessary data, novel experimental techniques have been developed.

At least partially due to the lack of data, there is an equal paucity of constitutive models capable of predicting the large-strain deformation of rigid particle-modified polymers. Most existing models are limited to small strains, one-dimensional deformations and/or rate-independent matrix materials. In this work, a large-strain constitutive model is presented that is capable of simulating the deformation, under arbitrary states of stress, of rate-dependent, strain hardening polymers modified with potentially debonding rigid particles.

The overarching goal of this work is to develop a thorough understanding of the deformation to large strains of rigid particle-modified thermoplastic polymers through a combination of experiments, micromechanical modeling, and constitutive modeling. The practical motivations are numerous. Most conspicuous is the problem of brittle fracture. Even intrinsically ductile polymers can be brittle under highly triaxial states of stress, at high strain rates, and at low temperatures. While judicious blending of rubber particles is well known to increase dramatically the toughness of virtually all intrinsically ductile polymers (Yee [81], Muratoglu et al. [50], Bartczak et al. [7]), the

role of rigid particles is not nearly so well established. It is thought that debonding rigid particles should have an effect on the toughness of a polymer similar to that of debonding or cavitating rubber particles. Rigid particles have been shown to toughen PE (Bartczak et al. [8]), PP (Thio et al. [71]) and PVC (Pukanszky and Maurer [58]) but have no positive macroscopic effect on the toughness of PA-6 (Wilbrink et al. [79]) or PC (Psarski et al. [56]). One of the attractions of toughening with rigid particles is that the blend becomes not only tougher but also stiffer than the homopolymer. In some applications, where stiffness, economy, thermal properties, or introducing porosity is the primary goal, it is important only to maintain, not necessarily increase, toughness with the addition of rigid particles. A better understanding of debonding and particle dispersion, two factors presumed to be closely related to toughness, is essential to maintaining or improving toughness.Furthermore, the phenomenon of localization of deformation in rigid particle-modified polymers has not been satisfactorily addressed in the literature. As the imposed macroscopic strains become larger, the stress fields around particles overlap. Voids around debonded particles no longer grow in isolation but interact with one another and, in some cases, even coalesce. Further knowledge of localization and its influences is necessary to understand and predict virtually all types of macroscopic behavior – from stress-strain and volumetric strain response to brittle or ductile failure. A constitutive model accurate to large strains will prove useful as a component of finite element models of engineered products. Porous, breathable materials are often manufactured by stretching mineral-filled ductile polymers to large strains. The constitutive model will enable engineers to predict properties such as porosity and diffusion rate while avoiding fracture. Matrix material properties, volume fraction of filler, and interface strength may all be parametrically varied in order to design the optimum material for a particular application.

The outline of the thesis is as follows: In Chapter 2, uniaxial tension of neat PC and rubber particle-modified PC is examined in depth. Strains obtained with the aid of digital image correlation (DIC) are analyzed as a function of position on the specimen and time. Drawing comparison between a finite element simulation of the tension

test and the experimentally measured strains, we determine how best to characterize the large-strain tensile deformation of necking polymers. Full-field strain contours, macroscopic true stress-true strain response, and local volumetric strains reduced from the raw test data elucidate the effects of soft fillers on polymer deformation. In Chapter 3, the quasi three-dimensional experimental technique presented in Chapter 2 is enhanced to enable simultaneous strain measurement in all three dimensions. Results are presented for HDPE, rubber-filled HDPE, and calcium carbonate-filled HDPE. Discussion of the effects of matrix properties, particle properties, and filler volume fraction on local and macroscopic deformation ensues. Chapter 4 provides a brief description of two constitutive models for homopolymers which are used to describe the response of the matrix in the micromechanical models and as a framework in which to develop the constitutive model for rigid particle-modified polymers. With material and interface constitutive models fit to the experimental data, single-particle and multi-particle finite element-based micromechanical simulations are performed in the following two chapters. The micromechanical simulations confirm experimental findings and provide a window into the local, particle-level deformation mechanisms responsible for the observed macroscopic behavior. In Chapter 5, the accuracy of the micromechanical models is verified by comparing the macroscopic predictions of the models with the results of the HDPE experiments. In the process, the effects on deformation of the particle-matrix interface properties and the volume fraction, material properties, and spatial distribution of the particles are investigated. The deformation of rigid particle-modified polymers under elevated stress triaxiality ratios and the consequences of particle clustering are then examined in Chapter 6. The knowledge gained from the experiments and micromechanical models is used to develop, calibrate, and verify the constitutive model for rigid particle-modified polymers presented in Chapters 7 and 8. In Chapter 9, key conclusions are summarized, and suggestions are made for future work.

Chapter 2

Tensile Testing of Neat and Rubber-Filled Polycarbonate

2.1 Overview

During a uniaxial tension test, most engineering polymers begin to deform inhomogeneously ("neck") at relatively small strains. Once necking begins, traditional extensometry methods provide little useful information. A contacting extensometer measures only the average strain over a gage length by tracking the relative position of two points on the specimen. Until the neck stabilizes and propagates the length of the specimen, however, the strain varies with axial position on the specimen. For this reason, polymer tensile stress-strain data is often limited to small strains, and comparably little is known about the post-yield tensile deformation of polymers. The macroscopic data typically measured, nominal stress versus machine crosshead displacement, does not capture the local characteristics of the deformation. In order to determine the true stress-true strain response after the onset of necking, one must measure the local displacement field.

In both their neat and filled forms, many polymers increase in volume during tensile extension. Volumetric strain is important to measure because it is a key macroscopic indicator of microscopic deformation processes. In homopolymers, small-scale internal fracture processes such as crazing (glassy polymers) or crystal fragmentation

(semi-crystalline polymers) are manifested by volumetric strain. In filled polymers, the debonding of rigid particulate fillers or the cavitation of elastomeric fillers allows void growth, an additional source of volumetric strain. Debonding and cavitation are important events to quantify for, by relieving stress triaxiality and enabling dissipative plastic flow, they are ingredients critical to toughening.

The presence of significant volumetric strain complicates the calculation of the true stress (load per current cross-sectional area) in the specimen during the tensile test. Traditional tensile testing techniques measure the axial strain and approximate the current cross-sectional area of the specimen by assuming the volume of each material point of the specimen to be constant. If the volumetric strain is not negligible, however, this assumption causes the true stress to be miscalculated. The determination of the true stress at a given axial location on the specimen therefore requires knowledge of the actual cross-sectional area at that location. Displacements and strains must be measured not only in the axial direction but also in one (if transversely isotropic deformations may be assumed) or both lateral directions.

It is true that, if the volumetric strain is minimal, true stress-true strain can be accurately measured in compression with traditional methods. With the specimen cross-sectional area growing larger with increasing axial strain, compressive deformation is inherently stable and does not localize. Many polymers, however, behave much differently in tension than in compression. Even neat, incompressible polymers show a pressure dependence of yield, and those that craze or fragment do so more readily under tension. Furthermore, particles in filled polymers are more likely to cavitate or debond during tensile deformation. Once cavitation or debonding occurs, void growth proceeds in an entirely different manner in tension than it does in compression. Finally, even the most ductile polymers eventually fail, and the stress and strain at fracture can only be measured in tension. Thus, in most cases, measuring the true stress-true strain response in tension is essential for a thorough understanding of the properties of a polymer.

Several investigators have attempted to characterize the large-strain tensile behavior of polymers. The most successful endeavors used some type of video sys-

tem to capture images of the specimen at various stages of extension. Buisson and Ravi-Chandar [15] applied a finely spaced grid to the surface of rectangular bar-type polycarbonate (PC) specimens. They calculated the axial and lateral displacement gradient at points along the specimen centerline by fitting polynomials to the grid line displacements. The true stress at the same points was obtained from a stress-optic method. In all of the studies described below, the true stress was calculated from the total load and the measured or assumed current cross-sectional area. Assuming incompressibility to obtain the axial strain, G'Sell et al. [28] calculated the true stress-strain behavior of several glassy and semi-crystalline polymers by using an optical diametral transducer to measure the instantaneous minimum diameter of hourglass-shaped cylindrical specimens. Nazarenko et al. [51] used a similar technique on round polycarbonate bars but applied a fine grid to the surface and also measured the behavior at points away from the site of neck initiation. Haynes and Coates [36] measured axial strain as a function of axial position in polypropylene and a styrene butadiene elastomer by tracking the axial position of transverse grid lines printed on the surface of rectangular bar-type specimens. The true axial strain was taken directly from the relative displacement between neighboring grid lines, and the true axial stress was then calculated by assuming constant volume deformation. Gloaguen and Lefebvre [25] calculated the true stress-strain and volumetric strain behavior of nylon and polypropylene by measuring the separation of pairs of ink marks on rectangular bar-type specimens. Two cameras were used to measure simultaneously the strains in all three directions. Homogeneous deformation between the ink marks was assumed. G'Sell et al. [27] later developed an optical technique for use on rectangular bar-type specimens which did not require the assumption of constant volume and also allowed for a degree of inhomogeneous axial deformation. The locations of seven dots on the surface of the specimen were used to calculate the true axial and lateral strains at a particular axial location. Assuming a transversely isotropic strain tensor, they calculated the true stress-strain and volumetric strain behavior of polyethylene terephthalate and high-impact polystyrene.

Any method that seeks to measure local strains in inhomogeneously deforming

polymers at moderate to large strains must either use an infinitesimally small gage length or, more practically, evaluate pointwise gradients in the displacement field. One technique that has been shown to be very effective in measuring displacements and displacement gradients is digital image correlation (DIC). DIC is the process of matching subsets of pixel gray-value patterns from one image to another. When DIC is applied to a mechanical test, an image of the undeformed specimen is correlated to an image of the deformed specimen, and the in-plane displacements and displacement gradients are calculated for one or more pixel subsets. From the displacement field or the displacement gradients, the strain measures are determined.

Laraba-Abbes et al. [42] used DIC to measure the nominal stress-stretch behavior of carbon black-filled natural rubber. During a tension test, they illuminated the rectangular bar-type specimen surface with a laser and captured images of the reflected light with a charged couple device (CCD) camera. Due to the imperfection of the specimen surface, the reflected light exhibited a spatial variation in intensity or "speckle" effect. Forming a digital signature of the specimen surface, the distribution of light detected at the camera sensor is what is known as a "speckle pattern." Starting with the undeformed image, Laraba-Abbes et al. incrementally obtained the in-plane displacement field by correlating subsets of the speckle pattern from one image to the next. They calculated the in-plane axial and transverse stretches by differentiating linear functions fit to subsets of the displacement field.

In this chapter, a method utilizing DIC is presented that measures, in two dimensions, the local displacement gradients and the full-field displacements during a standard uniaxial tension test. A random speckle pattern is applied with ink to the surface of rectangular bar-type neat PC and rubber particle-modified PC specimens. A CCD camera connected to a computer acquires digitized images of the specimen surface at regular intervals during a tensile test. The in-plane displacement gradients and displacements are calculated in the Lagrangian description by correlating subsets in the undeformed (reference) image to subsets in each deformed image. The correlation algorithm allows for large strain gradients and, hence, is capable of characterizing materials that deform inhomogeneously. The strains are calculated from the

displacement gradients or displacements. With all in-plane strain components known, the assumption of incompressibility made by several aforementioned authors is not necessary. True stress-true strain and volumetric strain behavior is reduced from the raw strain and displacement data, and full-field strain contours are constructed.

The purpose of the work on neat and rubber particle-modified PC presented in this chapter is threefold:

1. to examine on a local scale how deformation proceeds in a necking polymer;

2. to show how the desired mechanical properties to large strains can be extracted from raw test data;

3. to evaluate the effects that compliant filler particles have on polymer deformation.

$CaCO_3$ particle-modified PC was tested as well but unfortunately showed very little ductility. PC was chosen because it conserves its volume during plastic deformation. An experimentally measured post-yield volumetric strain of nearly zero in neat PC therefore partially validates the methodology. Furthermore, all volumetric strain in the blends can be attributed to void growth.

The outline of Chapter 2 is as follows: In Section 2.2, the procedure is described. The experimental technique and DIC algorithm are briefly discussed, and the method for calculating the large-strain measure and the true stress from the raw correlation (displacement) data and macroscopic load is then given. A finite element model of the neat PC uniaxial tension test is described as well. In Section 2.3, the experimental results are presented, and, at the same time, the algorithms for determining the true stress-strain and volumetric strain responses are developed and validated by drawing comparisons with the results of the finite element simulation. In order to illustrate the general features of polymer deformation, Section 2.3 begins with full-field contours of strain for neat PC and compares the experimental results to the simulation results. Next, in Section 2.3.2, the local axial and lateral strains in neat PC are investigated as a function of time and position on the tensile specimen. Finding that the strains are a

strong function of lateral position, macroscopic quantities are defined to represent the true axial and lateral strains. In Section 2.3.3, the spatial variation of the true stress-strain and axial strain rate history is investigated on the neat PC specimen. Data reduction schemes are developed to extract the material true stress-strain response from the raw specimen data. The simulation emulates the experimental conditions and verifies the efficacy of the data reduction strategies. Similarly, in Section 2.3.4, the simulation indicates how most accurately to calculate the volumetric strain in neat PC. Finally, in Section 2.3.5, the true stress-strain, volumetric strain and full-field strain results of rubber particle-modified PC at several volume fractions of filler are presented and discussed.

2.2 Procedure

2.2.1 Sample preparation

The polycarbonate used in these experiments, trade name Makrolon 2608, was supplied by Bayer Corporation (Pittsburgh, PA). Polycarbonate is an amorphous polymer. The homopolymer and blends containing, by volume, 5%, 15%, and 25% core-shell rubber particles were tested. The particles, supplied by Rohm and Haas, had a methyl-methacrylate/styrene shell and a polybutadiene core. Johnson [39] reported the particle diameters to range from 0.30 μm to 0.80 μm with a mean of 0.52 μm. The neat polymer and blends were injection molded into 12.7 mm $\times$ 12.7 mm $\times$ 127 mm bars. Tensile bars with gage section dimensions 19.05 mm $\times$ 7.62 mm $\times$ 3.20 mm were machined from the square bars.

2.2.2 Testing procedure

All tensile tests were conducted on an Instron model 5582 screw machine at a constant nominal strain rate of $0.005\,s^{-1}$. A random speckle pattern was applied to each specimen with a Badger airbrush filled with India ink. The pattern density was maximized under the constraint that individual speckles should generally not overlap.

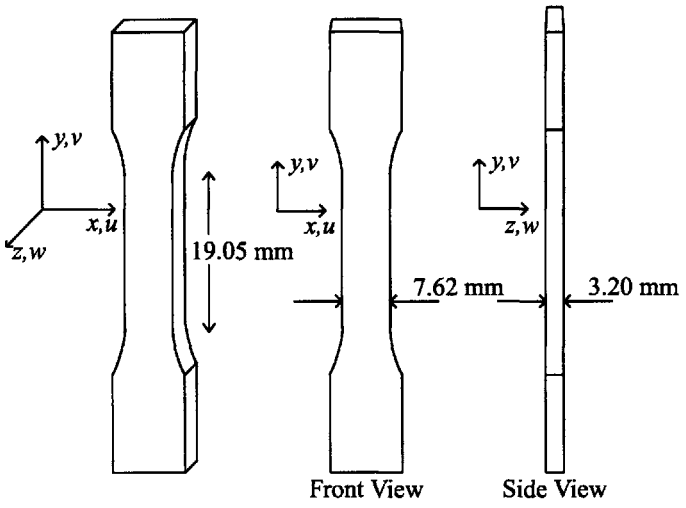

Figure 2-1: Specimen geometry and definition of views and coordinate directions. u, v, and w denote the displacements in the x, y, and z directions, respectively.

The minimum characteristic speckle size was three pixels (approximately 0.1 mm). 1280 pixels × 1024 pixels, 12-bit images were recorded at a frequency of 1 Hz with a Qimaging Retiga 1300 CCD camera equipped with a 200 mm Canon f/4.0 Canon lens and, in some cases, a Nikon 200 mm extension. The camera was placed at a distance of 1.0 m from the specimen. The load on the Instron load cell at the time of each image acquisition was recorded via a National Instruments DAQ board. It was not assumed that the specimens would deform isotropically in the two lateral directions. Therefore, as illustrated in Figure 2-1, companion tests were viewed from two orientations; the "front" view captured the deformation of the thick lateral dimension (x) and the "side" view captured the deformation of the thin lateral dimension (z).

2.2.3 Strain measurement

The images were analyzed with a DIC algorithm developed by Correlated Solutions Incorporated (CSI).[1] To correlate the deformed image to the reference image, the area of interest in each image is divided into small square subsets. The discrete matrix of the pixel gray level values in each subset forms a unique pattern within the image.

[1]West Columbia, SC 29169, USA; Tel.: +1-803-926-7272; *url*: www.correlatedsolutions.com.

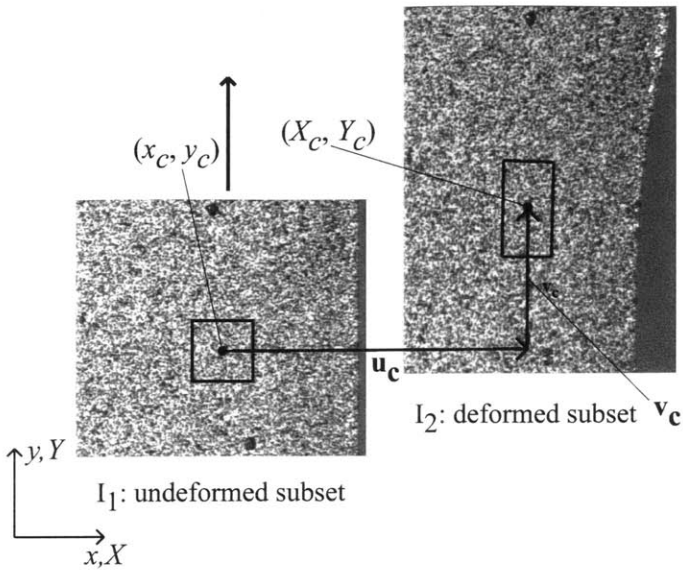

Figure 2-2: Illustration of speckle pattern subsets and correlation procedure. Reference coordinates are denoted by (x, y), and deformed coordinates are denoted by (X, Y).

The second-order shape functions

$$u(x,y) = u_c + \frac{\partial u}{\partial x}(x - x_c) + \frac{\partial u}{\partial y}(y - y_c) + \frac{1}{2}\frac{\partial^2 u}{\partial x^2}(x - x_c)^2 + \frac{\partial^2 u}{\partial x \partial y}(x - x_c)(y - y_c) + \frac{1}{2}\frac{\partial^2 u}{\partial y^2}(y - y_c)^2 \tag{2.1}$$

and

$$v(x,y) = v_c + \frac{\partial v}{\partial y}(y - y_c) + \frac{\partial v}{\partial x}(x - x_c) + \frac{1}{2}\frac{\partial^2 v}{\partial y^2}(y - y_c)^2 + \frac{\partial^2 v}{\partial y \partial x}(y - y_c)(x - x_c) + \frac{1}{2}\frac{\partial^2 v}{\partial x^2}(x - x_c)^2 \tag{2.2}$$

map the positions within the reference subset to positions in the image after deformation. As illustrated in Figure 2-2, u_c and v_c are the displacements of a point at reference image coordinates (x_c, y_c). Here, x and y are the reference coordinates of arbitrary points within the subset centered at (x_c, y_c). The coefficients of the polynomial are optimized by minimizing the normalized cross-correlation coefficient [6], r,

defined for an n pixel $\times$ n pixel subset as

$$r = \frac{\sum_{i=1}^{n}\sum_{j=1}^{n} \mathrm{I}_1(x_i, y_j)\mathrm{I}_2(x_i + u, y_j + v)}{\sum_{i=1}^{n}\sum_{j=1}^{n} \sqrt{\mathrm{I}_1{}^2(x_i, y_j)}\sqrt{\mathrm{I}_2{}^2(x_i + u, y_j + v)}}, \tag{2.3}$$

where I_1 and I_2 denote the gray level intensity patterns of the reference and deformed images, respectively. Its insensitivity to changes in lighting makes the normalized cross-correlation coefficient an excellent similarity measure. The displacement gradient at the subset center is calculated by evaluating the derivatives $\frac{\partial u}{\partial x}$, $\frac{\partial u}{\partial y}$, $\frac{\partial v}{\partial x}$, and $\frac{\partial v}{\partial y}$ at $(x, y) = (x_c, y_c)$. This algorithm was used to determine the local strain history at individual points on the specimen. Image resolution was 37.5 ("low" magnification) for all front view tests and 75 pixels/mm ("high" magnification via the 200 mm lens extension) for all side view tests. The subsets measured 75 pixels $\times$ 75 pixels. For reference, Figure 2-2 shows a subset of size 75 pixels $\times$ 75 pixels at a resolution of 75 pixels/mm.

Local strain calculation

Local lateral versus axial strain and volumetric strain behavior were calculated directly from the derivatives of the second-order mapping function described above. Formally, the derivatives define the two-dimensional displacement gradient,

$$\mathbf{H} = \begin{pmatrix} \frac{\partial u}{\partial x} & \frac{\partial u}{\partial y} \\ \frac{\partial v}{\partial x} & \frac{\partial v}{\partial y} \end{pmatrix}, \tag{2.4}$$

with

$$\mathbf{H} = \mathbf{F} - \mathbf{1}, \tag{2.5}$$

where $\mathbf{F}$ is the deformation gradient and $\mathbf{1}$ is the second-order identity tensor. $\mathbf{F}$ is defined as $\mathbf{1} + \mathrm{Grad}\,\mathbf{u}(\mathbf{x})$, where $\mathbf{x}$ is the position vector of a point in the reference configuration, and $\mathbf{u}(\mathbf{x})$ is the displacement of that point. From the polar decompo-

sition, $\mathbf{F} = \mathbf{VR}$, the true strain in the spatial configuration, or Hencky strain, $\mathbf{E}$, is calculated as

$$\mathbf{E} = \ln\mathbf{V}, \tag{2.6}$$

where $\mathbf{V}$ is the left stretch tensor and $\mathbf{R}$ is the rotation tensor. The volumetric strain E_{kk} is defined as

$$E_{kk} = \ln\left(\frac{V}{V_0}\right) = \ln(\det\mathbf{F}), \tag{2.7}$$

where V is the current volume and V_0 is the original volume.

Full-field strain calculation

Contours of true axial and shear strain were constructed from the displacement fields. Within the areas of interest, correlations were performed on pixel subsets of size 75 pixels × 75 pixels at a step size of two. The displacement of the center point of each subset was calculated and stored. The displacement of every second pixel in the area of interest was thus known. The raw full-field displacement data was then imported into MATLAB where the strains were calculated from least-squares approximations of the displacement field. Subsets of the displacement field of size 11 points × 11 points were taken at a step size of five. A temporary $(\tilde{x}, \tilde{y})$ coordinate system was translated to the center of each displacement field subset. Second-order polynomial expressions for $u(\tilde{x}, \tilde{y})$ and $v(\tilde{x}, \tilde{y})$ were then fit to each displacement field subset. Similar to the procedure described in Section 2.2.3, the displacement gradient $\mathbf{H}$ was calculated from the partial derivatives $\frac{\partial u}{\partial \tilde{x}}$, $\frac{\partial u}{\partial \tilde{y}}$, $\frac{\partial v}{\partial \tilde{x}}$, $\frac{\partial v}{\partial \tilde{y}}$ evaluated at each subset center. The logarithmic strain, $\mathbf{E} = \ln\mathbf{V}$, was then calculated and plotted to construct the full-field contours.

Error analysis

The total error for a given normal strain component is approximated as the random error plus the systematic error due to out-of-plane motion. It takes the form

$$\text{error}(\mu\epsilon) \approx \pm 100 + eE \times 10^6, \tag{2.8}$$

where E is the appropriate actual strain and e is the "out-of-plane" error due to the Poisson contraction of the specimen. The values of e for each strain component from each view are summarized in Table A.1. The complete error analysis is presented in Appendix A. The measured strains are clearly very accurate, and the error is significant only at strains similar in magnitude to that of the noise.

	E_{yy} (front)	E_{xx} (front)	E_{yy} (side)	E_{xx} (side)
e	-0.7×10^{-3}	1.4×10^{-3}	-1.7×10^{-3}	3.5×10^{-3}

Table 2.1: Maximum out-of-plane strain errors, e, expressed as a fraction of the corresponding actual strain value.

2.2.4 True stress calculation

At any cross-section, the stress and strain vary across the width and thickness of a specimen. While the local lateral strains can be measured, there is no way to determine the local stresses. An average (or "macroscopic") true stress for the whole specimen was therefore calculated from the total load and the current estimated cross-sectional area of the specimen. (All macroscopic quantities are indicated by a variable with an overbar.) The macroscopic true stress, $\overline{T}_{yy}$, was calculated as

$$\overline{T}_{yy} \equiv \frac{P}{A} = \frac{P}{A_0 \overline{\lambda}_{xx} \overline{\lambda}_{zz}}, \tag{2.9}$$

where P is the load cell measurement, A is the current cross-sectional area of the specimen at the axial location where the neck forms, A_0 is the initial cross-sectional area of the specimen, and $\overline{\lambda}_{xx}$ and $\overline{\lambda}_{zz}$ are the macroscopic lateral stretches. $\overline{\lambda}_{xx}$ and

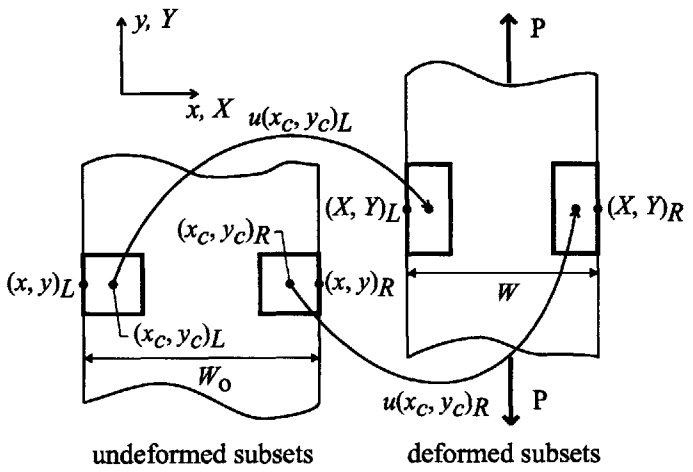

Figure 2-3: Definition of variables used in the true stress calculation. Reference coordinates are denoted by (x, y), and deformed coordinates are denoted by (X, Y).

$\overline{\lambda}_{zz}$ were calculated, respectively, from the specimen's overall width in the x-direction, W, and the specimen's overall thickness in the z-direction, T. From the front view, as illustrated in Fig. 2-3,

$$\overline{\lambda}_{xx} = \frac{W}{W_0} = \frac{X_L - X_R}{x_L - x_R}, \tag{2.10}$$

where, since DIC can only provide information at the center of a pixel subset,

$$X_L \approx x_L + u(x_c, y_c)_L + \frac{\partial u}{\partial x}\Big|_{(x_c, y_c)_L} (x_L - x_{cL}) \tag{2.11}$$

and

$$X_R \approx x_R + u(x_c, y_c)_R + \frac{\partial u}{\partial x}\Big|_{(x_c, y_c)_R} (x_R - x_{cR}). \tag{2.12}$$

Here, the positions of the edges of the specimen were projected from the positions of the centers of the left-most and right-most pixel subsets and the displacement gradients at those same locations. Analogously, from the side view,

$$\overline{\lambda}_{zz} = \frac{T}{T_0} = \frac{Z_L - Z_R}{z_l - z_r}, \tag{2.13}$$

where Z_L and Z_R are calculated from expressions similar to Equations 2.11 and 2.12.

As will be shown later, the specimens did not deform isotropically in the lateral directions, but the degree of anisotropy did not significantly affect the true stress calculation. Therefore, with $\overline{\lambda}_{xx} \approx \overline{\lambda}_{zz}$, the true stress was taken to be

$$\overline{T}_{yy} \approx \frac{P}{A_0 \overline{\lambda}_{xx}^2}. \tag{2.14}$$

2.2.5 Simulations

Due to the inhomogeneous nature of the deformation of polymers during necking, reduction of the accumulated (full-field) specimen data into a measure of the true stress-strain response of the material was not straightforward. In order to assess the validity of the procedure and the accuracy of the resulting material true stress-strain response, we performed the same date reduction process on a finite element simulation of the inhomogeneous tensile deformation. The simulation allowed us to reduce the simulated specimen data to a material stress-strain response and compare the result with the a priori known (input) constitutive response of the finite element model.

The tensile tests on neat polycarbonate (PC) were simulated with a three-dimensional finite element model of the entire specimen. The amorphous polymer constitutive model of Boyce et al. [12], as modified by Arruda and Boyce [4], was used to represent the constitutive response of PC. In one dimension, the constitutive model can be thought of as a linear elastic spring in series with a parallel arrangement of a viscoplastic dashpot and a non-linear hardening spring. The linear elastic spring provides the initial elastic stiffness of material. When the material reaches its yield strength, the dashpot is activated enabling viscoplastic flow and strain softening to occur. In this implementation, the evolution equation for the shear strength was modified in order to achieve more gradual post-yield softening. The non-linear hardening spring captures the post-yield strain hardening due to the stretching and orientation of the underlying macromolecular network during viscoplastic flow. The material model parameters were fit to the results of compression tests performed at several different strain rates by Johnson [39]. The tensile yield strength measured in this study was

used to calibrate the pressure sensitivity of the model. The analysis was performed with ABAQUS Standard, version 6.3.

A geometrically perfect finite element mesh does not neck. Therefore, in order to induce the experimentally observed localization, a small edge perturbation, $0.0075w$ deep in the x-direction (as defined in Figure 2-1), was created by perturbing a single row of nodes on the positive z-face of the mesh. The defect was small enough to have no significant effect on the results after necking initiated. Furthermore, the nodes on the z-direction faces were perturbed in accordance with the RMS (root mean square) surface roughness of the specimen, which was measured to be $3\,\mu$m with a Zygo interferometer. Further details of the finite element model are provided in Appendix B.

2.3 Results

2.3.1 Neat PC: Full-field strain contours and localization

Figures 2-4 a-e and 2-5 a-e show experimental contours of true strain, $\mathbf{E} = \ln\mathbf{V}$, for a neat PC tensile bar at crosshead displacements, U, of 3.0 mm, 3.5 mm, 4.0 mm, 5.0 mm, and 8.0 mm. The plots depict the front view of an initially 10 mm long section of the gage length centered at the site of neck initiation (defined as the axial location where the axial strain increased most rapidly). The corresponding load versus crosshead displacement behavior is shown in Figure 2-6.

Figures 2-4 a′-e′ and 2-5 a′-e′ show the simulation results at crosshead displacements corresponding to those in Figures 2-4 a-e and 2-5 a-e. Particularly at large displacements, there is good agreement between the measured and predicted behavior in terms of both strain levels and modes of deformation. The same pattern of localization followed by neck propagation is clearly present. Furthermore, comparing Figures 2-4d and 2-4d′, one sees that the neck stabilizes in both the experiment and the simulation at nearly the same axial strain. The major difference between the experiment and the simulation is the apparent delayed localization of the experiment.

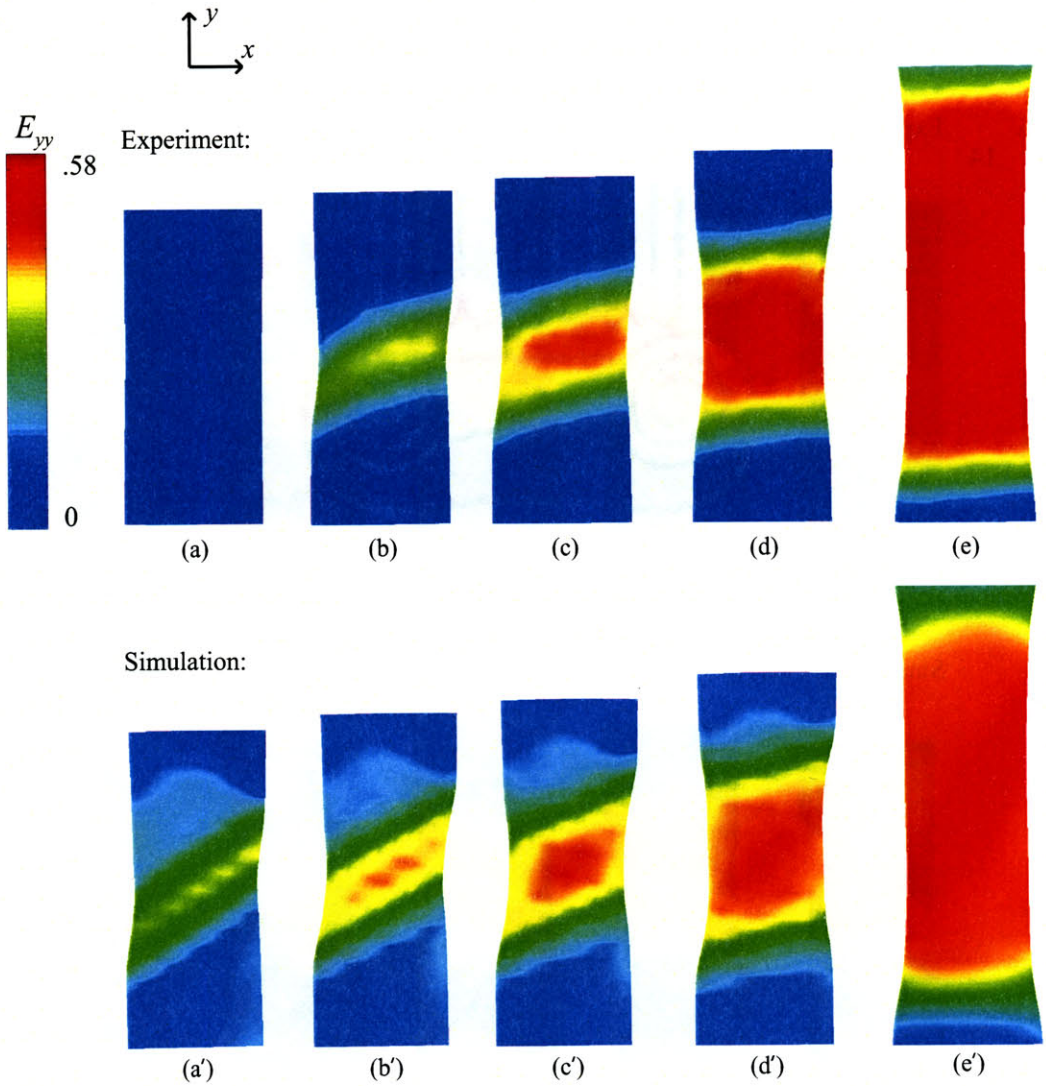

Figure 2-4: Experimental (top) and simulated (bottom) uniaxial tension of neat PC (front view). Contours of true axial strain, E_{yy}, for increasing crosshead displacement, U: (a), (a′) $U = 3.0\,\text{mm}$; (b), (b′) $U = 3.5\,\text{mm}$; (c), (c′) $U = 4.0\,\text{mm}$; (d), (d′) $U = 5.0\,\text{mm}$; (e), (e′) $U = 8.0\,\text{mm}$.

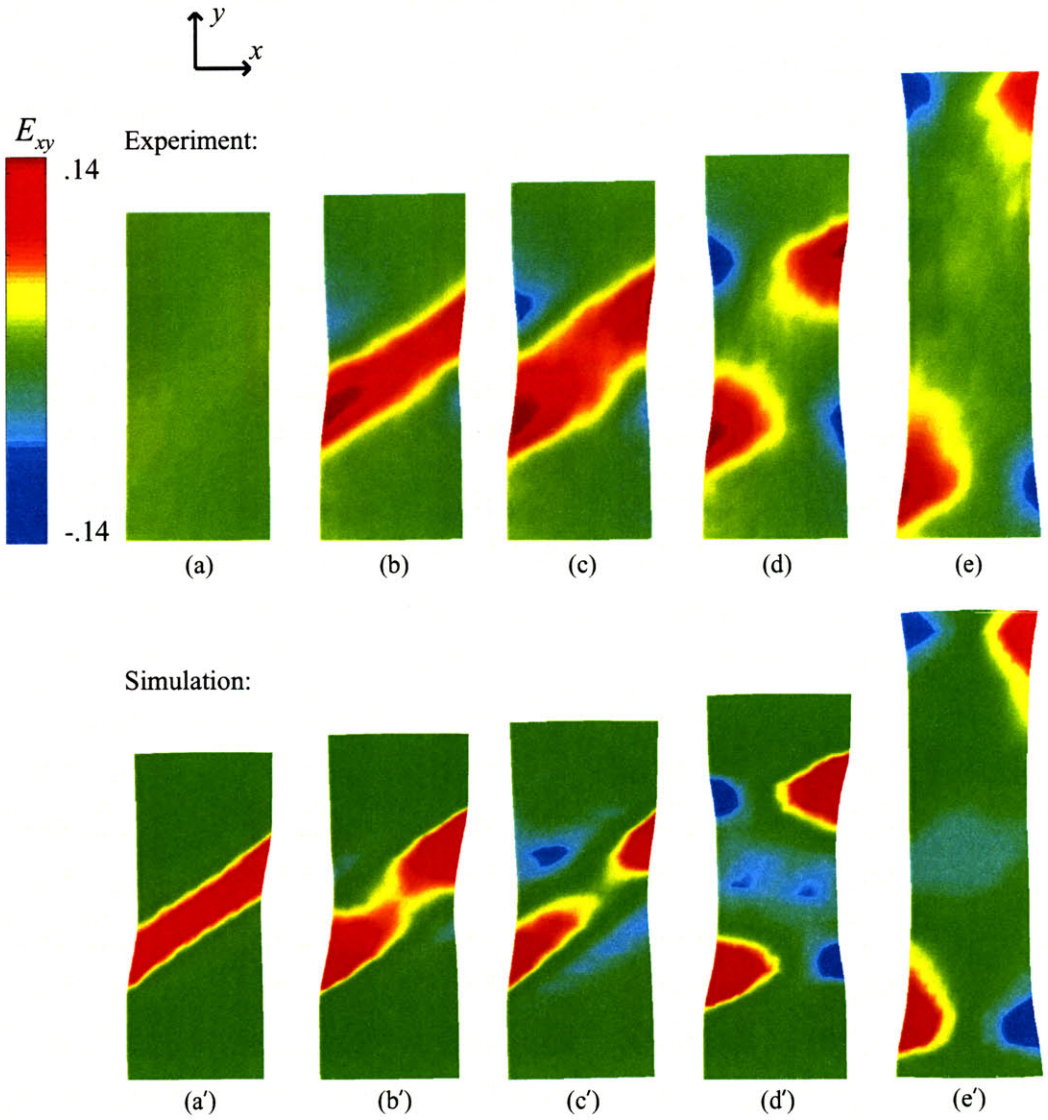

Figure 2-5: Experimental (top) and simulated (bottom) uniaxial tension of neat PC (front view). Contours of true shear strain, E_{xy}, for increasing crosshead displacement, U: (a), (a′) $U = 3.0\,\text{mm}$; (b), (b′) $U = 3.5\,\text{mm}$; (c), (c′) $U = 4.0\,\text{mm}$; (d), (d′) $U = 5.0\,\text{mm}$; (e), (e′) $U = 8.0\,\text{mm}$.

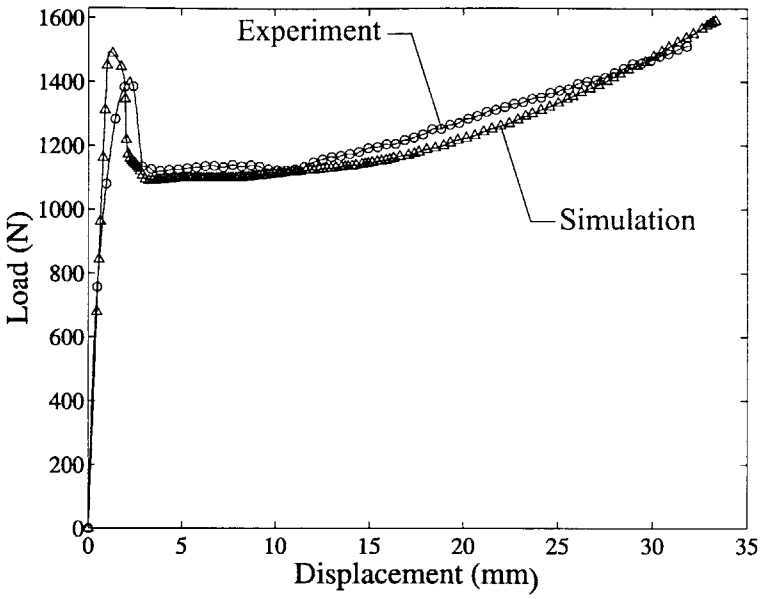

Figure 2-6: Uniaxial tension of neat PC. Experimental and simulated load, P, versus crosshead displacement, U.

At $U = 3.0\,\text{mm}$, in Figures 2-4a′ and 2-5a′, for example, the simulation has already passed through the peak in the load-displacement curve whereas the experiment has just reached the peak. The experiment yields at a larger crosshead displacement than the simulation (as shown in Figure 2-6) in part due to machine compliance, grip alignment, and possible slippage of the specimen. As will be mentioned later, evidence of these effects is also apparent in a smaller than expected initial true axial strain rate. An additional reason for the discrepancy is the fact that the material model does not capture the pre-peak nonlinearity observed in the experimental stress-strain curves. Thus, at any given crosshead displacement after the peak load, the simulation is further along in the deformation process than the experiment.

2.3.2 Neat PC: Strain versus time and position

Once necking begins, the behavior of PC becomes a strong function of time and position. Every axial location on the specimen has a unique strain versus time relationship. In order to characterize most accurately the behavior of PC, the local strain behavior was systematically probed using the algorithm described in Section 2.2.3.

Figure 2-7 depicts the matrix of points that were commonly analyzed. Location row

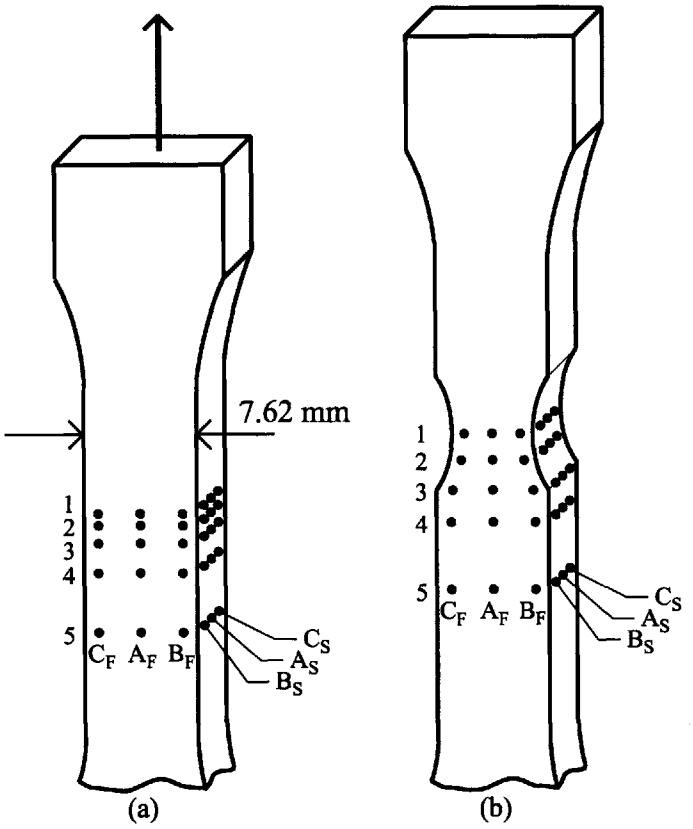

Figure 2-7: Definition of strain measurement locations: (a) undeformed specimen, (b) deforming specimen.

1 is where the neck initiates. Location rows 2, 3, 4, and 5 are 1.0 mm, 2.5 mm, 5.0 mm and 10.0 mm, respectively, from location row 1. Location column A is at the axial center line of the specimen. Location columns B and C are located one half of the correlation subset size, or 37 pixels, from the edge of the specimen. 37 pixels corresponds to 1.0 mm at low magnification and 0.5 mm at high magnification. Points with subscripts F and S were observed from the front and side views, respectively.

Figure 2-8 shows the true axial strain, E_{yy}, versus time behavior for four points along the front axial center line. In addition, contours of E_{yy} are shown for $t = 50$ s, $t = 100$ s, and $t = 150$ s. As observed in the full-field strain contours in Section 2.3.1, the specimen deforms homogeneously at axial strains less than 0.07. Until this point, the axial strain versus time behavior is identical at all four locations. Once necking

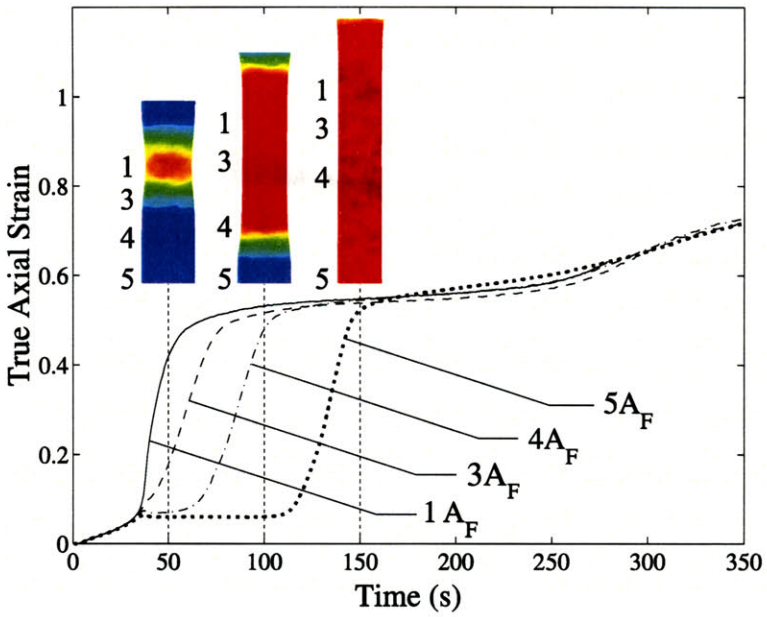

Figure 2-8: Uniaxial tension of neat PC (front view). True axial strain, E_{yy}, versus time and E_{yy} contours at times $t = 50\,\text{s}$, $t = 100\,\text{s}$, and $t = 150\,\text{s}$.

begins, however, the curves diverge. At point $1A_F$, the strain rises quickly to the drawing strain of $E_{yy} \approx 0.54$ before essentially leveling off for approximately 200 s. The strain at point $3A_F$, just 1.0 mm from the site of neck formation, rises slightly less rapidly but steadily also to $E_{yy} \approx 0.54$. The strain at points $4A_F$ and $5A_F$, however, plateaus for a period of time before increasing at a rate equal to that of point $3A_F$. During the periods of essentially zero strain rate at points $4A_F$ and $5A_F$, the deformation occurs entirely within the neck. The points a distance away from where the neck forms do not experience significant plastic deformation until the neck has propagated along the specimen. After leveling off at $E_{yy} \approx 0.54$, all four curves increase in slope again at $t \approx 250\,\text{s}$. At this time, the neck has propagated to the grip areas of the specimen, and the entire gage length begins to deform homogeneously once again.

Figure 2-9 shows the true axial strain versus time behavior for the three lateral locations, A_F, B_F, and C_F, at axial cross-sections 1, 4, and 5. At location row 1, the axial strain is a function of the lateral position, x. The strain increases more rapidly at the center of the specimen than at the edges. The discrepancy in the strains is

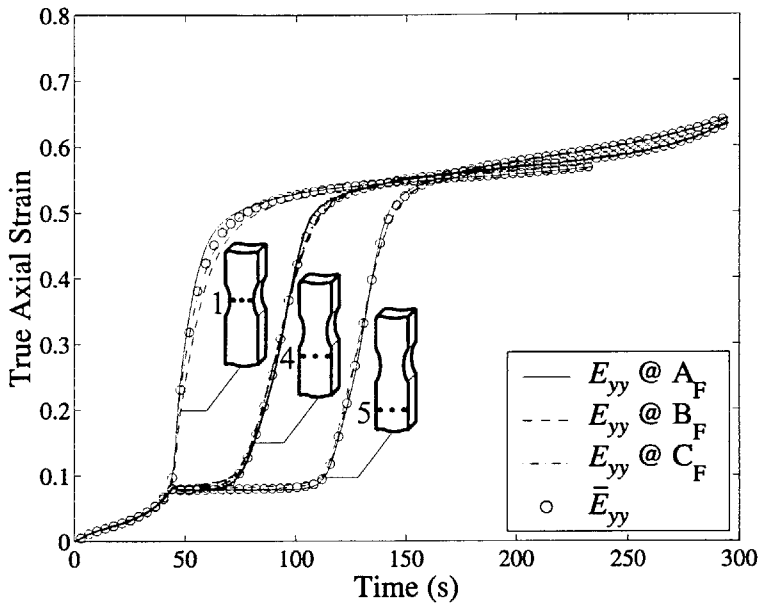

Figure 2-9: Uniaxial tension of neat PC (front view). Local true axial strain, E_{yy}, and macroscopic true axial strain, $\overline{E}_{yy}$, versus time at location rows 1, 4, and 5.

due to the fact that location 1 bisects the approximately 45° shear band depicted in Figures 2-4 a-c and 2-5 a-c. For the purpose of the true stress-strain calculation, a macroscopic true axial strain, $\overline{E}_{yy}$, was defined at each axial cross-section. The specimen was figuratively sliced in the y-direction into five equally-sized strips. At each axial location, the local axial strains, E_{yy}, at the centers of the five strips were calculated and averaged. Also plotted in Figure 2-9 at location rows 1, 4, and 5, $\overline{E}_{yy}$, as expected, lies comfortably between the local E_{yy} measurements. Moving down the specimen away from the point of neck initiation, one sees that, at locations rows 4 and 5, the axial strain is approximately constant across the width of the specimen. As illustrated in Figure 2-4d, after neck formation, the shear band quickly disappears, and the axial deformation at a particular cross-section becomes nearly uniform.

The true lateral strain, E_{xx}, versus time behavior at location rows 1, 4, and 5 is plotted in Figure 2-10. Unlike the axial strain, the lateral strain is a strong function of x at all axial locations. At each location row, the lateral strain is significantly smaller in magnitude at the center of the specimen (location A) than at the edges of the specimen (locations B and C). The strains at locations B and C are nearly

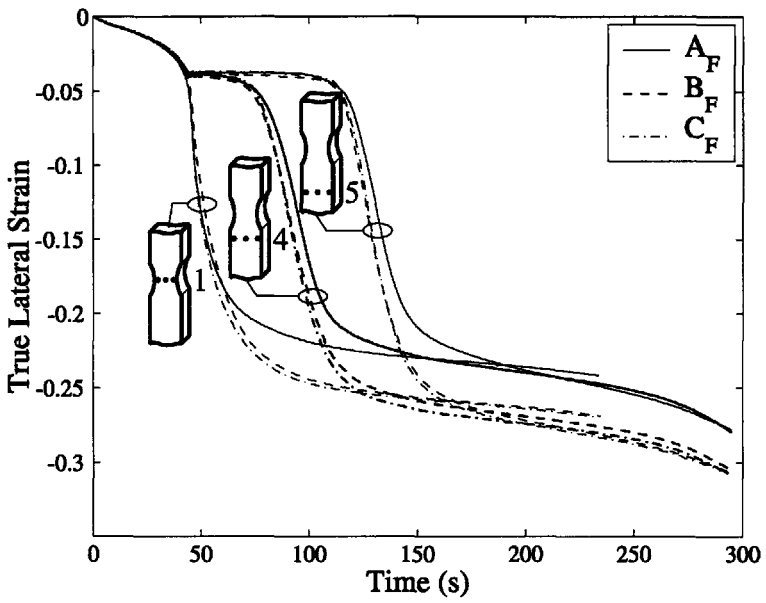

Figure 2-10: Uniaxial tension of neat PC (front view). Local true lateral strain, E_{xx}, versus time at location rows 1, 4, and 5.

identical.

Since the lateral strain is not constant across the width of the specimen, the macroscopic lateral stretch defined in Section 2.2.4 was used to calculate the current cross-sectional area of the specimen. Figure 2-11 shows the local true lateral strain at location row 4 and the macroscopic true lateral strain, $\overline{E}_{xx} = \ln\overline{\lambda}_{xx}$, with $\overline{\lambda}_{xx}$ defined by Equation 2.10, plotted as a function of time. The macroscopic curve fits nicely between the responses of the sides and the center. Figure 2-12 is a plot identical to Figure 2-11 but with the measurements taken from the side view of the specimen. The macroscopic strain again falls between the three local strain measurements.

Combining the results from this section, we plot the macroscopic true lateral strain versus macroscopic true axial strain at locations 3_F and 3_S in Figure 2-13. The initial slopes of these curves define the elastic Poisson's ratios, ν_{yx} and ν_{yz}. Both equal to 0.39, the values of ν_{yx} and ν_{yz} indicate that the specimen deforms in a transversely isotropic manner. Henceforth, the Poisson's ratio will thus be referred to as simply ν. At larger strains, however, the specimen does not deform isotropically in the two lateral directions. The specimen contracts more in the z-direction, particularly

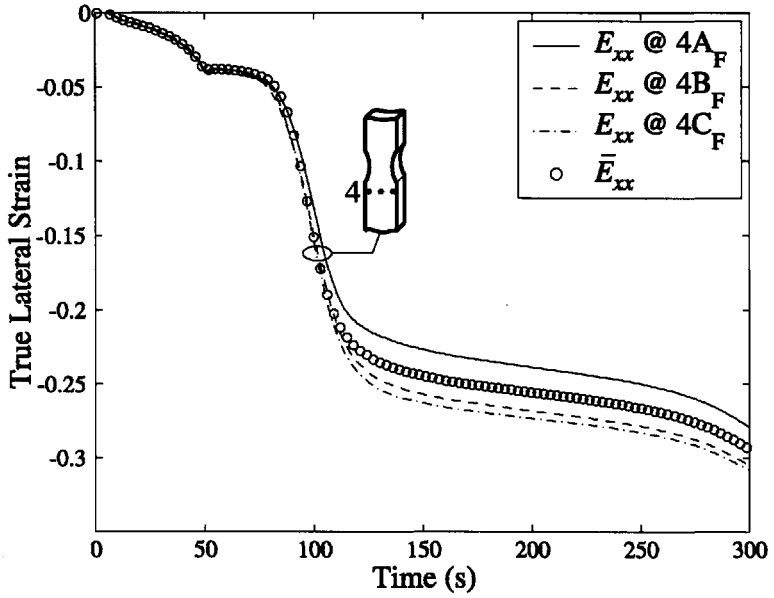

Figure 2-11: Uniaxial tension of neat PC (front view). Local true lateral strain, E_{xx}, and macroscopic true lateral strain, $\overline{E}_{xx}$, versus time at location row 4.

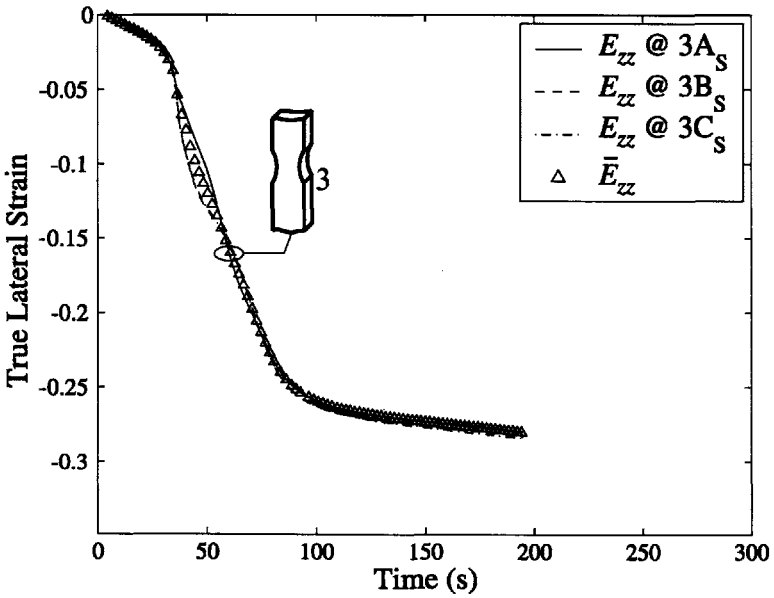

Figure 2-12: Uniaxial tension of neat PC (side view). True lateral strain, E_{zz}, and macroscopic true lateral strain, $\overline{E}_{zz}$, versus time at location row 3.

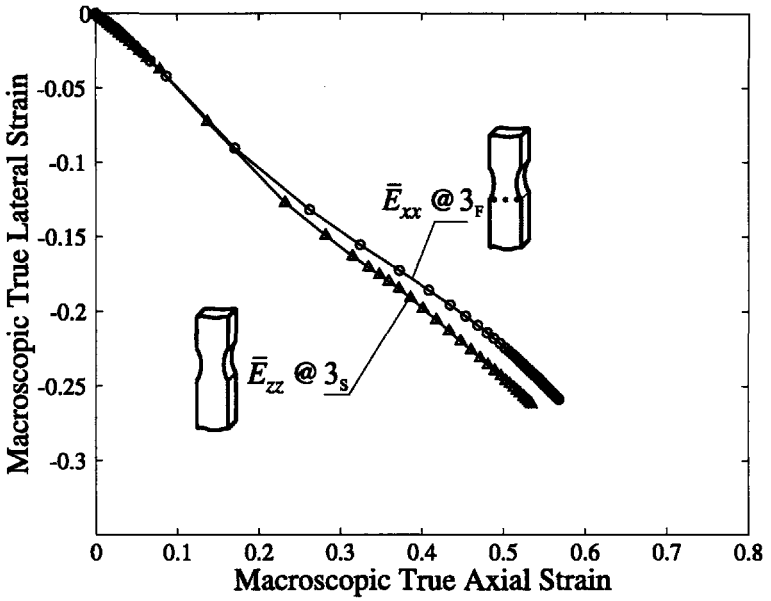

Figure 2-13: Uniaxial tension of neat PC. Macroscopic true lateral strains, $\overline{E}_{xx}$ and $\overline{E}_{zz}$, versus macroscopic true axial strain, $\overline{E}_{yy}$.

at axial strains greater than 0.25. While the degree of anisotropy is small enough to have virtually no effect on the true stress calculation (hence Equation 2.14), as will be shown in Section 2.3.4, the anisotropy must be taken into consideration when calculating the volumetric strain.

2.3.3 Neat PC: True axial stress-strain behavior

One of the primary goals of this experimental study was to develop a method to determine the constant strain rate constitutive behavior of a polymer in uniaxial tension from a standard tension test. It is well known that the response of polymers is a strong function of time due to the strain rate dependency of yield and the phenomenon of stress relaxation. Figures 2-8 and 2-9 show that the axial strain versus time behavior is different for every axial location on the specimen. It follows that the stress-strain response must also be a function of axial location. Furthermore, even at a particular axial location, the true axial strain rate is a function of axial strain. In order to determine how best to infer a single representative stress-strain curve from a test where every material point behaves differently, the simulation was consulted.

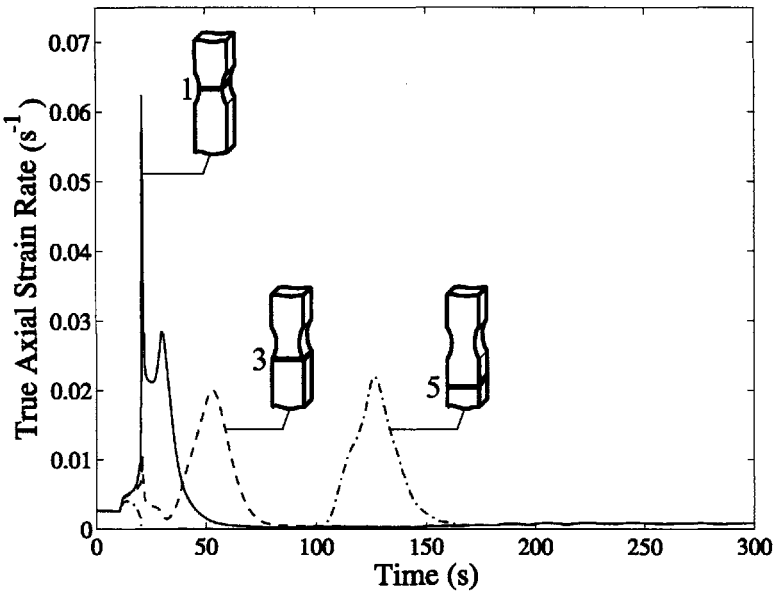

Figure 2-14: Tensile bar simulation results for uniaxial tension of neat PC. Macroscopic true axial strain rate, $\dot{\overline{E}}^{\text{ip}}_{yy}$, versus time at axial locations 1, 3, and 5.

We will show how the constitutive response of PC in uniaxial tension – viewed as a known in the simulation – can be "backed out" from the same macroscopic quantities that the experimental technique measures.

Figure 2-14 shows the macroscopic true axial strain rate of the simulation, $\dot{\overline{E}}^{\text{ip}}_{yy}$, at axial locations 1, 3, and 5 as a function of time. $\dot{\overline{E}}^{\text{ip}}_{yy}$ is given by

$$\dot{\overline{E}}^{\text{ip}}_{yy} = \frac{\overline{E}^{\text{ip}}_{yy}\,|_{t_{i+1}} - \overline{E}^{\text{ip}}_{yy}\,|_{t_i}}{t_{i+1} - t_i}, \tag{2.15}$$

where $\overline{E}^{\text{ip}}_{yy}$ is the weighted (by integration point volume) average of the true axial strains at all integration points ("ip"'s) at a given axial cross-section in the reference configuration. Over the three axial locations, $\dot{\overline{E}}_{yy}$ is constant during only the first few seconds of the test. Here, the material is still in the initial, homogeneous regime. Thereafter, the strain rate jumps an order of magnitude at location 1 as the neck forms. While the neck is at location 1, $\dot{\overline{E}}_{yy}$ at location 3 decreases, but remains positive, as material is slowly drawn into the neck, but, at location 5, $\dot{\overline{E}}_{yy}$ decreases to slightly less than zero due to elastic unloading in the wake of the macroscopic load

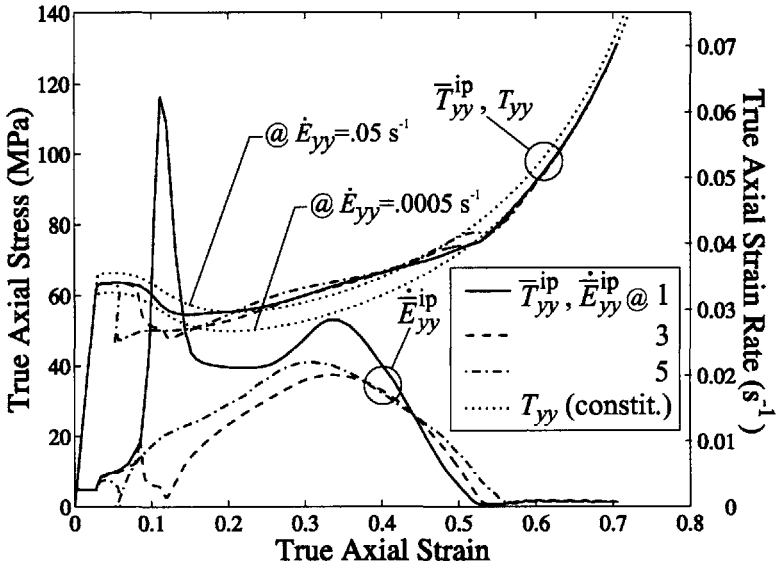

Figure 2-15: Tensile bar simulation results for uniaxial tension of neat PC. Macroscopic true axial stress, $\overline{T}^{ip}_{yy}$, (left hand axis) and macroscopic true axial strain rate, $\dot{\overline{E}}^{ip}_{yy}$, (right hand axis) versus macroscopic true axial strain, $\overline{E}^{ip}_{yy}$, at axial locations 1, 3, and 5. Constitutive model true axial stress, T_{yy}, versus true axial strain, E_{yy}, at true strain rates $\dot{E}_{yy} = 0.0005\,\mathrm{s}^{-1}$ and $\dot{E}_{yy} = 0.05\,\mathrm{s}^{-1}$.

drop. This period of approximately constant axial strain was observed in the experimental results presented in Figures 2-8 and 2-9. Once the drawing strain is reached at location 1, the neck propagates and the strain rate falls to essentially zero. Locations 3 and 5 undergo similar strain rate jumps when the neck reaches their vicinity. Eventually, at $t \approx 170\,\mathrm{s}$, the neck reaches the grip areas of the specimen, and the entire gage length begins to deform homogeneously again at a rate of approximately $0.0015\,\mathrm{s}^{-1}$. Every material point thus experiences a variation in strain rate exceeding two orders of magnitude over the course of a test with constant crosshead velocity test.

Figure 2-15 illustrates the relationship in the simulation between stress-strain response and strain rate. The macroscopic true axial stress, $\overline{T}^{ip}_{yy}$, analogous to $\overline{E}^{ip}_{yy}$, is the weighted average of the true axial stress at all integration points at a particular axial cross-section. In order to evaluate how well the measured behavior represents the material's actual uniaxial stress-strain response, the true stress-strain response predicted by the constitutive model for homogeneous uniaxial tension at strain rates

of $0.0005\,\mathrm{s}^{-1}$ and $0.05\,\mathrm{s}^{-1}$ is also plotted in Figure 2-15.

Locations 1, 3, and 5 exhibit, particularly at intermediate strains, significantly different stress-strain responses due to their disparate strain rate histories. The strain rate is not a function of position until after macroscopic yield, however, and hence yield at all three locations occurs at 65 MPa. At macroscopic yield, the strain rate is close to $0.005\,\mathrm{s}^{-1}$, and the measured yield strength sits squarely between the yield strengths predicted by the constitutive model for strain rates of $0.0005\,\mathrm{s}^{-1}$ and $0.05\,\mathrm{s}^{-1}$. After macroscopic yield, the rate of strain softening increases as the distance from the site of neck initiation grows larger. At location 1, the strain rate jumps by an order of magnitude and the stress-strain curve correspondingly shifts nearly up to the prediction for $\dot{E}_{yy} = 0.05\,\mathrm{s}^{-1}$. At strains larger than $\overline{E}_{yy} = 0.33$, the strain rate at location 1 steadily decreases to approximately $0.0005\,\mathrm{s}^{-1}$, and the stress-strain curve follows suit by gradually transitioning to the behavior predicted for a strain rate of $0.0005\,\mathrm{s}^{-1}$. Here, the decrease in strain rate is in competition with the tendency of the material to strain harden. Once the neck stabilizes at $\overline{E}^{\mathrm{ip}}_{yy} \approx 0.54$, the strain rate goes to zero as the neck propagates along the specimen. The strain rate at location 3 deviates from that at location 1 soon after macroscopic yield. The decrease to a minimum of near zero exaggerates the strain softening response and causes a rather sudden drop in the stress level below that predicted for $\dot{E}_{yy} \approx 0.0005\,\mathrm{s}^{-1}$. Once the neck begins to propagate, the strain rate at 3_{F} increases, and the behavior follows the pattern of location 1. The response at location 5 follows the same trend as locations 1 and 3, but, in this case, as illustrated in Figure 2-14, the strain rate falls to zero or less for over 60 s as elastic unloading occurs. The elastic unloading is manifested in Figure 2-15 by the parallel loading and unloading stress-strain curves. Finally, all three stress-strain curves exhibit a "kink" at $\overline{E}^{\mathrm{ip}}_{yy} \approx 0.53$ coincident with the neck reaching the grip regions of the specimen and the re-establishment of homogeneous deformation. This phenomenon is due to the fact that, after the neck propagates through, all sections but the last to localize experience a period of stress relaxation followed by a strain rate jump from zero to approximately $.0015\mathrm{s}^{-1}$.

For the most part, the stress-strain curves at all three locations are bracketed by

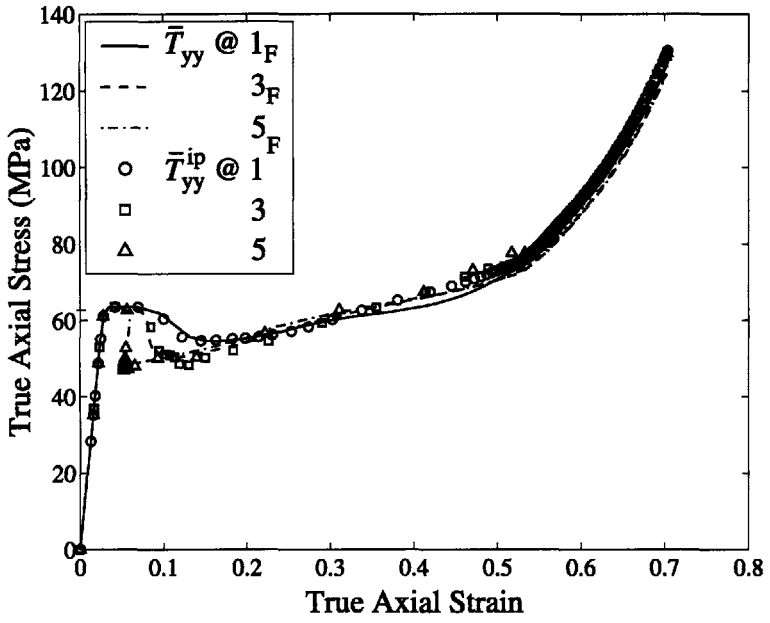

Figure 2-16: Tensile bar simulation results for uniaxial tension of neat PC. Macroscopic true axial stress, $\overline{T}_{yy}$, versus macroscopic true axial strain, $\overline{E}_{yy}$, and macroscopic true axial stress, $\overline{T}^{\text{ip}}_{yy}$, versus macroscopic true axial strain, $\overline{E}^{\text{ip}}_{yy}$, at axial locations 1, 3, and 5.

the constitutive behavior at $\dot{E}_{yy} = 0.0005\,\text{s}^{-1}$ and $\dot{E}_{yy} = 0.05\,\text{s}^{-1}$. Overall, when strain rate effects are included, the average stress and strain in a tensile bar is shown to represent adequately the material stress-strain response. The experimental technique, however, is not privy to the stress and strain at interior points. It can only measure the surface strains and the average stress in the specimen. In order to demonstrate the accuracy of the present technique, the average stress-strain response, calculated as above using all integration points at a cross-section ($\overline{T}^{\text{ip}}_{yy}$-$\overline{E}^{\text{ip}}_{yy}$) is compared, in Figure 2-16, to the average stress-strain response ($\overline{T}_{yy} - \overline{E}_{yy}$) evaluated using the quantities in the simulation corresponding most closely to those actually measured during the experiments. $\overline{T}_{yy}$ is computed from Equation 2.14, with P given by the sum of the nodal reaction forces at the grip. $\overline{E}_{xx}$ is calculated as $\ln\overline{\lambda}_{xx}$ with $\overline{\lambda}_{xx}$ computed from Equation 2.10 and X_{2L} and X_{2R} given by the displacements of nodes at the edges of the bar. $\overline{E}_{yy}$ is calculated from the axial strains at five equi-spaced integration points near the surface of the bar. The excellent agreement between the

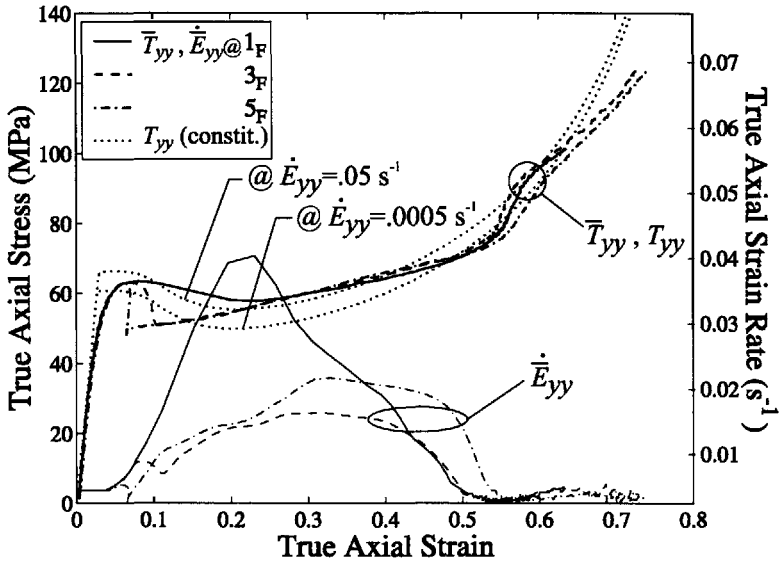

Figure 2-17: Experimental results for uniaxial tension of neat PC. Macroscopic true axial stress, $\overline{T}_{yy}$, (left hand axis) and macroscopic true axial strain rate, $\dot{\overline{E}}_{yy}$, (right hand axis) versus macroscopic true axial strain, $\overline{E}_{yy}$, at axial locations 1_F, 3_F, and 5_F. Constitutive model true axial stress, T_{yy}, versus true axial strain, E_{yy}, at true strain rates $\dot{E}_{yy} = 0.0005\,s^{-1}$ and $\dot{E}_{yy} = 0.05\,s^{-1}$.

two sets of stress-strain curves shown in Figure 2-16 proves that the assumptions of the experimental technique are valid.

The experimentally measured stress-strain and strain rate data depicted in Figure 2-17 exhibits the same trends observed in the simulation, but there are minor discrepancies. As alluded to in Section 2.3.1, the initial axial strain rate, when the deformation is still homogeneous, is smaller than expected due to the compliance of the machine and the alignment of the grips. The stress-strain response at location 1_F strain softens less and at a rate slower than that of the simulation. This is likely due to the peak in strain rate at location 1_F being substantially broader in the experiment than in the simulation (Figure 2-15). As observed in Figures 2-4 and 2-5 and discussed in Section 2.3.1, the shear band in the simulation is sharper than the shear band that forms during the experiment. The intensity of localization is proportional to the strain rate. The experimental and simulation results also differ at large axial strains. The experimental stress-strain curves exhibit a sharper kink at $\overline{E}_{yy} \approx 0.54$ and a lower rate of strain hardening than the stress-strain curves of the simulation.

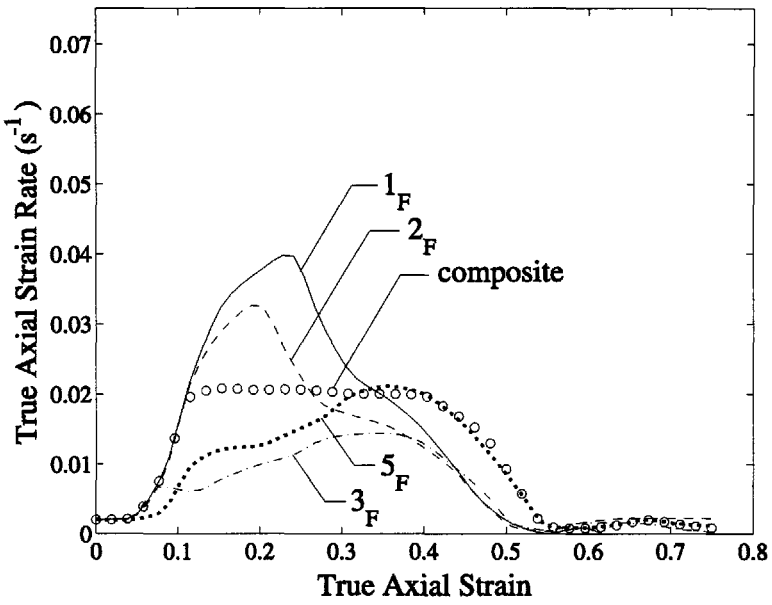

Figure 2-18: Uniaxial tension of neat PC. Macroscopic true axial strain rate, $\dot{\overline{E}}_{yy}$, versus true axial strain, $\overline{E}_{yy}$, at axial locations 1_F, 2_F, 3_F, and 5_F and composite curve.

This is, at least in part, an artifact of the parameters used in the material model of the simulation. Due to an increasingly gradual transition from localized deformation to homogeneous deformation, the magnitude of the kink in the experimental stress-strain curve decreases as the measurement location is moved away from the point of neck initiation. Figure 2-8 shows that, immediately after neck stabilization, the strain at point $5A_F$ increases almost monotonically while the strain at locations closer to the site of neck formation remains almost constant. Correspondingly, in Figure 2-17, at large axial strains, the strain rate at point 5_F remains positive. After the drawing strain is reached, the strain rate at locations 1_F and 3_F, however, is nearly zero until the neck reaches the grip regions of the specimen.

The fact that the strain rate versus axial strain relationship is different at every axial location on the specimen is used to approximate the constant strain rate true stress-strain response of the material. Every point on the specimen gage length eventually experiences the entire range of axial strains. A composite stress-strain curve based on strain rate can therefore be constructed from the results at any number of axial locations. The composite curve was assembled, in a manner similar to that de-

scribed in Section 2.2.3, by performing the correlation, macroscopic true stress-strain calculation, and macroscopic strain rate calculation at every fourth axial pixel location (for a total of approximately 100). The results were then interpolated to coincide with 40 macroscopic axial strains spaced equally between $\overline{E}_{yy} = 0$ and $\overline{E}_{yy} = 0.75$. The response chosen to represent each axial strain was taken from the axial location which exhibited a strain rate closest to a designated target rate. Figure 2-18 illustrates the locations and strain rates chosen for a target rate of $\dot{\overline{E}}_{yy} = 0.02\,\mathrm{s}^{-1}$. For clarity, the strain rate versus axial strain relationship is shown at only four locations, but it is apparent how the composite strain rate curve transitions from the behavior at location 1_F at small axial strains to the behavior at location 5_F at large axial strains. The target rate was chosen to maximize the width of the constant strain rate plateau while avoiding any strain rate drops during the early stages of deformation. While the strain rate is thus kept constant during much of the period of neck propagation, it is impossible to maintain a constant strain rate for all axial strains due to the large disparity in strain rates experienced over the course of a test.

The macroscopic stress-strain curves corresponding to the strain rate curves in Figure 2-18, together with the constitutive response at $\dot{E}_{yy} = 0.02\,\mathrm{s}^{-1}$, are shown in Figure 2-19. The composite macroscopic stress-strain curve transitions from the results at location 1_F to those at location 5_F. While the target strain rate is maintained, there is excellent agreement between the composite response and the constitutive model prediction. Because, at large axial strains, it takes on the behavior of the point on the gage section furthest from the site of neck formation, the composite curve also successfully avoids the kinking phenomenon.

2.3.4 Neat PC: Volumetric behavior

The final goal of this experimental study was to measure the volume change during a tensile test. In general, volumetric strain is an important measure for quantifying modes of deformation and/or identifying events such as debonding or cavitation. An amorphous, non-crazing polymer, polycarbonate is known to conserve volume during plastic deformation. The incompressibility of the material and the constraints of the

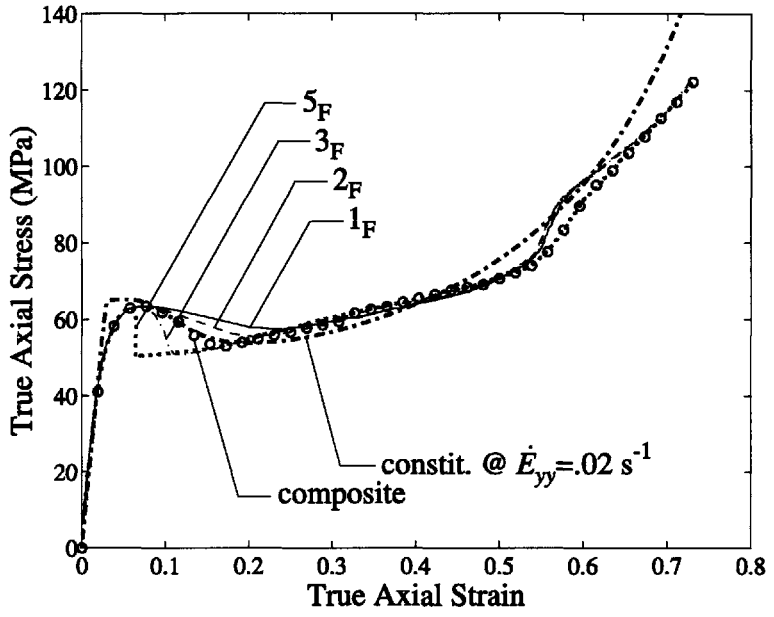

Figure 2-19: Uniaxial tension of neat PC. Macroscopic true axial stress, $\overline{T}_{yy}$, versus true axial strain, $\overline{E}_{yy}$, at axial locations 1_F, 2_F, 3_F, and 5_F and composite curve. Constitutive model true axial stress, T_{yy}, versus true axial strain, E_{yy}, at true strain rate $\dot{E}_{yy} = 0.02\,\mathrm{s}^{-1}$.

specimen geometry cause the tensile bar to deform laterally in an inhomogeneous manner. The inhomogeneity is readily apparent upon examination of the surface of a deformed specimen. From the front view, the surface of the specimen exhibits an out-of-plane concave shape with the largest through-thickness macroscopic strains ($\overline{E}_{zz}$) occurring at the center, along the y-axis. This observation is in accord with Figure 2-10 which shows that E_{xx} is of minimum magnitude at $x = 0$. Therefore, the current area is slightly overestimated in Equations 2.9 and 2.14, which assume that $\overline{E}_{zz}$ is constant across the width of the specimen. While negligible when calculating the true stress, the error in the calculation of the current area prohibits determining the volumetric strain from macroscopic measurements. Very small in PC and a function of the *change* in area (not the area itself as in the case of the true stress), the volumetric strain is significantly overestimated by a macroscopic calculation.

Thus, for the volumetric strain, a local measurement and Equation 2.7 were used. The shape of the deformed specimens and the lateral strain behavior presented in Figures 2-10 and 2-13 indicate that, even locally, the material does not deform isotropi-

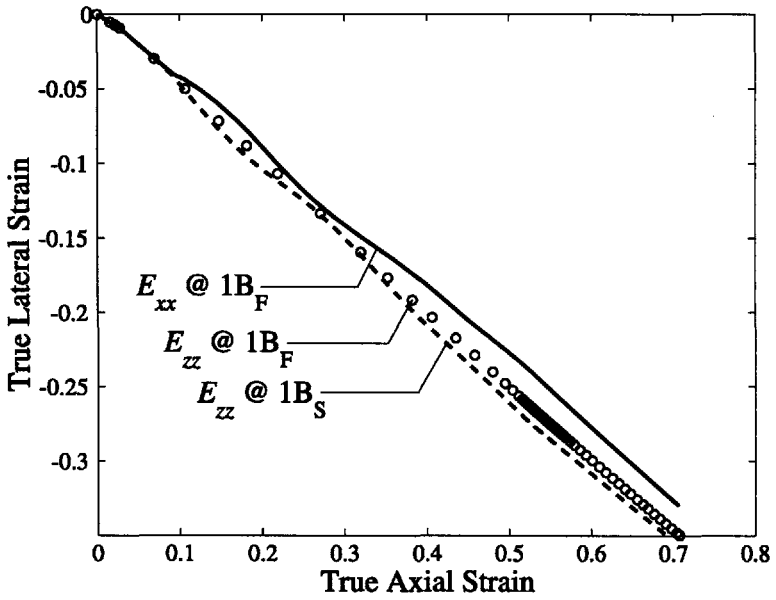

Figure 2-20: Tensile bar simulation results for uniaxial tension of neat PC. True lateral strains, E_{xx} and E_{zz}, versus true axial strain, E_{yy}, at axial location 1B.

cally in the two transverse directions. Since the current technique can only measure in-plane strains, the simulation was used to evaluate the degree of anisotropy and determine how best to measure the volumetric strain. Figure 2-20 shows that, at point $1B_F$, for example, the strains in the z-direction are substantially larger in magnitude than those in the x-direction. Assuming that the quantity measurable from the front view, E_{xx}, is identical to E_{zz} would thus overestimate the volume change. Figure 2-20, however, also indicates that the through-thickness lateral strain, E_{zz}, versus axial strain behavior at point $1B_S$ is nearly identical to that at point $1B_F$. Since it is impossible to measure both E_{xx} and E_{zz} at the same location, points $1B_F$ and $1B_S$ were assumed to represent approximately the same material point. The behavior measured on the z-plane at $1B_F$ and the behavior measured on the x-plane at $1B_S$ were combined in order to evaluate the volume change via Equation 2.7.

Combining two tests to obtain the volumetric strain introduces additional sources of error. The simulation showed that the results at points $1B_F$ and $1B_S$ accurately represent the behavior of a single material point. The experimental results, however, must be taken from separate tests, and unfortunately no two specimens deform iden-

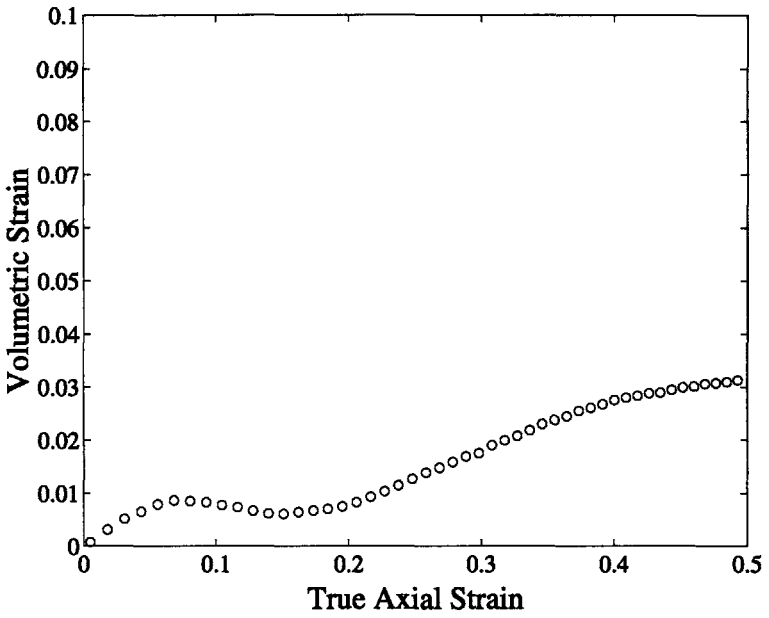

Figure 2-21: Uniaxial tension of Neat PC. Volumetric strain, E_{kk}, versus true axial strain, E_{yy}, at axial location 1.

tically. Therefore, from each perspective, up to six tests were performed, and the results at points 1B and 1C were interpolated and averaged for each axial strain, E_{yy}, to form the mean displacement gradients $\overline{\mathbf{H}}^{\mathrm{F}}$ and $\overline{\mathbf{H}}^{\mathrm{S}}$. $\overline{\mathbf{H}}^{\mathrm{F}}$ and $\overline{\mathbf{H}}^{\mathrm{S}}$ were correlated at each axial strain, and the deformation gradient was defined as

$$\mathbf{F} = \begin{pmatrix} \overline{H}^{\mathrm{F}}_{xx} + 1 & \overline{H}^{\mathrm{F}}_{xy} & 0 \\ \overline{H}^{\mathrm{F}}_{yx} & (\overline{H}^{\mathrm{F}}_{yy} + \overline{H}^{\mathrm{S}}_{yy})/2 + 1 & \overline{H}^{\mathrm{S}}_{yz} \\ 0 & \overline{H}^{\mathrm{S}}_{zy} & \overline{H}^{\mathrm{S}}_{zz} + 1 \end{pmatrix}. \tag{2.16}$$

The volumetric strain calculated from Equations 2.7 and 2.16 for uniaxial tension of neat PC is shown in Figure 2-21. At small strains, the volumetric strain increases linearly due to the elastic Poisson effect. At $E_{yy} \approx 0.07$, the volume change levels off at $E_{kk} \approx 0.01$ as the mode of deformation switches to incompressible plastic flow. Immediately thereafter, the volumetric strain decreases slightly. The decrease in volume is likely due to the elastic recovery that occurs as the stress level drops during the strain softening stage of deformation. At $E_{yy} \approx 0.20$, the volumetric strain increases again before finally leveling off at $E_{kk} \approx 0.03$ at $E_{yy} = 0.50$. Further

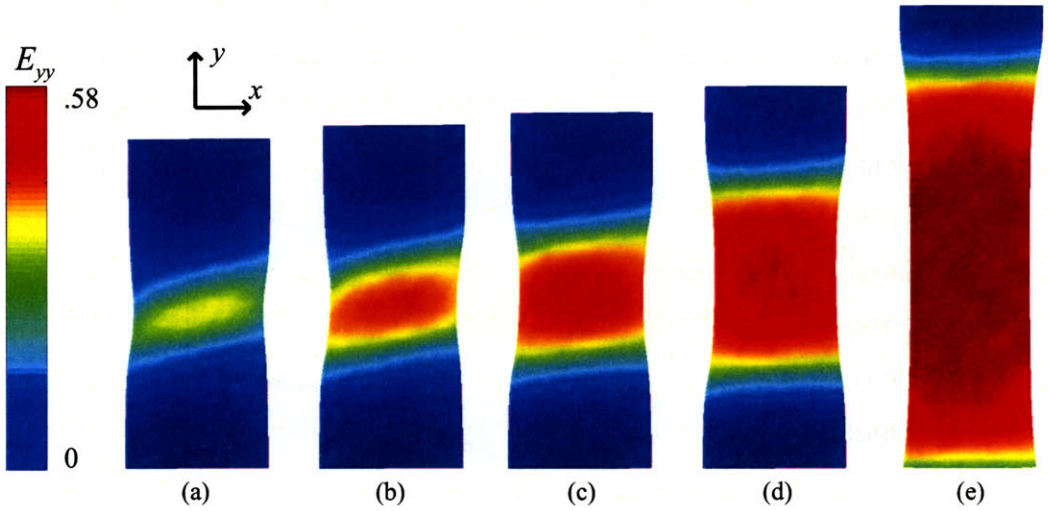

Figure 2-22: Experimental uniaxial tension of rubber-filled PC, $f = 0.05$ (front view). Contours of true axial strain, E_{yy}, for increasing crosshead displacement, U: (a) $U = 3.0\,\text{mm}$, (b) $U = 3.5\,\text{mm}$, (c) $U = 4.0\,\text{mm}$, (d) $U = 5.0\,\text{mm}$, (e) $U = 8.0\,\text{mm}$.

dilatation is attributed to the additional elastic deformation which takes place during the strain hardening stage of deformation and possible small-scale cavitation events at defects (such as dust particles) in the material.

The maximum error in the volumetric strain calculation is approximated from Equations 2.7 and 2.8 by neglecting the shear strains and assuming that the noise acts in the same direction as the out-of-plane error (i.e. minimizing E_{yy} and maximizing E_{xx} and E_{zz}). The error ranges almost linearly from -300 $\mu\epsilon$ at $E_{yy} = 0$ to -2100 $\mu\epsilon$ at $E_{yy} = 0.5$. Even at its absolute theoretical maximum, this error is only roughly 10% of E_{kk} and is within acceptable bounds.

2.3.5 Rubber-filled PC

Confident in our methodology, we conducted the full-field strain, macroscopic stress-strain, and volumetric strain analyses described in the previous sections on blends with volume fractions of rubber particles ranging from 5% to 25%.

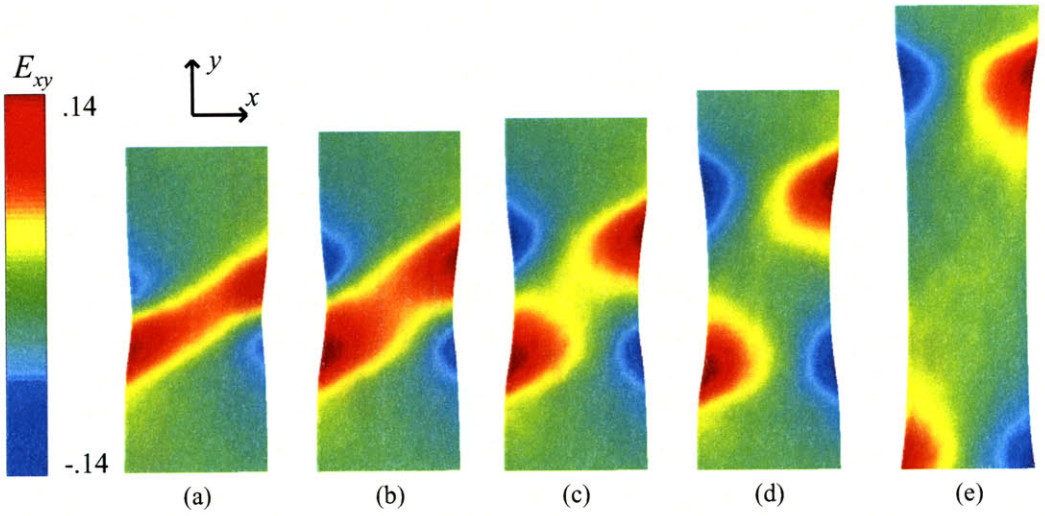

Figure 2-23: Experimental uniaxial tension of rubber-filled PC, $f = 0.05$ (front view). Contours of true shear strain, E_{xy}, for increasing crosshead displacement, U: (a) $U = 3.0\,\text{mm}$, (b) $U = 3.5\,\text{mm}$, (c) $U = 4.0\,\text{mm}$, (d) $U = 5.0\,\text{mm}$, (e) $U = 8.0\,\text{mm}$.

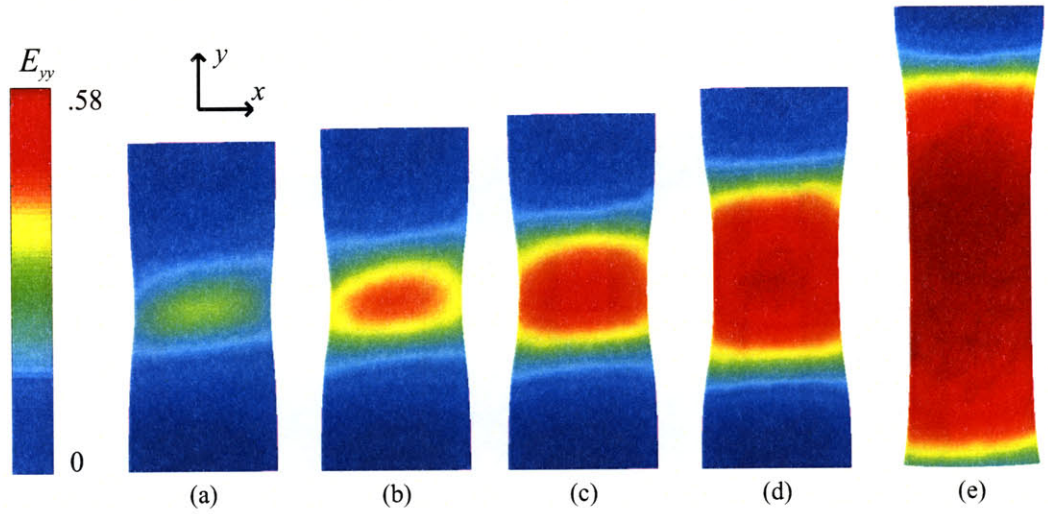

Figure 2-24: Experimental uniaxial tension of rubber-filled PC, $f = 0.15$ (front view). Contours of true axial strain, E_{yy}, for increasing crosshead displacement, U: (a) $U = 3.0\,\text{mm}$, (b) $U = 3.5\,\text{mm}$, (c) $U = 4.0\,\text{mm}$, (d) $U = 5.0\,\text{mm}$, (e) $U = 8.0\,\text{mm}$.

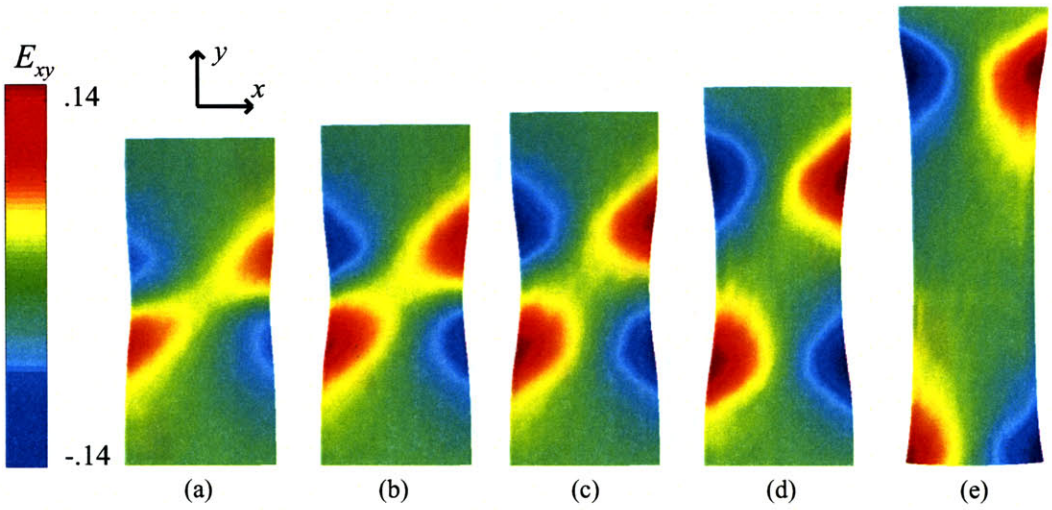

Figure 2-25: Experimental uniaxial tension of rubber-filled PC, $f = 0.15$ (front view). Contours of true shear strain, E_{xy}, for increasing crosshead displacement, U: (a) $U = 3.0\,\text{mm}$, (b) $U = 3.5\,\text{mm}$, (c) $U = 4.0\,\text{mm}$, (d) $U = 5.0\,\text{mm}$, (e) $U = 8.0\,\text{mm}$.

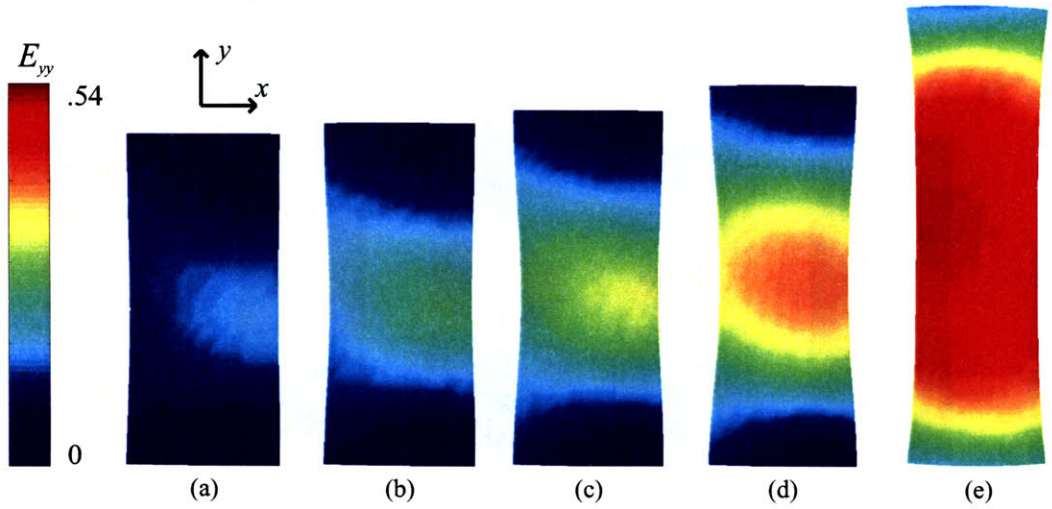

Figure 2-26: Experimental uniaxial tension of rubber-filled PC, $f = 0.25$ (front view). Contours of true axial strain, E_{yy}, for increasing crosshead displacement, U: (a) $U = 3.0\,\text{mm}$, (b) $U = 3.5\,\text{mm}$, (c) $U = 4.0\,\text{mm}$, (d) $U = 5.0\,\text{mm}$, (e) $U = 8.0\,\text{mm}$.

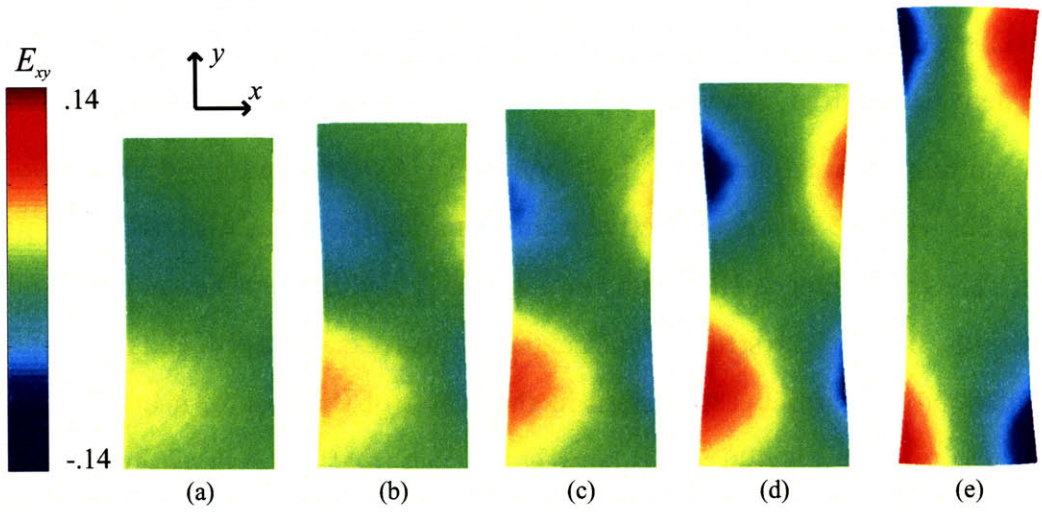

Figure 2-27: Experimental uniaxial tension of rubber-filled PC, $f = 0.25$ (front view). Contours of true shear strain, E_{xy}, for increasing crosshead displacement, U: (a) $U = 3.0\,\text{mm}$, (b) $U = 3.5\,\text{mm}$, (c) $U = 4.0\,\text{mm}$, (d) $U = 5.0\,\text{mm}$, (e) $U = 8.0\,\text{mm}$.

Full-field strain contours

Contours of true axial and shear strain for the three rubber-filled blends are plotted in Figures 2-22 through 2-27. The corresponding load versus crosshead displacement data for neat PC and the blends is presented in Figure 2-28. One further measure of the deformation is the local true axial strain, E_{yy}, at the center of the neck ($1A_F$ in Figure 2-7), equal to the maximum local strain, which is plotted versus crosshead displacement in Figure 2-29.

Comparing Figures 2-22a and 2-24a for $f = 0.05$ and $f = 0.15$, respectively, to Figure 2-4a′, one sees that localization begins at a lower crosshead displacement in the blends than it does in neat PC. The load versus displacement plot shows that, at U=3.0 mm, the load on the two blends has dropped nearly to its post-yield minimum while the load on the neat specimen has just passed its peak. Correspondingly, mirroring the full-field strain contours, the maximum local strain of all three blends accelerates at a lower crosshead displacement than the maximum local strain of neat PC. Localization occurs when the load drops, and its intensity is determined by how steep and prolonged the load drop is. Although the blends exhibit decreasing stiffness with increasing f, they also show a decreasing peak load with increasing f. These two

factors conspire to cause localization to occur at approximately the same crosshead displacement in all three blends.

The contours of axial strain of the blends with $f = 0.05$ and $f = 0.15$, shown in Figures 2-22 c-e and 2-24 c-e, respectively, are remarkably similar to those of the neat polymer. These two blends show substantial, sharp load drops that are comparable in magnitude. In turn, the strain in the center of the necks of these blends accelerates at virtually the same rate as the strain in the center of the neck of neat PC. There are, however, two notable differences between the deformation observed in the blends with the two lower volume fractions of filler and the deformation of neat PC. First, the shear strain contours for $f = 0.05$ in Figure 2-23 and, particularly, for $f = 0.15$ in Figure 2-25 show substantially less shear deformation than the contours for neat PC in Figure 2-5. Even at low volume fractions, the rubber particles stabilize the deformation in the sense that they inhibit the sudden shear band formation which occurs in the homopolymer. Second, up to $f = 0.15$, the drawing strain, the axial strain at which the axial strain in the neck plateaus with respect to the crosshead displacement and the neck propagates, grows larger with increasing f. In Figure 2-29, the axial strain in neat PC and the blends with $f = 0.05$ and $f = 0.15$ has reached the plateau at $U = 8.0\,\text{mm}$. The corresponding axial strain contours exhibit increasing maximum strains with increasing f. It is noted that the strain in the neck never actually attains a perfect plateau. During the time between when the neck begins to propagate and when the neck reaches the grip regions of the specimen, the strain at the location where necking began increases very slowly at a nearly constant rate. Defining the drawing strain somewhat arbitrarily as the center of the linear portion of the strain versus displacement curve, we calculate the drawing strains to be 0.54, 0.58, and 0.61 for $f = 0$, $f = 0.05$, and $f = 0.15$, respectively.

The deformation of the blend with $f = 0.25$ is quite different than that of the homopolymer and the blends with the lower volume fractions of particles. The contours of axial strain in Figure 2-26 depict a pattern of deformation substantially more uniform than that observed in any of the other materials. The plots of shear strain in Figure 2-27 show negligible shearing except where material is being drawn into the

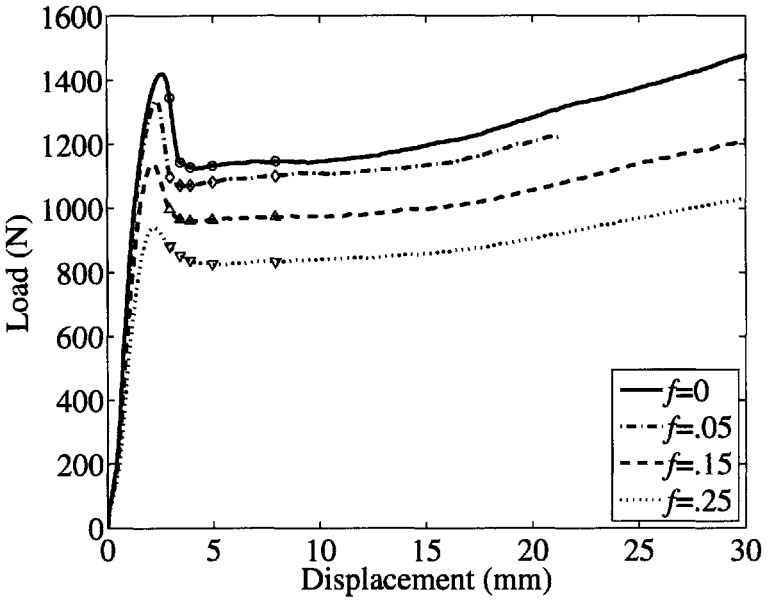

Figure 2-28: Uniaxial tension of neat and rubber-filled PC. Load, P, versus crosshead displacement, U. $\circ, \diamond, \triangle$, and $\triangledown$ denote displacements at which strain contours are shown.

neck. At $f = 0.25$, as mentioned previously, necking begins at the same displacement as in the other two blends, but, as evident in both the strain contours and the slope of the maximum local strain versus displacement plot, the neck forms at a slower rate and encompasses more material initially than the necks of the other blends and the homopolymer. The curvature of the neck itself is not as sharp, nor are the peak axial strain levels as high, as they are in the other materials. The reduced intensity of necking at $f = 0.25$ is due to the comparably small and gradual load drop. Furthermore, the plateau in the maximum local strain at $f = 0.25$ is not as pronounced as it is at the other volume fractions of particles. The strain in the neck during the period of neck propagation increases at a rate greater than that observed in the other three materials, adding to the relative homogeneity of the deformation at $f = 0.25$.

Further discussed in Section 2.3.5, the yield strength and post-yield strain softening, closely related to the peak load and rate and magnitude of the load drop, decrease with increasing f. These factors combine to diminish the intensity of localization, resulting in a substantially more homogeneous deformation at large f.

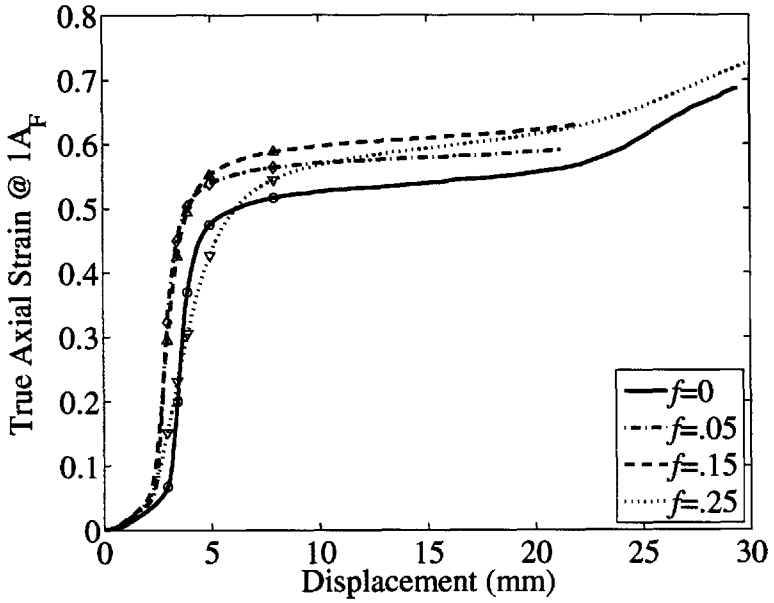

Figure 2-29: Uniaxial tension of neat and rubber-filled PC. True axial strain, E_{yy}, at location $1A_F$ versus crosshead displacement, U. $\circ, \diamond, \triangle$, and $\triangledown$ denote displacements at which strain contours are shown.

True axial stress-strain behavior

Figure 2-30 displays the composite macroscopic true stress-strain curves for the homopolymer and the three blends, and Figure 2-31 illustrates the true axial strain rates associated with each composite curve. As the volume fraction of rubber increases,

f	Yield Strength (MPa)	Young's Modulus, E (MPa)	E_{blend}/E	Poisson's ratio, ν
0	65.8	2280	1.0	0.392
.05	59.0	2140	0.94	0.397
.15	50.1	1760	0.77	0.414
.25	40.2	1430	0.63	0.423

Table 2.2: Yield strength and elastic properties of neat and rubber particle-modified PC.

the degree of localization and maximum strain rate decrease, allowing a smaller target strain rate to be chosen. In fact, with a target strain rate of $\dot{\bar{E}}_{yy} = 0.007\text{s}^{-1}$, the composite curves for $f = 0.15$ and $f = 0.25$ exhibit a nearly constant true strain rate. The stress-strain curves in Figure 2-30 show the expected decrease in modulus and yield strength with increasing volume fraction of rubber. Rubber has a tensile

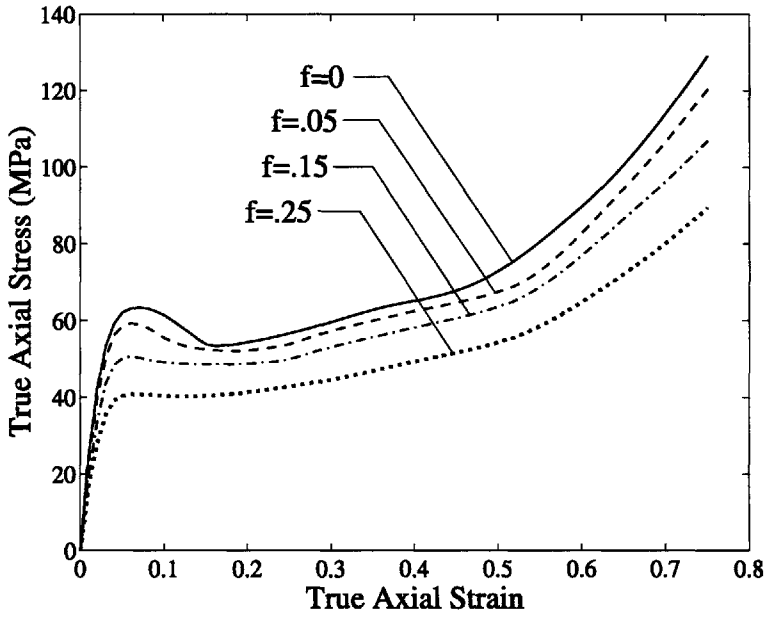

Figure 2-30: Uniaxial tension of neat and rubber-filled PC. Macroscopic true axial stress, $\overline{T}_{yy}$, versus true axial strain, $\overline{E}_{yy}$.

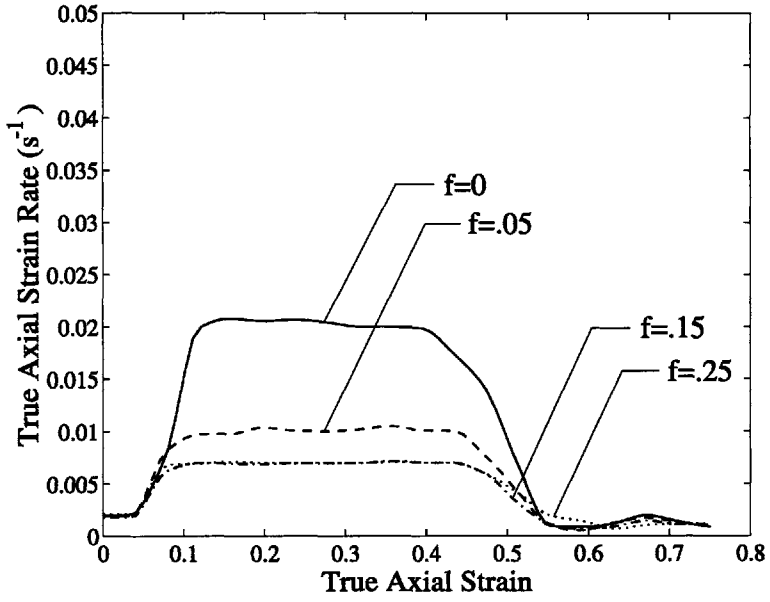

Figure 2-31: Uniaxial tension of neat and rubber-filled PC. True axial strain rate, $\dot{\overline{E}}_{yy}$, versus true axial strain, $\overline{E}_{yy}$.

modulus several orders of magnitude less than the elastic modulus of PC and provides negligible reinforcement in uniaxial tension. The elastic properties of the blends agree closely with the predictions of the composite model of Mori and Tanaka [48]. Details of the model and the specific form used are given in Appendix C. The predicted ratios of blend modulus to neat modulus, E_{blend}/E, for volume fractions of $f = 0.05$, $f = 0.15$, and $f = 0.25$, are 0.92, 0.77, and 0.64, respectively, while the measured ratios are 0.94, 0.77, and 0.63, respectively. Also calculated for each material from the elastic part of the true macroscopic axial versus lateral strain curve is the Poisson's ratio, ν. Possessing a Poisson's ratio approaching 0.5, the rubber particles increase the Poisson's ratios of the blends via a volume average effect. The predicted Poisson's ratios, for volume fractions of $f = 0.05$, $f = 0.15$, and $f = 0.25$, are 0.398, 0.409, and 0.420, respectively, while the measured values are 0.397, 0.414, and 0.423, respectively. Averaged over a minimum of four tests for each volume fraction of particles, the yield strengths and elastic properties are summarized in Table 2.2. Furthermore, consistent with the compression data of Johnson [39] and the micromechanical modeling of Danielsson et al. [19], the stress-strain data exhibits a decrease in post-yield strain softening and, at large strains, a decrease in strain hardening slope with increasing volume fraction of rubber. The reduction in rate and magnitude of post-yield strain softening with increasing f correlates well with the increasingly homogeneous deformation observed with increasing f in the full-field strain contours. As discussed in Section 2.3.1, the axial location where necking initiates is the first to yield. The instability is due to the inability of the plastic resistance of the material to balance the shrinking cross-sectional area of the specimen. Strain softening exacerbates the localization phenomenon by causing adjacent areas to unload elastically. As the rate and magnitude of strain softening decreases, the deformation becomes more diffuse and the neck less pronounced.

Volumetric behavior

The volumetric strain in neat PC and the three blends is depicted in Figure 2-32. In general, the rubber-modified blends behave very similarly. All three blends exhibit

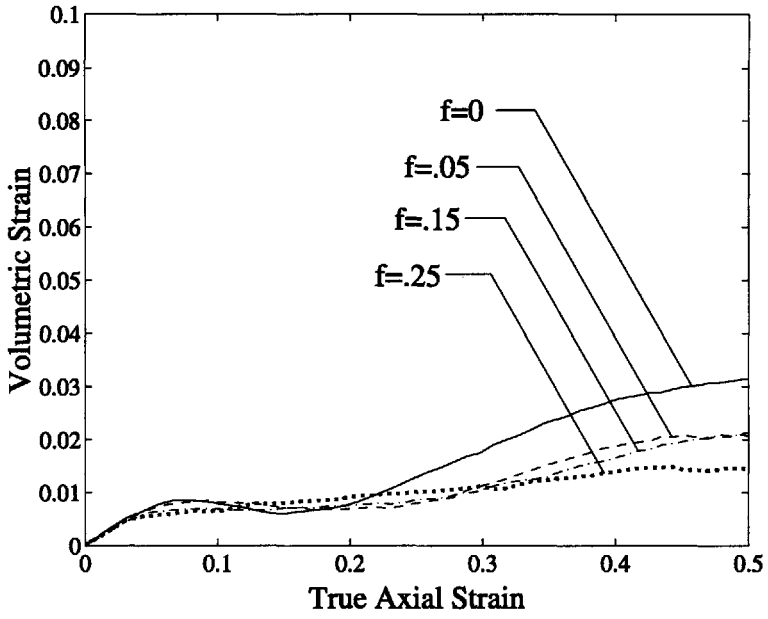

Figure 2-32: Uniaxial tension of neat and rubber-filled PC. Volumetric strain, E_{kk}, versus true axial strain, E_{yy}, at axial location 1.

less dilatation – both in the elastic and plastic regimes – than neat PC. The lack of volume change is a clear indication that the rubber particles do not cavitate. As f increases, consistent with the decrease in Poisson's ratio, the initial slopes of the curves, $\mathrm{d}E_{kk}/\mathrm{d}E_{yy}$, decrease and the curves plateau at lower axial strains. Well predicted by the Mori-Tanaka model, the slight decrease in slope with increasing f in the elastic regime is simply due to the volume averaging of the elastic behavior of the two constituent materials. The leveling off at decreasing axial strains with increasing f corresponds to the decrease in yield strain with increasing f observed in the stress-strain responses in Figure 2-30. After macroscopic yield, the blend with $f = 0.05$ shows, presumably due to elastic unloading, a drop in volumetric strain similar to that of the homopolymer but smaller and more elongated. In the blends with $f = 0.15$ and $f = 0.25$, there is no discernable decrease in volumetric strain. This trend agrees with the reduction in magnitude and slope of post-yield strain softening with increasing f observed in Figure 2-30.

2.4 Conclusions

The methodology developed in this chapter was successful in characterizing to large tensile strains the behavior of inhomogeneously deforming neat and particle-modified polymers. It proved capable of measuring true stress-strain response, full-field strain contours and volumetric strain. Tensile true stress-strain response is one of the most fundamental mechanical properties of a material, but it has been largely unavailable for polymers that neck and draw in the manner of PC. Experimental full-field strain contours provide invaluable information about deformation mechanisms. As illustrated in Section 2.3.5, they quantify not only the degree of localization but also modes of deformation such as shearing and axial stretching. Volumetric strain is a quantity critical for the thorough understanding of polymer deformation. In homopolymers, it is an indicator of cavitation, crazing, or crystal fragmentation. In filled polymers, cavitation or debonding of particles may be a source of volumetric strain. These three types of data paint a nearly complete picture of the deformation of a neat or particle-modified polymer. Armed with this data and other, more traditional test data (such as Izod impact energy, for example), one can confidently assess the performance of these types of material systems. Furthermore, as will be apparent in the latter half of this thesis, all experimental data necessary for the development of constitutive models of the tensile deformation of particle-modified polymers can be obtained with this methodology.

In the following chapter, an enhancement of this technique that enables simultaneous measurement of strain in all three dimensions is presented. Data for neat, $CaCO_3$-filled, and rubber-filled high-density polyethylene is reported. Discussion of the observed effects of the properties of the matrix and particles on the deformation of particle-modified polymers (including PC) occurs at the conclusion of Chapter 3.

Chapter 3

Tensile Testing of Neat, Rubber-Filled, and Calcium Carbonate-Filled High-Density Polyethylene

In chapter 2, stress and strain quantities during uniaxial tension tests were reduced from raw two-dimensional DIC data. In this chapter, a similar method is applied to neat and particle-modified high-density polyethylene (HDPE), but the full-field displacements and strains are measured simultaneously in all three dimensions with a single camera. The chapter concludes with a discussion of all experimental results.

3.1 Procedure

3.1.1 Sample preparation

The material used in this study was high-density polyethylene, trade name Dowlex IP-10, supplied by Dow Chemical Co. HDPE is a highly crystalline semi-crystalline polymer. The neat polymer and blends containing, by volume, 10% and 20% rubber or calcium carbonate ($CaCO_3$ or CC) particles were tested. The rubber particles were

a semi-crystalline ethylene-propylene-diene terpolymer (EPDM), trade name Nordel 2722, manufactured by Dow Elastomers. Bartczak et al. [7] reported the geometrical mean diameter to be 0.87 μm. Two types of $CaCO_3$ particles, both manufactured and surface-treated with calcium stearate by Specialty Minerals Inc., were used as fillers: "CC1", trade name Hi-Pflex 100, with a supplier reported mean geometrical diameter of 3.50 μm and "CC2", trade name Superpflex 200, with a supplier reported mean geometrical diameter of 0.70 μm. The neat polymer and blends were injection-molded into 12.7 mm × 3.2 mm × 144 mm bars. The mixing and molding process was conducted similarly to the method reported by Bartczak et al. [7, 8]. Tensile specimens (shown in Figure 3-1) with gage section dimensions 19.05 mm × 7.62 mm × 3.20 mm were machined from the molded bars.

3.1.2 Testing procedure

Except where noted, the tensile testing and image acquisition procedure was identical to that described in Section 2.2.2. Again it was not assumed that the specimens would deform isotropically in the two lateral directions. Therefore, as illustrated in Figure 3-1, *each* test was viewed from two orientations: the "front" view captured the deformation of the thick lateral dimension (x), and the "side" view captured the deformation of the thin lateral dimension (z). Following the work of Roux et al. [61], the two views were recorded simultaneously in the same image by utilizing a right-angle prism.

Figure 3-2 is a schematic of the experimental set-up. The camera captured the front view of the specimen directly. The right-angle prism reflected light from the side view 90°, allowing both views to appear in the same image. As shown in Figure 3-3, a fixture positioned the prism 12 mm from the side of the specimen.

3.1.3 Strain measurement

Displacements and strains were evaluated at individual points on the surfaces of the specimen. Similar to polycarbonate (PC), HDPE and its blends neck at fairly small

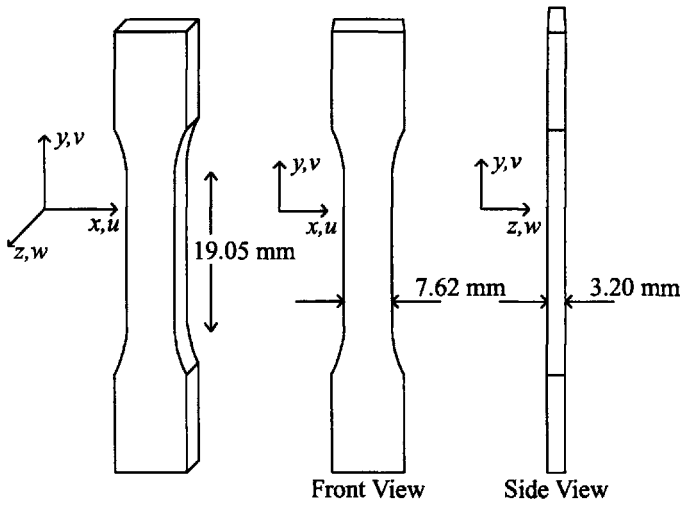

Figure 3-1: Specimen geometry and definition of views and coordinate directions. u, v, and w denote the displacements in the x, y, and z directions, respectively.

strains. Within the neck, the axial strain henceforth varies with axial position on the specimen, and, with the displacement gradient no longer constant, the concept of a gage length becomes obsolete. Digital image correlation was thus used to measure directly the pointwise displacements and displacement gradients. As explained in Chapter 2 for the two-dimensional case, second-order, two-dimensional shape functions, $u(x, y)$ and $v(x, y)$ from the front view, and $v(y, z)$ and $w(y, z)$ from the side view, map the positions within the reference subset to positions within each deformed image. The displacement and displacement gradient at the center of the subset are calculated by evaluating the shape functions and their partial derivatives at the center of the subset. Image resolution was 37.5 pixels/mm, and the subsets measured 51 pixels × 51 pixels. Local axial, lateral, and volumetric strains were calculated from the displacement gradients. Full-field contours of strain were constructed in a two step process from the local displacements.

Local strain calculation

Local lateral, axial, and volumetric strains were calculated directly from the derivatives of the second-order mapping functions described above. Formally, the derivatives

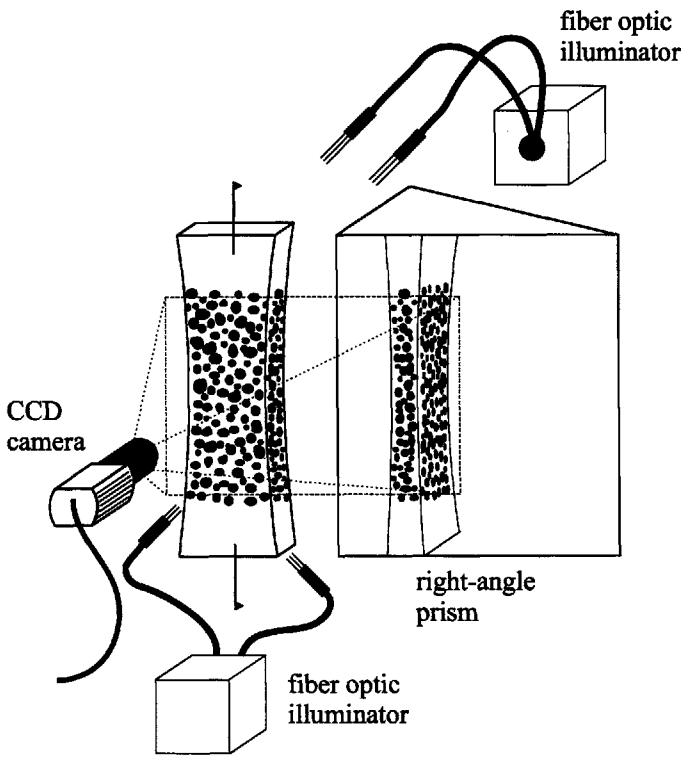

Figure 3-2: Schematic of experimental set-up (not to scale).

define the two-dimensional displacement gradients from the front and side views,

$$[\mathbf{H}_F] = \begin{pmatrix} \frac{\partial u}{\partial x} & \frac{\partial u}{\partial y} \\ \frac{\partial v}{\partial x} & \frac{\partial v}{\partial y} \end{pmatrix} \text{ and } [\mathbf{H}_S] = \begin{pmatrix} \frac{\partial v}{\partial y} & \frac{\partial v}{\partial z} \\ \frac{\partial w}{\partial y} & \frac{\partial w}{\partial z} \end{pmatrix}, \tag{3.1}$$

respectively. The two-dimensional deformation gradients from the front and side views, respectively,

$$\mathbf{F}_F = \mathbf{H}_F + 1 \text{ and } \mathbf{F}_S = \mathbf{H}_S + 1, \tag{3.2}$$

are thus known. From the polar decomposition, $\mathbf{F} = \mathbf{VR}$, the Hencky strain is calculated for each view as

$$\mathbf{E} = \ln \mathbf{V}. \tag{3.3}$$

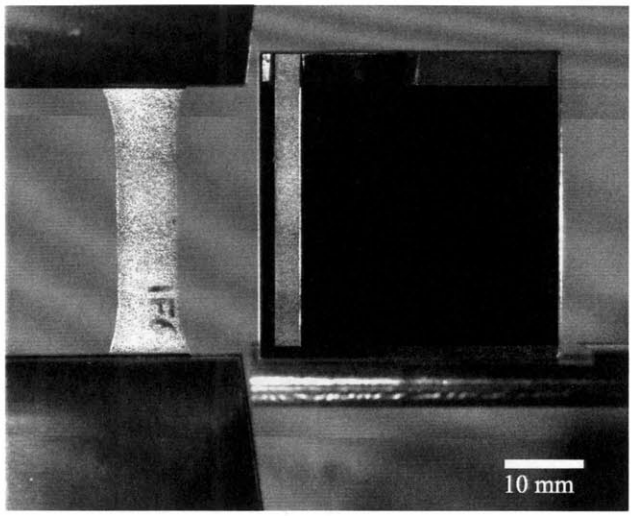

Figure 3-3: Specimen held between tensile machine grips (left) and right-angle prism (right).

The volumetric strain E_{kk} is defined as

$$E_{kk} = \ln\left(\frac{V}{V_0}\right) = \ln(\det \mathbf{F}_{FS}), \tag{3.4}$$

where $\mathbf{F}_{FS}$, constructed from $\mathbf{H}_F$ and $\mathbf{H}_S$, is an approximation of the three-dimensional deformation gradient at the edge of the specimen.

The local volumetric strain is calculated by approximating the pointwise deformation gradient from a cubic volume element at the edge of the specimen. Therefore, as shown in Figure 3-4, the components of $\mathbf{F}_{FS}$ are taken partially from a front-view subset and partially from a side-view subset. The two subsets are at identical y-coordinates and have a common edge. $\dfrac{\partial v}{\partial y}$ is taken from the front view, and $\dfrac{\partial u}{\partial z}$ and $\dfrac{\partial w}{\partial x}$ are assumed to be zero, giving

$$[\mathbf{F}_{FS}] = \begin{pmatrix} \dfrac{\partial u}{\partial x} + 1 & \dfrac{\partial u}{\partial y} & 0 \\ \dfrac{\partial v}{\partial x} & \dfrac{\partial v}{\partial y} + 1 & \dfrac{\partial v}{\partial z} \\ 0 & \dfrac{\partial w}{\partial y} & \dfrac{\partial w}{\partial z} + 1 \end{pmatrix}. \tag{3.5}$$

The front and side macroscopic true lateral strain versus true axial strain relationships

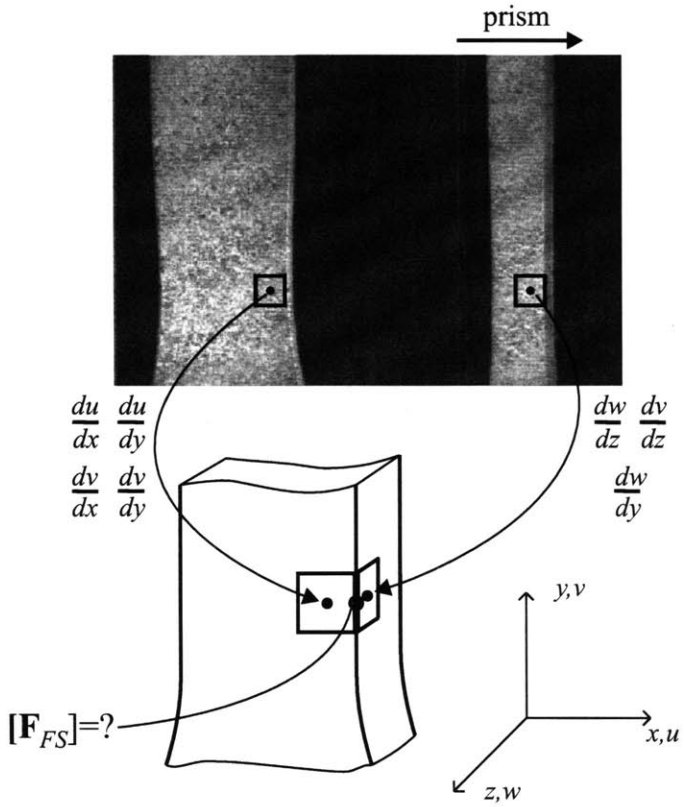

Figure 3-4: Data from adjacent subsets on the front and side of the specimen is combined to form $\mathbf{F}_{FS}$ in order to calculate the volumetric strain.

for 10% CC1-filled HDPE, depicted in Figure 3-5, illustrate the importance of using data from both the front and side views. The macroscopic true lateral strains were calculated from the specimen's dimensions as $\overline{E}_{xx} = \ln\overline{\lambda}_{xx}$ and $\overline{E}_{zz} = \ln\overline{\lambda}_{zz}$, with $\overline{\lambda}_{xx}$ and $\overline{\lambda}_{zz}$ defined by Equations 2.10 and 2.13, respectively. For $\overline{E}_{xx}$, the true axial strain, E_{yy}, was taken at the lateral center of the specimen from the front view, while, for $\overline{E}_{zz}$, E_{yy} was taken at the lateral center of the specimen from the side view. (In the HDPE experimental study, unlike the PC study, the axial strains were found to be approximately constant across the width of the specimen due to the fact that macroscopic shear bands did not form in either HDPE or any of its blends.) All strains were measured at the axial location where necking initiated. Readily apparent from a plot of axial strain versus time, the axial strain measures from each view are identical at any given instant. Up to an axial strain of approximately 0.4, the lateral versus axial strain relationship is nearly the same from both views. The specimen shrinks in the

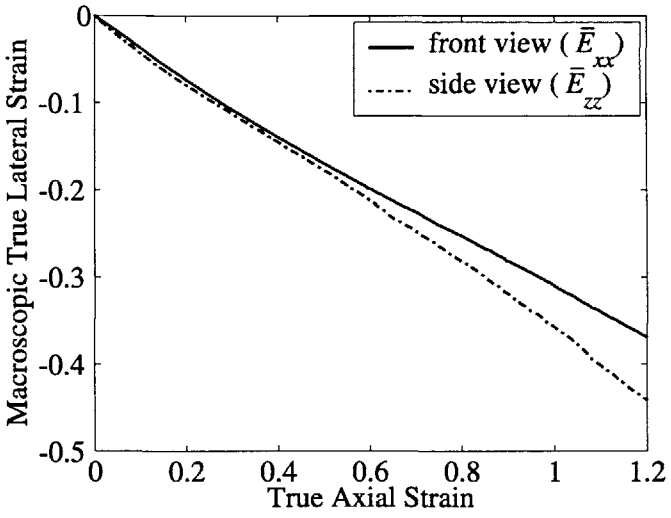

Figure 3-5: Uniaxial tension of 10% CC1-filled HDPE. Macroscopic true lateral strains, $\overline{E}_{xx}$ and $\overline{E}_{zz}$, versus true axial strain, E_{yy}, at the axial location where necking initiated ($1A_F$ in Figure 2-3).

lateral directions as it elongates in the axial direction, exhibiting an elastic Poisson's ratio of approximately 0.375. Beyond $E_{yy} = 0.4$, $\overline{E}_{zz}$ becomes larger in magnitude than $\overline{E}_{xx}$ as the specimen contracts more in the thinner z-direction than it does in the wider x-direction. The difference between $\overline{E}_{xx}$ and $\overline{E}_{zz}$ increases with increasing axial strain. At large axial strains, it is thus imperative to measure the strains in all three dimensions to calculate accurately the true stress and volumetric strain. The assumption of transversely isotropic deformations does not hold past axial strains of approximately 0.4.

As an example of the magnitude of the error in volumetric strain which is introduced if strains are measured in only two dimensions, Fig. 3-6 shows the volumetric strain for 10% CC1-filled HDPE calculated in three different ways: (1) using front-view data only and assuming transverse isotropy, (2) using side-view data only and assuming transverse isotropy, (3) using both front-view and side-view data to construct $\mathbf{F}_{FS}$ in Equation 3.4. It is apparent that using data from just one view results in errors in inferred volumetric strain of up to 30%.

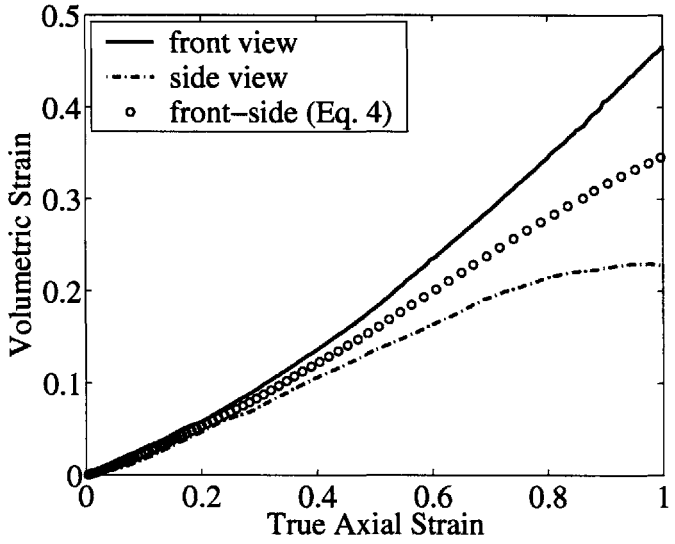

Figure 3-6: Uniaxial tension of 10% CC1-filled HDPE. Volumetric strain, E_{kk}, calculated with and without the assumption of transversely isotropic deformations, versus true axial strain, E_{yy}, at the axial location where necking initiated.

Full-field strain calculation

Contours of true axial strain were constructed from the displacement fields. Within the areas of interest, correlations were performed on pixel subsets of size 51×51 at a horizontal and vertical step size of four. The displacement of the center point of each subset was calculated and stored. Subsets of the displacement field of size 11 points $\times$ 11 points were then taken at a horizontal and vertical step size of two. A temporary $(\tilde{x}, \tilde{y})$ (front view) or $(\tilde{y}, \tilde{z})$ (side view) coordinate system was translated to the center of each displacement field subset. Second-order polynomial expressions for $u(\tilde{x}, \tilde{y})$ and $v(\tilde{x}, \tilde{y})$, or $v(\tilde{y}, \tilde{z})$ and $w(\tilde{y}, \tilde{z})$, were fit by least-squares approximation to each displacement field subset. The displacement gradient, $\mathbf{H}_F$ or $\mathbf{H}_S$, was constructed from the partial derivatives evaluated at each subset center. The logarithmic strain, $\mathbf{E} = \ln\mathbf{V}$, was then calculated and plotted to form the full-field contours of strain.

As an example of how the strains can now be visualized in three dimensions, Fig. 3-7 shows contours of true axial strain, E_{yy}, for a 10% CC1-filled HDPE tensile bar at increasing crosshead displacements, U. The plots depict an isometric view of

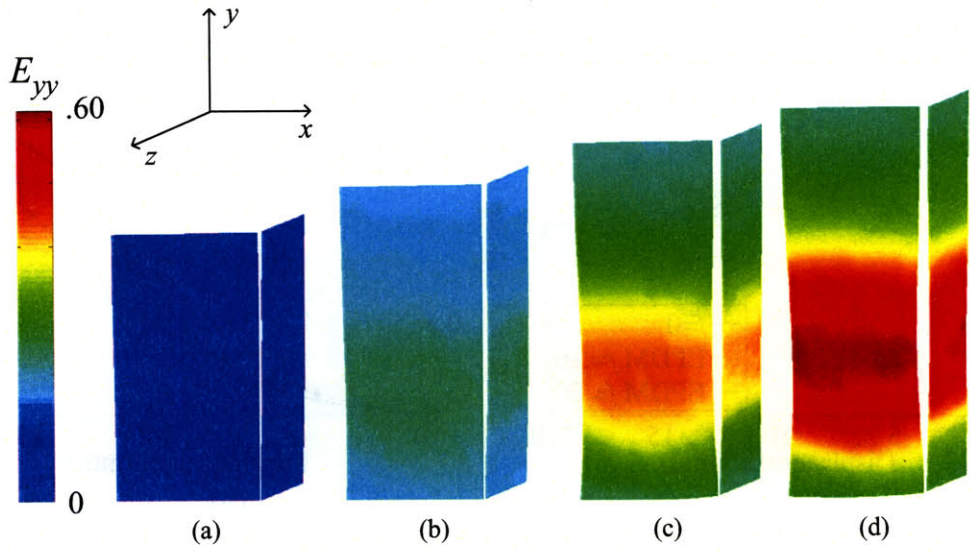

Figure 3-7: Uniaxial tension of 10% CC1-filled HDPE. Contours of true axial strain, E_{yy}, for increasing crosshead displacement, U: (a) $U = 3.1\,\text{mm}$, (b) $U = 6.3\,\text{mm}$, (c) $U = 8.7\,\text{mm}$, (d) $U = 10.1\,\text{mm}$.

an initially 12.7 mm long section of the gage length. Localization of the same general character as that observed in PC in Chapter 2 is apparent.

3.1.4 True stress calculation

As described in Section 2.2.4, the macroscopic true stress, $\overline{T}_{yy}$, was calculated as

$$\overline{T}_{yy} \equiv \frac{P}{A} = \frac{P}{A_0 \overline{\lambda}_{xx} \overline{\lambda}_{zz}}, \tag{3.6}$$

However, in this case, $\overline{\lambda}_{xx}$ and $\overline{\lambda}_{zz}$ were not assumed to be equal.

3.2 Results

3.2.1 Full-field strain contours and localization

As observed in Chapter 2 with polycarbonate, adding particles to a polymer can dramatically alter the localization process during a tension test. Here, the effect of hard and soft particles on localization is examined and compared. Figures 3-10

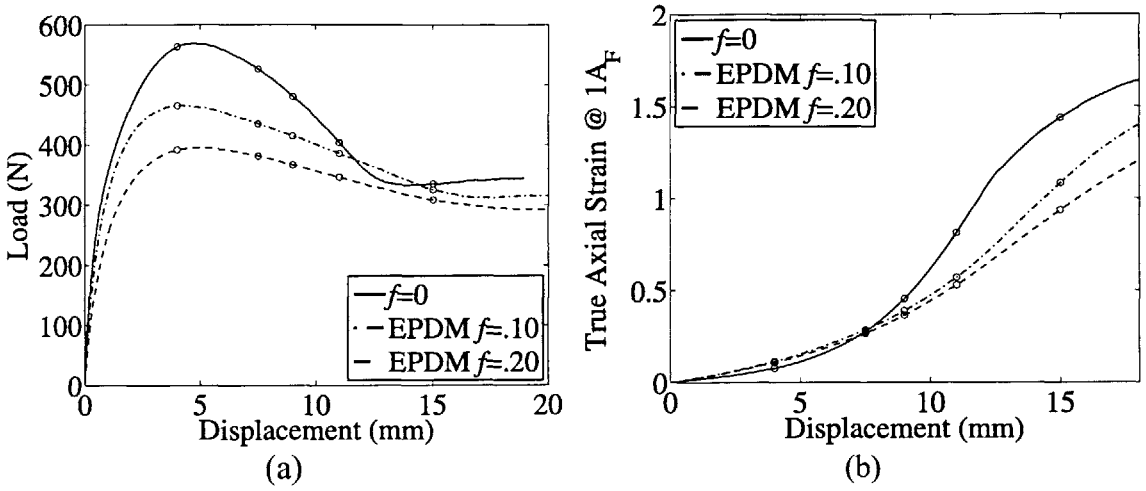

Figure 3-8: Uniaxial tension of neat and rubber-filled HDPE. (a) Load, P, versus crosshead displacement, U. (b) True axial strain, E_{yy}, at the center of the neck (maximum local strain) versus crosshead displacement, U. ○ denotes a displacement at which images and strain contours, where available, are plotted in Figures 3-10 through 3-14.

through 3-14 show images of the deformed specimens (a – e) and, where available, contours of true axial strain, E_{yy}, (a′–e′) for neat, rubber-filled, and CC2-filled HDPE at crosshead displacements, U, of 4.0 mm, 7.5 mm, 9.0 mm, 11.0 mm, and 15.0 mm. The strain contours are plotted for the region of the specimen within the dashed box in image (a) of each figure. The corresponding load versus crosshead displacement data is presented in Figures 3-8a and 3-9a . The local true axial strain, E_{yy}, at the center of the neck ($1A_F$ in Figure 2-7), equal to the maximum local strain, is plotted versus crosshead displacement in Figures 3-8b and 3-9b.

Taking neat HDPE first, we see in Figure 3-10a and 3-10a′, that the specimen initially deforms homogeneously. The sides of the specimen are parallel, and the axial strain contour plot shows an almost uniform axial strain range of $E_{yy} = 0.073 - 0.079$. The peak load has yet to be reached. At U=7.5 mm (b, b′), the load is decreasing as localization begins, and the strain field becomes non-uniform as the specimen "pinches in." The axial strain varies from 0.165 to 0.283. Correspondingly, the maximum local axial strain accelerates as all of the crosshead displacement is accommodated within the neck region of the specimen. In Figures 3-14 c-e, the strain steadily increases

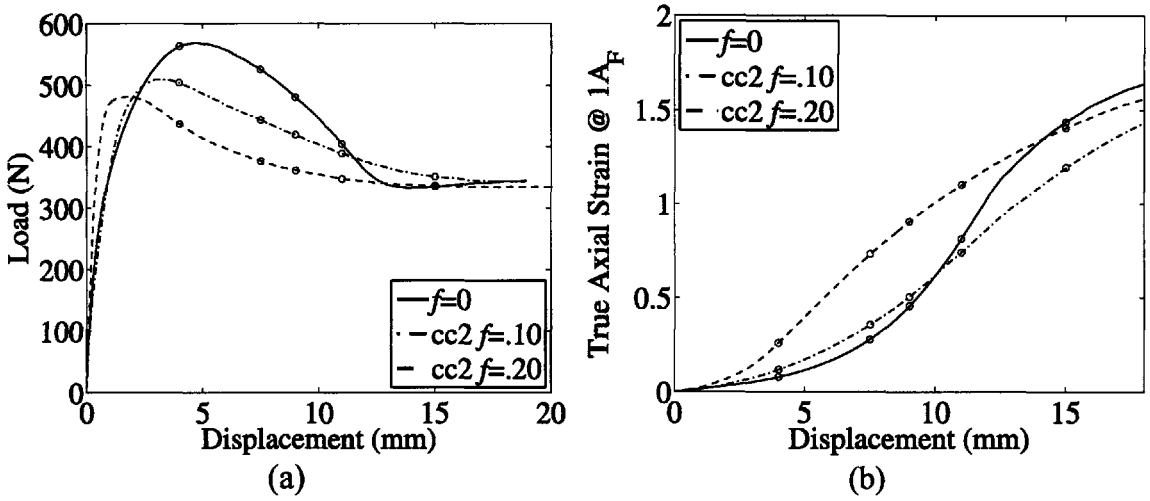

Figure 3-9: Uniaxial tension of neat and calcium carbonate-filled HDPE. (a) Load, P, versus crosshead displacement, U. (b) True axial strain, E_{yy}, at the center of the neck (maximum local strain) versus crosshead displacement, U. ○ denotes a displacement at which images and strain contours, where available, are plotted in Figures 3-10 through 3-14.

in this relatively small portion of the specimen while the rest of the specimen remains at an approximately constant strain. At the last available strain contour plot (U=11.0 mm) the axial strain range is $E_{yy} = 0.195 - 0.865$. Even at $U = 18.0$ mm and a maximum local axial strain exceeding 1.6, the maximum local axial strain continues to increase, indicating that the deformation is still concentrated within the region where the neck initiated. The material has not yet strain hardened sufficiently for the neck to stabilize and propagate. The flow stress of the material, increasing with strain, must catch up with the counteracting effect of the decreasing cross-sectional area of the specimen in order for the material to draw. These observations agree with Bartczak et al.'s [7] reporting of a natural draw ratio of 9 (drawing strain of 2.2) for this particular HDPE.

Introducing rubber filler particles vastly changes how the specimen deforms. The load versus displacement plot in Figure 3-8a shows a decrease in stiffness and peak load with increasing f. Since, as the slope decreases, the peak load also decreases, the peak load occurs at approximately the same crosshead displacement with all three volume fractions of particles. Accompanying the load drop is the increase in

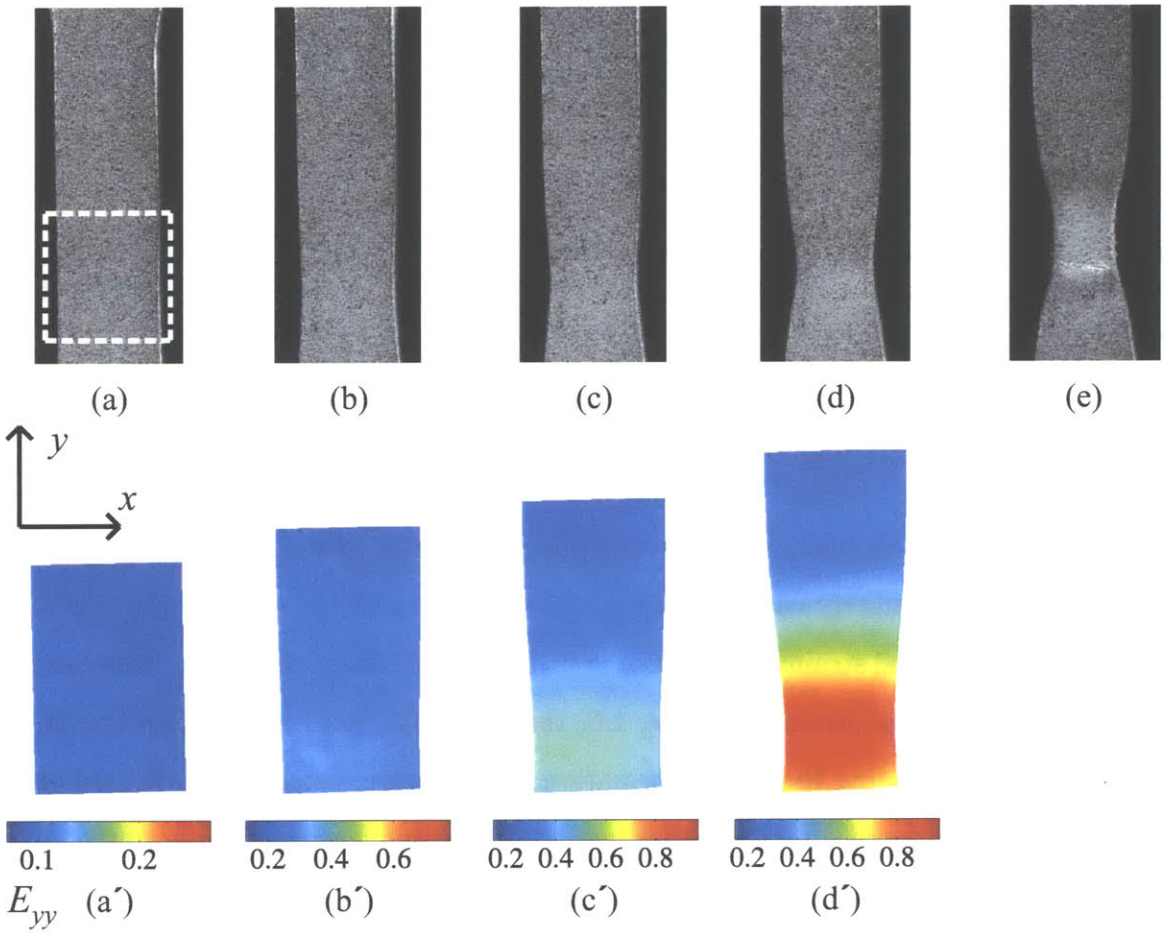

Figure 3-10: Uniaxial tension of neat HDPE (front view). Deformed specimen (top) and contours of true axial strain, E_{yy}, (bottom) for increasing crosshead displacement, U: (a), (a′) $U = 4.0\,\text{mm}$; (b), (b′) $U = 7.5\,\text{mm}$; (c), (c′) $U = 9.0\,\text{mm}$; (d), (d′) $U = 11.0\,\text{mm}$; (e), $U = 15.0\,\text{mm}$.

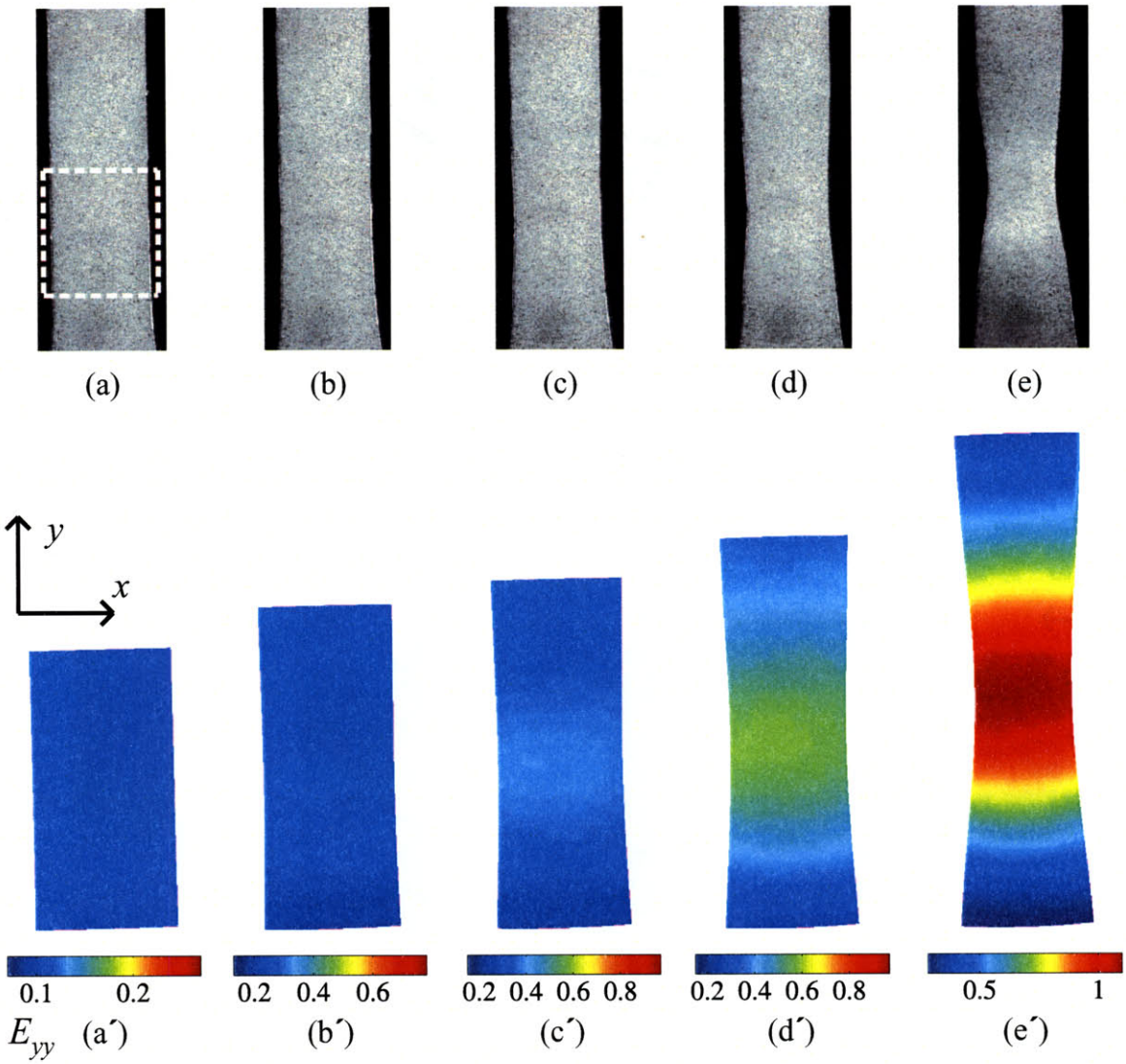

Figure 3-11: Uniaxial tension of 10% rubber-filled HDPE (front view). Deformed specimen (top) and contours of true axial strain, E_{yy}, (bottom) for increasing crosshead displacement, U: (a), (a′) $U = 4.0\,\text{mm}$; (b), (b′) $U = 7.5\,\text{mm}$; (c), (c′) $U = 9.0\,\text{mm}$; (d), (d′) $U = 11.0\,\text{mm}$; (e), (e′) $U = 15.0\,\text{mm}$.

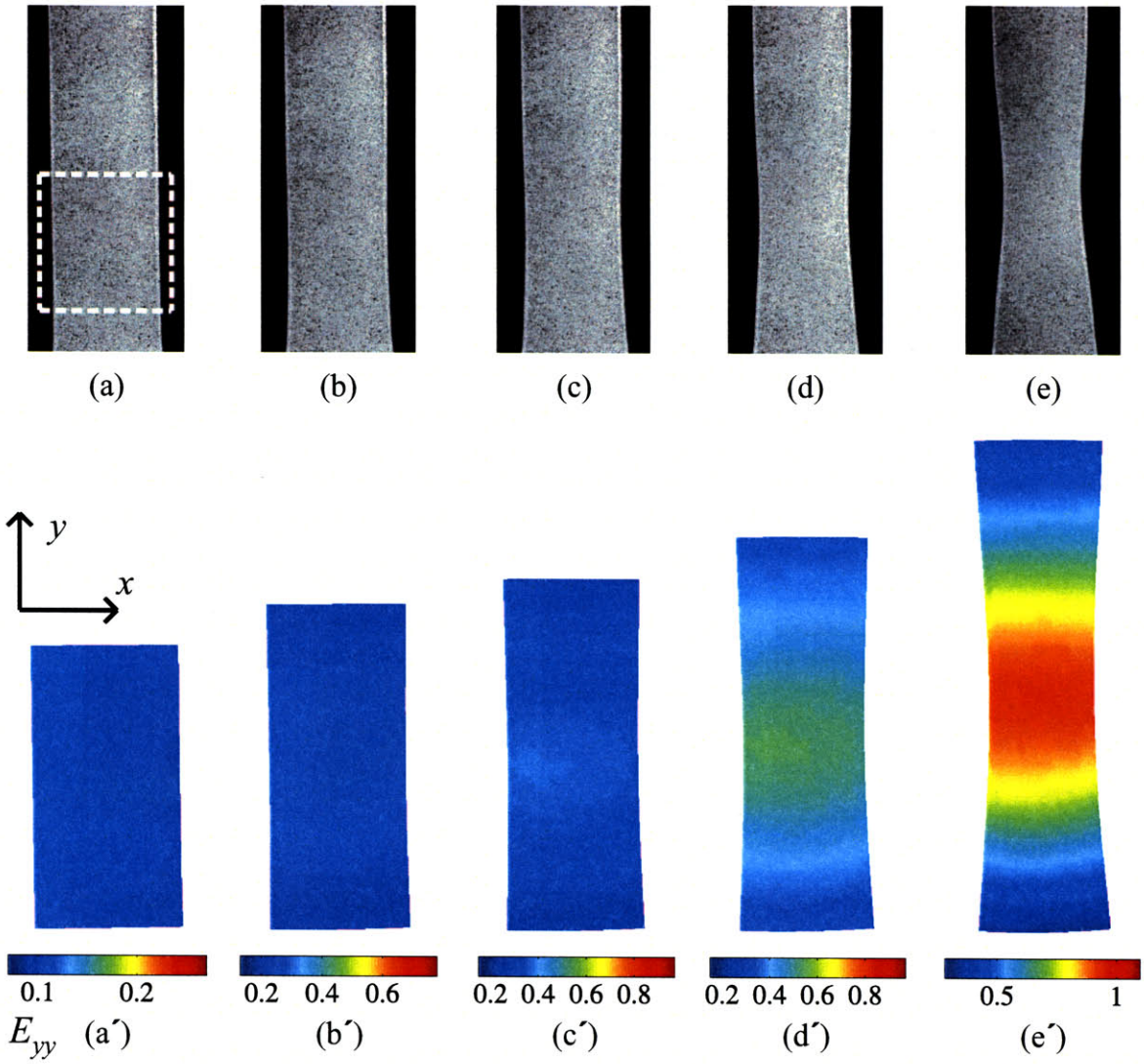

Figure 3-12: Uniaxial tension of 20% rubber-filled HDPE (front view). Deformed specimen (top) and contours of true axial strain, E_{yy}, (bottom) for increasing crosshead displacement, U: (a), (a′) $U = 4.0\,\text{mm}$; (b), (b′) $U = 7.5\,\text{mm}$; (c), (c′) $U = 9.0\,\text{mm}$; (d), (d′) $U = 11.0\,\text{mm}$; (e), (e′) $U = 15.0\,\text{mm}$.

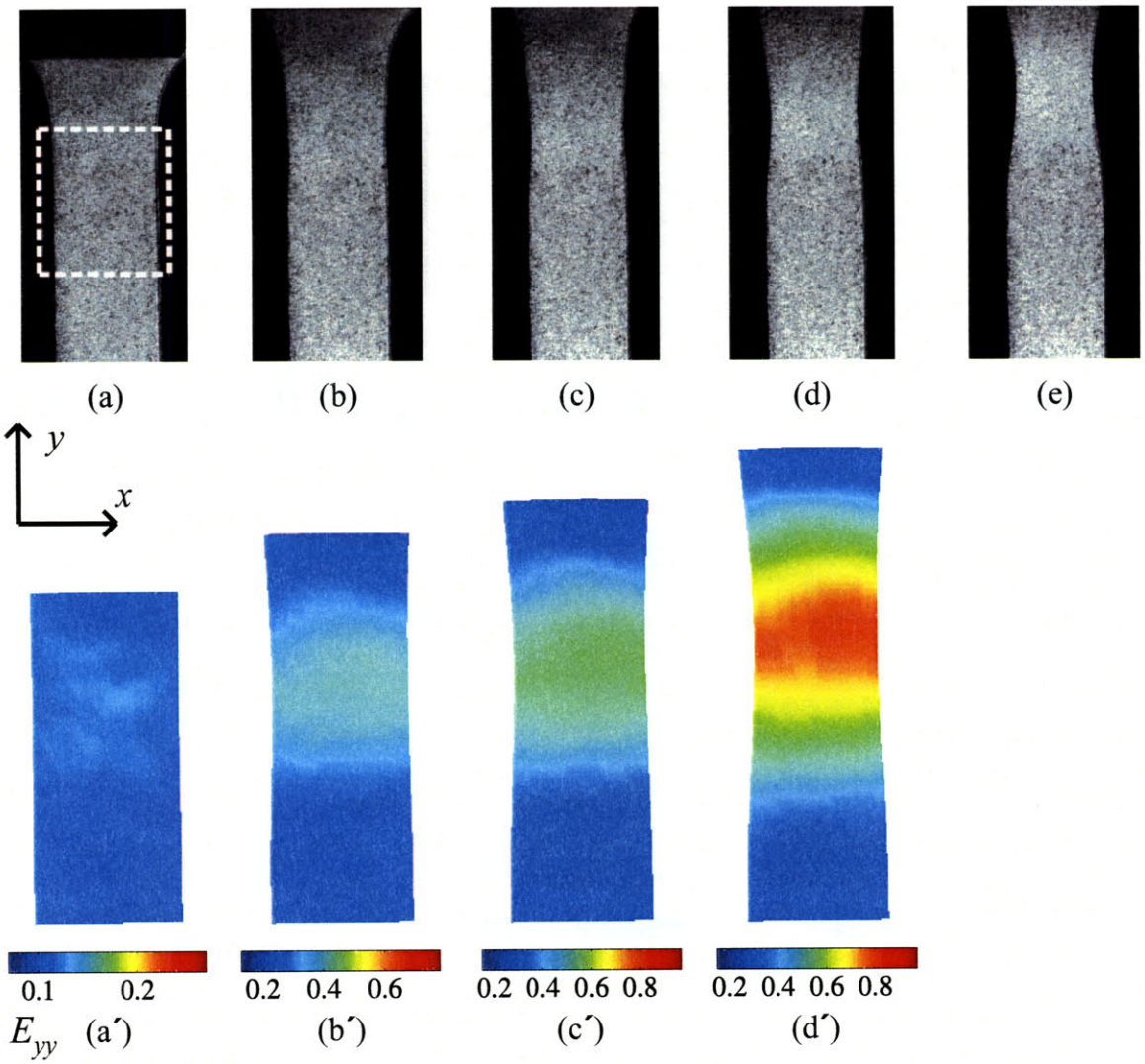

Figure 3-13: Uniaxial tension of 10% CC2-filled HDPE (front view). Deformed specimen (top) and contours of true axial strain, E_{yy}, (bottom) for increasing crosshead displacement, U: (a), (a′) $U = 4.0\,\text{mm}$; (b), (b′) $U = 7.5\,\text{mm}$; (c), (c′) $U = 9.0\,\text{mm}$; (d), (d′) $U = 11.0\,\text{mm}$; (e), $U = 15.0\,\text{mm}$.

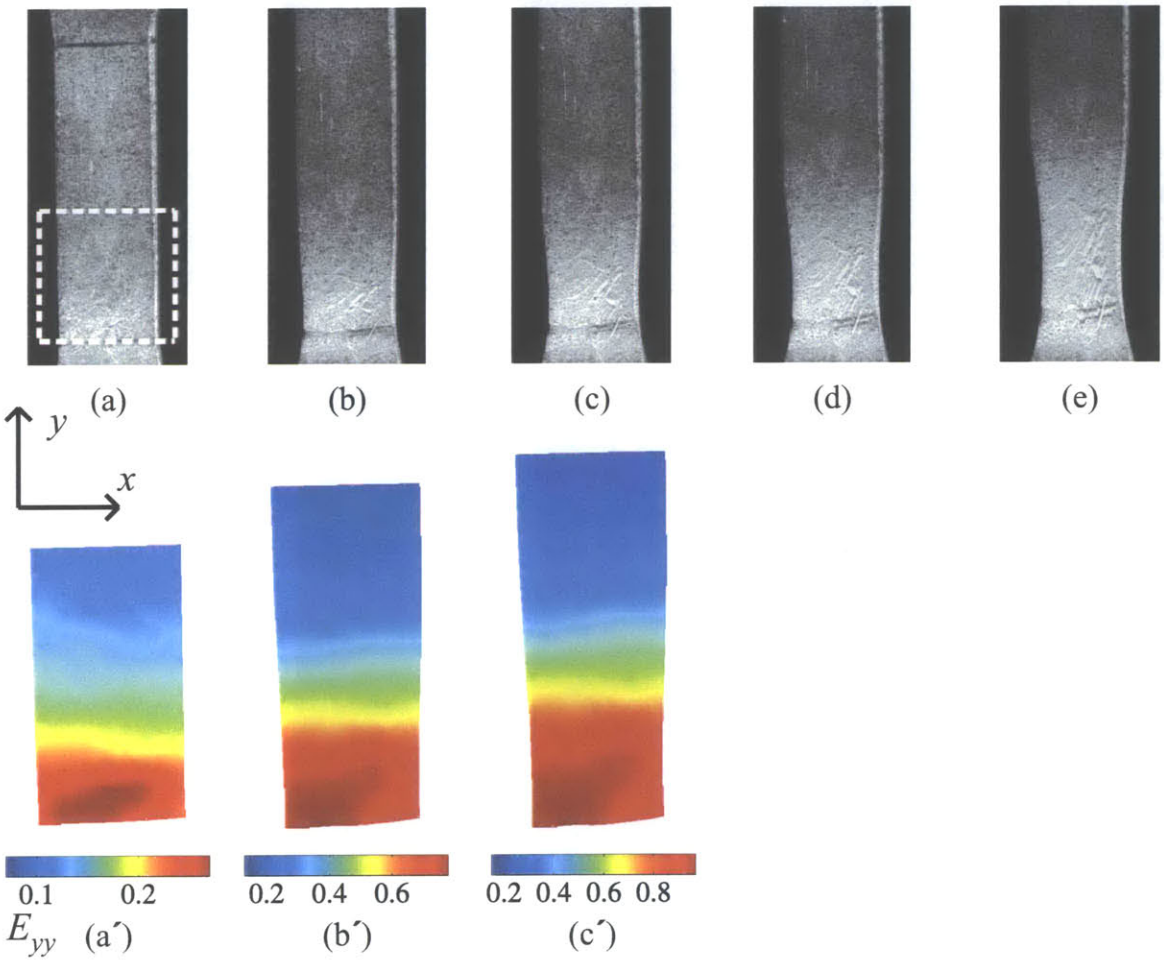

Figure 3-14: Uniaxial tension of 20% CC2-filled HDPE (front view). Deformed specimen (top) and contours of true axial strain, E_{yy}, (bottom) for increasing crosshead displacement, U: (a), (a′) $U = 4.0\,\text{mm}$; (b), (b′) $U = 7.5\,\text{mm}$; (c), (c′) $U = 9.0\,\text{mm}$; (d), $U = 11.0\,\text{mm}$; (e), $U = 15.0\,\text{mm}$.

slope of the maximum local axial strain versus displacement plot (Figure 3-8b) which indicates that necking has begun. Localization thus begins at approximately the same crosshead displacement in all three materials. As f increases, however, the intensity of localization diminishes. Weakening localization is apparent in all three of the indicators: the load drop is smaller and more gradual with increasing f; once necking begins, the maximum local axial strain at a given crosshead displacement decreases with increasing f; the axial strain contours in Figures 3-11 and 3-12 become more diffuse with increasing f. At U=11.0 mm, the axial strain range has shrunk to $E_{yy} = 0.259 - 0.583$ and $E_{yy} = 0.282 - 0.537$ at f=0.10 and f=0.20, respectively.

The effects of calcium carbonate filler particles on the deformation of the specimens are initially different than the effects of rubber filler particles. The load versus displacement plot in Figure 3-9a shows an increase in stiffness and decrease in peak load with increasing volume fraction of CC2 particles. As a result, the peak load and the onset of necking occur at smaller crosshead displacements with increasing f. This is readily apparent in Figure 3-9b where the maximum local strain accelerates at a lower crosshead displacement as f increases. Furthermore, the axial strain contour plots in Figures 3-13 and 3-14 show the strain fields becoming non-uniform at smaller crosshead displacements as f increases. At U=4.0 mm, the load is already decreasing in both blends, and, in Figure 3-13a′, signs of localization are faintly apparent while, in Figure 3-14a′, full-blown necking has occurred. After the peak load, the initial part of the load drop becomes more precipitous and, at moderate displacements, the maximum local strain at a given crosshead displacement increases with increasing f. Hence, we see, in Figures 3-13 a′-c′ and 3-14 a′-c′, the necks in the filled specimens developing more quickly and with greater intensity than the neck in the neat specimen. The magnitude of the slope of the load drop in the filled specimens gradually decreases with further crosshead displacement, and the maximum local strain in the neat specimen surpasses that in the filled specimens at $U \approx 10$ mm and $U \approx 14$ mm for f=0.10 and f=0.20, respectively. The strain contour for f=0.10 at U=11.0 mm shows less localization than that for f=0 at the same crosshead displacement. (The strain range is $E_{yy} = 0.191 - 0.764$.) In turn, the deformed filled specimens in Fig-

ures 3-13 d,e and 3-14 d,e show less narrowing and a greater radius of curvature than their unfilled counterpart. At moderate to large strains, the calcium carbonate filler particles diffuse the deformation in a manner similar to, albeit not quite as strongly as, the rubber filler particles.

3.2.2 Volumetric strain

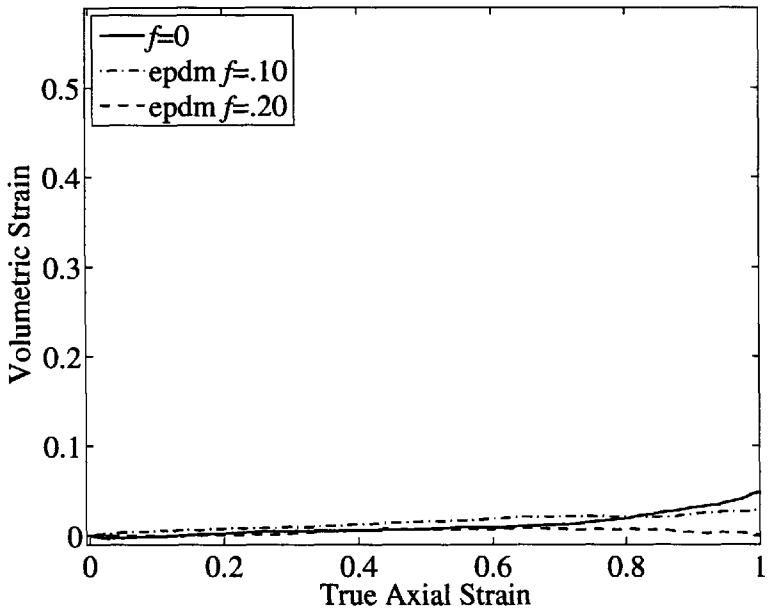

Figure 3-15: Uniaxial tension of neat and rubber-filled HDPE. Volumetric strain, E_{kk}, versus true axial strain, E_{yy}, at the axial location where necking initiated.

The volumetric strain, calculated from Equation 3.4, in neat HDPE and the blends is displayed in Figures 3-15 and 3-16. Neat HDPE exhibits very little volume change, even in the elastic regime, with increasing axial strain. It is concluded that crystal fragmentation does not take place at these strain levels, indicating that any volumetric strain in the blends must be due solely to cavitation or debonding of the particles.

The rubber-filled blends, like neat HDPE, exhibit negligible volumetric strain. The absence of volume change can only mean that, as in the rubber-filled PC blends, the rubber particles do not cavitate.

The calcium carbonate-filled blends, however, exhibit overwhelming evidence of

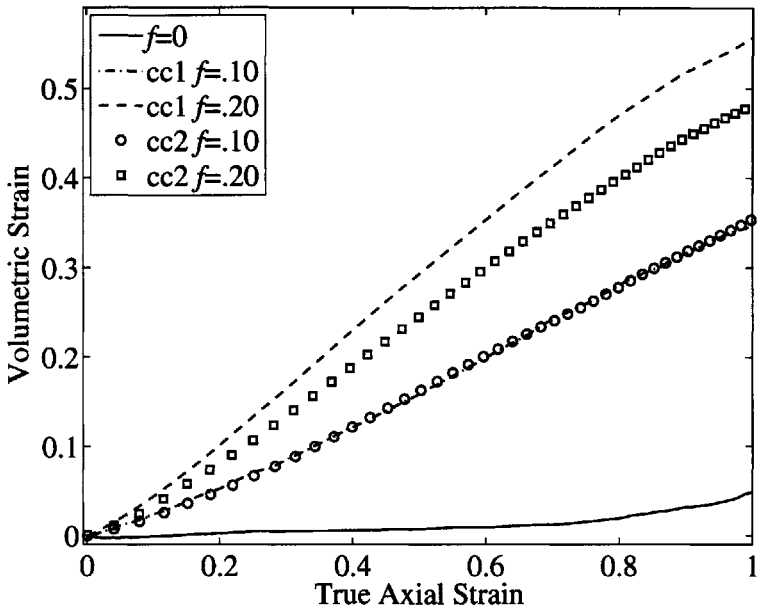

Figure 3-16: Uniaxial tension of neat and calcium carbonate-filled HDPE. Volumetric strain, E_{kk}, versus true axial strain, E_{yy}, at the axial location where necking initiated.

particle debonding and the subsequent void growth. The results in Figure 3-16 show massive dilatation which increases with increasing f with both the 3.5 μm CC1 particles and the 0.7 μm CC2 particles. At f=0.10, the volumetric strains are virtually identical in the CC1 and CC2 blends, but, at $f = 0.20$, the CC1 blend dilates approximately 15% more than the CC2 blend. As evidenced by the SEM micrograph[1] in Fig. 3-17, once debonding occurs, elongated cavities form around the particles. The enormity of the measured volumetric strains is attributed to the particles preventing interparticle ligaments from "pinching in."

3.2.3 True axial stress-strain

Figures 3-18 and 3-19 display representative macroscopic true stress-true strain results for neat, rubber-filled, and calcium carbonate-filled HDPE. The macroscopic true stress, $\overline{T}_{yy}$, was calculated from Equation 3.6, and the true axial strain, E_{yy}, was

[1]Reprinted from Polymer, Vol. 40, Bartczak Z, Argon AS, Cohen RE, Weinberg M, "Toughness mechanism in semi-crystalline polymer blends: II. High-density polyethylene toughened with calcium carbonate filler particles", pp. 2347-2365, 1999, with permission from Elsevier.

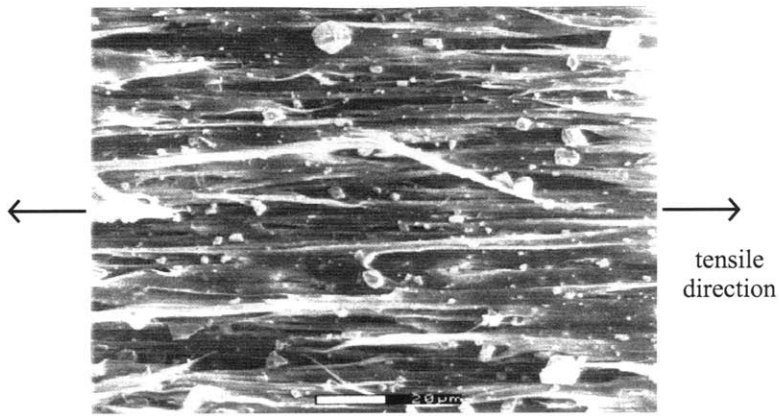

Figure 3-17: SEM micrograph taken in the necked region of a CC1-filled HDPE ($f = .25$) tensile specimen from Bartczak et al. [8]

filler	f	Young's modulus, E (MPa)	Yield strength (MPa)	E_{blend}/E measured	E_{blend}/E predicted
	0	1320	25.1	1.00	1.00
EPDM	0.10	890	21.1	0.67	0.84
EPDM	0.20	700	17.9	0.53	0.70
CC1	0.10	1630	21.5	1.23	1.24
CC1	0.20	2050	18.6	1.55	1.54
CC2	0.10	1690	22.1	1.28	1.24
CC2	0.20	2090	20.2	1.58	1.54

Table 3.1: Elastic modulus and yield strength of HDPE blends.

taken from the front-view lateral center of the specimens. All strains were measured at the axial location on the specimen where necking initiated. (The strain rate in HDPE specimens over the course of a test does not vary nearly as much as it does in PC specimens, and, therefore, the strain rate compensation algorithm of Chapter 2 produced results nearly identical to the results from the site of neck initiation.) All of the materials were ductile and drew to large strains.

For neat HDPE, we see an initial linear region followed by a roll-over as yield occurs and then a very gradually increasing strain hardening slope. There is no strain softening at $f = 0$.

Rubber filler particles have an effect on the stress-strain response of HDPE similar to their effect on that of PC. With a tensile modulus negligible compared to the elastic

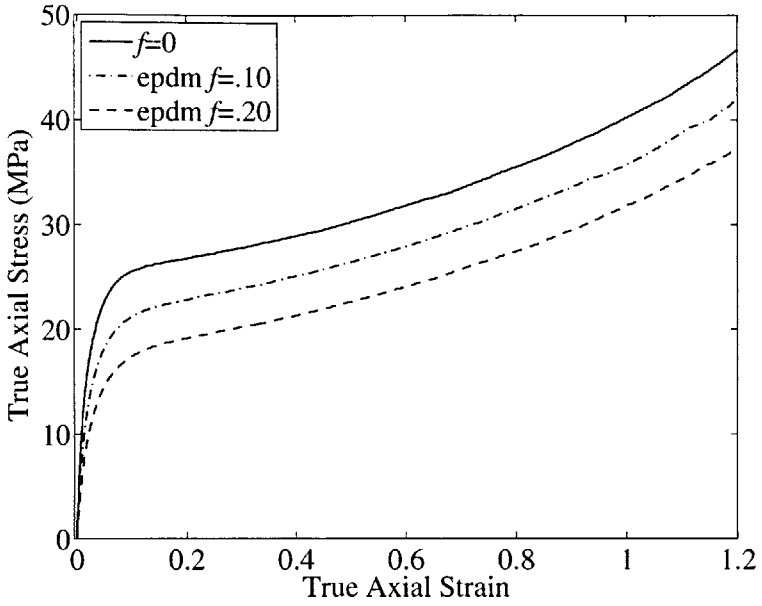

Figure 3-18: Uniaxial tension of neat and rubber-filled HDPE. Macroscopic true axial stress, $\overline{T}_{yy}$, versus true axial strain, E_{yy}, at the axial location where necking initiated.

tensile modulus of HDPE, rubber contributes little to the load-bearing capacity of the blend under a uniaxial state of stress. Thus, as summarized in Table 3.1, the modulus and yield strength decrease with increasing volume fractions of rubber particles. After macroscopic yield, the stress-strain curves of the blends are almost parallel to the stress-strain curve of the homopolymer but are offset by an amount approximately equal to the reduction in yield strength. There is a slight decrease in strain hardening slope with increasing f apparent only at strains exceeding 1.0. Unlike rubber-filled PC, the modulus measurements for rubber-filled HDPE fall short of the composite model predictions of Mori and Tanaka [48] (also given in Table 3.1) by approximately 20%. The measured moduli of the rubber-filled blends, relative to the modulus of neat HDPE, are, however, similar to those reported by Bartczak et al. [7]

Calcium carbonate-filled HDPE exhibits a stress-strain response significantly different than that of rubber-filled HDPE. The yield strength of calcium carbonate-filled HDPE decreases with increasing f, but, unlike rubber-filled HDPE, the modulus of calcium carbonate-filled HDPE increases with increasing f. It is apparent that the particles, with an elastic tensile modulus approximately two orders of magnitude

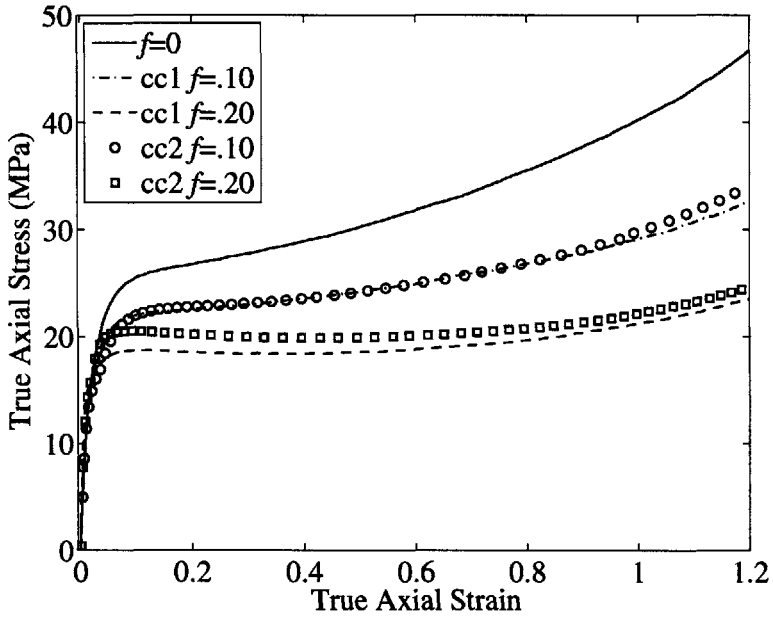

Figure 3-19: Uniaxial tension of neat and calcium carbonate-filled HDPE. Macroscopic true axial stress, $\overline{T}_{yy}$, versus true axial strain, E_{yy}, at the axial location where necking initiated.

greater than the elastic tensile modulus of HDPE, initially adhere to and reinforce the matrix, resulting in a response stiffer than that of neat HDPE. The modulus measurements for the calcium carbonate-filled blends are in excellent agreement with the Mori-Tanaka predictions for composites with perfectly bonded rigid particles. Soon thereafter, before pervasive yielding in the interparticle volumes of matrix material (or matrix "ligaments"), the local stresses at the matrix-particle interfaces reach the adhesive strength of the interface, enabling the particles to debond. The debonded particles essentially act as voids in the matrix, reducing the effective load-bearing cross-sectional area of the specimen. Intensified by the load shed from the particles to the matrix, the stress in the matrix ligaments increases rapidly, forcing the matrix to yield and the stress-strain curve to roll over. As the volume fraction of (debonded) particles increases, the matrix ligaments are more highly stressed, and macroscopic yield occurs at a decreasing macroscopic stress. Thus, when the particles debond prior to matrix yielding, the yield strength of a rigid particle-filled blend resembles that of a rubber-filled or porous material. After macroscopic yield in the calcium

carbonate-filled blends, the strain hardening slope decreases substantially with increasing volume fraction of filler. As noted previously, neat HDPE begins to strain harden immediately after macroscopic yield, and the strain hardening slope gradually increases with increasing axial strain. The blends with $f = .10$ behave similarly but exhibit less strain hardening than the homopolymer. At $f = .20$, however, there is a slight amount of strain softening before strain hardening begins.

The CC1-filled and CC2-filled blends do not behave identically. The sub-micron particle, CC2 blends exhibit slightly higher moduli than the CC1 blends. In addition, the CC2 blends, particularly at f=0.20, have substantially higher yield strengths than the CC1 blends. The elevated plastic resistance with the smaller particles is apparent in Figure 3-19 where, at f=0.20, the stress at macroscopic yield is approximately 10% higher with the CC2 particles than it is with the CC1 particles. After macroscopic yield, the stress-strain response of the CC2 blend gradually approaches that of the CC1 blend. Similar increases in yield strength with decreasing size of $CaCO_3$ particles were observed by Bartczak et al. [8] in HDPE and Lazzeri et al. [43] and Thio et al. [71] in isotactic polypropylene.

3.2.4 Strain rate effects

Fig. 3-20 shows how the local true axial strain rate, $\dot{E}_{yy}$, at the axial location where necking began, varies over the course of tests on neat, rubber-filled and CC2-filled HDPE. $\dot{E}_{yy}$ is taken as the slope of the front-view E_{yy} versus time curves in Figures 3-8b and 3-9b. The initial local strain rate is slightly less than that predicted from the crosshead velocity of the machine due to the effects of system compliance. The crosshead velocity is constant, but, as the deformation localizes, the strain rate in the neck increases. As discussed in Section 3.2.1, the displacement of the crosshead becomes accommodated almost entirely by a small section of the gage length of the specimen. At a crosshead displacement which decreases with increasing f, the strain rate peaks and begins to decrease as the deformation gradually spreads to regions adjacent to the neck. Eventually, as observed in Chapter 2 for PC, when the drawing strain is reached, the strain rate will fall nearly to zero, and the neck will propagate

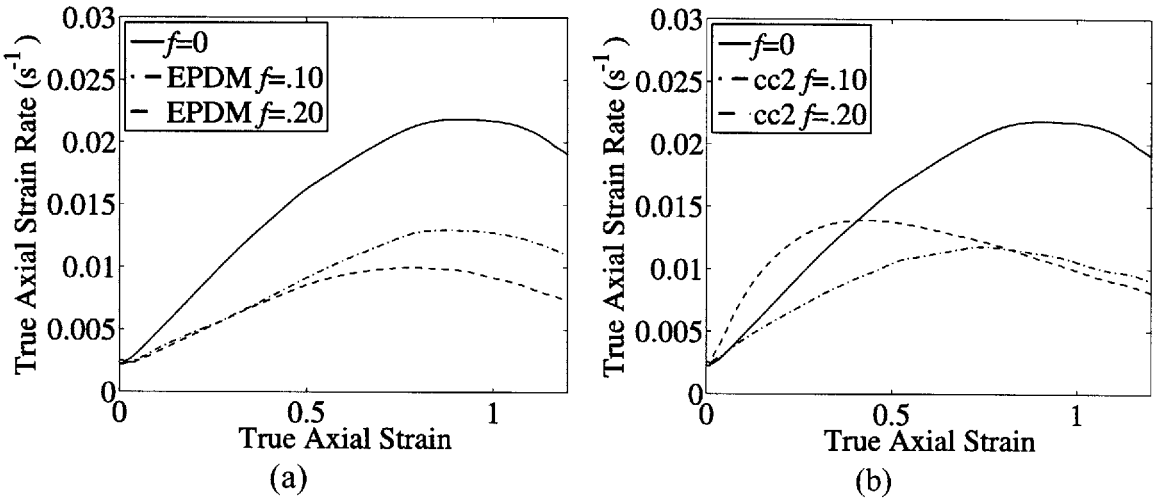

Figure 3-20: Uniaxial tension of neat, rubber-filled (a) and CC2-filled (b) HDPE. True axial strain rate, $\dot{E}_{yy}$, versus true axial strain, E_{yy}, at the axial location where necking initiated.

along the specimen. The maximum strain rate decreases with increasing volume fraction of soft and hard particles, another indication that both types of particle reduce the severity of material localization.

The stress-strain and volumetric strain data presented in the previous two sections only approximates the constant true strain rate response of the materials. In Chapter 2, for PC and rubber-filled PC, a data reduction strategy was presented that minimizes the change in local strain rate during a test by acquiring data at axial locations where the strain rate is closest to a specified target strain rate. In HDPE and its blends, the variation in strain rate is gradual and was found not to affect the results significantly. Therefore, for the HDPE material systems, all data was acquired at the axial location where necking began.

3.3 Conclusions

By capturing the deformation on adjacent sides of the specimen simultaneously, the technique presented in this chapter removes a source of significant error from the analysis. Three-dimensional strain and displacement data is available for every test,

and, requiring only one camera, the technique involves only slightly more equipment and labor than the largely two-dimensional technique described in Chapter 2.

In Chapters 2 and 3, two neat polymers and four different polymer composites have been thoroughly characterized.

PC and HDPE are two very different polymers. PC is an amorphous polymer below its glass transition temperature, while HDPE is a semi-crystalline polymer with amorphous domains above their glass transition temperature. PC is almost twice as stiff and over twice as strong (based on yield strength) as HDPE. PC's natural draw ratio was measured as approximately 1.7, while HDPE's draw ratio has been reported to be roughly 9. PC exhibited a sharp load drop and strain softened while HDPE exhibited a gradual load drop and did not strain soften at all. The low natural draw ratio and strain softening characteristic of PC cause the local strain rate to vary much more in PC than it does in HDPE over the course of a test to $E_{yy} \approx 1$.

Despite the very different properties of their respective matrix materials, rubber-filled PC and rubber-filled HDPE exhibit somewhat similar behavior. Elastic modulus and yield strength decrease predictably with increasing f. Although more apparent in rubber-filled PC, which, unlike rubber-filled HDPE, was strained past its natural draw ratio, the strain hardening slope decreases with increasing f in both systems. Strain contours show more diffuse deformation and less necking with increasing f in both types of blend. In this aspect, the rubber particles have a greater effect on HDPE, particularly at the lower volume fractions of filler, due to the absence of strain softening in neat HDPE. In neither matrix material do the particles cavitate.

Calcium carbonate particles and rubber particles have substantially different effects on the deformation of HDPE. The $CaCO_3$ particles are initially bonded to the matrix and enhance the elastic modulus of HDPE. Although the particles debond prior to macroscopic yield, $CaCO_3$-filled HDPE exhibits yield strengths slightly higher than those of rubber-filled HDPE. Whether the elevation in yield strength is due to particle dispersion, particle properties, interface properties, or some combination thereof will be addressed in the micromechanical modeling of Chapters 5 and 6. After macroscopic yield, the $CaCO_3$-filled blends show a much larger decrease in strain hard-

ening slope with increasing f than the rubber-filled blends. Void growth around the debonded particles causes the $CaCO_3$-filled specimens to dilate. The cross-sectional area of the $CaCO_3$-filled HDPE specimens, therefore, does not decrease nearly as much as the cross-sectional area of the isochorically deforming rubber-filled HDPE specimens. Thus, at a given load, the true stress is higher in the rubber-filled blends than it is in the $CaCO_3$-filled blends.

The CC1-filled and CC2-filled HDPE blends do not deform identically. The yield strengths of the CC2-filled blends, particularly at $f = 0.20$, are superior to those of the CC1-filled blends. The debonding stress of the CC2 particles appears to be higher than that of the CC1 particles. For a given shape, volume fraction and dispersion of particles, the debonding stress is typically inversely proportional to the size of the particles (Lazzeri et al. [43], Pukanszky et al. [59], Vollenberg et al. [76], etc.). This trend is attributed to the energy considerations (Griffith [26]) associated with the increasing specific surface area of the particles with decreasing particle size. However, the effect is often smaller than theoretically predicted due to the competing effect of interface defects (Kraus et al. [40]). Debonding initiates at defects on the surfaces of the particles. If the size of the defects is independent of the size of the particles, the defects become proportionally larger, and hence more critical, as the particles become smaller. Given that, at $f = 0.20$, the CC2 blend exhibits less volumetric strain than the CC1 blend, it is possible as well that the CC2 particles only partially debond. Some particles may not debond at all, or some or all particles may not debond at all points on their surfaces.

Chapter 4

Constitutive Modeling of Unfilled Polymers

The second half of the thesis focuses on the micromechanical and constitutive modeling of particle-modified polymers. A constitutive model of homogeneous polymers is needed as a component of the micromechanical models and as a base from which to develop the constitutive model. In order to assess their accuracy, the micromechanical modeling results are compared with the experimental results of the HDPE systems. Although HDPE is a semi-crystalline polymer, it can be effectively modeled with an amorphous polymer constitutive model. In this chapter, slightly modified versions of the models of Arruda and Boyce [4] ("series" model) and Boyce et al. [13] ("parallel" model) are presented. The predictions of the two models are nearly identical under monotonic loadings.

4.1 Kinematics

The kinematics of the two models are the same. The total deformation gradient, $\mathbf{F}$, is multiplicatively decomposed into elastic and plastic parts,

$$\mathbf{F} = \mathbf{F}^{e}\,\mathbf{F}^{p}, \tag{4.1}$$

where $\mathbf{F}^p$, the plastic deformation gradient, is obtained by elastically unloading via $\mathbf{F}^{e-1}$ to the relaxed, or stress-free, state. The elastic deformation gradient, $\mathbf{F}^e$, is decomposed as

$$\mathbf{F}^e = \mathbf{V}^e\mathbf{R}^e, \tag{4.2}$$

where , $\mathbf{V}^e$ and $\mathbf{R}^e$ are the elastic left stretch tensor and the elastic rotation, respectively.

The total velocity gradient, $\mathbf{L}$, can likewise be decomposed into elastic and plastic components:

$$\mathbf{L} = \dot{\mathbf{F}}\,\mathbf{F}^{-1} = \mathbf{L}^e + \mathbf{F}^e\mathbf{L}^p\mathbf{F}^{e-1}. \tag{4.3}$$

The velocity gradient in the relaxed configuration, $\mathbf{L}^p = \dot{\mathbf{F}}^p\mathbf{F}^{p-1}$, may be expressed as the sum of its symmetric and skew-symmetric components,

$$\mathbf{L}^p = \mathbf{W}^p + \mathbf{D}^p, \tag{4.4}$$

where $\mathbf{W}^p$ is the plastic spin and $\mathbf{D}^p$ is the rate of plastic stretching in the relaxed configuration. Following Boyce et al. [14], the relaxed configuration is made unique by specifying $\mathbf{W}^p \equiv \mathbf{0}$, and thus the flow rule becomes

$$\dot{\mathbf{F}}^p = \mathbf{D}^p\mathbf{F}^p = \mathbf{F}^{e-1}\mathbf{D}^p\mathbf{F}, \tag{4.5}$$

where $\mathbf{D}^p$ is constitutively prescribed for each model below.

4.2 Constitutive Description

4.2.1 Arruda and Boyce (series) model

The Arruda and Boyce model as presented herein was used for the initial micromechanical modeling of rubber-filled and calcium carbonate-filled HDPE. The Arruda

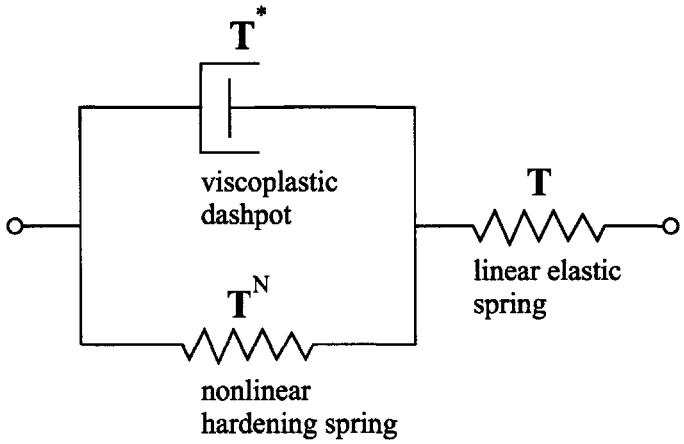

Figure 4-1: Schematic of the Arruda and Boyce amorphous polymer constitutive model. $\mathbf{T}^*$, $\mathbf{T}^N$, and $\mathbf{T}$ are the tensorial stress quantities which act on each element in the three-dimensional implementation of the model.

and Boyce model is among a number of polymer constitutive models developed over the past several decades that draw inspiration from the one-dimensional network model of Haward and Thackray [35] shown in Figure 4-1. In these types of models, a linear elastic spring acts in series with two elements in parallel that represent the dual resistances to plastic flow present in polymers. In an amorphous polymer, where the molecular chains are entirely randomly oriented, the initial barrier to inelastic deformation, modeled by the viscoplastic dashpot, is due to an isotropic intermolecular resistance to chain segment rotation. A number of flow models can be used to capture this viscous deformation. As the material is deformed, an additional resistance, modeled by the nonlinear hardening spring, develops due to the anisotropic resistance to chain alignment. The hardening is typically represented by a model of rubber elasticity. In a semi-crystalline polymer such as HDPE, however, amorphous domains are interspersed with spherulitic crystals. Initial inelastic deformation is accommodated by chain segment rotation and crystal slip. The viscoplastic dashpot is thus taken to represent both the crystalline and amorphous yield mechanisms in the modeling of HDPE. While the dashpot loses some of its physical significance when the model is applied to HDPE, the hardening spring stands on strong physical ground for Parks and Ahzi [54] have shown the post-yield strain hardening of HDPE to be dominated

by the deformation of the amorphous regions. (In fact, the Haward-Thackray model was proposed to represent the behavior of partially crystalline polymers.)

In the three-dimensional implementation of the one-dimensional schematic of Figure 4-1, each element is acted upon by a tensor. The total Cauchy stress, $\mathbf{T}$, acting on the material is the stress in the linear elastic spring or, identically, the sum of the stress in the dashpot and the stress in the hardening spring. The stress in the linear elastic spring is constitutively described by the fourth-order elasticity tensor, $\mathscr{L}^{\mathrm{e}}$:

$$\mathbf{T} = \frac{1}{J^{\mathrm{e}}} \mathscr{L}^{\mathrm{e}} \left[\mathbf{E}^{\mathrm{e}} \right], \tag{4.6}$$

where $\mathbf{E}^{\mathrm{e}} = \ln \mathbf{V}^{\mathrm{e}}$ is the elastic Hencky strain and $J = \det \mathbf{V}^{\mathrm{e}}$ is the elastic volume change.

The stress in the nonlinear hardening spring, $\mathbf{T}^{\mathrm{N}}$, accounting for the orientation of the macromolecular network in the amorphous domains, is taken to be deviatoric and is prescribed by the Arruda-Boyce [5] eight-chain model of rubber elasticity:

$$\mathbf{T}^{\mathrm{N}} = \frac{\mu_{\mathrm{R}}}{3} \frac{\sqrt{N}}{\lambda^{\mathrm{p}}_{\mathrm{chain}}} \mathscr{L}^{-1} \left(\frac{\lambda^{\mathrm{p}}_{\mathrm{chain}}}{\sqrt{N}} \right) \mathrm{dev} \left(\mathbf{B}^{\mathrm{p}} \right), \tag{4.7}$$

where μ_{R} is the initial hardening modulus, $\sqrt{N}$ is the limiting chain extensibility, $\mathbf{B}^{\mathrm{p}} = \mathbf{F}^{\mathrm{p}} \mathbf{F}^{\mathrm{p}\mathrm{T}}$ is the plastic left Cauchy-Green strain, $\lambda^{\mathrm{p}}_{\mathrm{chain}} = \sqrt{\dfrac{\mathrm{tr}\, \mathbf{B}^{\mathrm{p}}}{3}}$ is the stretch on each chain in the network, and $\mathscr{L}^{-1}$ is the inverse Langevin function. Initially, the hardening spring provides little resistance to deformation, but, as $\lambda^{\mathrm{p}}_{\mathrm{chain}}$ approaches $\sqrt{N}$, its stiffness increases dramatically.

The stress which drives the time and temperature dependent plastic flow via the viscoplastic dashpot, $\mathbf{T}^{*}$, is calculated from the tensorial difference between the total Cauchy stress and the network stress (pushed forward to the current configuration):

$$\mathbf{T}^{*} = \mathbf{T} - \frac{1}{J^{\mathrm{e}}} \mathbf{F}^{\mathrm{e}} \mathbf{T}^{\mathrm{N}} \mathbf{F}^{\mathrm{e}\mathrm{T}}. \tag{4.8}$$

$\mathbf{T}^*$ is expressed in terms of its effective equivalent shear stress,

$$\tau^* = \left[\frac{1}{2}\mathbf{T}^{*'}\mathbf{T}^{*'}\right]^{1/2}, \tag{4.9}$$

and its tensorial direction,

$$\mathbf{N} = \frac{1}{\sqrt{2}\tau}\mathbf{T}^{*'}, \tag{4.10}$$

where $\mathbf{T}^{*'}$ is the deviatoric part of the stress driving plastic flow. The plastic flow is assumed to be incompressible, and the rate of plastic stretching, $\mathbf{D}^{\mathrm{p}}$, is taken to be aligned with the deviatoric stress state:

$$\mathbf{D}^{\mathrm{p}} = \dot{\gamma}^{\mathrm{p}}\mathbf{N}, \tag{4.11}$$

where the plastic shear strain rate, $\dot{\gamma}^{\mathrm{p}}$, depends on the stress state, material properties, and temperature. $\dot{\gamma}^{\mathrm{p}}$ is prescribed by the Argon [1] equation,

$$\dot{\gamma}^{\mathrm{p}} = \dot{\gamma}_0 \exp\left(-\frac{\Delta G}{k\,\Theta}\left\{1 - \frac{\tau^*}{s}\right\}\right), \tag{4.12}$$

where $\dot{\gamma}_0$ is the pre-exponential factor proportional to the attempt frequency, ΔG is the zero-stress level activation energy, k is Boltzmann's constant, Θ is the absolute temperature, and s is the athermal shear strength. Isotropic post-yield strain-hardening is incorporated into the model by taking the shear strength to evolve with strain from its initial value, $s_0 = \dfrac{0.077\mu}{1-\nu}$ (where μ is the elastic shear modulus, and ν is the Poisson's ratio), to a steady state, s_{ss}, according to

$$\dot{s} = h\left(1 - \frac{s}{s_{\mathrm{ss}}}\right)\dot{\gamma}^{\mathrm{p}}, \tag{4.13}$$

where $h > 0$ is the hardening slope. The shear strength is further modified to capture

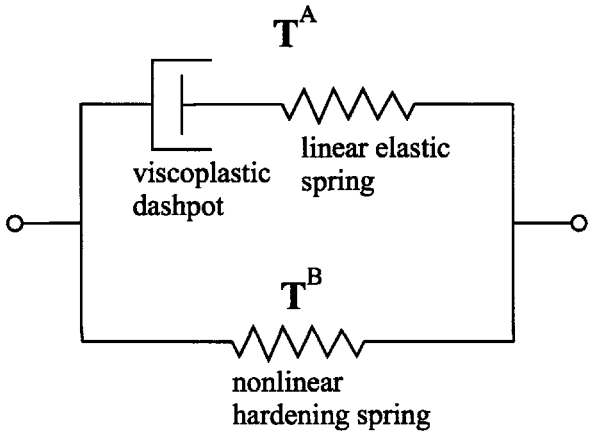

Figure 4-2: Schematic of the parallel amorphous polymer constitutive model. $\mathbf{T}^{\mathrm{A}}$ and $\mathbf{T}^{\mathrm{B}}$ are the tensorial stress quantities which act on each leg in the three-dimensional implementation of the model.

the pressure dependence of yield of polymers by adding a linear pressure term,

$$s \rightarrow s + \alpha p, \tag{4.14}$$

where α is a dimensionless constant, and $p = -\frac{1}{3}\,\mathrm{tr}\,\mathbf{T}$.

4.2.2 Parallel model

A newer constitutive model, the parallel model of Boyce et al. [13], was used to represent the matrix response in the more general micromechanical study of rigid particle-modified polymers and, in conjunction, the development of the constitutive model for rigid particle-modified polymers. Its components, as illustrated in Figure 4-2, are identical to those of the series model. In the parallel model, however, the linear elastic spring and viscoplastic dashpot are in series (network A), and, these two elements together act in parallel with the nonlinear hardening spring (network B). The parallel arrangement provides a more accurate representation of molecular relaxation than the series model, particularly in polymers above their glass transition temperature, where the post-yield strain hardening depends also on time and temperature.

The total Cauchy stress acting on the material, $\mathbf{T}$, is the sum of the stresses in networks A and B. The linear elastic spring in network A provides virtually all

of the stiffness at strains in the elastic range and is constitutively described by the fourth-order elasticity tensor:

$$\mathbf{T}^{\mathrm{A}} = \frac{1}{J^{\mathrm{e}}} \mathscr{L}^{\mathrm{e}} \left[\mathbf{E}^{\mathrm{e}} \right]. \tag{4.15}$$

The stress in network B, representing the effect of orientation-induced strain hardening, is prescribed by one of two models of rubber elasticity:

1. the neo-Hookean (Gaussian) model with

$$\mathbf{T}^{\mathrm{B}} = \frac{\mu_{\mathrm{R}}}{J} \left(\mathbf{B} - \mathbf{1} \right) + \kappa_{\mathrm{B}} \left(J - 1 \right) \mathbf{1} \tag{4.16}$$

2. the Arruda-Boyce eight-chain model with

$$\mathbf{T}^{\mathrm{B}} = \frac{\mu_{\mathrm{R}}}{3J} \frac{\sqrt{N}}{\lambda_{\mathrm{chain}}} \mathscr{L}^{-1} \left(\frac{\lambda_{\mathrm{chain}}}{\sqrt{N}} \right) \left[\mathbf{B} - \mathbf{1} \right] + \kappa_{\mathrm{B}} \left(J - 1 \right) \mathbf{1} \tag{4.17}$$

where μ_{R} is the initial hardening modulus, $J = \det \mathbf{F}$ is the total volume change (identical to J^{e} in this case), $\sqrt{N}$ is the limiting chain extensibility, $\mathbf{B} = \mathbf{F}\mathbf{F}^{\mathrm{T}}$ is the left Cauchy-Green strain, $\lambda_{\mathrm{chain}} = \sqrt{\dfrac{\mathrm{tr}\,\mathbf{B}}{3}}$ is the stretch on each chain in the network, and $\mathscr{L}^{-1}$ is the inverse Langevin function. The bulk modulus, κ_{B}, is taken to be zero in both instances, effectively lumping all of the resistance to volumetric strain into network A.

In the version of the parallel model used in this thesis, the plastic flow in the dashpot is derived from a plastic strain rate potential,

$$\Phi = \frac{\sqrt{2} \dot{\nu}_0 s_0}{1/m + 1} \left(\frac{\tau^{\mathrm{A}}}{s_0} \right)^{1/m+1}, \tag{4.18}$$

where $\dot{\nu}_0$ is a material constant, m is the strain rate sensitivity parameter, s_0 is the athermal shear strength, and τ^{A} is the effective shear stress in network A. The

incompressible plastic stretching is calculated as

$$\mathbf{D}^{\mathrm{p}} = \frac{\partial \Phi}{\partial \mathbf{T}^{\mathrm{A}}} = \dot{\gamma}^{p}\mathbf{N}, \tag{4.19}$$

with the plastic shear strain rate given by

$$\dot{\gamma}^{\mathrm{p}} = \dot{\nu}_0 \left(\frac{\tau^{\mathrm{A}}}{s_0} \right)^{1/m}. \tag{4.20}$$

Yield occurs when the deviatoric stress in network A, $\mathbf{T}^{\mathrm{A}'}$, is sufficient to activate the viscoplastic element. Analogously to the series model, the effective shear stress and the direction of plastic flow are computed, respectively, as

$$\tau^{\mathrm{A}} = \left[\frac{1}{2} \mathbf{T}^{\mathrm{A}'} \mathbf{T}^{\mathrm{A}'} \right]^{1/2} \tag{4.21}$$

and

$$\mathbf{N} = \frac{1}{\sqrt{2}\tau^{\mathrm{A}}} \mathbf{T}^{\mathrm{A}'}. \tag{4.22}$$

4.3 Material Parameters

4.3.1 Arruda and Boyce (series) model

To be used as a component of the micromechanical models of the HDPE blends tested in Chapter 3, the series model was fit as closely as possible to the results of uniaxial tension and compression tests on neat HDPE. The uniaxial tension data is presented in Section 3.2.3. Uniaxial compression tests were performed on a servo-hydraulic Instron testing machine with self-aligning grips at constant true strain rates of $-0.001\,\mathrm{s}^{-1}$,$-0.01\,\mathrm{s}^{-1}$, and $-0.1\,\mathrm{s}^{-1}$. Cylindrical specimens, machined from the injection-molded bars, of diameter 10 mm and height 6.4 mm were tested with sheets of Teflon placed between the grips and the specimen in order to minimize friction.

The fitting procedure was a three step process: First, the elastic properties were

Elastic		Viscoplastic		Softening			Hardening	
E (MPa)	ν	$\dot{\gamma}_0$ (s^{-1})	ΔG (J)	h (MPa)	s_{ss}/s_0	α	μ_R (MPa)	N
1320	0.45	6.7×10^{15}	2.4×10^{-19}	3000	1.08	0.5	2.0	13.0

Table 4.1: Material parameters for the series constitutive model of HDPE.

taken from the tensile data. Second, the viscoplastic, strain softening, and strain hardening parameters were fit to the uniaxial compression results with the pressure dependence, α, set to an arbitrary value. Third, in an iterative process, α and the viscoplastic properties were adjusted such that the yield strength of the model in tension and compression matched the experimental data. The values of the material parameters are summarized in Table 4.1.

The predictions of the model and the experimental data are presented in Figure 4-3. As discussed in Section 3.2.4, due to necking, the local axial stain rate was not

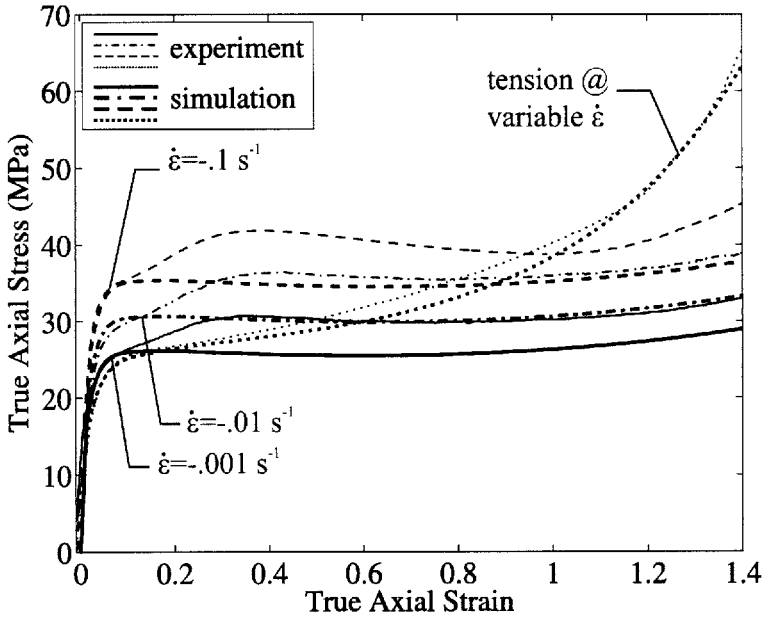

Figure 4-3: Predictions of the series constitutive model of HDPE versus neat HDPE uniaxial tension and compression data.

constant over the course of the tension tests. As shown in Figure 3-20, the strain rate varied approximately from $0.0025\,s^{-1}$ to 0.02^{-1}, with the strain rate at yield

approximately equal to $0.004\,s^{-1}$. Therefore, in order to compare the predictions of the model in tension to the experimental tensile data, the model was subjected to the same local axial strain rate history measured in the tensile specimens. The model simulates the initial flow strengths in tension and compression exceptionally well. In tension, the model closely matches the experimental data over the course of the entire stress-strain curve. (Even better agreement could be obtained if the model were fit only to the tension data.) In compression, however, at axial strains exceeding 0.2, the model systematically underpredicts the flow stress by 3-5 MPa. Consistent with the uniaxial compression results of Bartczak et al. [9] on neat HDPE, the experimental data in compression exhibits a kink, for lack of a better term, between strains 0.1 and 0.3 at all three applied strain rates. After initial yield, the material strains hardens sharply during this period before the stress-strain curve rolls over and gradual strain softening occurs. Some authors have termed this phenomenon a "double yield point." If yield in compression were taken to occur at the stress where the stress-strain curve begins to decrease (i.e. the second yield point), an unrealistically high pressure dependence would result. Thus, it is concluded that tensile loadings must activate deformation mechanisms that are inoperative or less favorable in compression. Since tensile states of stress are the emphasis of this thesis, the model was effectively fit to the compression data with the initial strain hardening sections of the curves removed. While speculating on the interplay between the deformation of the amorphous domains and the activation of the various crystal slip systems in HDPE (see, for example, Lin and Argon [44], Bartczak et al. [9], and Hiss et al. [38]) under the two states of stress is outside the focus of this work, we reiterate that the phenomenon of microstructural cavitation known as "micronecking" (Peterlin [55]), often observed in the tensile deformation of HDPE, did not occur as evidenced by the near incompressibility of neat HDPE.

4.3.2 Parallel model

The form of the parallel model used in this study was purposefully chosen to be less complex than the series model. Strain softening and the pressure dependence of the

Elastic		Viscoplastic		Hardening	
E (MPa)	ν	$\dot{\nu}_0$ (s^{-1})	m	μ_R (MPa)	(N)
1380	0.40	6.7×10^4	0.093	1.8	(15.0)

Table 4.2: Material parameters for the parallel constitutive model.

flow strength were omitted in order to focus on the effect of the rigid particles on polymer deformation. Furthermore, in most cases, the orientation hardening was captured with the Gaussian model. As a result, the matrix constitutive response in the more general micromechanical study of Chapter 6 does not match the stress-strain response of neat HDPE as closely as the series model. The goal of these micromechanical models, however, was not to simulate the experimentally characterized blends but to simulate a typical rigid particle-modified polymer. As such, the response of neat HDPE was used only as a general guide when determining the material parameters of the parallel model. The parameters are given in Table 4.2. The predictions of the

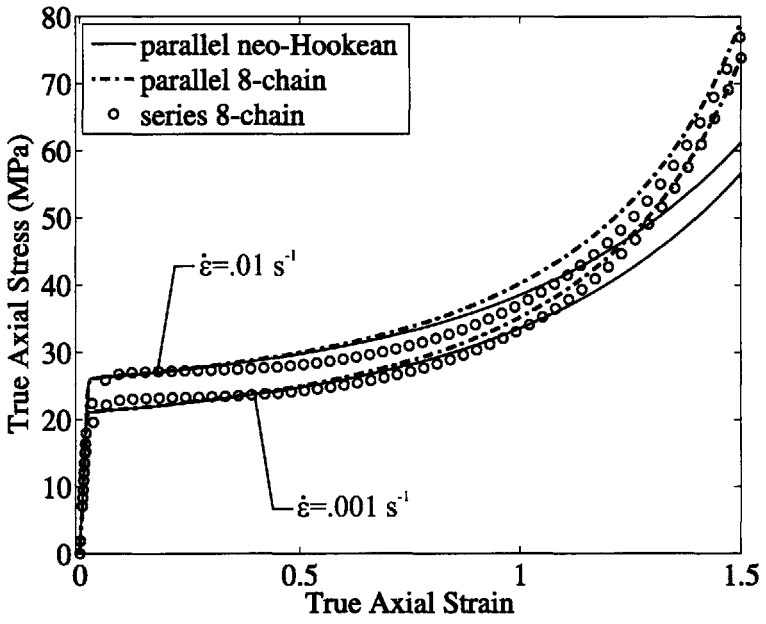

Figure 4-4: Predictions of the parallel constitutive model with neo-Hookean and eight-chain strain hardening and the series constitutive model. Loading is uniaxial tension at constant true axial strain rates of $0.001\,s^{-1}$ and $0.01\,s^{-1}$

parallel model for uniaxial tension at two strain rates with both neo-Hookean and eight-chain hardening are presented in Figure 4-4. The predictions of the series model at the same strain rates are also shown for reference.

Chapter 5

Micromechanical Modeling of Calcium Carbonate-Filled High-Density Polyethylene

Micromechanical models are frequently invoked to study the mechanisms by which elasto-plastic heterogeneous solids, such as particle-modified polymers, deform. The underlying assumption is that a continuum material can be decomposed into an infinite number of identical representative volume elements (RVE's). An RVE of a particle-modified material may encompass one or more particles. The macroscopic response of a suitable RVE closely approximates that of the continuum material. A micromechanical model is, by definition, a finite element (FE) realization of an RVE. It consists of the RVE geometry and resulting FE mesh, a homogenization scheme to evaluate the macroscopic response of the RVE, and the constitutive descriptions of the phases and phase interfaces. Appropriately defined micromechanical models may be used to study the local, particle-level mechanics and micro-mechanisms which govern observed experimental behavior. Furthermore, micromechanical models are able to predict the macroscopic response of a material under any loading state.

In this chapter, micromechanical models are presented to simulate the deformation of rubber-filled and calcium carbonate-filled HDPE. The accuracy of the models is evaluated by comparing the model predictions to the experimental results of Chap-

ter 3. The validity of true models is discussed, and, in the process, features of the deformation of particle-modified polymers are made clear. While only results for uniaxial tension are presented in this chapter, the technique for applying general states of loading, used in later chapters, is described as well.

5.1 RVE Geometries and Homogenization Schemes

The first step in the development of a micromechanical model is to determine what constitutes a suitable RVE. If the particles are relatively uniform in size and well dispersed throughout the matrix, the microstructural representation may be substantially simplified by the use of a spatially periodic single-particle RVE. A single-particle RVE consists of one particle and its surrounding matrix material. If, however, the particles are not equi-sized and/or evenly distributed throughout the matrix, a single particle RVE cannot accurately represent the response of the continuum. In this case, the RVE must include multiple particles.

5.1.1 Single-particle RVE's

Single particle RVE's are based on the assumption that a well dispersed, random distribution of particles may be approximated by some regular, repeating array of particles. The RVE may be axisymmetric, provided that the loading state to be modeled is axisymmetric. The classic axisymmetric RVE, introduced by Tvergaard [73] for the study of porous plasticity, is based on a stacked hexagonal array (SHA) of particles. As depicted in Figure 5-1a, in the SHA model a random distribution of particles is approximated as a regular three-dimensional array of hexagonal cells of matrix material, each containing a spherical particle. Since each cell behaves identically to its neighbors, with appropriate periodic boundary conditions, only one cell needs to be modeled. Further approximating the hexagonal cells as cylinders allows a two-dimensional axisymmetric RVE to be constructed. The symmetry of the RVE requires only one-half of the cylinder (see Figure 5-1 b,c) to be modeled. In order to maintain compatibility with adjacent cells, the outside of the RVE is constrained to

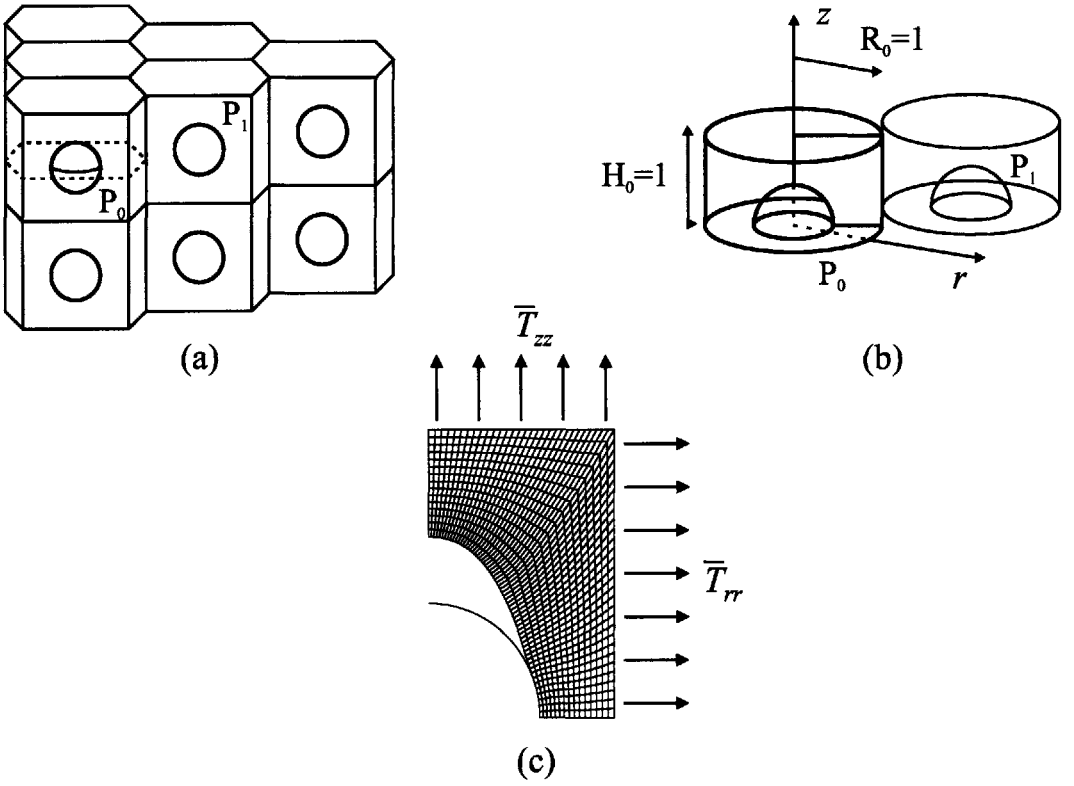

Figure 5-1: Derivation of the SHA model: (a) three-dimensional array of stacked hexagonal cells, (b) SHA axisymmetric unit cells, (c) deformed SHA axisymmetric finite element mesh.

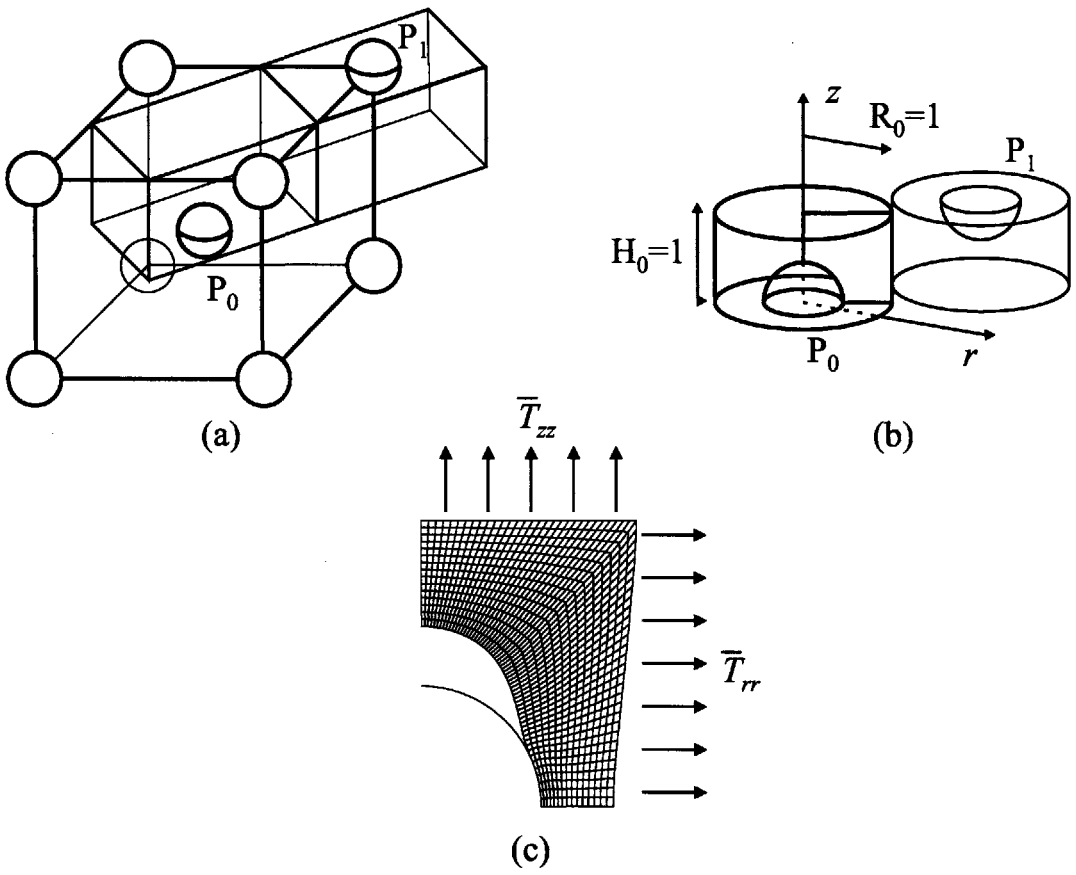

Figure 5-2: Derivation of the SA model: (a) rectangular tessellation of BCT lattice (lattice spacings $\{\sqrt{\pi/2}, \sqrt{\pi/2}, 1\}$), (b) SA axisymmetric unit cells, (c) deformed SA axisymmetric finite element mesh.

remain a right circular cylinder throughout the deformation.

In response to the SHA model, Socrate and Boyce [65] proposed an axisymmetric RVE based on a staggered array (SA) of particles. The random distribution of particles was simulated by arranging particles on a body centered cubic (BCC) or body centered tetragonal (BCT) lattice. Figure 5-2 demonstrates how an axisymmetric RVE, which completely fills space, is constructed based on a rectangular tessellation of the BCT lattice. (Socrate and Boyce showed that the predictions of BCC and BCT RVE's are nearly identical.) The same arguments used for the SHA RVE limit the SA RVE to one-half of a cylinder. As with the SA model, axial compatibility requires the top and bottom of the RVE to remain planar during deformation. In this case, however, as shown in Figure 5-2c, the radial boundary of the deforming RVE does not

remain straight. The lateral boundary conditions required to maintain compatibility with an SA RVE cell, originally proposed by Tvergaard [73], are given in Tzika et al. [74].

Symmetry considerations impose further constraints on the finite element model (FEM) implementations of both the SA and SHA RVE's. Specifically, nodes along the z-axis have zero radial displacement, and nodes along on the z=0 plane have zero axial displacement.

Only axisymmetric loadings may be modeled with these representations of the SHA and SA cells. All loadings during a given simulation are of constant macroscopic stress triaxiality ratio, $X = \frac{\overline{T}_{\mathrm{m}}}{\overline{T}_{\mathrm{eq}}}$, where $\overline{T}_{\mathrm{eq}}$ and $\overline{T}_{\mathrm{m}}$, the macroscopic Mises stress and mean macroscopic stress, respectively, are given by

$$\overline{T}_{\mathrm{eq}} = ||\overline{T}_{zz} - \overline{T}_{rr}|| \tag{5.1}$$

and

$$\overline{T}_{\mathrm{m}} = \frac{1}{3}(\overline{T}_{zz} + 2\overline{T}_{rr}). \tag{5.2}$$

The macroscopic Cauchy stress in the axial direction, $\overline{T}_{zz}$, is calculated as the volume average of the local axial stresses:

$$\overline{T}_{zz} = \frac{1}{V_{\mathrm{RVE}}} \int_{V_{\mathrm{RVE}}} T_{zz}(\mathbf{x}) \mathrm{d}V, \tag{5.3}$$

where $\mathbf{x}$ is the position vector of an arbitrary point in the deformed RVE and V_{RVE} is the volume of the deformed RVE. In the FEM implementation of the RVE's, $\overline{T}_{zz}$ is computed via the divergence theorem in terms of surface integrals along the outside of the cells (Smit et al. [63], Tzika et al.). $\overline{T}_{rr}$ is calculated from $\overline{T}_{zz}$ and the imposed stress triaxiality ratio. As in Tzika et al., the loading is applied via a user-defined element which monitors the macroscopic axial stress and applies radial tractions consistent with the chosen triaxiality ratio to the lateral boundary.

The macroscopic strains are easily calculated from the displacements at the bound-

aries of the cells. The true axial strain is given by the displacement of the top plane,

$$\overline{E}_{zz} = \ln(1 + u_z|_{z=1.0}), \tag{5.4}$$

and true radial strain is given by the displacement of the axial midpoint of the radial boundary,

$$\overline{E}_{rr} = \ln(1 + u_r|_{z=0.5, r=1.0}), \tag{5.5}$$

where the reference configuration dimensions of the cells are unity. Thus, the macroscopic effective strain and macroscopic volumetric strain are calculated, respectively, as

$$\overline{E}_{\text{eq}} = \frac{2}{3}||\overline{E}_{zz} - \overline{E}_{rr}|| \tag{5.6}$$

and

$$\overline{E}_{kk} = E_{zz} + 2\overline{E}_{rr}. \tag{5.7}$$

The finite element meshes consist of 900 8-node biquadratic elements, ABAQUS type CAX8. The mesh density was verified by also performing analyses with 3600 elements. The two mesh densities produced identical macroscopic responses.

5.1.2 Multi-particle RVE's

Multi-particle RVE's are required in order to capture the effects of a truly random spatial distribution of particles. In this study, an algorithm developed by Danielsson [18] was utilized to build three-dimensional, space-filling, fully periodic RVE's and the corresponding finite element meshes.

A two-dimensional schematic of the construction procedure for a 10-particle RVE, taken from Danielsson et al. [21], is shown in Figure 5-3. First, $P = 10$ particles are added one-by-one to a reference unit cube (the center box in Figure 5-3a). For the

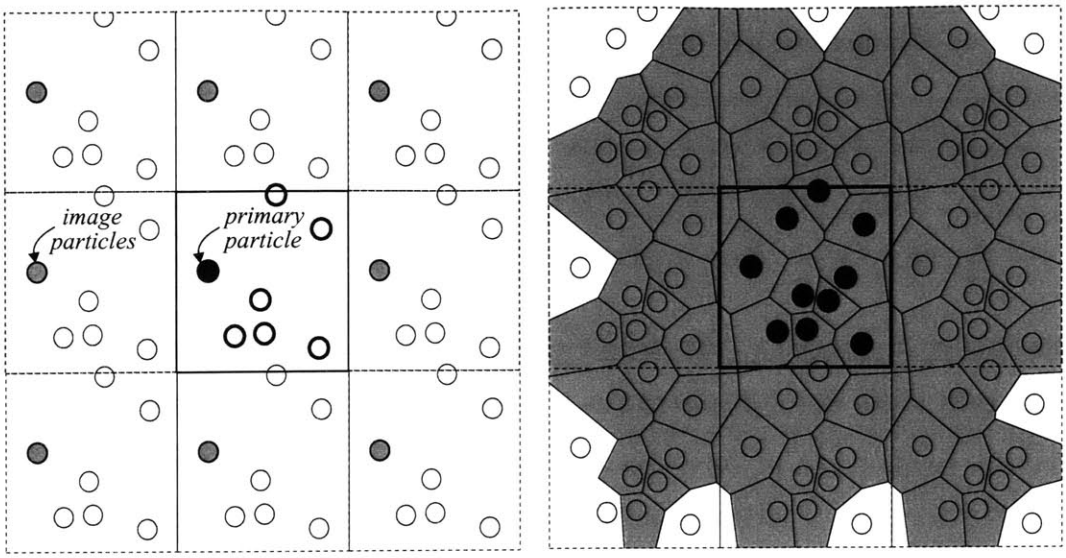

Figure 5-3: Two-dimensional schematic of the construction of a 10-particle RVE (Danielsson et al. [21]). (a) Addition of a primary particle and its eight periodic image particles. (b) Voronoi tessellation of all particles. Only bounded cells are shown. The Voronoi cells with particles in or intersecting the solid box comprise the RVE.

purpose of making the RVE spatially periodic, for each "primary" particle added to the reference box, 26 "image" particles (eight, in the two-dimensional case) are added to the 26 unit boxes surrounding the reference box. Each image particle is offset by a linear unit combination of the Cartesian basis vectors. Particles are not allowed to overlap existing primary or image particles. Furthermore, except where it is noted, the centers of the particles are constrained to be no closer than 2.5 times the particle radius, $r = \left(\frac{3f}{4\pi P}\right)^{(1/3)}$, in order to prevent excessively distorted finite elements from being formed during the meshing process. In total, there are $27P$ particles ($9P$, in the two-dimensional case). Next, as shown in Figure 5-3b, a Voronoi tessellation is performed on the $27P$ particle centers. The Voronoi cells containing the image particles are then discarded, and the result is the P-cell, space-filling, periodic RVE at the center of Figure 5-3b.

In the finite element implementation, the RVE is deformed via the displacements of three "dummy" nodes: $n1$, $n2$, $n3$. The displacement components of the dummy

nodes make up the macroscopic deformation gradient, $\overline{\mathbf{F}}$, at each increment:

$$\begin{bmatrix} (\overline{F}_{11}-1) & \overline{F}_{12} & \overline{F}_{13} \\ \overline{F}_{21} & (\overline{F}_{22}-1) & \overline{F}_{23} \\ \overline{F}_{31} & \overline{F}_{32} & (\overline{F}_{33}-1) \end{bmatrix} = \begin{bmatrix} u_1|_{n1} & u_2|_{n1} & u_3|_{n1} \\ u_1|_{n2} & u_2|_{n2} & u_3|_{n2} \\ u_1|_{n3} & u_2|_{n3} & u_3|_{n3} \end{bmatrix}. \tag{5.8}$$

The deformation is applied to the surface of the RVE through a series of constraint equations, each made up of displacement components of the dummy nodes and the displacement components of corresponding pairs of nodes on the outer surfaces of the RVE. For example, if nodes A and B are a periodic pair, their displacements are controlled by

$$\mathbf{u}|_B - \mathbf{u}|_A = \left(\overline{\mathbf{F}} - \mathbf{1}\right)\left\{\mathbf{X}|_B - \mathbf{X}|_A\right\}, \tag{5.9}$$

where $\mathbf{X}$ is the position vector in the reference configuration. These constraint equations maintain periodicity throughout the deformation. The macroscopic Cauchy stress components, derived through the principle of virtual work (Danielsson et al. [19]), are computed from the macroscopic deformation gradient and the reaction forces at the dummy nodes. The macroscopic true strain is calculated from the polar decomposition $\overline{\mathbf{F}} = \overline{\mathbf{V}}\,\overline{\mathbf{R}}$ as

$$\overline{\mathbf{E}} = \ln \overline{\mathbf{V}}, \tag{5.10}$$

and the macroscopic volumetric strain is given by

$$\overline{E}_{kk} = \ln\left(\det\overline{\mathbf{F}}\right). \tag{5.11}$$

The multi-particle RVE's are loaded by specifying either the macroscopic material velocity gradient, $\dot{\overline{\mathbf{F}}}$, or a constant macroscopic stress triaxiality ratio, X. In the former case, $\overline{\mathbf{F}}$ is known a priori; in the latter case, a user-defined element, similar to that used with the single-particle RVE's, drives $\overline{\mathbf{F}}$ such that X is maintained constant.

Following Danielsson [18], RVE's containing six and ten particles were constructed

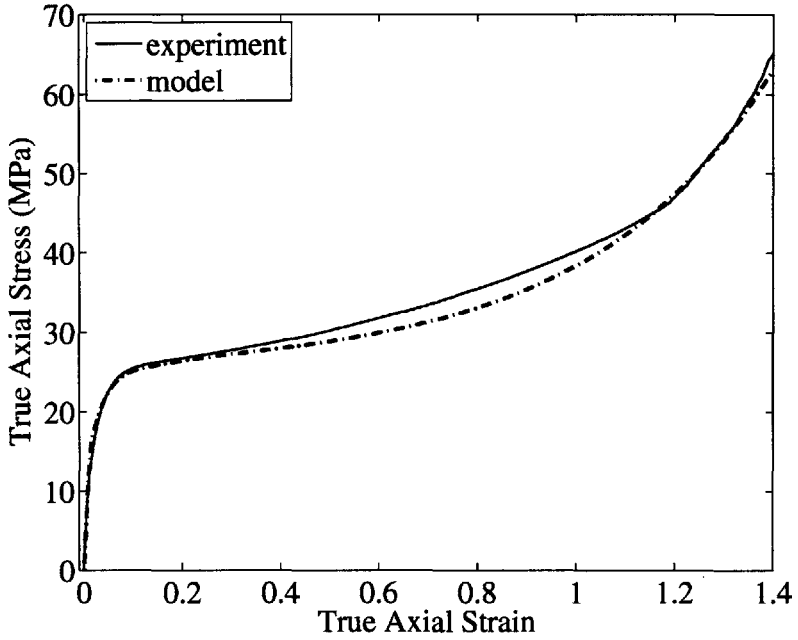

Figure 5-4: Prediction of series constitutive model and experimental results for uniaxial tension of neat HDPE.

from 10-node tetrahedral elements, ABAQUS type C3D10M. The number of elements, approximately 2000 elements per particle, was chosen based on an abbreviated mesh refinement study buttressed by the more comprehensive analysis of Danielsson.

5.2 Constitutive Descriptions

5.2.1 Matrix

The constitutive response of the HDPE matrix is described by the amorphous polymer model of Arruda and Boyce [4] as presented in Sections 4.2.1 and 4.3.1. The prediction of the model results for uniaxial tension of neat HDPE are reproduced in Figure 5-4.

5.2.2 Particles

The $CaCO_3$ particles are approximated as perfectly rigid spheres. Non-cavitating EPDM particles are modeled as spherical fluid cavities in which the fluid has zero shear modulus and a bulk modulus of 2000 MPa. Cavitating rubber particles are

modeled as spherical voids.

5.2.3 Interface

The experimental results of Chapter 3 show that $CaCO_3$ particles have a substantial reinforcement effect on HDPE before they debond. Thus, the $CaCO_3$ particles and HDPE matrix are initially modeled as perfectly bonded to one another and are then allowed to separate as the deformation progresses.

Debonding from the $CaCO_3$ particles is controlled via a continuum cohesive-zone type interface model formulated within the phenomenological framework of Needleman [52] and further developed by Socrate [64]. The interface constitutive response is elastic and fully prescribed by a potential function, ϕ, which allows for both normal and tangential decohesion. The traction, $\mathbf{t}$, across the interface is dependent only on the displacement jump, $\mathbf{u}$, across the interface. As illustrated in Figure 5-5, at each point on the interface, $\mathbf{u}$ is defined in terms of its local normal and tangential components,

$$u_{\mathrm{n}} = \mathbf{u} \cdot \mathbf{n} \tag{5.12}$$

and

$$u_{\mathrm{t}} = \mathbf{u} \cdot \mathbf{t}, \tag{5.13}$$

respectively, where $\mathbf{n}$ and $\mathbf{t}$ are unit vectors normal and tangent, respectively, to the interface. The normal and tangential components of the traction per unit interface area are obtained by differentiating ϕ:

$$t_{\mathrm{n}} = -\frac{\partial \phi}{\partial u_{\mathrm{n}}} \tag{5.14}$$

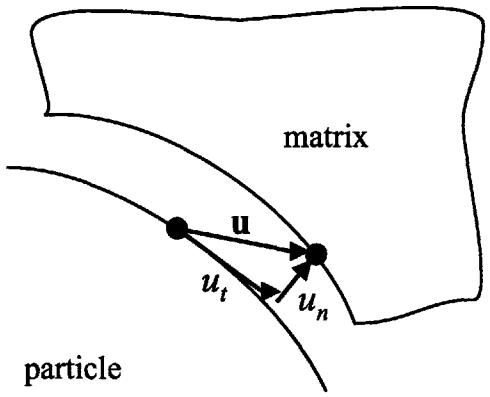

Figure 5-5: Definition of the components of the displacement jump, **u**, across the interface in two dimensions.

and

$$t_{\mathrm{t}} = -\frac{\partial \phi}{\partial u_{\mathrm{t}}}. \tag{5.15}$$

As the interface separates, the traction across the interface rapidly increases, reaches a maximum, and then eventually falls to zero when complete decohesion occurs.

The specific form of the potential function ϕ, proposed by Xu and Needleman [80], is given by

$$\phi(\mathbf{u}) = \phi_n - \phi_n \exp\left(-\frac{u_n}{\delta_n}\right)\left\{\left[1+\frac{u_n}{\delta_n}\right](1-q) - q\left[1+\frac{u_n}{\delta_n}\right]\exp\left(-\frac{u_t^2}{\delta_t^2}\right)\right\}, \tag{5.16}$$

with

$$\phi_{\mathrm{n}} = \mathrm{e}\,\sigma_{\max}\delta_{\mathrm{n}}, \tag{5.17}$$

$$\phi_{\mathrm{t}} = \sqrt{\frac{\mathrm{e}}{2}}\,\tau_{\max}\delta_{\mathrm{t}}, \tag{5.18}$$

and

$$q = \frac{\phi_{\mathrm{n}}}{\phi_{\mathrm{t}}}, \tag{5.19}$$

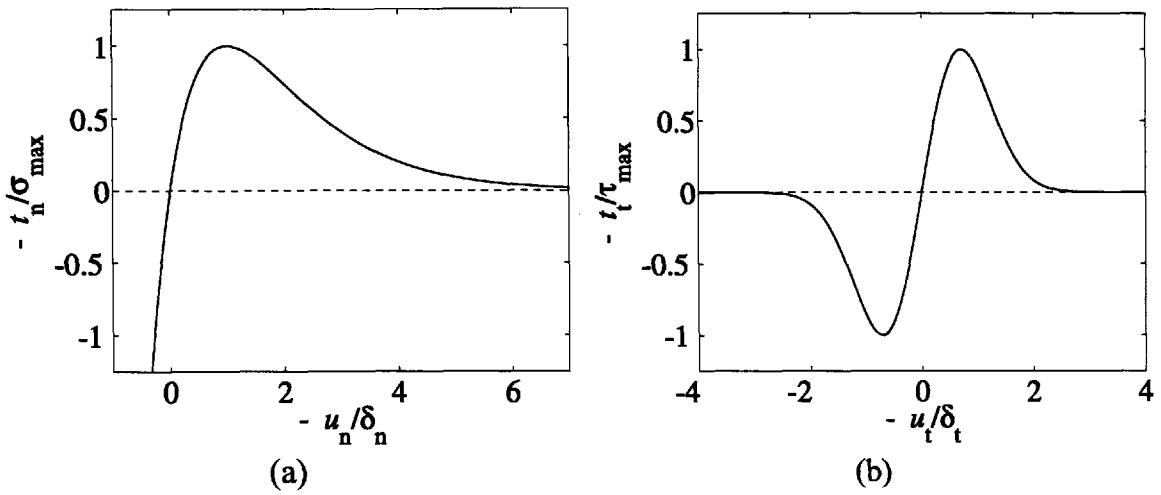

Figure 5-6: The relationship between the traction, $\mathbf{t}$, across the $CaCO_3$/HDPE interface and the displacement jump, $\mathbf{u}$, across the interface: (a) normal traction, t_n, versus u_n for $u_t \equiv 0$; (b) shear traction, t_t, versus u_t for $u_n \equiv 0$.

where e = exp(1), ϕ_n and ϕ_t are, respectively, the normal and tangential works of separation, δ_n and δ_t are characteristic separation lengths, and σ_{max} and τ_{max} are characteristic interface strengths. Figure 5-6a shows a plot of the normal traction-displacement relation with $u_t \equiv 0$. The maximum value of $-t_n$, σ_{max}, occurs at $u_n = \delta_n$. Similarly, Figure 5-6b shows a plot of the shear traction-displacement relation with $u_n \equiv 0$. The maximum value of $|t_t|$, τ_{max}, occurs at $u_t = \sqrt{2}\delta_t/2$. In this study, $\delta_n = \delta_t$ and $\tau_{max} = \sqrt{2\,e}\sigma_{max}$ so that the normal and tangential works of separation are equal, and, as a result, $q = 1$ in Equation 5.16.

5.3 Results

The micromechanical models were loaded in uniaxial tension. Here, their macroscopic predictions are compared with the results of the uniaxial tension experiments on CC1-filled and rubber-filled HDPE presented in Chapter 3. In each case, in accordance with the experimental measurements, the macroscopic axial strain rate is a function of the macroscopic axial strain. The elastic and yield properties are summarized in Tables 5.1 and 5.2. (For consistency of comparison, "yield" is taken to occur when the engineering stress peaks.) With the exception of the debonding cases, the properties

	f	Young's modulus, E (MPa)	Yield strength (MPa)	$E_{\text{blend}}/E_{\text{neat}}$ (Mori-Tanaka)
exp./sim.	0	1320	25.1	1.00
exp. CC1	0.10	1630	21.5	1.23 (1.24)
exp. CC1	0.20	2050	18.6	1.55 (1.54)
SHA PB	0.10	1730	26.0	1.31
SHA PB	0.20	2430	29.6	1.84
SA PB	0.10	1650	25.8	1.25
SA PB	0.20	2080	27.3	1.58
SHA NB	0.10	1130	21.1	0.86
SHA NB	0.20	960	18.4	0.73
SA NB	0.10	1130	19.6	0.85
SA NB	0.20	960	17.2	0.73
SHA debond	0.10	1670	21.3	1.26
SHA debond	0.20	2220	18.6	1.68
SA debond	0.10	1610	19.7	1.22
SA debond	0.20	1960	17.9	1.48
Multi-p PB	0.10	1660	26.5	1.26
Multi-p PB	0.20	2160	30.4	1.64
Multi-p NB	0.10	1130	20.9	0.86
Multi-p NB	0.20	950	18.0	0.72
Multi-p debond*	0.10	1440	20.7	1.10
Multi-p debond*	0.20	1710	18.1	1.30

Table 5.1: Summary of experimental results and micromechanical modeling predictions for CC1-filled HDPE (SA=staggered array, SHA=stacked hexagonal array, PB=perfect bonding, NB=no bonding). *Distributed debonding.

of the multi-particle RVE's are the average of several simulations, each of which consisted of either a different spatial distribution of particles or a different loading direction.

5.3.1 Rigid particles

Single-particle RVE's

Stacked hexagonal array: perfect bonding and no bonding

Figure 5-7 shows the macroscopic true stress-strain (a) and volumetric strain (b) predictions of the stacked hexagonal array (SHA) RVE at $f = 0.10$ and $f = 0.20$ with perfect bonding ("PB") and no bonding ("NB") between the matrix and the rigid

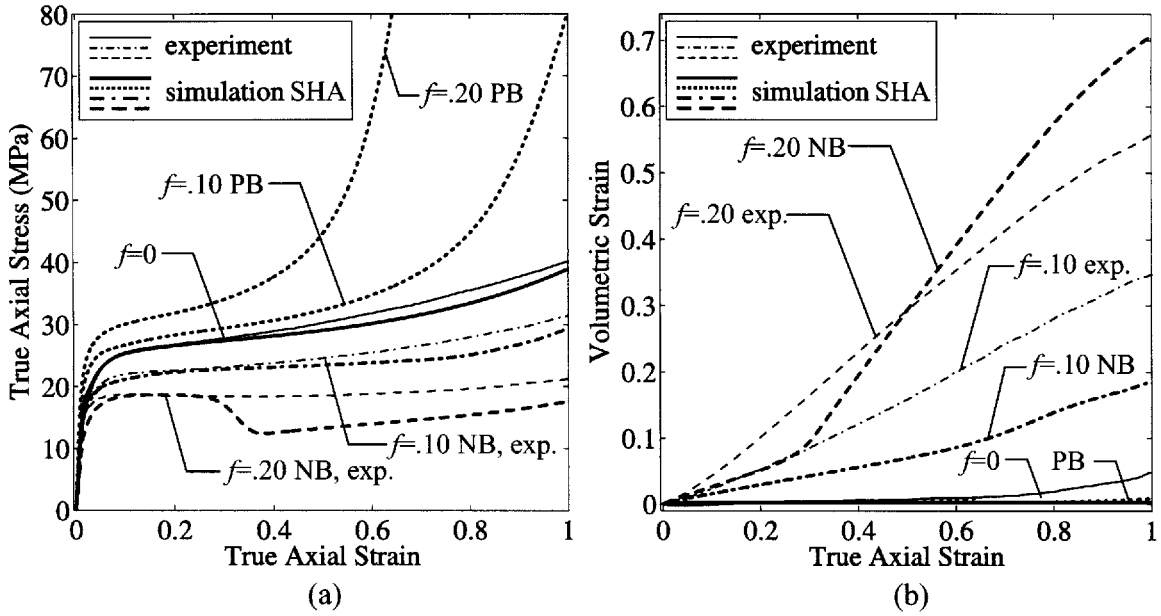

Figure 5-7: Macroscopic predictions of stacked hexagonal array (SHA) under uniaxial tension with rigid particles with perfect bonding (PB) and no bonding (NB) compared with CC1-filled HDPE uniaxial tension experiments: (a) true axial stress versus true axial strain, (b) volumetric strain versus true axial strain.

particle. With perfect bonding, the particle bears load and reinforces the matrix, resulting in an elastic modulus, flow stress, and rate of post-yield strain hardening superior to that of the homopolymer. Perfect bonding does not allow void growth around the particle and, hence, the only volumetric strain apparent in Figure 5-7b is due solely to the elastic volume change. The trend of increasing modulus with increasing f agrees with the CC1-filled HDPE experimental data, but the moduli predicted by the SHA-PB model (1730 MPa and 2430 MPa) are significantly greater than those measured experimentally (1630 MPa and 2050 MPa). The predictions of the SHA-PB model clearly do not match the flow stress or the volumetric strains observed in the experiments, which show a reduction in flow stress and an increase in volumetric strain with increasing f. With no bonding, the modulus and flow stress decrease with increasing f, and void growth at the particle surface is manifested in substantial volumetric strain in Figure 5-7b. The SHA-NB model predicts the experimentally measured yield strengths exceptionally well at both f=0.10 and f=0.20. At f=0.10, the model's macroscopic stress-strain response shows good agreement

with the experiment over the course of the entire stress-strain curve. The predicted volumetric strain is, however, approximately one-half of the measured volumetric strain. At f=0.20, the predicted stress-strain response deviates from the measured response at $\overline{E}_{zz} \approx 0.30$, where the prediction drops precipitously before stabilizing at $\overline{T}_{zz} \approx 12.5$ MPa. Concurrent with the stress drop, the slope of the model's volumetric strain response increases sharply, and the predicted volumetric strain eventually surpasses the measured volumetric strain.

Figure 5-8 illustrates the evolution of equivalent (Mises) stress in the matrix with the SHA-PB and SHA-NB models at $f = 0.20$. (The neighboring unit cell is mirrored in all contour plots for visualization purposes.) In the PB model at $\overline{E}_{zz} = 0.005$ (a), still in the elastic regime, the stress concentrates over the pole of the particle due to the proportionally large tensile strains in this short section of the matrix and at the surface of the particle due to the large shear strains generated by the constraint there. At $\overline{E}_{zz} = 0.04$ (b), corresponding approximately to macroscopic yield, these two areas of stress concentration connect to form wing-like bands tangent to the surface of the particle. As $\overline{E}_{zz}$ increases further, the bands dissipate in strength, and the stress becomes fairly evenly distributed throughout the matrix with the exception of the concentrations at the surface of the particle and at the root of the vertical interparticle ligament. In the NB model (a′-d′), on the other hand, through $\overline{E}_{zz} = 0.20$, the stress concentrates in the entire vertical ligament (i.e. from $z = 0$ to $z = 1$) between the particles with the material above the pole of the particle remaining relatively unstressed as it translates vertically. The stress is highest near the equator of the particle, the site of the highest geometric stress concentration and also the narrowest section of the ligament. The resulting yield strength, as a proportion of the homopolymer's yield strength, relates closely to the area fraction of matrix on the $z = 0$ plane. At $\overline{E}_{zz} = 0.40$ (d′), the stress has localized in the now very thin ligament section at the equator of the particle. The deformation mechanism is analogous to the necking and drawing of the neat HDPE tensile specimen. As the material at the equator strain hardens, the deformation there stabilizes and the deformation traverses up the ligament. Accompanying the drop in stress is an equally sudden increase in

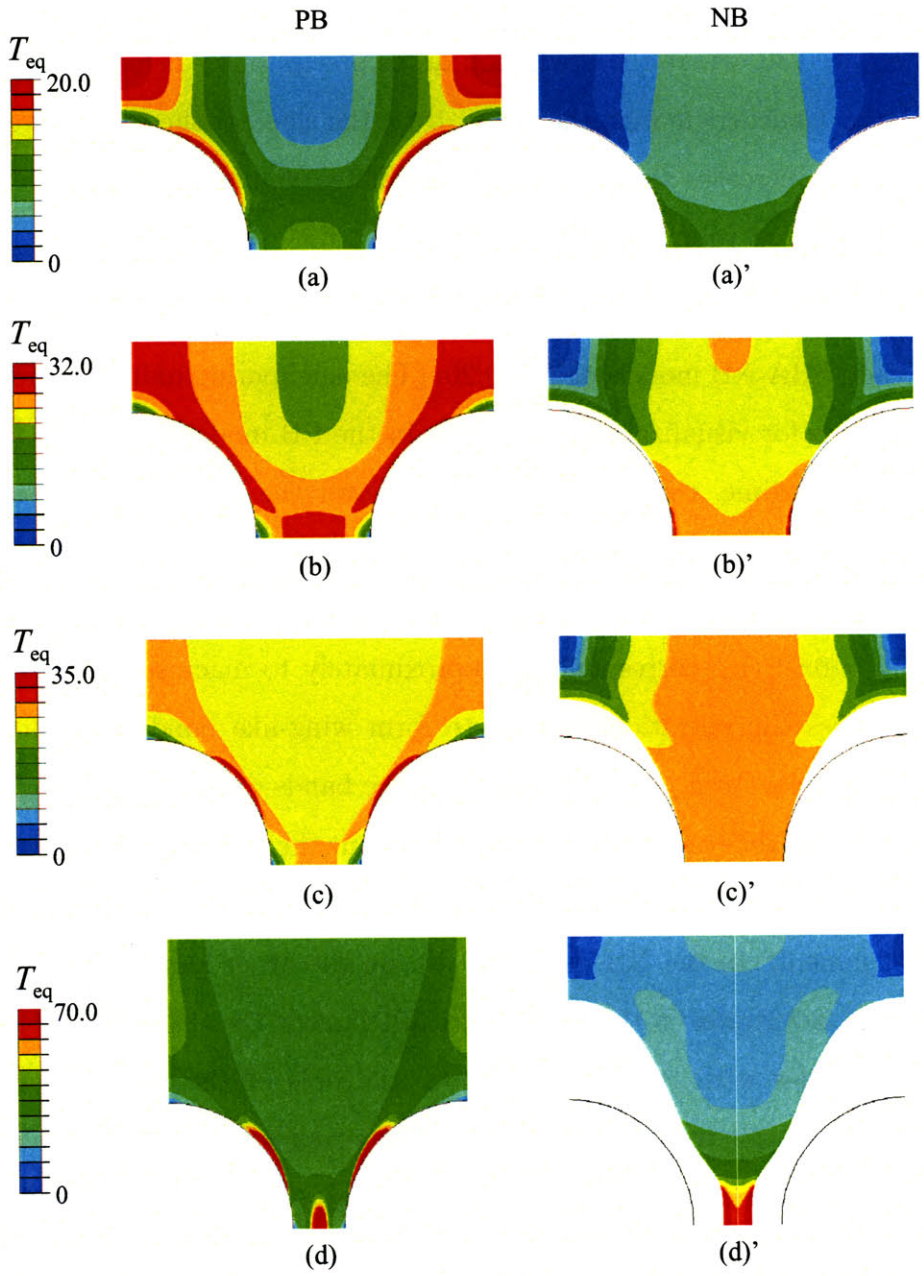

Figure 5-8: $f = 0.20$, stacked hexagonal array (SHA) RVE under uniaxial tension with rigid particles with perfect bonding (left) and no bonding (right). Contour plots of local Mises stress, T_{eq}, for increasing macroscopic axial strain, $\overline{E}_{zz}$: (a), (a′) $\overline{E}_{zz} = 0.005$; (b), (b′) $\overline{E}_{zz} = 0.04$; (c), (c′) $\overline{E}_{zz} = 0.20$; (d), (d′) $\overline{E}_{zz} = 0.40$.

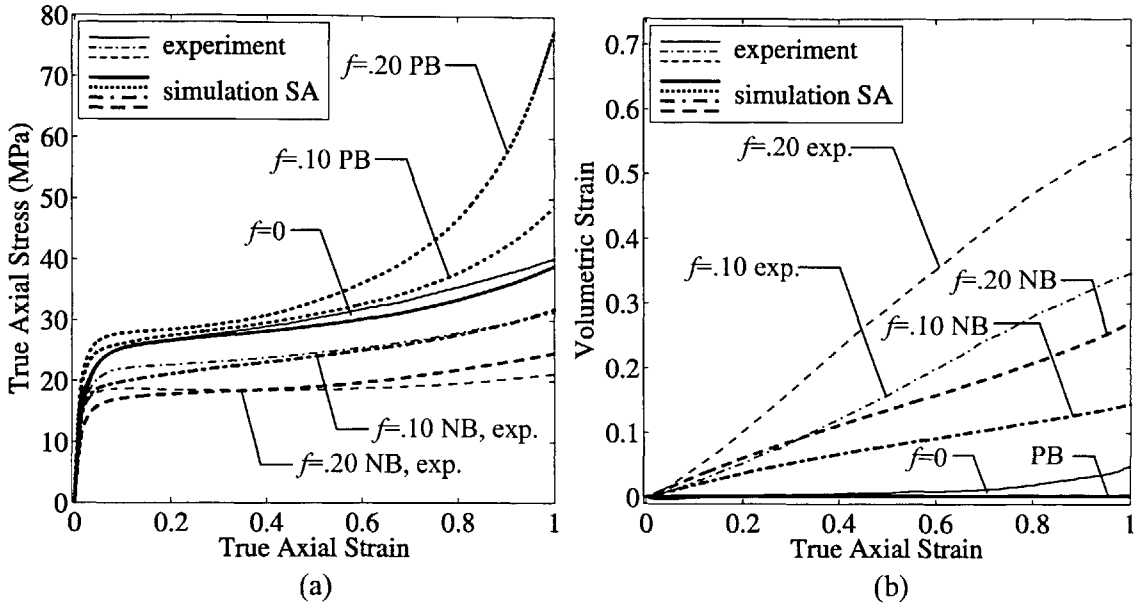

Figure 5-9: Macroscopic predictions of staggered array (SA) under uniaxial tension with rigid particles with perfect bonding (PB) and no bonding (NB) compared with CC1-filled HDPE uniaxial tension experiments: (a) true axial stress versus true axial strain, (b) volumetric strain versus true axial strain.

the rate of dilatation. The lateral constraint on the radial boundary provided by the adjacent, symmetric particle limits the extent to which the cell can shrink in the radial direction. Excessive void growth around the particle therefore occurs. A similar pattern of deformation is apparent at $f = 0.10$, but the ligament localization occurs at a larger macroscopic axial strain, as indicated by the upturn of the volumetric strain curve at $\overline{E}_{zz} \approx 0.70$.

Staggered array: perfect bonding and no bonding

Figure 5-9 depicts the macroscopic true stress-strain (a) and volumetric strain (b) predictions of the staggered array (SA) RVE at $f = 0.10$ and $f = 0.20$ with perfect bonding and no bonding between the matrix and the rigid particle. The general trends in elastic modulus, floor stress, and volumetric strain, as a function of f, are similar to those observed with the SHA model. The SA-PB model, however, exhibits a smaller increase in elastic modulus, yield strength, and rate of strain hardening with increasing f than does the SHA-PB model. The predicted elastic moduli are very close to the CC1-filled elastic HDPE moduli. While the yield strengths of the SA-NB

models are approximately 5% less than the SHA-NB and experimental values, the stress-strain predictions of the SA-NB models show overall better agreement with the CC1-filled HDPE experiments than the SHA-NB models. The increased accuracy of the stress-strain predictions comes, however, at the expense of less accurate volumetric strain predictions. The volumetric strains exhibited by the SA RVE's are smaller than the SHA predictions and less than half of those measured in CC1-filled HDPE.

The corresponding contour plots of equivalent stress for the SA RVE's at $f = 0.20$ are presented in Figure 5-10. At all strain levels, the maximum stress in the PB model is located in the short matrix section at the pole of the particle. Once macroscopic yield occurs at $\overline{E}_{zz} \approx 0.04$ (b), the stress remains fairly well distributed. There is a very thin layer of highly stressed matrix at the surface of the particle, but the wing-like band observed in the SHA RVE does not appear. In the SA-NB model, as in the SHA-NB model, the maximum stress is located in the interparticle ligament near the equator of the particle. At macroscopic yield (b'), the stress fields of the two particles connect, forming a diagonal band. As the macroscopic axial strain increases, the band widens to encompass the entire vertical interparticle ligament. The localization and rapid void growth exhibited by the SHA RVE do not occur. The antisymmetric boundary conditions on the lateral surface of the RVE allow the ligament to contract in the radial direction. From the irregular shape of the developing void (in contrast to the nearly elliptical shape of the void in the SHA-NB model prior to localization), it is also apparent that the particle prevents the ligament from pinching in.

Contours of an additional measure, the normalized equivalent plastic shear strain rate, $\overline{\dot{\gamma}^{\mathrm{p}}} = \dfrac{\dot{\gamma}^{\mathrm{p}}}{\sqrt{3}\,\dot{\overline{E}}_{\mathrm{eq}}}$, are plotted at similar axial macroscopic strains in Figure 5-11. These plots, to a degree, mirror the corresponding contour plots of stress but provide a more accurate picture of the regions of the matrix that are most actively shearing at a given macroscopic strain. (Recall, from Equation 4.12, that it is not the total stress that drives plastic flow.) Prior to macroscopic yield, at $\overline{E}_{zz} = 0.01$ (a), viscoplastic shearing initiates at the sections where the stress is highest – near the pole of the particle in the PB case and near the equator of the particle in the NB case. Macroscopic yield, shortly before $\overline{E}_{zz} = 0.04$, is manifested by plasticity

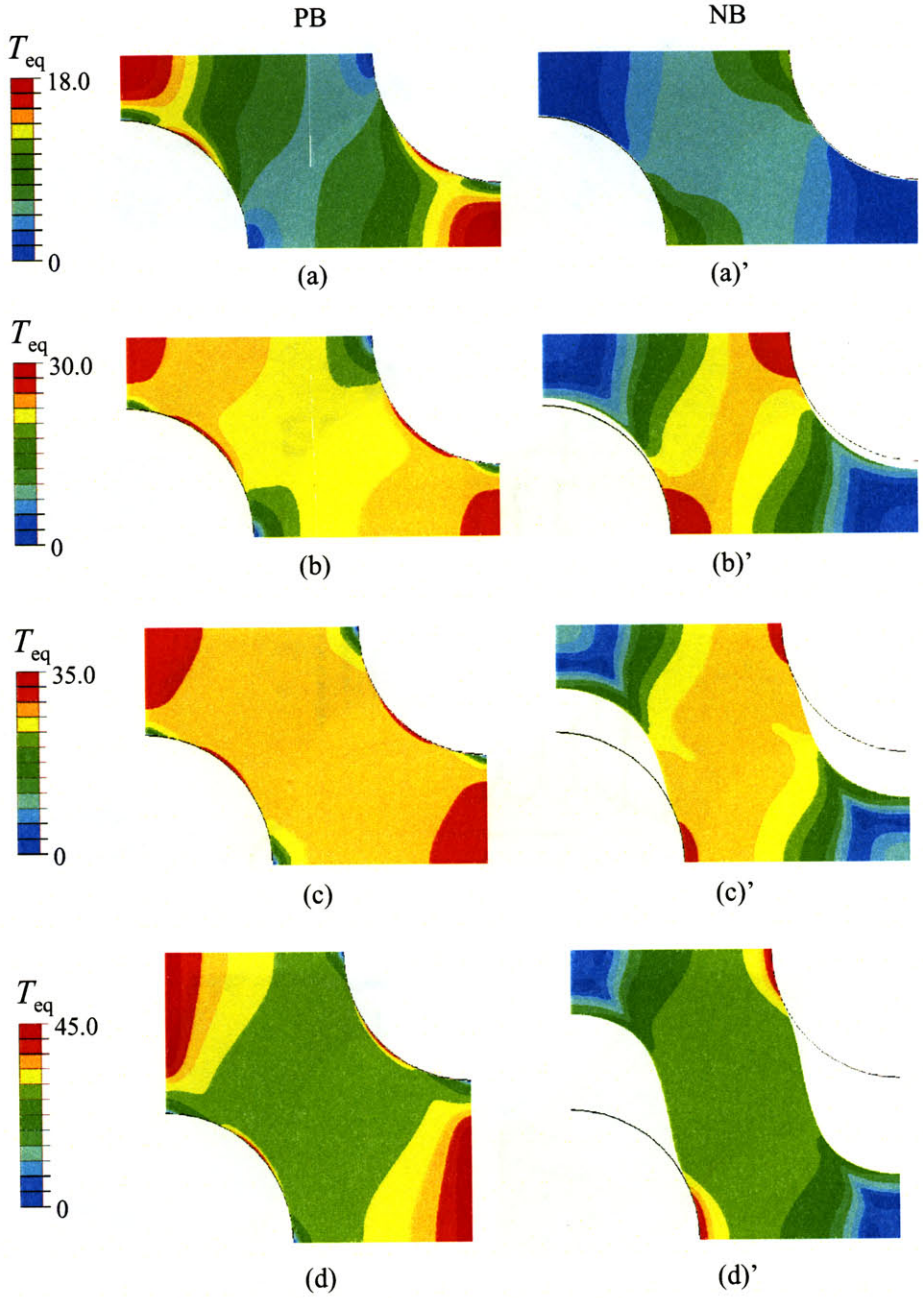

Figure 5-10: $f = 0.20$, staggered array (SA) RVE under uniaxial tension with rigid particles with perfect bonding (left) and no bonding (right). Contour plots of local Mises stress, T_{eq}, for increasing macroscopic axial strain, $\overline{E}_{zz}$: (a), (a′) $\overline{E}_{zz} = 0.005$; (b), (b′) $\overline{E}_{zz} = 0.04$; (c), (c′) $\overline{E}_{zz} = 0.20$; (d), (d′) $\overline{E}_{zz} = 0.40$.

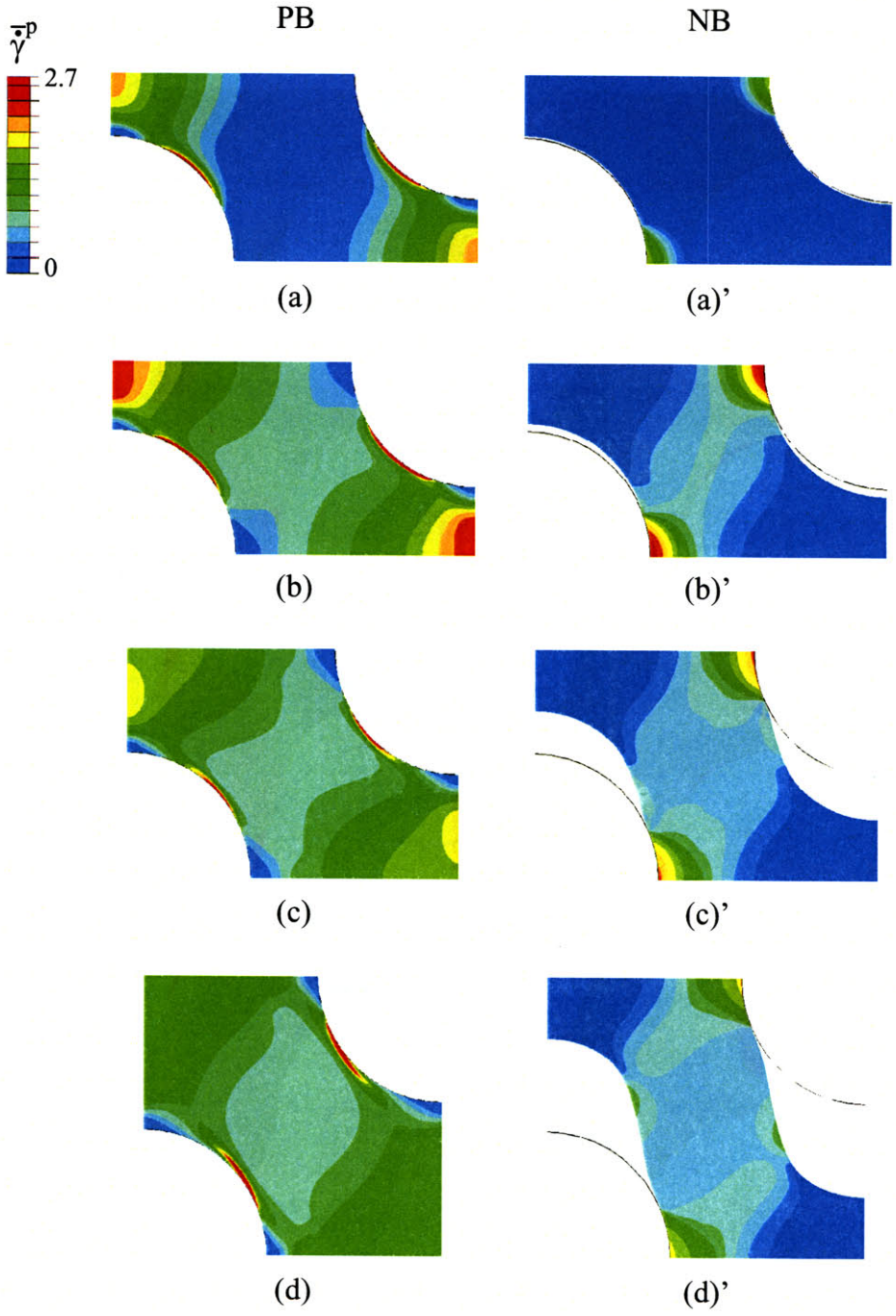

Figure 5-11: $f = 0.20$, staggered array (SA) RVE under uniaxial tension with rigid particles with perfect bonding (left) and no bonding (right). Contour plots of normalized equivalent plastic shear strain rate, $\dot{\overline{\gamma}}^{\mathrm{p}}$, for increasing macroscopic axial strain, $\overline{E}_{zz}$: (a), (a′) $\overline{E}_{zz} = 0.01$; (b), (b′) $\overline{E}_{zz} = 0.04$; (c), (c′) $\overline{E}_{zz} = 0.20$; (d), (d′) $\overline{E}_{zz} = 0.40$.

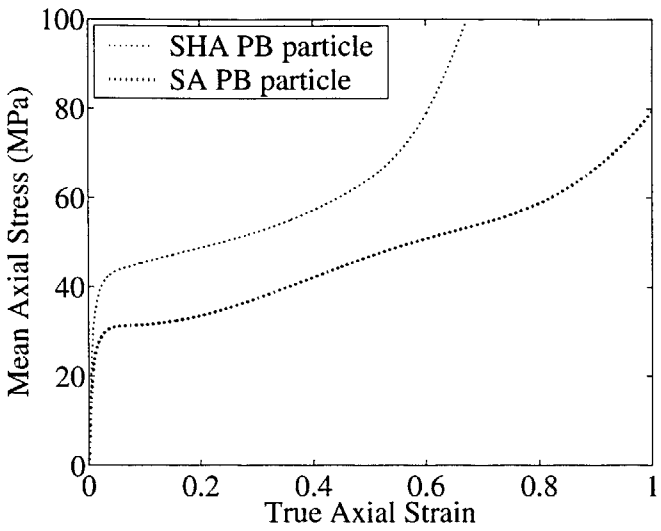

Figure 5-12: Mean axial stress in the particle at $f = 0.20$ with the SHA-PB and SA-PB models as a function of the macroscopic true axial strain, $\overline{E}_{zz}$.

spanning the entire vertical interparticle ligament as shown in Figure 5-11 b, b'. Continued deformation of the RVE's causes the plasticity to become increasingly diffuse as regions with high rates of shearing strain harden. At $\overline{E}_{zz} = 0.40$ (c), plastic flow is nearly evenly distributed throughout the entire matrix in the PB model. In the NB model, only the relatively unstressed region above the pole of the particle has yet to yield.

Discussion: stacked hexagonal array versus staggered array

Comparing the SHA RVE's to the SA RVE's, the macroscopic responses and modes of deformation are substantially different. In the PB case, the SHA model exhibits a stiffer elastic response and a greater flow stress at all strains than the SA model. Particles in a stacked arrangement provide more reinforcement than particles in an staggered arrangement. In Figure 5-12, it is shown that, at $f = 0.20$, the mean axial stress in the particle in the SHA-PB model is, at a minimum, 35% greater than the mean axial stress in the particle in the SA-NB model. With no bonding, the two types of RVE's exhibit identical moduli, but the SHA RVE has a superior yield strength and also, until moderate strain levels, a higher flow stress than the SA RVE. In general, as evidenced by the shearing of the vertical interparticle ligament

and the ability of the ligament to rotate and contract non-uniformly in the SA-NB model, a staggered array generates an initially more compliant cell than a stacked array. Assuming that the particles lie in the same z-plane artificially constrains the SHA cell. However, at moderate to large strains, depending on the volume fraction of filler, this same constraint and the high area fraction of particles at $z = 0$ promote localization in the ligament in both the NB and PB models. In the SHA-NB model, ligament necking and the associated accelerated void growth ensue in the thinnest section of the ligament, causing the macroscopic flow stress to drop below that of the SA-NB model.

In a sense, the SHA and SA RVE's represent the two extremes of the spatial distribution of particles: clustering and good dispersion. With the SHA representation, particles are concentrated on identical z-planes, producing axial layers with a high area fraction of filler alternating with axial layers that are entirely matrix. With the SA representation, the variation in area fraction of filler with axial position is not nearly as large. In fact, unless $f < 0.084$, the axial projections of adjacent particles overlap. The SA RVE clearly is a much better approximation of a well dispersed arrangement of particles than the SHA RVE.

In summary, none of the micromechanical models introduced up to this point are capable of reproducing the results of the experiments on CC1-filled HDPE. However, features of the model predictions do show good agreement with the experimental data: the SA-PB model provides an excellent modulus prediction; the SHA-NB model predicts the yield strength and volumetric strain (at $f = .20$, at least) quite well; the SA-NB model predictions show the best agreement with the flow stress at moderate to large strains. While it is not clear what is the most appropriate spatial distribution of particles, it is apparent that, as surmised in Chapter 3, a debonding criterion is required in order to develop a model which can predict both the elastic and yield properties of CC1-filled HDPE.

Single-particle RVE with debonding

The interface properties described in Section 5.2.3 were chosen such that debonding in the models initiates at approximately the macroscopic stresses at which the

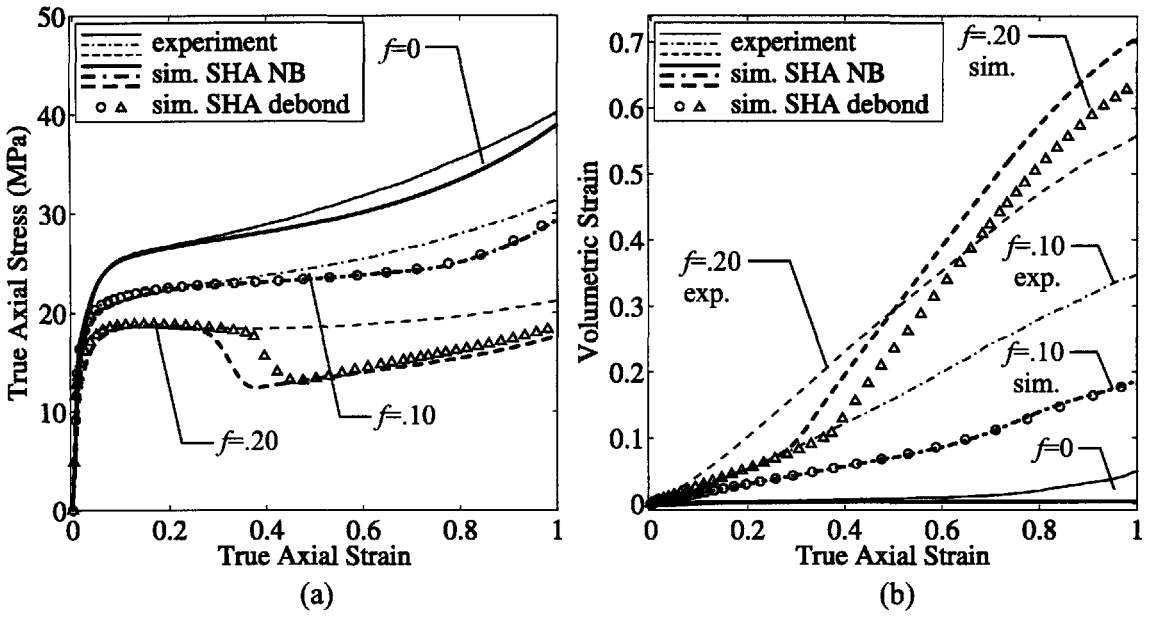

Figure 5-13: Macroscopic predictions of stacked hexagonal array (SHA) under uniaxial tension with rigid particles with debonding and no bonding (NB) compared with CC1-filled HDPE uniaxial tension experiments: (a) true axial stress versus true axial strain, (b) volumetric strain versus true axial strain.

experimental true stress-strain curves deviate from linearity. Debonding is defined to begin when the separation of the matrix from the pole of the particle is at its maximum velocity relative to the macroscopic strain rate of the unit cell. This criterion corresponds approximately to a separation of twice the characteristic interface lengths, δ_n and δ_t. For both types of unit cells, σ_{max} was chosen to be 12.5 MPa and δ_n and δ_t were set at $0.0025r$, where r is the radius of the particle in the simulations. These properties specify the normal and tangential works of separation to be $\phi_n = \phi_t = 85.0r$ kN/m^2.

The macroscopic true stress-strain and volumetric strain predictions of the SHA RVE's with debonding, compared with the SHA-NB and CC1-filled HDPE experimental results, are given in Figure 5-13. The elastic moduli, listed in Table 5.1, are slightly lower than those predicted with the perfectly bonded interface due to the compliance of the interface. The SHA-debond moduli are, however, still larger than the experimental values. Debonding begins prior to macroscopic yield at ($\overline{E}_{zz} = 8.14 \times 10^{-3}$, $\overline{T}_{zz} = 12.4$ MPa) for $f = 0.10$ and at ($\overline{E}_{zz} = 7.43 \times 10^{-3}$, $\overline{T}_{zz} = 12.8$ MPa) for

$f = 0.20$. Figure 5-15a shows that debonding rapidly occurs to an angle of $\phi \approx 60°$, measured from the positive z-direction, before progressing much more slowly at larger macroscopic axial strains. While, by the definition of yield strength used in this study, the SHA-NB and SHA-debond models exhibit virtually identical yield strengths, careful inspection of Figure 5-13a reveals that the debonding interface response improves the predictions of the SHA RVE at macroscopic axial strains less than $\overline{E}_{zz} \approx 0.15$. From $\overline{E}_{zz} \approx 0.01$ to $\overline{E}_{zz} \approx 0.20$, the partially debonded particle still somewhat reinforces the cell matrix. Thereafter, at $f = 0.10$, the stress-strain predictions of the SHA-NB and SHA-debond models essentially coincide. At all strains, the debonding interface response has negligible effect on the volumetric strain at $f = 0.10$. At $f = 0.20$, the drop in true stress predicted by the SHA-NB model at $\overline{E}_{zz} \approx 0.30$ is delayed until $\overline{E}_{zz} \approx 0.40$ with the SHA-debond model. It is at this macroscopic axial strain that complete debonding, marked by the separation of the matrix from the particle at the equator of the particle ($\phi = 90°$), occurs. Once the stress prediction of the debonding model drops, the true stress-strain responses of the two models are very similar. The increase in slope of the volumetric strain that accompanies the drop in stress is also delayed by the debonding interface behavior. While the slope of the volumetric strain is the same for both models after $\overline{E}_{zz} \approx 0.4$, the actual volumetric strain predicted by the SHA-debond model remains always less than that predicted by the SHA-NB model.

Contours of equivalent stress for the SHA RVE at $f = 0.20$ with debonding are plotted in Figure 5-16 a-d. At $\overline{E}_{zz} = 0.005$ (a), still in the linear regime of the macroscopic stress-strain response and prior to debonding, the distribution of stress closely resembles that of the SHA-PB model in Figure 5-8a. The stress is highest above the pole of the particle and at the surface of the particle. By $\overline{E}_{zz} = 0.04$ (b), macroscopic yield has occurred, and the angle of debonding exceeds $\phi = 60°$. The SHA-debonding model exhibits a stress concentration at the point of debonding and a distribution of stress in the vertical interparticle ligament different than that of the SHA-NB model. The material above the pole of the particle has elastically unloaded, but the stress contours and slightly superior macroscopic flow stress at $\overline{E}_{zz} = 0.04$ indicate that the

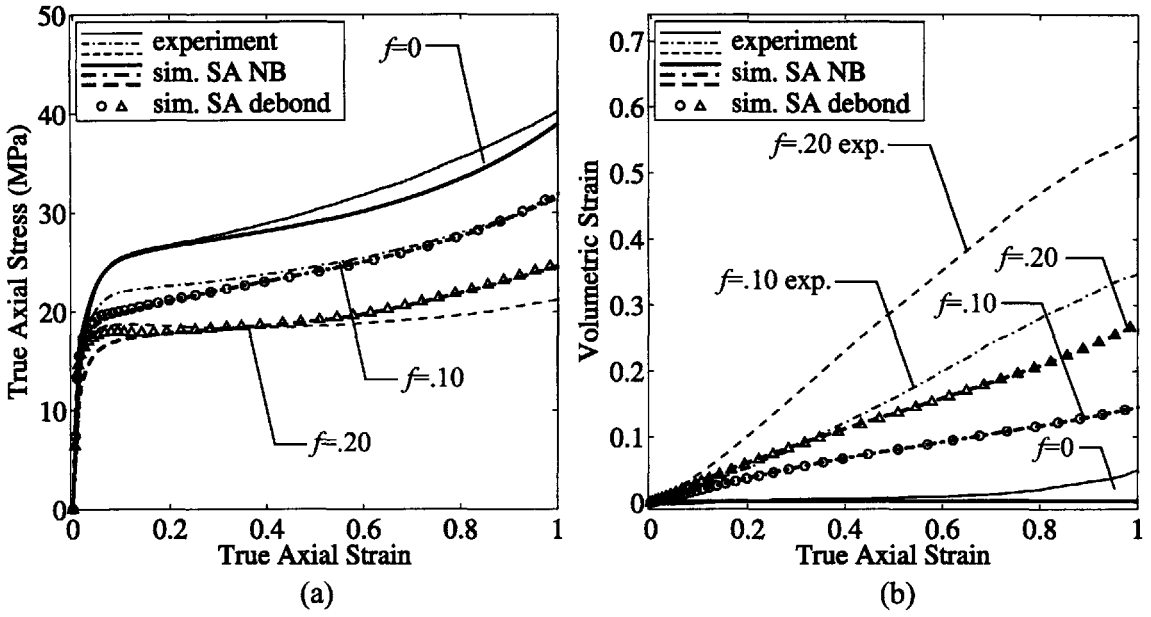

Figure 5-14: Macroscopic predictions of staggered array (SA) RVE's under uniaxial tension with rigid particles with debonding and no bonding (NB) compared with CC1-filled HDPE uniaxial tension experiments: (a) true axial stress versus true axial strain, (b) volumetric strain versus true axial strain.

particle, although clearly partially debonded, still exerts a small amount of reinforcement on the matrix. At $\overline{E}_{zz} = 0.20$ (c), the macroscopic flow stresses and contour plots of the two types of model are nearly equivalent except for the still present, but moving closer to the equator of the particle, stress concentration at the surface of the particle in the debonding model. The stress concentration indicates that the particle has yet to debond fully. While this limited adhesion provides no strength enhancement at $\overline{E}_{zz} = 0.20$, it does delay the impending stress drop by preventing the thinnest section of the ligament from stretching vertically and contracting laterally. At $\overline{E}_{zz} = 0.40$, in Figure 5-16d, complete debonding has just occurred and ligament localization is beginning.

The macroscopic predictions of the SA RVE's with debonding, compared to the SA-NB predictions and CC1-filled HDPE experimental results, are shown in Figure 5-14. The elastic modulus predictions, listed in Table 5.1, are slightly less than the SA-PB predictions but are still within 5% of the experimental values. Debonding begins prior to macroscopic yield at ($\overline{E}_{zz} = 9.05 \times 10^{-3}$, $\overline{T}_{zz} = 13.3$ MPa) for $f = 0.10$

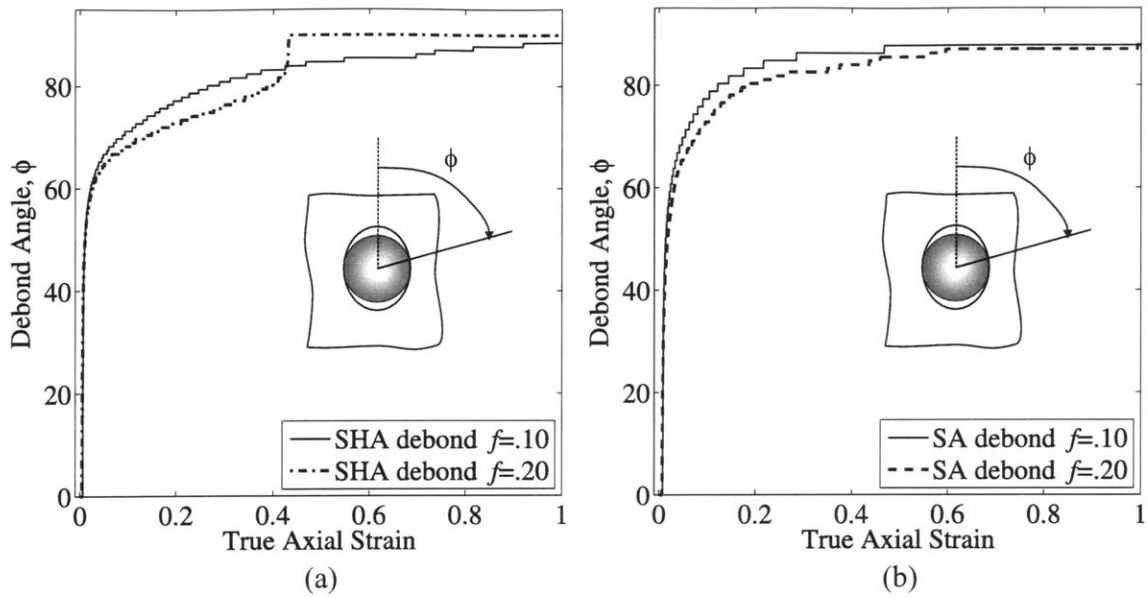

Figure 5-15: Angle of particle debonding, ϕ, as a function of macroscopic axial strain, $\overline{E}_{zz}$: (a) SHA-debond model, (b) SA-debond model.

and at ($\overline{E}_{zz} = 8.35 \times 10^{-3}$, $\overline{T}_{zz} = 13.6$ MPa) for $f = 0.20$. Figure 5-15b shows that debonding occurs almost instantaneously to an angle of $\phi \approx 60°$ and proceeds much more slowly thereafter. The SA-debond model, like the SA-NB model, underpredicts the yield strength at both volume fractions of filler, but, with an increased flow stress during the period of partial debonding, it does improve the agreement between the SA RVE and the experimental data at macroscopic axial strains less than $\overline{E}_{zz} = 0.20$. At larger strains, the macroscopic responses of the SA-debond and SA-NB models are virtually indistinguishable. For $\overline{E}_{zz} > 0.20$, the particle and matrix are still bonded to one another near the equator of the particle, but this configuration provides no enhancement in strength relative to the NB models. The volumetric strains with and without debonding are nearly identical.

Figure 5-16 a′-d′ depicts the equivalent stress contours for the SA-debond model at $f = 0.20$. Comparing the contour plots to those of the SA-NB model in Figure 5-10, a familiar pattern emerges. At small, primarily elastic strains, the distribution of stress resembles that of a perfectly bonded RVE with the peak stresses above the pole of the particle and at the surface of the particle. As debonding and local unloading

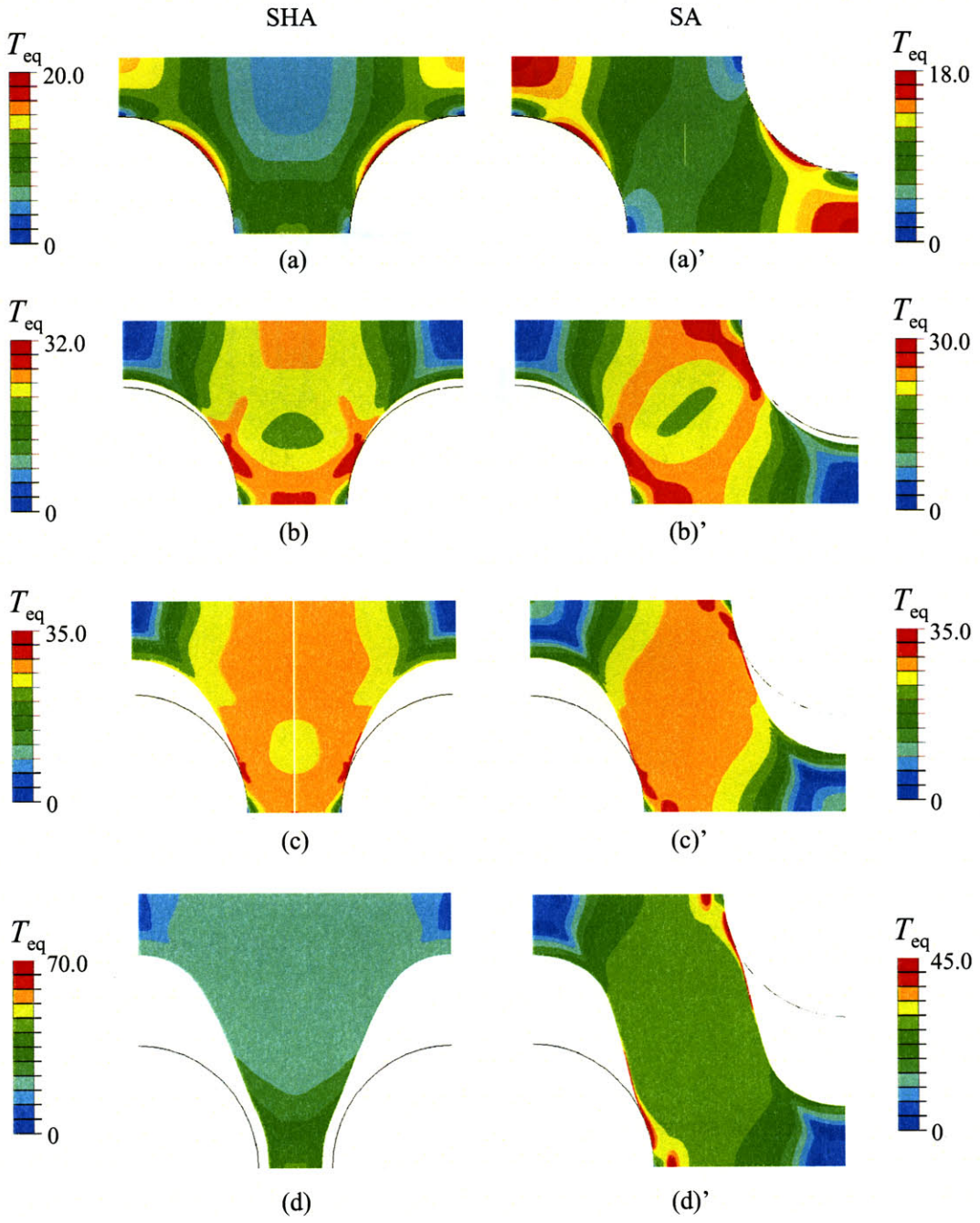

Figure 5-16: $f = 0.20$ SHA (left) and SA (right) RVE's under uniaxial tension with debonding rigid particles. Contour plots of local Mises stress, T_{eq}, for increasing macroscopic axial strain, $\overline{E}_{zz}$: (a), (a′) $\overline{E}_{zz} = 0.005$; (b), (b′) $\overline{E}_{zz} = 0.04$; (c), (c′) $\overline{E}_{zz} = 0.20$; (d), (d′) $\overline{E}_{zz} = 0.40$.

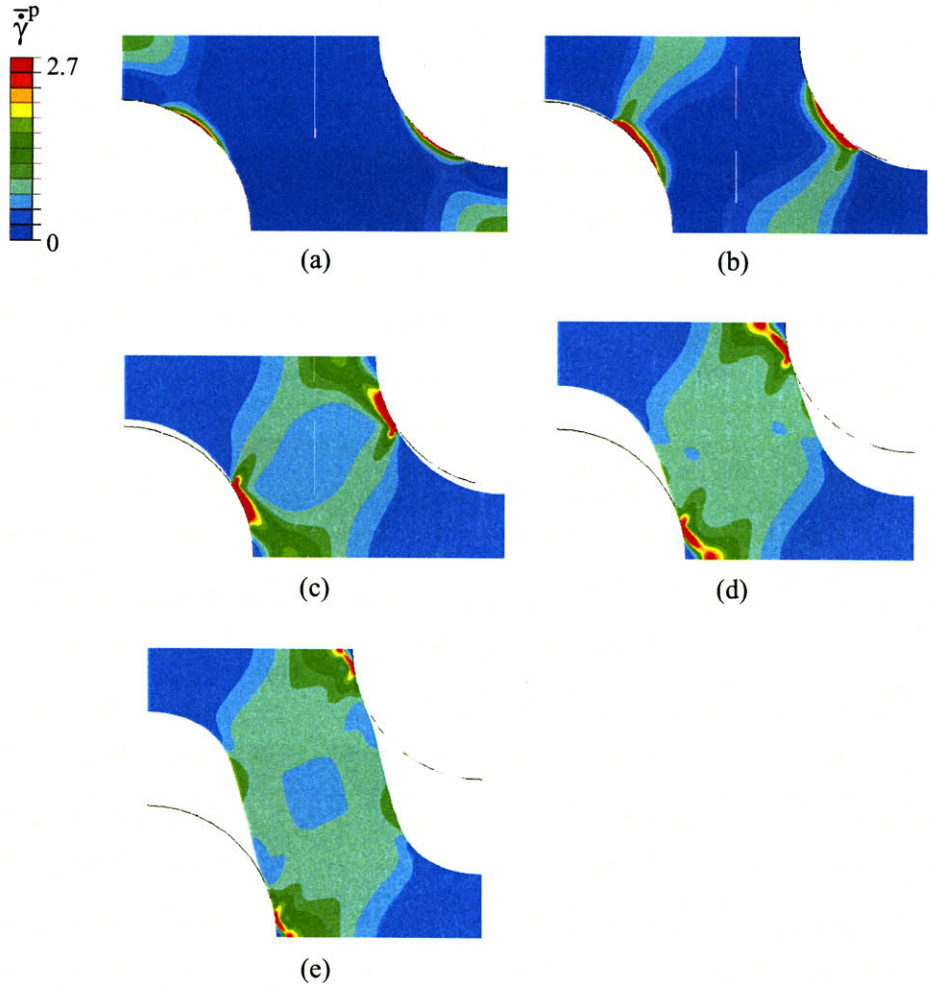

Figure 5-17: $f = 0.20$, SA RVE under uniaxial tension with a debonding rigid particle. Contour plots of normalized equivalent plastic shear strain rate, $\dot{\overline{\gamma}}^{p}$, for increasing macroscopic axial strain, $\overline{E}_{zz}$: (a) $\overline{E}_{zz} = 0.005$, (b) $\overline{E}_{zz} = 0.0125$, (c), $\overline{E}_{zz} = 0.04$, (d) $\overline{E}_{zz} = 0.20$, (e) $\overline{E}_{zz} = 0.40$.

occur, the distribution of stress becomes similar to that of an RVE without bonding. Unlike the SHA-debond RVE, even at $\overline{E}_{zz} = 0.40$ (d), the particle does not debond completely. The adhesion near the equator of the particle has no effect, however, on the macroscopic response of the RVE.

In order to assess further the interplay between debonding and yield and for future comparison, contours of normalized equivalent plastic shear strain rate for the SA-debond model at $f = 0.20$ are plotted in Figure 5-17. At $\overline{E}_{zz} = 0.005$ (a), still in the linear regime of the macroscopic stress-strain response, only local yielding due

to the stress concentration caused by the completely bonded particle is apparent. By $\overline{E}_{zz} = 0.0125$ (b), debonding has begun, causing the macroscopic stress-strain response to deviate from linearity. Plastic flow is still only local, and macroscopic yield has not yet occurred. Debonding progresses, and, by $\overline{E}_{zz} = 0.04$ (c), plasticity has spanned the entire interparticle ligament, enabling macroscopic yield to occur. The stress concentration at the point of debonding spawns two perpendicular shear bands, distinct from the single band between particles observed with the SA-NB model. As the point of debonding moves closer to the equator, these bands coalesce, and, at $\overline{E}_{zz} = 0.20$ and $\overline{E}_{zz} = 0.40$ (d and e), the pattern of viscoplastic shearing closely resembles that of the SA-NB model.

The addition of a debonding criterion to the micromechanical models significantly improves their ability to simulate the deformation of CC1-filled HDPE. Of the two idealized spatial distributions of particles, the staggered array provides the better predictions. The SA RVE predictions with debonding, however, are not without their deficiencies. They underestimate the yield strength, overestimate the rate of strain hardening, and severely underpredict the amount of volumetric strain. The predictions of the SHA RVE provide a better match to the yield strengths and volumetric strains, but at the expense of far too much strain softening at $f = 0.20$. It appears that the actual spatial distribution of particles in CC1-filled HDPE embodies features of both types of RVE.

Toughening implications

Figure 5-18 displays contour plots of hydrostatic stress for the SA RVE with perfectly bonded and debonding rigid particles. Regions of elevated hydrostatic stress initially develop at the pole of the particle in both RVE's. In the RVE with the perfectly bonded particle, the pattern persists throughout the deformation. In the RVE with the debonding particle, debonding begins at $\overline{E}_{zz} \approx 0.01$, and, thereafter, the stress at the pole is essentially non-existent. The maximum hydrostatic stress in the RVE with the debonded particle is roughly one-half of that in the RVE with the perfectly bonded particle. The result is that yield occurs at a lower state of principal stress when debonding takes place. Figure 5-19 illustrates that the maximum

principal stress in the matrix is roughly twice as large if the particle does not debond. The likelihood of brittle fracture increases with increasing stress level in the matrix, and thus, if toughness is a primary concern, debonding is desired to occur at small stresses/strains.

Multi-particle RVE's

In an effort to assess the effects on deformation of the random spatial distributions of particles in actual materials, multi-particle RVE's containing six and ten particles were constructed. As noted in Section 5.1.2, the particle positions were chosen at random under the constraint that particle centers must be at least $2.5r$ apart. As such, the particles are fairly well dispersed. Excepting the debonding simulations, each of the following macroscopic predictions is a typical result chosen from the responses of at least two RVE's deformed in at least two perpendicular directions.

Multi-particle RVE with perfect bonding

While not directly applicable to the deformation of CC1-filled HDPE, which was shown in Section 5.3.1 to debond prior to macroscopic yield, the case of perfectly bonded particles is taken first. The macroscopic true stress-strain predictions of the multi-particle RVE's with perfect bonding are plotted in Figure 5-20 together with the predictions of the lattice-based RVE's. Referring back to Table 5.1, we see that the elastic moduli of the multi-particle RVE's at $f = 0.10$ and $f = 0.20$, 1660 MPa and 2160 MPa, respectively, are slightly superior to those of the SA models (1650 MPa and 2080 MPa) and the experiments (1630 MPa and 2050 MPa) but substantially less than those of the SHA models (1730 MPA and 2430 MPa). As do both the SHA and SA RVE's, at $f = 0.10$, the multi-particle RVE predicts only a small increase in yield strength, on the order of 5%, over that of the unfilled polymer. At $f = 0.20$, however, surpassing even the SHA RVE, the multi-particle RVE predicts a yield strength over 20% greater than that of the unfilled polymer. After the yield point, the macroscopic responses of the multi-particle RVE's lie between the responses of the lattice-based RVE's. At large strains, exceeding $\overline{E}_{zz} = 0.80$ at $f = 0.10$ and exceeding $\overline{E}_{zz} = 0.60$ at $f = 0.20$, the predictions of multi-particle RVE's tend toward the predictions of

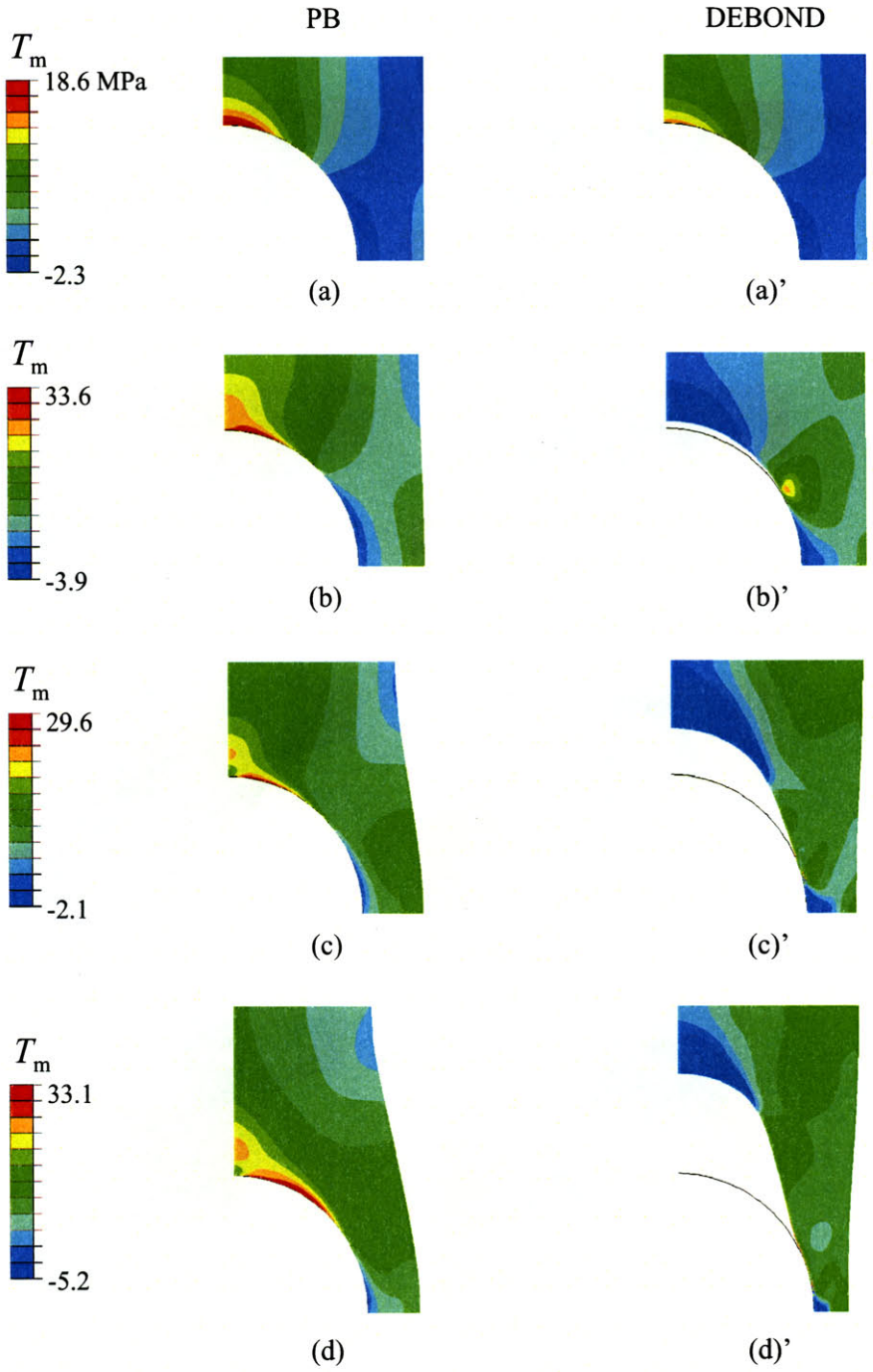

Figure 5-18: $f = 0.20$, SA RVE under uniaxial tension with perfectly bonded (left) and debonding (right) rigid particles. Contour plots of local hydrostatic stress, T_m, for increasing macroscopic axial strain, $\overline{E}_{zz}$: (a), (a′) $\overline{E}_{zz} = 0.005$; (b), (b′) $\overline{E}_{zz} = 0.04$; (c), (c′) $\overline{E}_{zz} = 0.20$; (d), (d′) $\overline{E}_{zz} = 0.40$.

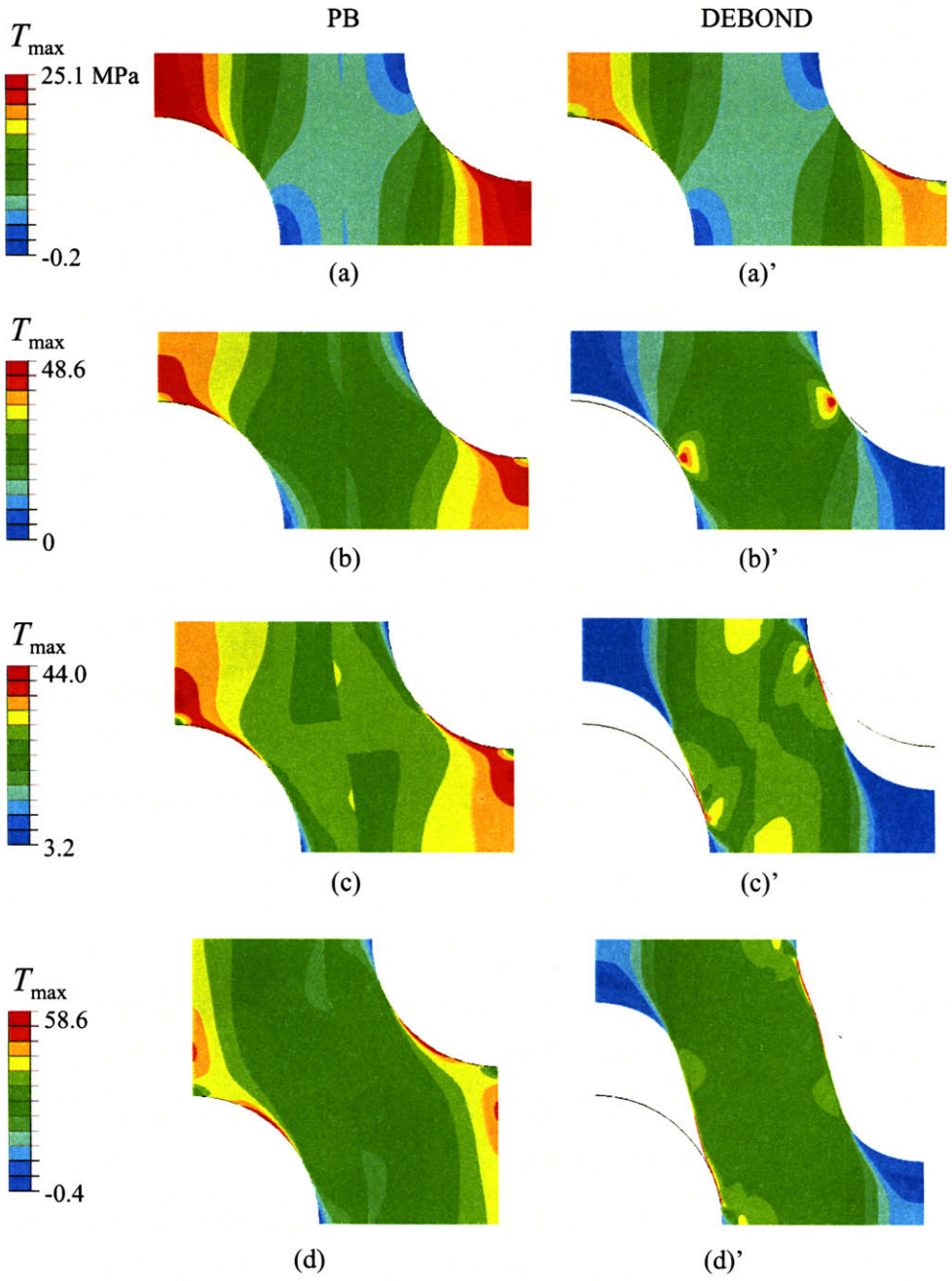

Figure 5-19: $f = 0.20$, SA RVE under uniaxial tension with perfectly bonded (left) and debonding (right) rigid particles. Contour plots of local maximum principal stress, T_{max}, for increasing macroscopic axial strain, $\overline{E}_{zz}$: (a), (a′) $\overline{E}_{zz} = 0.005$; (b), (b′) $\overline{E}_{zz} = 0.04$; (c), (c′) $\overline{E}_{zz} = 0.20$; (d), (d′) $\overline{E}_{zz} = 0.40$.

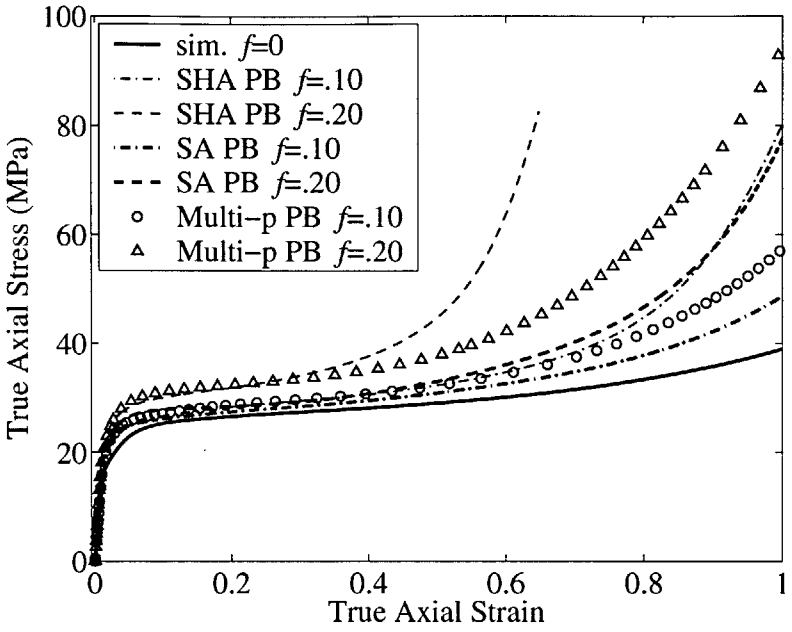

Figure 5-20: Macroscopic predictions of multi-particle SHA and SA RVE's under uniaxial tension with perfectly bonded rigid particles: true axial stress, versus true axial strain.

the SA RVE's.

Contours of normalized equivalent plastic shear strain rate are plotted in Figure 5-22 a-d at a cross-section of a 10-particle RVE with perfectly bonded rigid particles at $f = 0.20$. A pattern of plastic deformation similar to that observed with the SA-PB model is apparent. At $\overline{E}_{zz} = 0.01$ (a), prior to macroscopic yield, plasticity is concentrated at the poles of the particles, and a large portion of the matrix has yet to yield. As the strain increases to $\overline{E}_{zz} = 0.40$ (b-d), viscoplastic shearing percolates throughout the matrix, and macroscopic yield occurs. Except for thin layers of material at the surfaces of the particles, the entire matrix is dissipating energy via plastic deformation.

Multi-particle RVE with no bonding

Figure 5-21 shows the macroscopic predictions of several multi-particle RVE's with no bonding compared with the predictions of the SA-NB models and the experimental data. The elastic moduli (see Table 5.1) of the multi-particle and single-particle models are identical. The yield strengths of the multi-particle RVE's are approximately

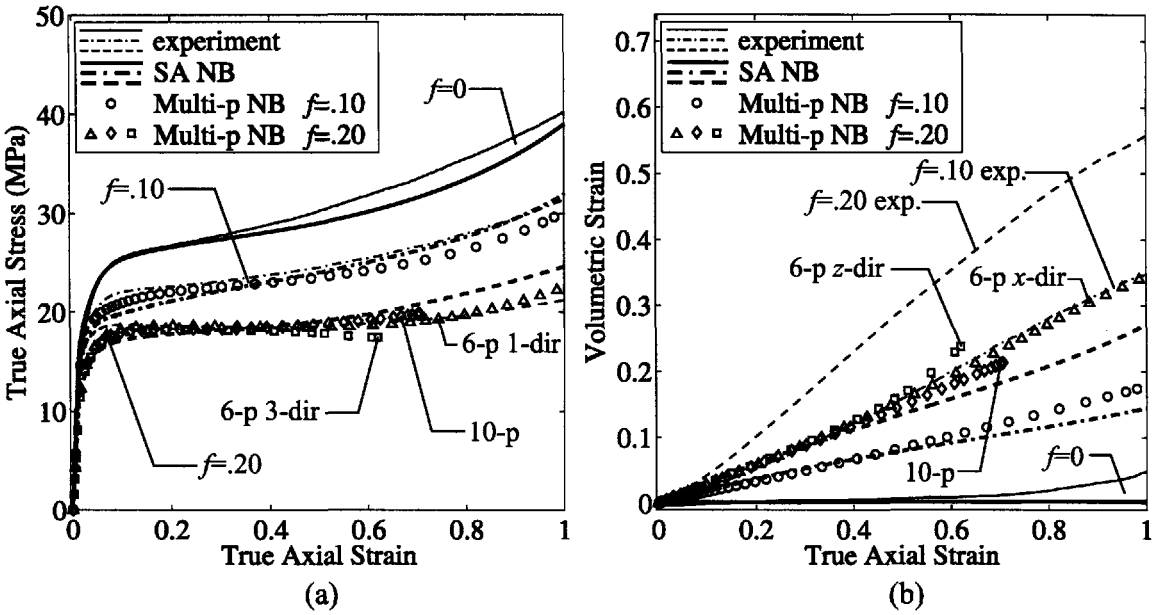

Figure 5-21: Macroscopic predictions of multi-particle and SA RVE's under uniaxial tension with rigid particles with no bonding compared with CC1-filled HDPE uniaxial tension experiments: (a) true axial stress versus true axial strain, (b) volumetric strain versus true axial strain.

5% greater than those of the SA-NB RVE's but are still slightly less than the yield strengths of CC1-filled HDPE. After macroscopic yield, of all the model predictions presented thus far, the macroscopic true stress-strain responses of the multi-particle RVE's provide the best agreement with the experimental data. They do not exhibit a sudden drop in flow stress, nor do they overestimate the rate of strain hardening. Furthermore, the volumetric strain predictions, while still substantially shy of the volumetric strains measured in CC1-filled HDPE, are approximately 25% larger than those of the SA-NB models.

Figure 5-22 a′-d′ displays contours of normalized equivalent plastic shear strain rate at a cross-section of the 10-particle (10-p) RVE with $f = 0.20$ referred to in Figure 5-21. As with the SA-NB model, at small strains prior to macroscopic yield, $\overline{E}_{zz} = 0.01$ and $\overline{E}_{zz} = 0.02$ (a′, b′), the viscoplastic shearing is confined to the regions near the equators of the particles. By $\overline{E}_{zz} = 0.10$ (c′), plasticity has spanned the interparticle ligaments, enabling macroscopic yield to occur. The regions at the poles of the particles remain free of plasticity as they translate rigidly in a hinge-like

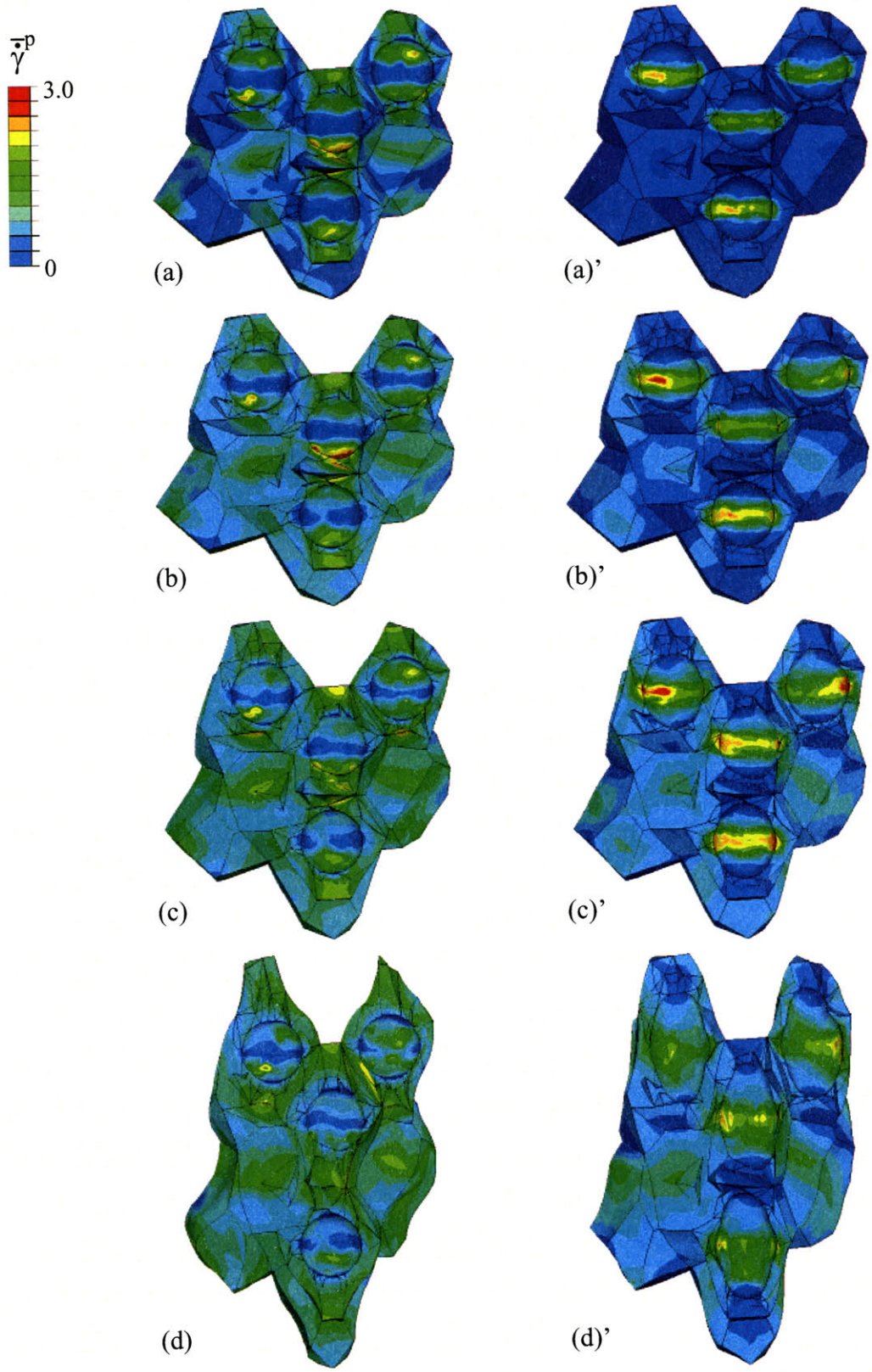

Figure 5-22: $f = 0.20$, 10-particle RVE under uniaxial tension with rigid particles with perfect bonding (left) and no bonding (right). Contour plots of normalized equivalent plastic shear strain rate, $\overline{\dot{\gamma}^p}$, for increasing macroscopic axial strain, $\overline{E}_{zz}$: (a), (a′) $\overline{E}_{zz} = 0.01$; (b), (b′) $\overline{E}_{zz} = 0.02$; (c), (c′) $\overline{E}_{zz} = 0.10$; (d), (d′) $\overline{E}_{zz} = 0.40$.

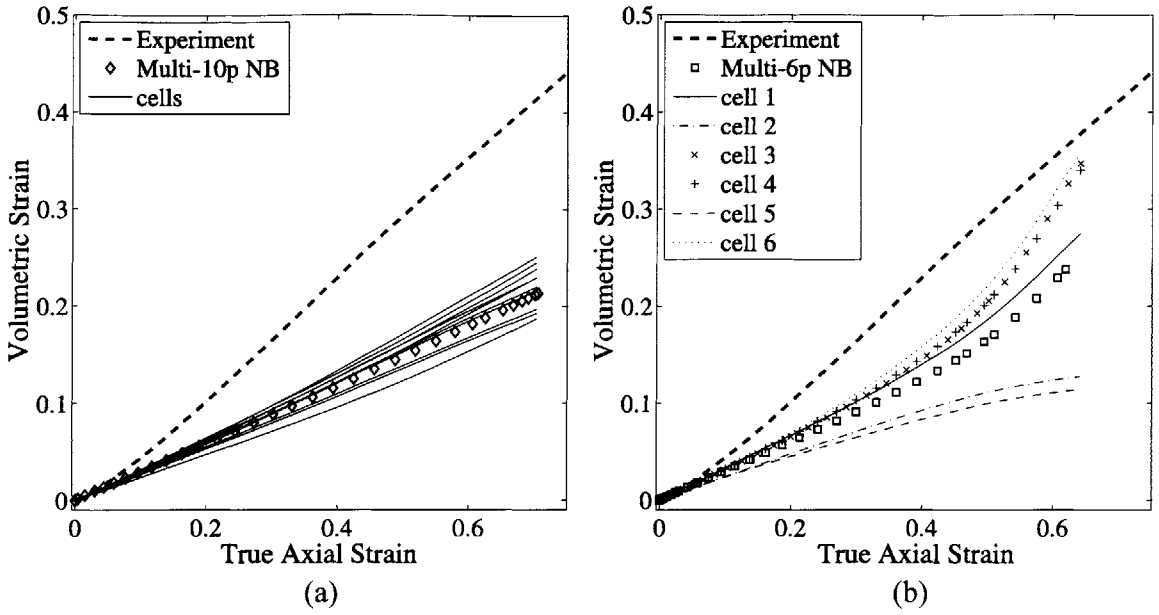

Figure 5-23: Macroscopic and cell-level volumetric strain predictions of multi-particle RVE's under uniaxial tension compared with CC1-filled HDPE uniaxial tension experiments at $f = 0.20$: (a) 10-particle RVE with rigid particles with no bonding (10-p), (b) 6-particle RVE with rigid particles with no bonding deformed in z-direction (6-p z-dir).

manner. At $\overline{E}_{zz} = 0.40$ (d′), excessive void growth has occurred. The irregular void shapes are remniscient of the SA-NB model. Lastly, it is noted that the particles are reasonably well dispersed in this RVE. As a result, the contours of viscoplastic shearing around and the evolving void shapes in each cell of the RVE are very similar. Not coincidentally, as will be shown, this RVE exhibits the highest flow stress and lowest volumetric strain of the RVE's with $f = 0.20$ plotted in Figure 5-21.

In Figure 5-23, the volumetric strain predictions of two of the multi-particle RVE's with rigid particles without bonding at $f = 0.20$ are analyzed further. In Figure 5-23a, the macroscopic volumetric strain of the 10-particle RVE is plotted together with the volumetric strain due to void growth in each individual cell. As the void shapes in Figure 5-22 a′-d′ indicate, the voids all grow at a similar rate. The volumetric strain in each individual cell is within 15% of the total volumetric strain. In Figure 5-23b, the analogous plot for the 6-particle RVE deformed in the z-direction (6-p z-dir), however, there is a huge discrepancy between the volumetric strains of the slowest

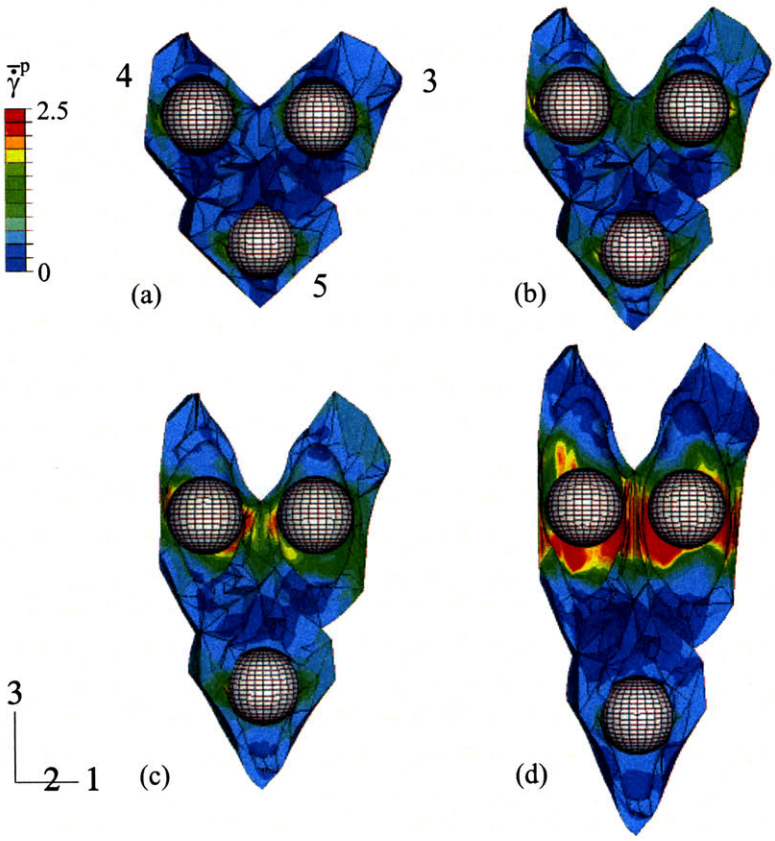

Figure 5-24: $f = 0.20$, 6-particle RVE under uniaxial tension with rigid particles with no bonding. Contour plots of normalized equivalent plastic shear strain rate, $\overline{\dot{\gamma}^p}$, for increasing macroscopic axial strain, $\overline{E}_{zz}$: (a) $\overline{E}_{zz} = 0.10$, (b) $\overline{E}_{zz} = 0.20$, (c) $\overline{E}_{zz} = 0.40$, (d) $\overline{E}_{zz} = 0.60$. Cell numbers are indicated in (a).

and fastest growing cells.

Contour plots of viscoplastic shearing at a cross-section that cuts through cells 3 and 4, two of the cells expanding more rapidly than the average, and cell 5, the slowest growing cell, are given in Figure 5-24. The particles in cells 3 and 4 are located on nearly the same axial plane, much like the SHA particle distribution, and these cells behave similarly to the SHA-NB model: at $\overline{E}_{zz} = 0.10$ (a), yielding has begun only at the equators of the particles; at $\overline{E}_{zz} = 0.20$ (b), the deformation is occuring uniformly in the vertical interparticle ligaments shared by cells 3 and 4 and their periodic neighbors; at $\overline{E}_{zz} = 0.40$ (c), the plasticity in the center ligament has intensified, the center ligament has thinned substantially, and the voids have taken an elliptical shape; at $\overline{E}_{zz} = 0.60$ (d), nearly all of the active shearing visible in the

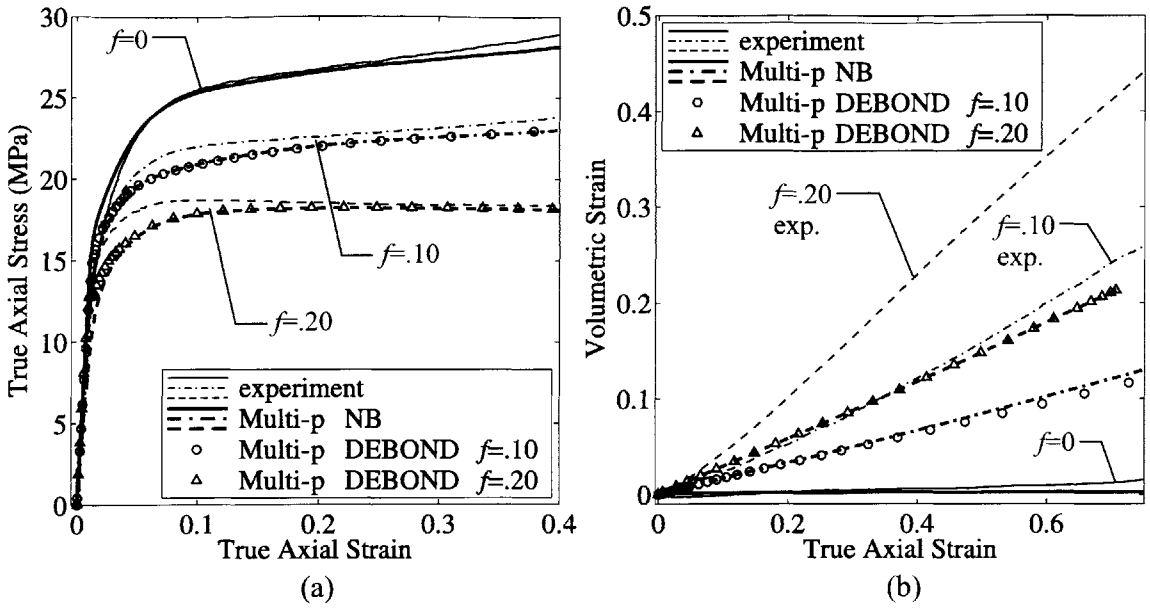

Figure 5-25: Macroscopic predictions of multi-particle RVE's under uniaxial tension with rigid particles with debonding and no bonding (NB) compared with CC1-filled HDPE uniaxial tension experiments: (a) true axial stress versus true axial strain, (b) volumetric strain versus true axial strain.

RVE has concentrated in the ligaments of cells 3 and 4 and the voids expand radially. Meanwhile, the rate of shearing in cell 5 is approximately constant for $\overline{E}_{zz} = 0.10$ through $\overline{E}_{zz} = 0.40$ and actually decreases at $\overline{E}_{zz} = 0.60$ when the deformation has localized in the upper ligaments.

The localization of deformation in cells 3 and 4 is manifested in the macroscopic response by a decline in the true stress and an increase in the slope of the volumetric strain at $\overline{E}_{zz} \approx 0.40$. Cells 3 and 4 effectively form a weak porous layer favorable to plastic flow.

Multi-particle RVE with debonding

The results of including the debonding interface response in the multi-particle simulations are presented in Figure 5-25. The normal and tangential works of separation in the interface constitutive response were the same as in the single-particle debonding simulations, $\phi_n = \phi_t = 85.0r$ kN/m^2. In order for the analysis to converge with the lower mesh density of the multi-particle meshes, the interface normal strength and separation length were set at $\sigma_{max} = 4.17$ MPa and $\delta_n = 0.0075r$ respec-

tively. These properties produce an interface response slightly more "ductile" than that specified in the single-particle simulations. Debonding initiates at each particle at nearly the same macroscopic axial strain. For $f = 0.10$, debonding begins, at the first particle to debond, at ($\overline{E}_{zz} = 1.26 \times 10^{-2}$, $\overline{T}_{zz} = 14.8$ MPa) and, at the last particle to debond, at ($\overline{E}_{zz} = 1.36 \times 10^{-2}$, $\overline{T}_{zz} = 15.2$ MPa). For $f = 0.20$, debonding begins, at the first particle to debond, at ($\overline{E}_{zz} = 1.01 \times 10^{-2}$, $\overline{T}_{zz} = 12.7$ MPa) and, at the last particle to debond, at ($\overline{E}_{zz} = 1.16 \times 10^{-2}$, $\overline{T}_{zz} = 12.8$ MPa). Scrutiny of the deforming finite element meshes reveals that, in contrast to the single-particle models where partial debonding persists to large macroscopic axial strains, the particles in the multi-particle models debond completely by $\overline{E}_{zz} \approx 0.05$. The abruptness and comprehensiveness of debonding is manifested macroscopically by the true stress-strain predictions of the models with debonding merging with the predictions of the models with no bonding at or prior to macroscopic yield.

Figure 5-26 shows contours of equivalent plastic shear strain rate for a 10-particle RVE at $f = 0.20$ with debonding rigid particles. Before debonding, at $\overline{E}_{zz} = 0.01$ (a), similar to the contour plot of the model with perfect bonding in Figure 5-22a, plasticity is concentrated in the highly stressed matrix around the poles of the particles with the shielded regions of matrix at the equators of the particles relatively inactive in the shearing process. At $\overline{E}_{zz} = 0.02$ (b), debonding has begun at each particle as evidenced by the sharp band of plasticity in the matrix surrounding each particle due to the stress concentration at the point of debonding. By $\overline{E}_{zz} = 0.10$ (c), the bands have disappeared. As in the contour plot of the model with no bonding in Figure 5-22c′, plastic flow has percolated throughout the matrix, and the regions most actively shearing are those near the equators of the particles. The volumetric strain predictions with debonding are virtually the same as the predictions with no bonding. As such, in summary, other than improving the prediction of the elastic modulus, the multi-particle RVE's with debonding do not provide a significantly better representation of the true stress-true strain response of CC1-filled HDPE than the multi-particle RVE's with no bonding.

While the multi-particle RVE's with debonding rigid particles predict the onset

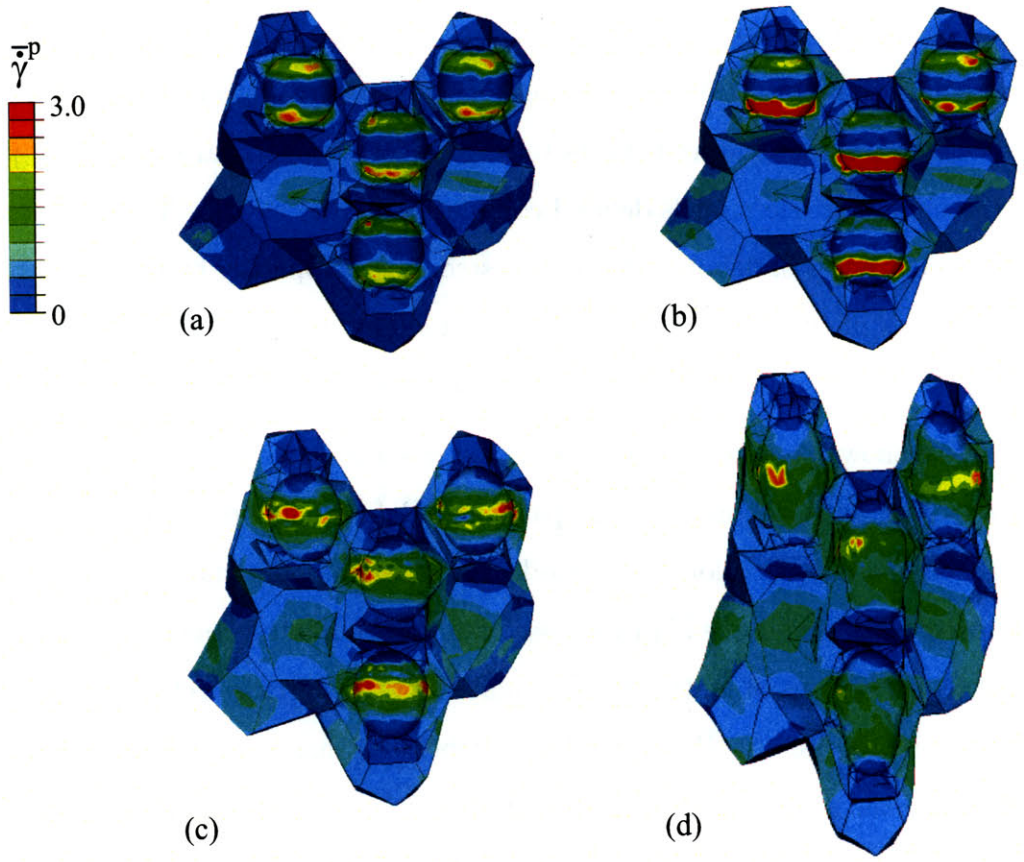

Figure 5-26: $f = 0.20$, 10-particle RVE under uniaxial tension with debonding rigid particles. Contour plots of normalized equivalent plastic shear strain rate, $\dot{\overline{\gamma}}^p$, for increasing macroscopic axial strain, $\overline{E}_{zz}$: (a) $\overline{E}_{zz} = 0.01$, (b) $\overline{E}_{zz} = 0.02$, (c) $\overline{E}_{zz} = 0.10$; (d) $\overline{E}_{zz} = 0.40$.

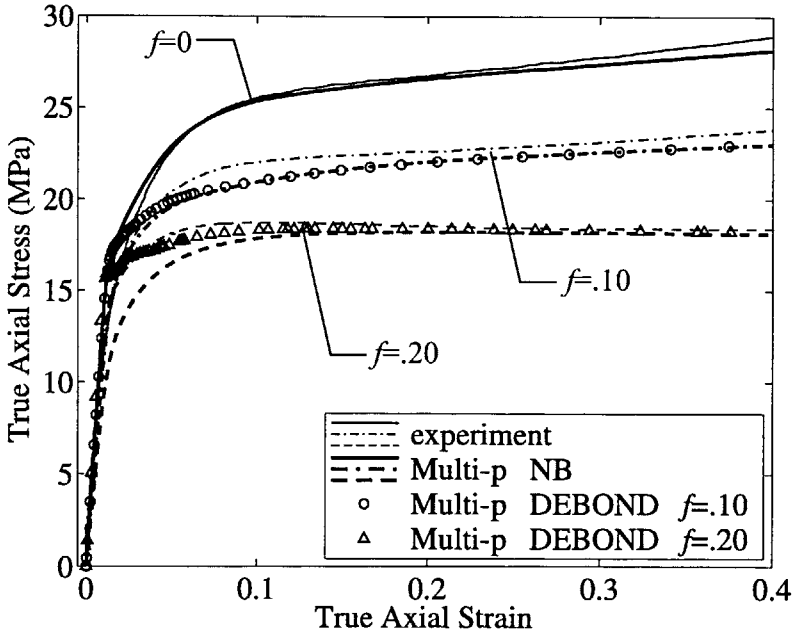

Figure 5-27: Macroscopic predictions of multi-particle RVE's under uniaxial tension with rigid particles with distributed debonding and no bonding (NB) compared with CC1-filled HDPE uniaxial tension experiments: (a) true axial stress versus true axial strain, (b) volumetric strain versus true axial strain.

of debonding in CC1-filled HDPE reasonably well, they are not able to match the experimental true stress-strain data at strains post debonding but less than $\overline{E}_{zz} = 0.20$. The reason for this discrepancy is that the particles all debond simultaneously and completely at small macroscopic axial strains. It was conjectured that, in an actual material, particles debond over a larger range of macroscopic strains. Interface strengths may vary due to small differences in particle size and/or shape, or the degree of wetting during processing. Thus, a "distributed debonding" model was constructed with a range of interface properties. The average normal and tangential works of separation in the interface constitutive response were doubled to $\phi_n = \phi_t = 170.0r$ kN/m^2. The individual particle strengths were evenly distributed between the original work of separation, $\phi_n = \phi_t = 85.0r$ kN/m^2, and $\phi_n = \phi_t = 255.0r$ kN/m^2. The macroscopic true stress-strain predictions, presented in Figure 5-27, show significantly better agreement, particularly at $f = 0.20$, with the experimental data. Locally, at $f = 0.10$, the particles now begin to debond at strains ranging from $\overline{E}_{zz} = 0.0130$ to $\overline{E}_{zz} = 0.0257$ and stresses ranging from $\overline{T}_{zz} = 16.3$ MPa to $\overline{T}_{zz} = 18.4$ MPa. At $f = 0.20$, the strain range and stress range are, respectively, $\overline{E}_{zz} = 0.0112 - 0.0256$ and $\overline{T}_{zz} = 15.7 - 16.8$ MPa. At each particle, once debonding initiates, the amount of additional macroscopic deformation required to complete the debonding process is proportional to the strength of the interface.

5.3.2 Rubber particles

While they will not all be presented here, a series of simulations similar to those conducted for rigid particle-modified HDPE were also performed for the case of rubber particle-modified HDPE. Their macroscopic predictions are summarized in Table 5.2. As for the simulations with rigid particles, the multi-particle RVE's exhibit yield strengths superior to those of the SA RVE's, but there is no appreciable difference between the models' predictions of the elastic modulus. The modulus predictions are substantially larger than the moduli measured in EPDM-filled HDPE, but show good agreement with the predictions of the Mori-Tanaka model.

Figure 5-28 displays the macroscopic responses of the multi-particle RVE's with

	f	Young's modulus, E (MPa)	Yield strength (MPa)	$E_{\text{blend}}/E_{\text{neat}}$ (Mori-Tanaka)
exp./sim.	0	1320	25.1	1.00
exp. EPDM	0.10	890	21.1	0.67 (0.84)
exp. EPDM	0.20	700	17.9	0.53 (0.70)
SA void	0.10	1080	19.4	0.82
SA void	0.20	880	16.1	0.66
SA rubber	0.10	1100	20.1	0.84
SA rubber	0.20	910	16.6	0.69
Multi-p void	0.10	1100	20.9	0.83
Multi-p void	0.20	900	17.5	0.68
Multi-p rubber	0.10	1120	21.3	0.85
Multi-p rubber	0.20	930	18.3	0.71

Table 5.2: Summary of experimental results and micromechanical modeling predictions for EPDM-filled HDPE.

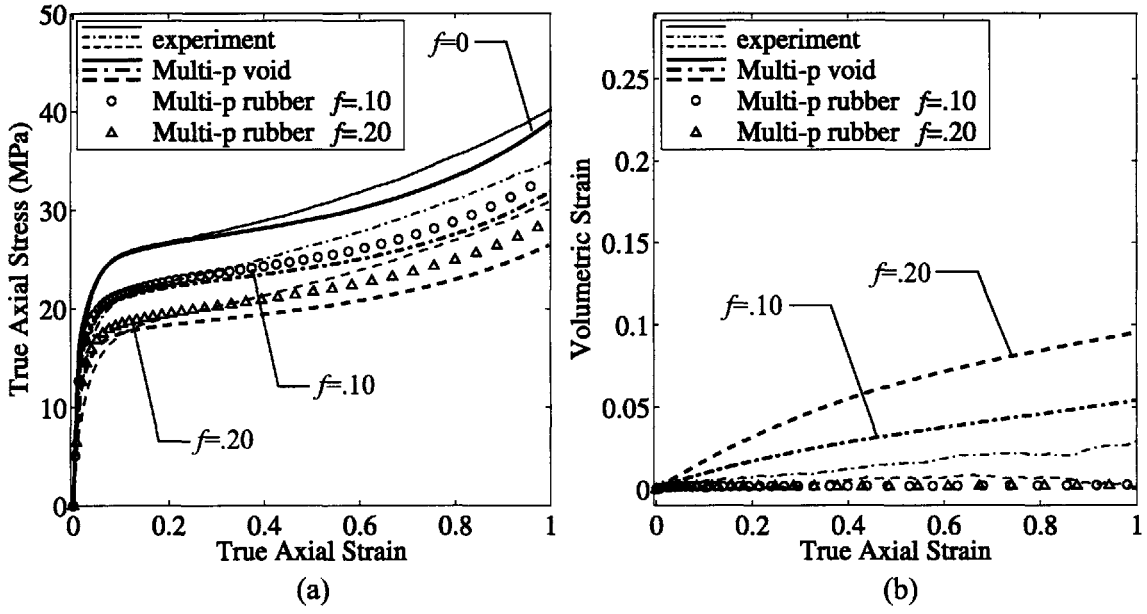

Figure 5-28: Macroscopic predictions of multi-particle RVE's under uniaxial tension with voids and rubber particles compared with EPDM-filled HDPE uniaxial tension experiments: (a) true axial stress versus true axial strain, (b) volumetric strain versus true axial strain.

voids and non-cavitating rubber particles plotted with the EPDM-filled HDPE data. The true stress-strain and volumetric strain predictions of the models with rubber particles are significantly better than the predictions with voids. Clearly, the EPDM particles do not cavitate. The effect of the rubber particles is to increase slightly, relative to voids, the flow stress as well as to prevent all volumetric strain due to void growth. The increase in flow stress at large strains is due solely to the absence of volumetric strain, but the rubber particles do provide a small amount of reinforcement at small strains which is apparent in the yield strengths. The effect, although difficult to quantify, appears to be due to a slightly less intense stress concentration and a higher mean stress at the equators of rubber particles than at the equators of voids.

Contour plots of equivalent plastic shear strain rate for a 10-particle RVE with rubber particles at $f = 0.20$ are given in Figure 5-29 alongside those for a 10-particle RVE with rigid particles at $f = 0.20$. The onset and spread of plastic deformation is similar in the two models. The concentration of plasticity is, however, much more severe at the equators of the rigid particles than it is at the equators of the rubber particles. The local compressive lateral stresses induced by the rigid particles reduce the levels of mean stress in these regions and, thus, increase the effective stress and the plastic strain rate there. The contrast in the constraint provided by the two types of particle is most apparent in the shapes of the voids in Figure 5-29 d,d′. Corresponding contour plots for RVE's with (initial) voids rather than rubber particles are essentially identical to Figure 5-29 a′-d′ but with slightly less oblong void shapes.

5.4 Conclusions

In this chapter, it has been verified, by drawing direct comparison with experimental uniaxial tension data, that micromechanical models can represent with reasonable accuracy the deformation of particle-modified polymers. In the process, a number of valuable discoveries were made.

Debonding aside, it was shown that a three-dimensional, random distribution of particles, whether rigid (PB or NB), rubber, or voids, produces a material with a

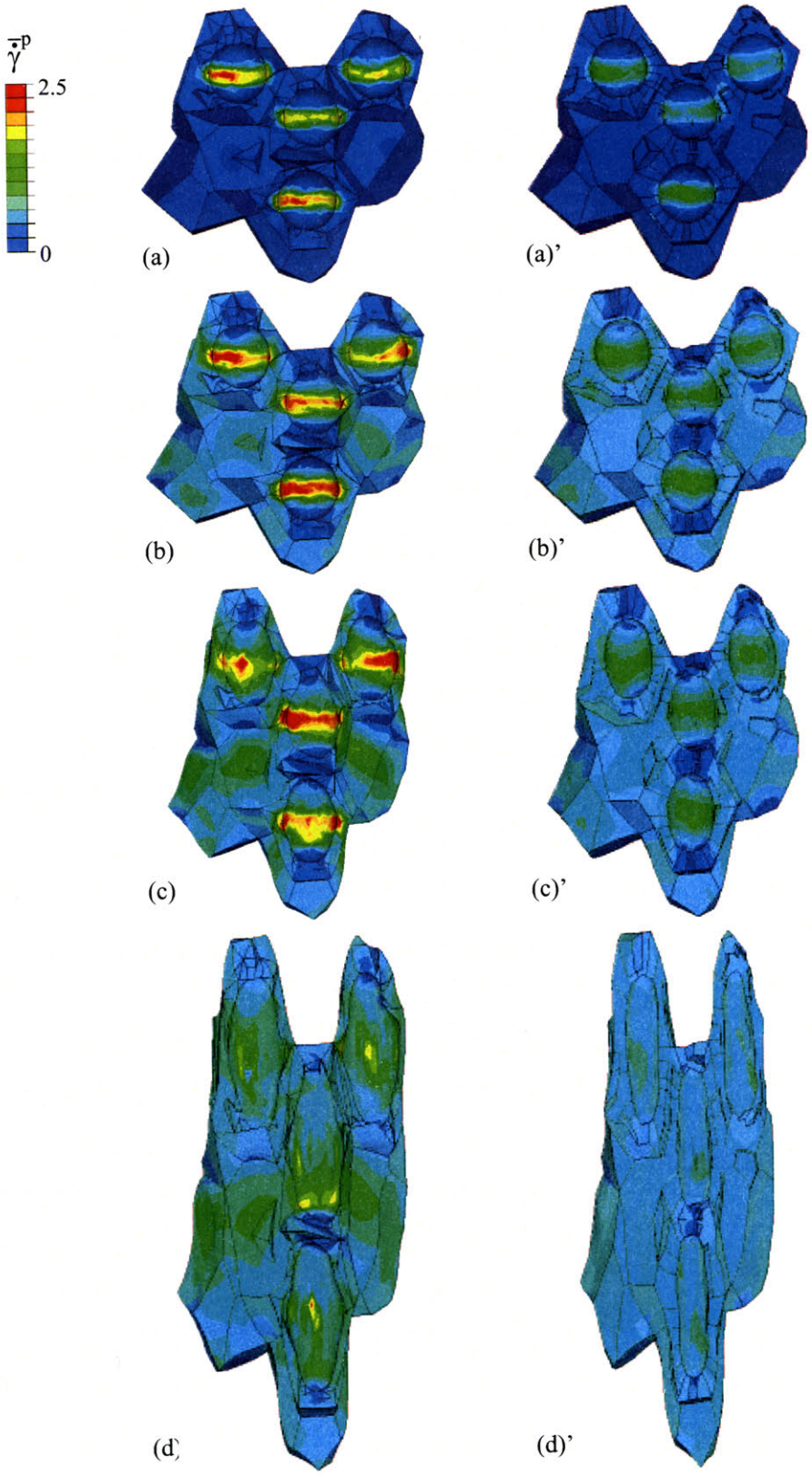

Figure 5-29: $f = 0.20$, 10-particle RVE under uniaxial tension with rigid particles with no bonding (left) and rubber particles (right). Contour plots of normalized equivalent plastic shear strain rate, $\dot{\overline{\gamma}}^p$, for increasing macroscopic axial strain, $\overline{E}_{zz}$: (a), (a′) $\overline{E}_{zz} = 0.01$; (b), (b′) $\overline{E}_{zz} = 0.05$; (c), (c′) $\overline{E}_{zz} = 0.20$; (d), (d′) $\overline{E}_{zz} = 0.70$.

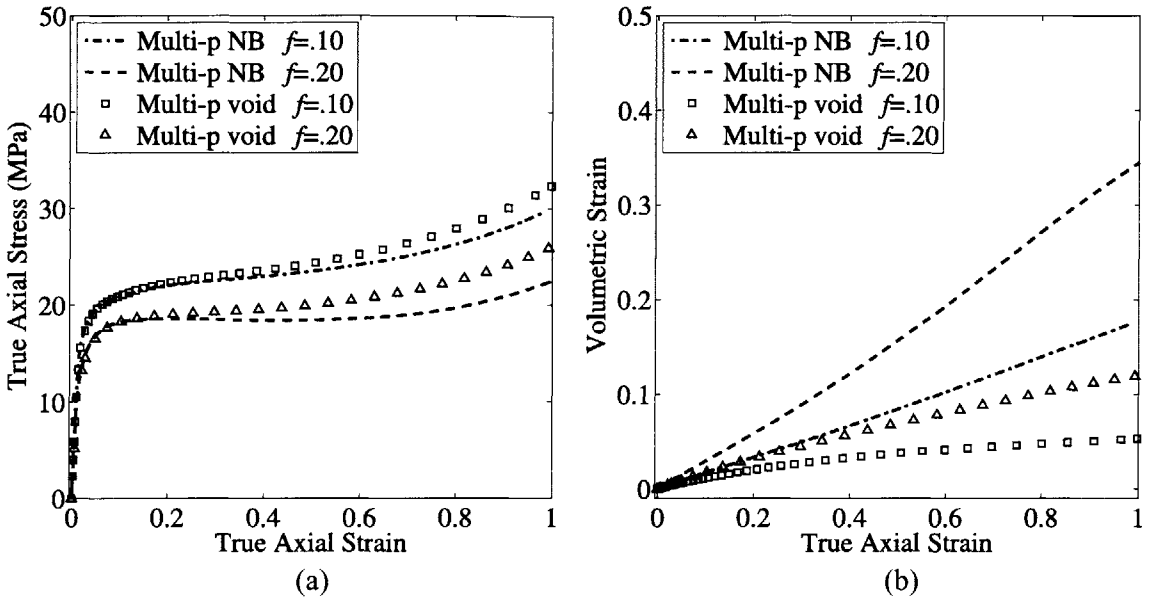

Figure 5-30: Macroscopic predictions of multi-particle RVE's under uniaxial tension with voids and rigid particles with no bonding (NB): (a) true axial stress versus true axial strain, (b) volumetric strain versus true axial strain.

yield strength superior to that of a material with the particles perfectly dispersed on a staggered array lattice (the best axisymmetric representation of perfect dispersion). The lower strength of the lattice-based distribution is due to the assumed instantaneous, complete percolation of plastic flow throughout the entire matrix, whereas, in the multi-particle RVE's, regions of the matrix are constrained, effectively increasing the volume fraction of particles, and do not yield until larger macroscopic strains. Without perfect bonding, any deviation from perfect dispersion, however, increases the interactions between certain particles, eventually leading to ligament localization, and, as a result, the multi-particle RVE's exhibit less strain hardening and more volumetric strain than the SA RVE's. It was shown also that, locally, cells in a multi-particle RVE may deform in a manner similar to that of an SHA RVE. On the other hand, dispersion does not significantly affect elastic modulus except in the extreme case of an RVE with perfectly bonded rigid particles positioned on an SHA lattice.

Comparing Tables 5.1 and 5.2, it is apparent that rigid particles without bonding do not provide significant reinforcement. The models with rigid particles with no

bonding exhibit moduli and yield strengths just slightly greater than those of the models with voids. Figure 5-30 shows a comparison between the macroscopic predictions of multi-particle RVE's with rigid particles without bonding and multi-particle RVE's with voids loaded at constant, identical macroscopic axial strain rates. The predictions are very similar until strain hardening begins. The strain hardening slope is more gradual with rigid particles than it is with rubber particles. The discrepancy is due solely to the lateral constraint of the particles preventing the matrix from shrinking transversely. (The engineering stress-strain curves of the two materials are nearly identical.)

None of the models is successful in predicting exactly both the true stress-strain and volumetric strain response of CC1-filled HDPE. The sizeable volumetric strains predicted by the SHA-NB model at $f = 0.20$ and the deformation of the multi-particle RVE in Figure 5-24 suggest that particle clustering may be the source of the large volumetric strains measured experimentally. The corresponding decrease in flow stress predicted in the aforementioned simulations, however, does not occur in the experiments. It is likely that the constitutive response of neat HDPE in Figure 5-4 underestimates the strain hardening modulus of the matrix at large strains. When the deformation concentrates at a cluster of particles, the axial strains in the interparticle ligaments become several times greater than the macroscopic axial strain. Not only is it difficult to measure experimentally the strain hardening slope of neat HDPE at strains greater than 150%, but it has been shown by Bartczak et al. [8] that the matrix morphology changes when HDPE crystallizes in the presence of particles. Highly oriented crystalline layers form at the surfaces of the particles, and, locally, the matrix is no longer isotropic.

In the following chapter, similar models are used to study the deformation of rigid particle-modified polymers under multiaxial states of stress as well as the effects of particle clustering.

Chapter 6

Micromechanics of Rigid Particle-Modified Polymers: Triaxiality, Clustering, and Localization

In the previous chapter, various aspects of the micromechanics and macromechanics of deformation in particle-modified polymers subject to macroscopic uniaxial tension were investigated. By drawing comparisons with the experimental data, the micromechanical models were validated. In this chapter, the analysis is extended to more complex states of stress such as those found at the root of a notch or crack. In order to focus unambiguously on the effects of the volume fraction of rigid particles and the type of loading, the simplified, parallel constitutive model presented in Section 4.3.2 is used to represent the polymer matrix. The version with neo-Hookean strain hardening is used predominantly, but the effects of a matrix with a locking stretch are examined as well.

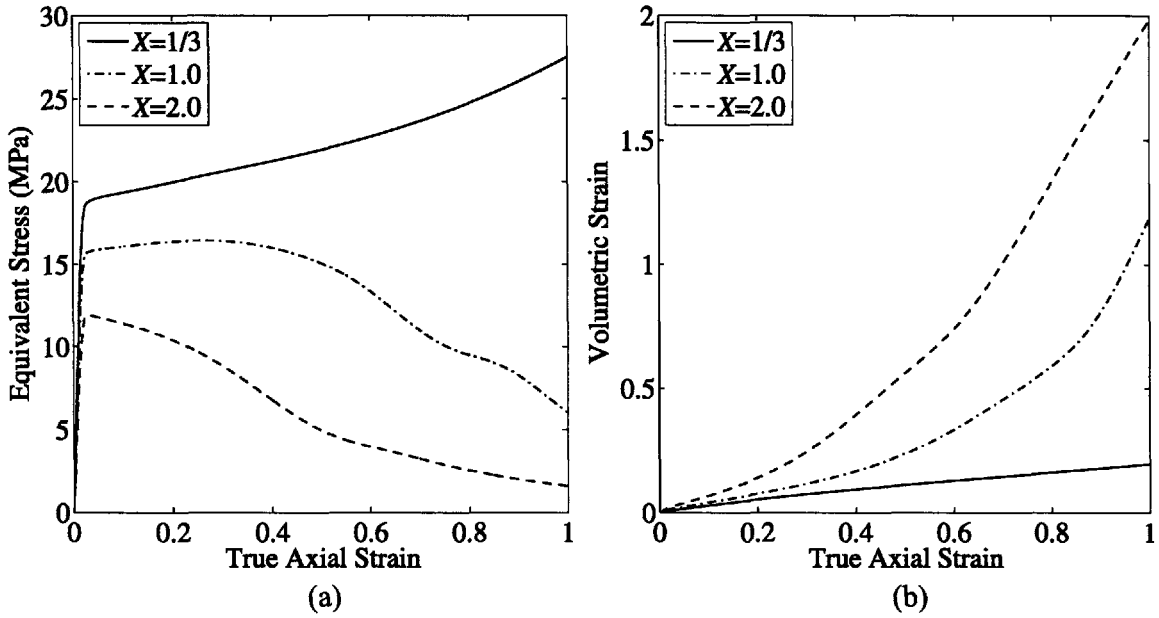

Figure 6-1: Macroscopic predictions of $f = 0.15$, staggered array (SA) RVE with rigid particles with no bonding (NB) as a function of stress triaxiality, X: (a) equivalent stress versus true axial strain, (b) volumetric strain versus true axial strain.

6.1 Effect of Stress Triaxiality

RVE's identical or similar to those presented in Chapter 5 were subjected to macroscopic states of stress with constant triaxiality ratio, $X = \frac{\overline{T}_m}{\overline{T}_{eq}}$, as described in Section 5.1. Triaxialities of 1/3 (low, equivalent to uniaxial tension), 1.0 (intermediate, representative of a mild notch), and 2.0 (high, representative of a crack tip environment) were applied in principal stress state such that there are two equal minor stresses. (Other types of loading, such as plane strain tension and biaxial tension, will be examined in Chapters 7 and 8.)

6.1.1 Single-particle RVE's

No bonding

The macroscopic responses of $f = 0.15$, axisymmetric RVE's with rigid particles with no bonding (NB), as a function of stress triaxiality ratio, are presented in Figures 6-1 and 6-2. Both types of RVE exhibit the inverse relationship between effective yield

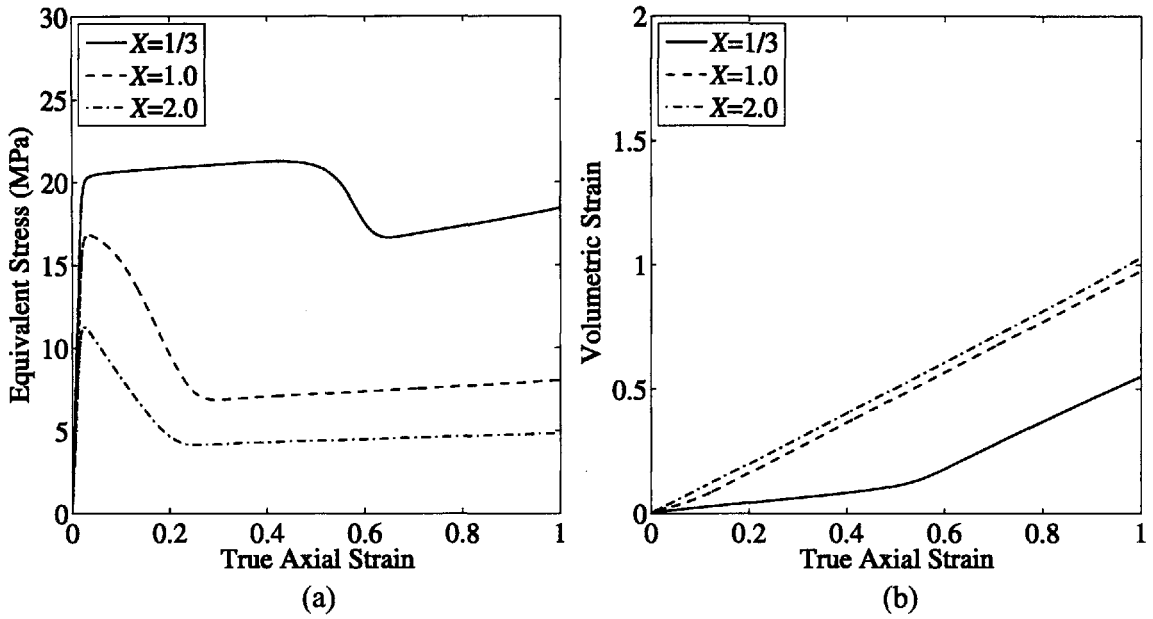

Figure 6-2: Macroscopic predictions of $f = 0.15$, stacked hexagonal array (SHA) RVE with rigid particles with no bonding as a function of stress triaxiality, X: (a) equivalent stress versus true axial strain, (b) volumetric strain versus true axial strain.

strength and stress triaxiality well known to exist in porous polymers. In addition to the reduction in strength, an increase in volumetric strain with increasing triaxiality ratio is apparent. While the trends in macroscopic response are similar with the SA and SHA RVE's, the RVE deformations and the responses themselves, as described in Chapter 5 for $X = 1/3$, are very different. Contour plots of normalized equivalent plastic shear strain rate, $\overline{\dot{\gamma}^{\mathrm{p}}}$, are provided in Figures 6-3 and 6-4 to aid in the comparison.

With the SA RVE, at $X = 1.0$, between macroscopic yield at $\overline{E}_{zz} \approx 0.03$ (Figure 6-3a) and $\overline{E}_{zz} \approx 0.4$ (c), the macroscopic stress-strain prediction is nearly constant, and the volumetric strain prediction increases monotonically. Similar to the results for $X = 1/3$ in Figure 5-11, the contour plots show plasticity initiating at the equator of the particle followed by a reasonably diffuse pattern of shearing throughout the entire vertical interparticle ligament. Thinning at an increasing, but uniform, rate, the ligament has separated from the equator of the particle at $\overline{E}_{zz} = 0.40$. At strains larger than $\overline{E}_{zz} \approx 0.40$, however, dramatic strain softening occurs, and the

volumetric strain increases in slope. The contour plot at $\overline{E}_{zz} = 0.60$ (d) shows that the viscoplastic shearing has concentrated in a small section at the center of the ligament. The ligament is necking in a manner analogous to the tensile specimens in Chapters 2 and 3, and the instability is reflected in the RVE's macroscopic response. Increasing the triaxiality to $X = 2.0$ causes the SA RVE to strain soften immediately after macroscopic yield. The pattern of plastic deformation at $\overline{E}_{zz} = 0.20$ in Figure 6-4a is very similar to that for $X = 1.0$, but, due to the larger macroscopic radial stress imposed, the interparticle ligament has already separated considerably from the equator of the particle. Localization at the center section of the ligament begins at $\overline{E}_{zz} \approx 0.30$ (b) and coincides with the decrease in slope of the macroscopic stress-strain prediction and the increase in slope of the macroscopic volumetric strain prediction. The deformation remains concentrated within the neck for a time before eventually stabilizing at $\overline{E}_{zz} \approx 0.60$ when additional material begins to be drawn into the neck. The transition to a drawing type mode of deformation is manifested in the macroscopic response by an increase in the slope of the stress-strain curve. The volumetric strain at $X = 2.0$ is approximately twice that at $X = 1.0$.

The macroscopic stress-strain prediction of the SHA RVE strain softens immediately after macroscopic yield at both levels of stress triaxiality. The contours of viscoplastic shearing for $X = 1.0$ in Figure 6-3 a′-d′ show necking of the vertical interparticle ligament to occur simultaneously with macroscopic yield. The material outside of the neck undergoes little plastic deformation. Eventually the neck stabilizes (c′), and, as with the SHA RVE, the deformation switches to a drawing mode. Accompanying this transition is the stabilization of the macroscopic stress-strain response. Increasing the triaxiality to $X = 2.0$ has little effect on the macroscopic volumetric strain prediction of the SHA RVE. With the lateral boundary of the cell constrained to remain vertical, the radial response of the RVE is dictated by the stiff, non-yielding horizontal interparticle ligament.

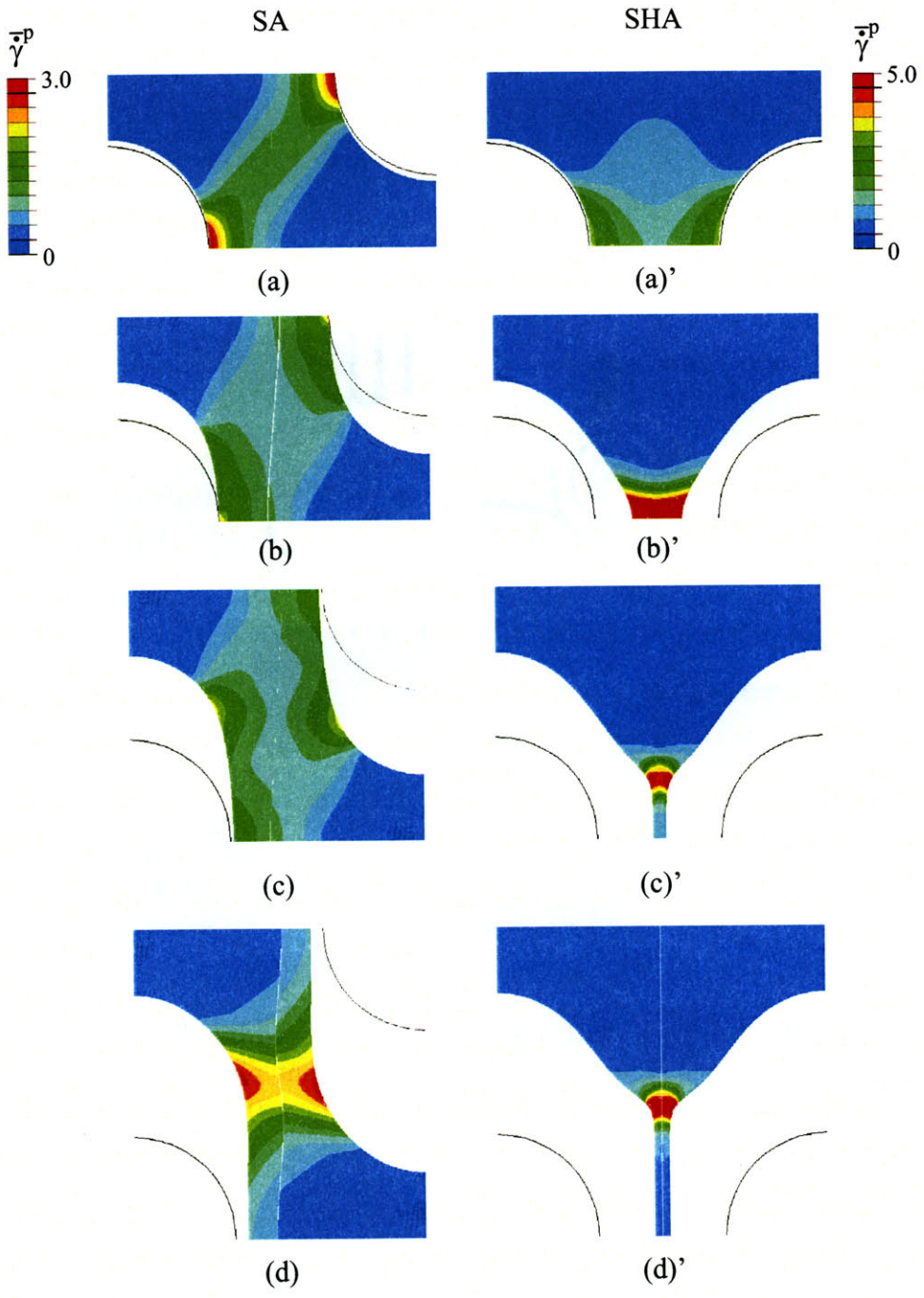

Figure 6-3: $f = 0.15$, SA (left) and SHA (right) RVE's, with rigid particles with no bonding, under triaxial loading, $X = 1.0$. Contour plots of normalized equivalent plastic shear strain rate, $\dot{\overline{\gamma}}^p$, for increasing macroscopic axial strain, $\overline{E}_{zz}$: (a), (a′) $\overline{E}_{zz} = 0.03$; (b), (b′) $\overline{E}_{zz} = 0.20$; (c), (c′) $\overline{E}_{zz} = 0.40$; (d), (d′) $\overline{E}_{zz} = 0.60$.

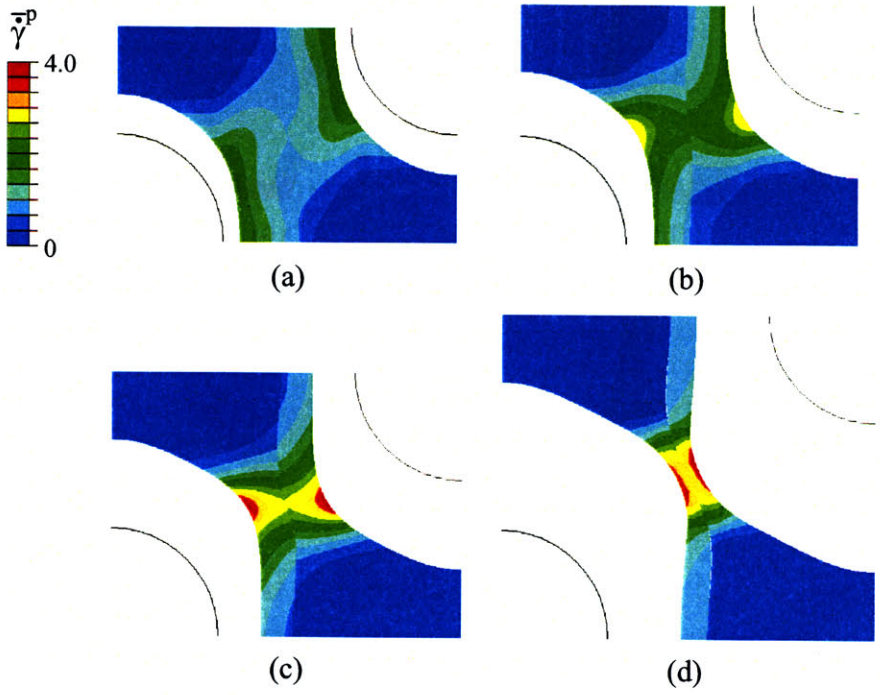

Figure 6-4: $f = 0.15$, SA RVE, with rigid particles with no bonding, under triaxial loading, $X = 2.0$. Contour plots of normalized equivalent plastic shear strain rate, $\dot{\overline{\gamma}}^p$, for increasing macroscopic axial strain, $\overline{E}_{zz}$: (a) $\overline{E}_{zz} = 0.20$, (b) $\overline{E}_{zz} = 0.30$, (c) $\overline{E}_{zz} = 0.40$, (d) $\overline{E}_{zz} = 0.60$.

Debonding

The focus of this work being *large – strain* deformations and "debonding" (i.e. the particle, initially bonded to the matrix, debonds during deformation) having been shown to be important only at small strains in CC-filled HDPE and other mineral particle-filled polymers (Bartczak et al. [8], Thio et al. [71], Wilbrink et al. [79]), the effect of stress triaxiality on debonding is given only cursory attention here.

Figure 6-5 portrays the role of triaxiality in debonding of an SA RVE at $f = 0.15$. The interface properties were set at $\sigma_{\max} = 15.0$ MPa and $\delta_{\mathrm{n}} = \delta_{\mathrm{t}} = 0.0025r$. Manifested by a "jog" in the stress-strain predictions at strains less than $\overline{E}_{zz} = 0.01$, debonding, like macroscopic yield, begins at a decreasing macroscopic effective stress and axial strain with increasing triaxiality ratio. However, plotting the responses of the RVE's in terms of the maximum macroscopic principal stress ($\overline{T}_{zz}$ in this case) in Figure 6-6 shows the macroscopic stress required to initiate debonding to increase slightly with increasing triaxiality ratio. At strains greater than $\overline{E}_{zz} \approx 0.10$, the macroscopic stress-strain and volumetric strain predictions, irrespective of the triaxiality ratio, are not a function of the interface behavior.

While increasing the triaxiality does not affect dramatically the stress at which debonding initiates, it does significantly change the way that debonding progresses around the particle. Figure 6-7 shows the relationship between the angle of debonding, ϕ, as defined in Figure 5-15, and the macroscopic axial strain of the RVE at the three triaxiality ratios. In each case, debonding begins at the pole of the particle and proceeds towards the equator of the particle. As shown in Figure 6-7a, for $X = 1/3$, the progression of debonding, when plotted in terms of ϕ versus $\overline{E}_{zz}$, can be broken down into three stages: (1) an initial, very steep linear regime when separation occurs at the pole of the particle and the elastic energy stored in the surrounding matrix is released; (2) a non-linear regime of decreasing slope as debonding approaches the equatorial region of the particle; (3) a long, gently sloped regime as debonding slowly travels the remaining distance to the equator of the particle. Best illustrated in Figure 6-7b, the initial stage extends to larger angles with increasing triaxiality ratio.

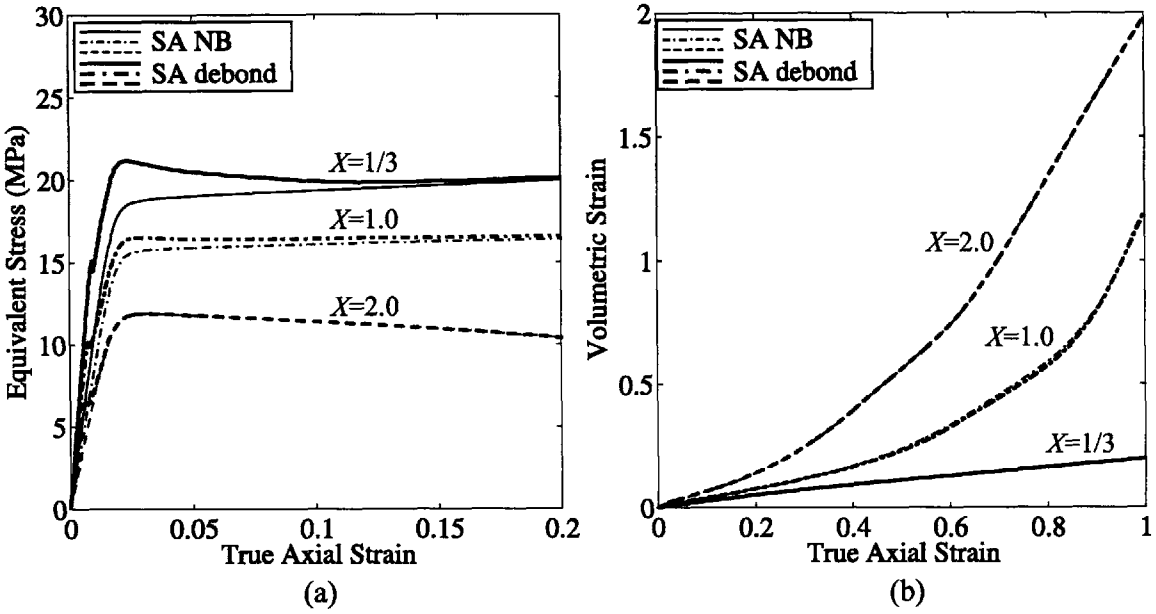

Figure 6-5: Macroscopic predictions of $f = 0.15$, SA RVE, with rigid particles with debonding and no bonding (NB), under uniaxial tension as a function of stress triaxiality, X: (a) equivalent stress versus true axial strain, (b) volumetric strain versus true axial strain.

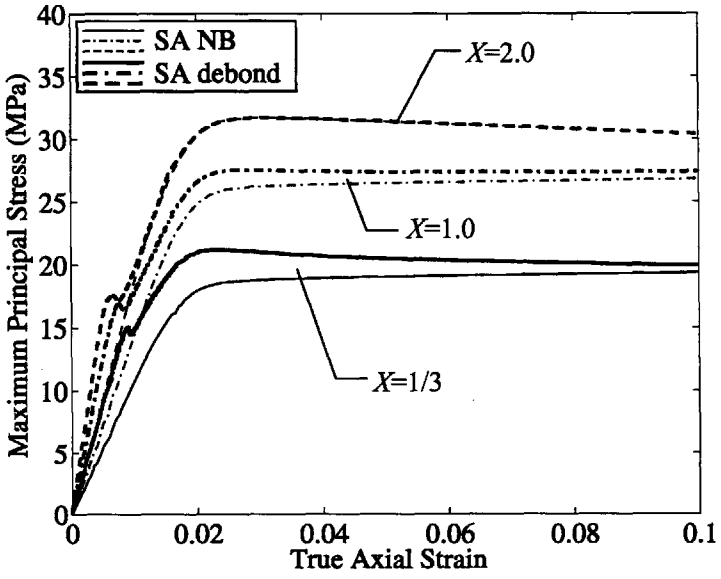

Figure 6-6: Macroscopic predictions of $f = 0.15$, SA RVE, with rigid particles with debonding and no bonded (NB), under uniaxial tension as a function of stress triaxiality, X: maximum principal stress versus true axial strain.

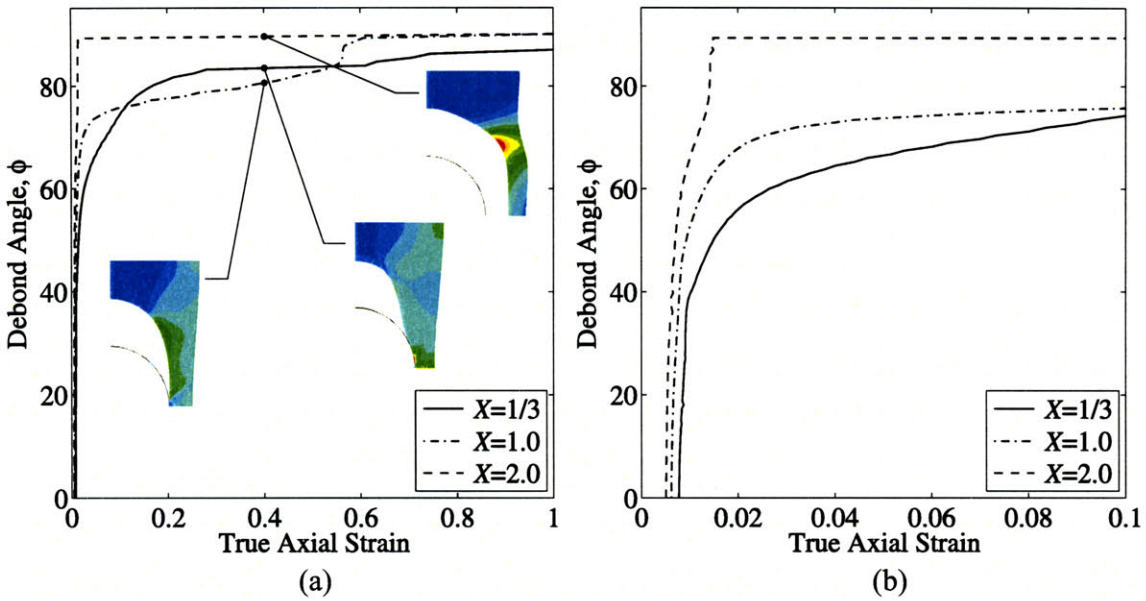

Figure 6-7: Angle of particle debonding, ϕ, versus macroscopic true axial strain for the $f = 0.15$, SA RVE as a function of stress triaxiality ratio, X. (Contours in (a) are of normalized equivalent plastic shear strain rate, $\overline{\dot{\gamma}^{\mathrm{p}}}$. (b) is equivalent to (a) but on a different scale.)

At $X = 1.0$, the particle remains partially bonded well into stage 3 and then abruptly debonds completely at $\overline{E}_{zz} \approx 0.55$. At $X = 2.0$, the particle debonds completely early in stage 2 at $\overline{E}_{zz} \approx 0.015$. Thus it is evident that the increasing levels of local radial stress and mean stress that develop with increasing triaxiality facilitate debonding.

6.1.2 Multi-particle RVE's

Next, the question of how a material with a random spatial distribution of particles responds to increasing stress triaxiality is addressed. Figure 6-8 displays the macroscopic predictions, at three triaxiality ratios, of an $f = 0.15$, 6-particle RVE with rigid particles with no bonding versus the predictions of the SA-NB model. The yield strengths of the two types of RVE are similar with, for the same reasons given in the previous chapter for the case of uniaxial tension, the multi-particle RVE holding a slight advantage at low to intermediate triaxialities. After macroscopic yield, however, at $X = 1.0$ and $X = 2.0$, the multi-particle RVE predicts significantly more

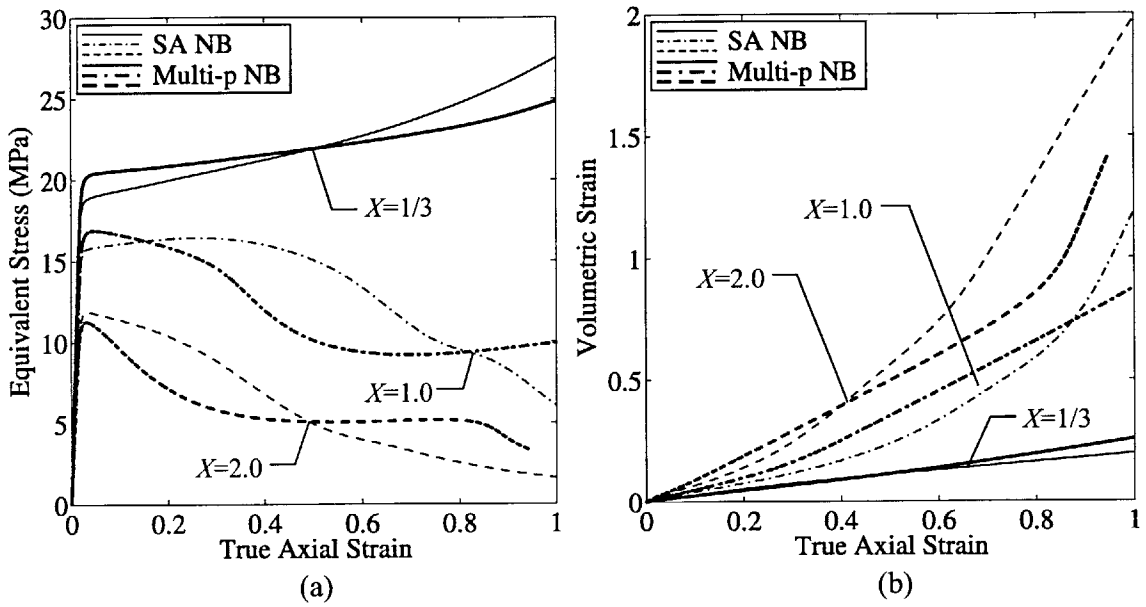

Figure 6-8: Macroscopic predictions of $f = 0.15$, multi-particle and SA RVE's, with rigid particles with no bonding, under triaxial loadings, $X = 1/3$, $X = 1.0$, and $X = 2.0$: (a) equivalent stress versus true axial strain, (b) volumetric strain versus true axial strain.

strain softening than the SA RVE before the stress stabilizes at $\overline{T}_{\text{eq}} \approx 10$ MPa and $\overline{T}_{\text{eq}} \approx 5$ MPa, respectively. With immediate post-yield strain softening and a nearly constant flow stress at large strains, the stress-strain predictions of the multi-particle RVE resemble, in shape, if not in magnitude, the SHA predictions more closely than the SA predictions. The similarities to the SHA RVE are present also in the volumetric strain predictions where, at triaxiality ratios greater than unity, the multi-particle RVE exhibits volumetric responses that are not a strong function of triaxiality and have nearly constant slope.

In Figure 6-9, for the multi-particle RVE at $X = 1/3$ and $X = 1.0$, the macroscopic volumetric strain as well as the volumetric strain in each cell of the RVE are plotted alongside the deformed finite element meshes at $\overline{E}_{zz} = 0.50$. At $X = 1/3$ (a), the volumetric strains of the cells are essentially all equal to the macroscopic volumetric strain, and the deformed mesh shows approximately equi-sized voids growing around the (not shown) particles. At $X = 1.0$ (b), however, the volumetric strains of the cells deviate from the macroscopic volumetric strain at $\overline{E}_{zz} \approx 0.30$. At this point, cells

1-3, the cells in the upper half of the RVE, become virtually inactive, and nearly all of the ensuing void growth occurs in cells 4-6. The deformed mesh clearly illustrates the discrepancy between the rates of void growth in the two halves of the RVE. Not coincidentally, it is at $\overline{E}_{zz} \approx 0.30$ that the rate of strain softening increases in the macroscopic stress-strain prediction of Figure 6-8a.

Figure 6-10 displays contour plots of normalized equivalent plastic shear strain rate for this RVE at $X = 1/3$ and $X = 1.0$. The low and intermediate triaxiality simulations exhibit similar behavior at $\overline{E}_{zz} = 0.02$ (a, a′) and $\overline{E}_{zz} = 0.20$ (b, b′). Plastic deformation is approximately equally allocated to each of the six cells in both cases. By $\overline{E}_{zz} = 0.40$, the similarity has disappeared for, at $X = 1.0$, the viscoplastic shearing has localized in the vertical ligaments of the bottom half of the RVE (c′). The rate of shearing in the upper half of the RVE is now negligible. At $\overline{E}_{zz} = 0.40$, the ligaments of cells 4-6 are necking in a manner reminiscent of the pattern of deformation exhibited by the SHA RVE in Figure 6-3. The necking instability is the cause of the aforementioned increase in rate of strain softening at $\overline{E}_{zz} \approx 0.30$. At $\overline{E}_{zz} = 0.75$, the ligaments continue to narrow, and long, sausage-like cavities form around the particles. The ligaments have not strain hardened sufficiently for the necks to stabilize and propagate.

The responses of 6-particle and SA RVE's at the intermediate triaxiality ratio are considered as a function of filler volume fraction in Figure 6-11. The SA stress-strain predictions show an inverse relationship between the macroscopic axial strain at which strain softening begins and f. The stress-strain predictions of the multi-particle RVE's strain soften after macroscopic yield at all filler volume fractions, but the rate of strain softening increases at a macroscopic axial strain also inversely proportional to f. It is apparent that localization of deformation, both within an individual cell's ligament and within an array of cells, occurs at a decreasing axial strain as f increases. The SA volumetric strain predictions increase steadily with increasing f, but the predictions of the multi-particle RVE's, despite increasing dramatically between $f = 0.05$ and $f = 0.10$, plateau, particularly at intermediate axial strains, at $f > 0.10$. As f increases, the predictions of the multi-particle RVE's more closely resemble those

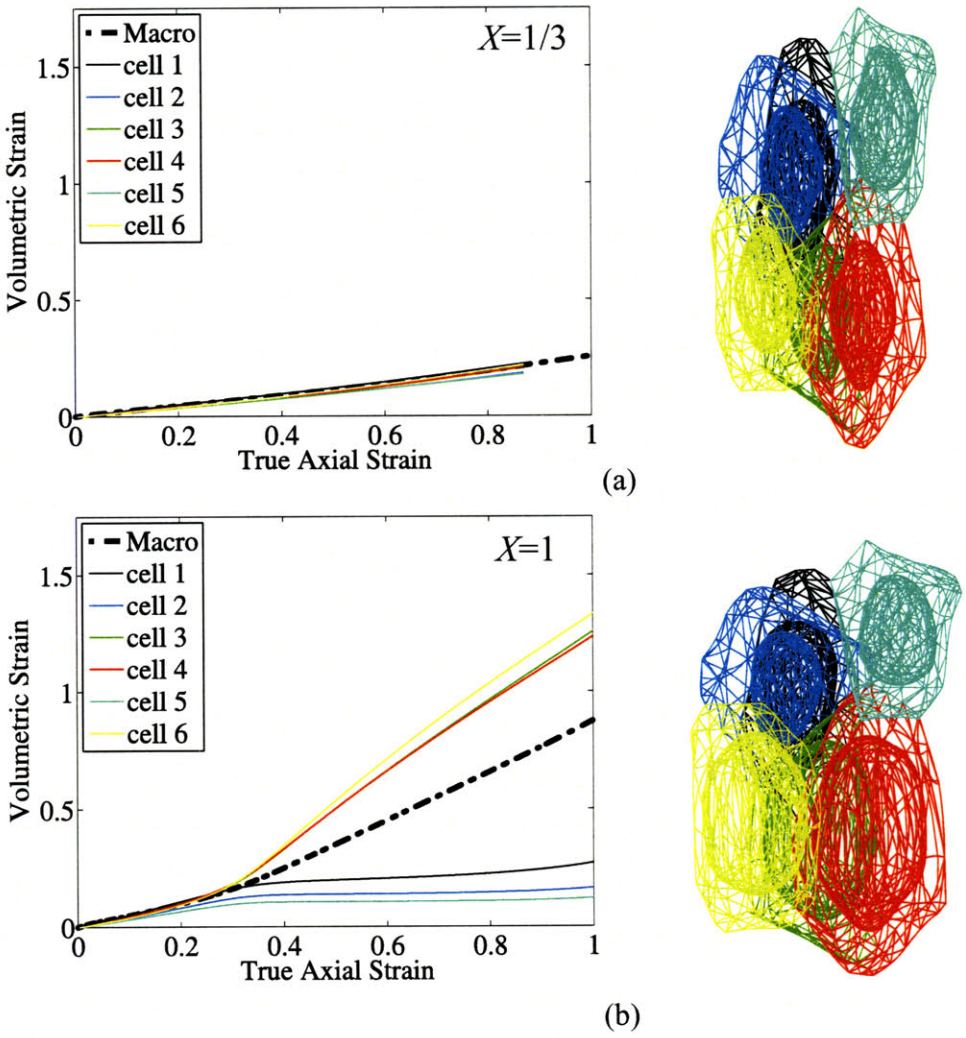

Figure 6-9: Macroscopic and cell volumetric strains (left) and color-coded deformed meshes (right) at $\overline{E}_{zz} = 0.50$ of an $f = 0.15$, multi-particle RVE with rigid particles with no bonding: (a) $X = 1/3$, (b) $X = 1.0$. (Color of cell in deformed mesh matches color of line plot.)

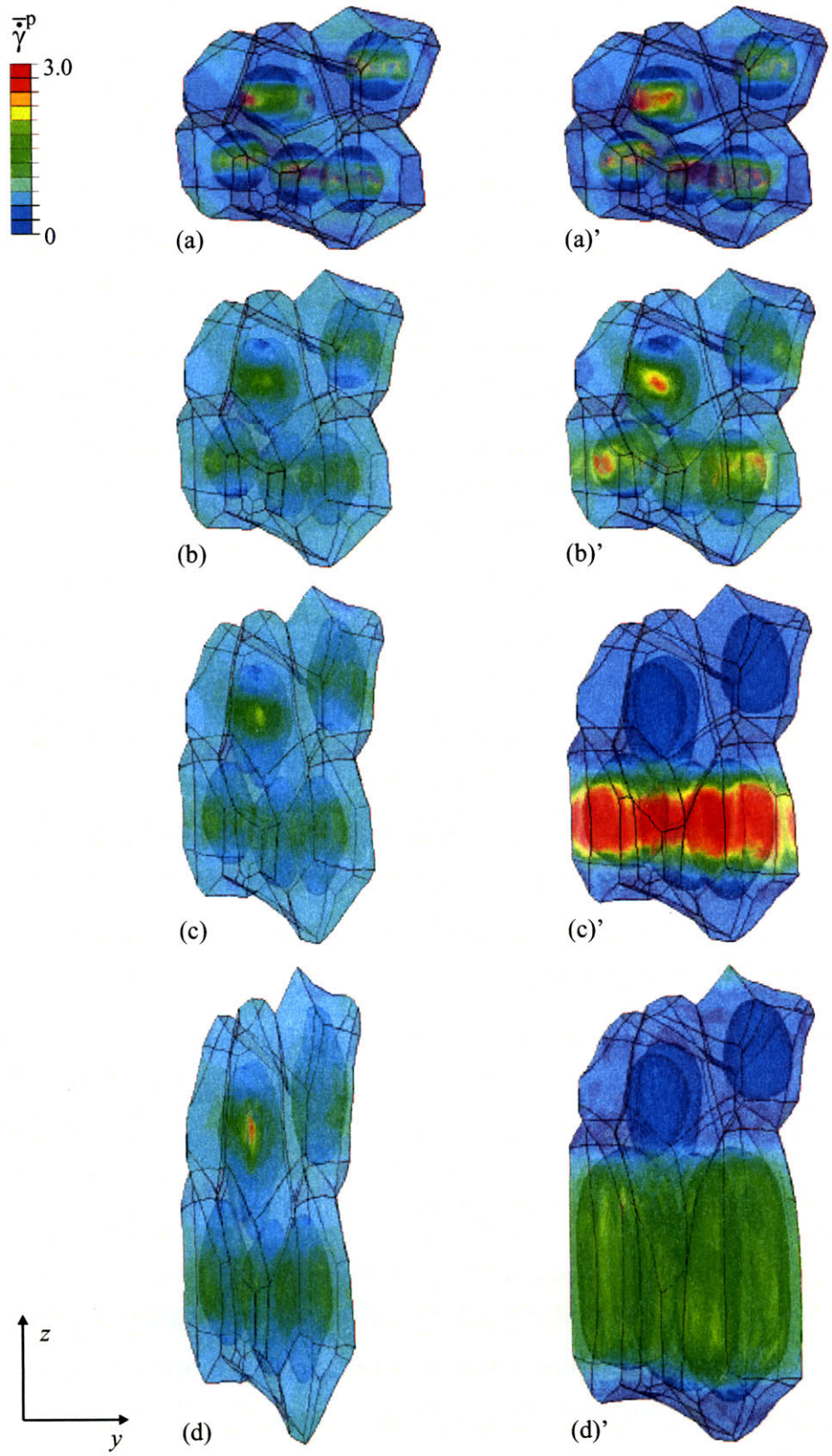

Figure 6-10: $f = 0.15$, 6-particle RVE with no bonding under uniaxial tension (left) and triaxial loading, $X = 1.0$ (right). Contour plots of normalized equivalent plastic shear strain rate, $\dot{\overline{\gamma}}^p$, for increasing macroscopic axial strain, $\overline{E}_{zz}$: (a), (a′) $\overline{E}_{zz} = 0.02$; (b), (b′) $\overline{E}_{zz} = 0.20$; (c), (c′) $\overline{E}_{zz} = 0.40$; (d), (d′) $\overline{E}_{zz} = 0.75$.

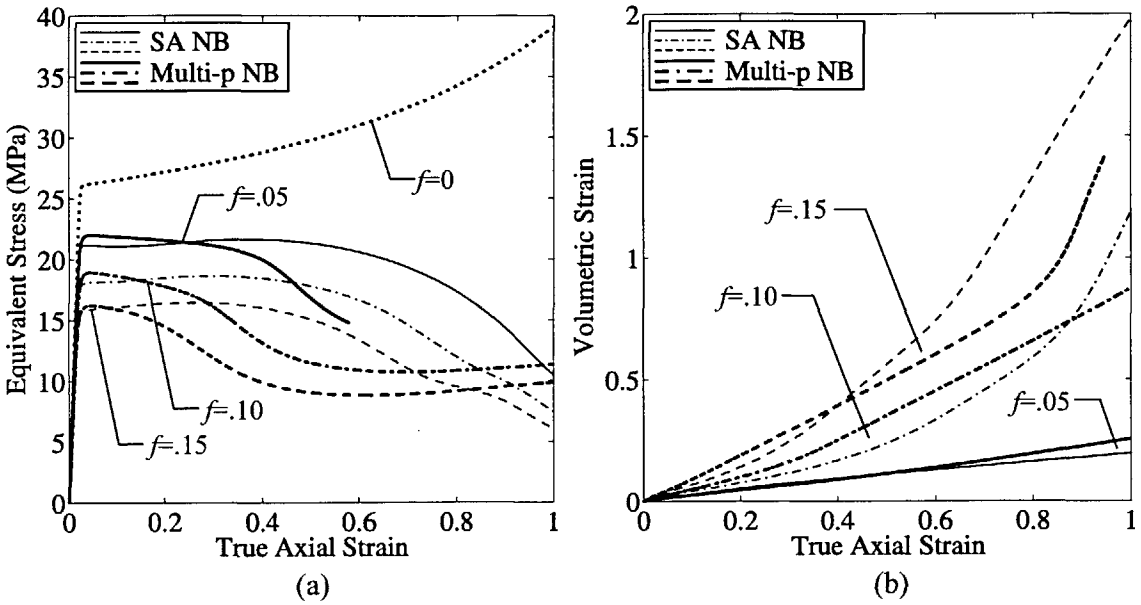

Figure 6-11: Macroscopic predictions of $f = 0.05$, $f = 0.10$, and $f = 0.15$ multi-particle and SA RVE's under triaxial loading, $X = 1.0$: (a) equivalent stress versus true axial strain, (b) volumetric strain versus true axial strain.

of the SHA RVE. Figure 6-12 illustrates how increasing the triaxiality ratio applied to the $f = 0.05$ (a) and $f = 0.10$ (b) 6-particle RVE's induces the deformation to concentrate in certain cells. At $f = 0.05$, the lower three cells are most active, and, at $f = 0.10$, the cells at the top and bottom of the RVE accommodate the majority of the deformation. Furthermore, Figure 6-12c shows that increasing the RVE size to 10 particles at $f = 0.10$ does not prevent localization from occurring. In this case, the cells at the center of the RVE deform the most.

The effects of increasing the triaxiality ratio to $X = 2.0$ with the $f = 0.15$, 6-particle RVE (compare to Figures 6-9 and 6-10) are illustrated in Figure 6-13. From both the cell volumetric strains (a) and the contours of plastic shearing (b), it is apparent that the localization of deformation to cells 4-6 occurs at a decreasing macroscopic axial strain with increasing triaxiality ratio.

Multi-particle RVE's exhibit significantly different macroscopic responses under intermediate and high triaxiality loadings than single-particle RVE's The SA model is a valid representation of a blend with perfectly dispersed particles. In this idealized

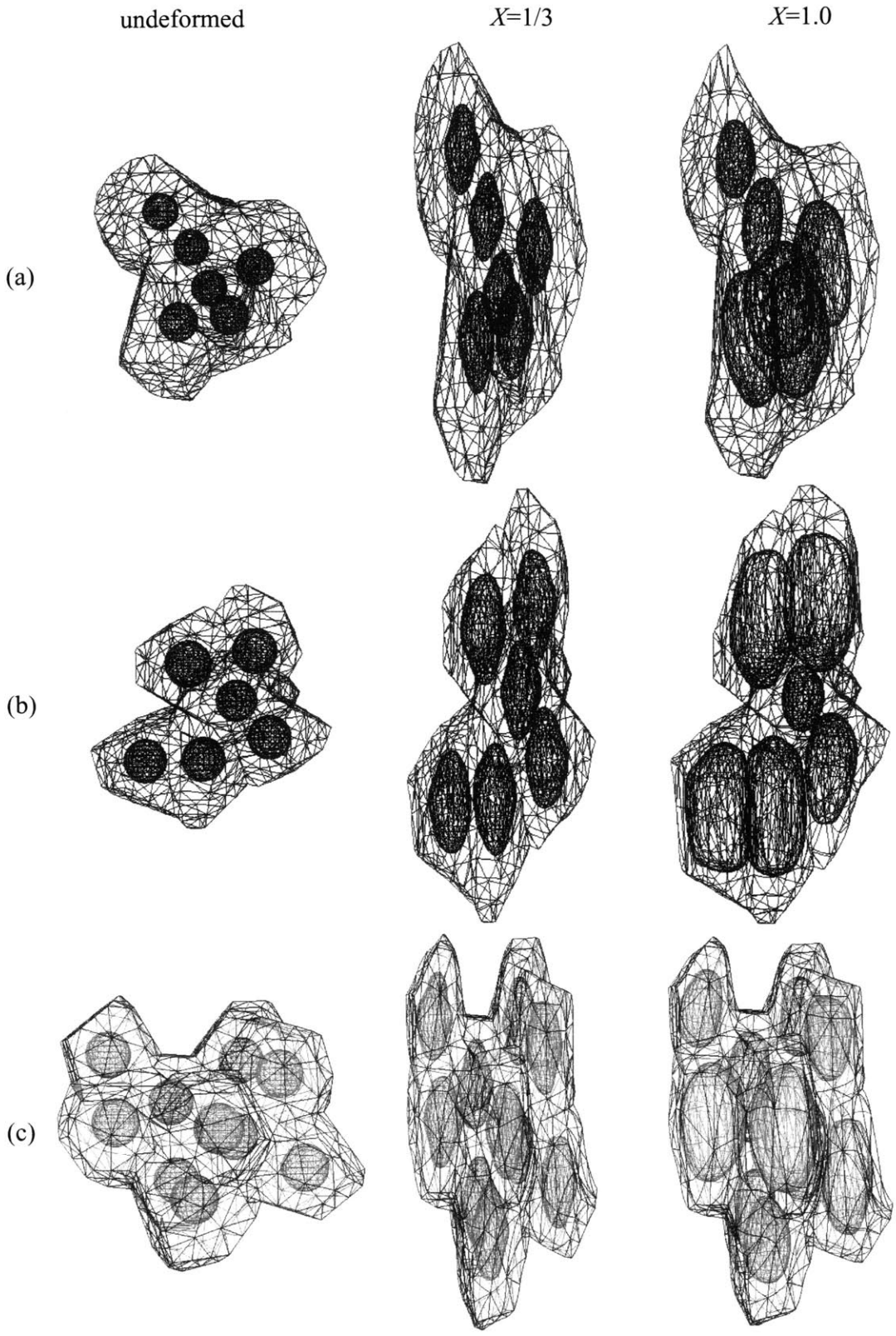

Figure 6-12: Triaxiality induced localization of deformation in multi-particle RVE's, with rigid particles with no bonding, at $\overline{E}_{zz} = 0.50$: (a) $f = 0.05$, 6-particle RVE; (b) $f = 0.10$, 6-particle RVE; (c) $f = 0.10$, 10-particle RVE.

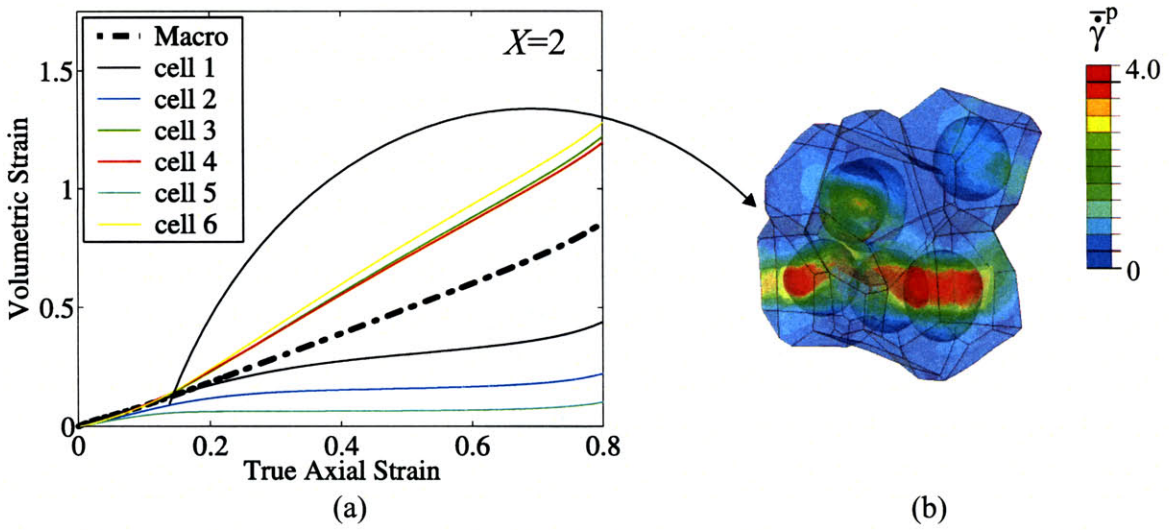

Figure 6-13: Localization at high triaxiality, $X = 2.0$, in an $f = 0.15$, multi-particle RVE with rigid particles with no bonding: (a) macroscopic and cell volumetric strains, (b) contour plots of normalized equivalent plastic shear strain rate, $\overline{\dot{\gamma}}^{\mathrm{p}}$, at $\overline{E}_{zz} = 0.12$.

material, yielding and void growth occur identically at each particle. In the previous chapter, it was shown with multi-particle simulations that an RVE composed of randomly positioned particles exhibits a higher yield strength and less strain hardening than the SA RVE, but, in general, the deformation proceeds similarly within each cell of the RVE. When the triaxiality is increased, however, particle interactions become stronger, and the deformation consistently localizes in cells that are grouped together in planes perpendicular to the major principal stress. Macroscopically, localization is reflected in an increased rate of strain softening, and the stress-strain predictions deviate sharply from those of the SA RVE's.

The matrix constitutive response used in the preceding micromechanical models is based on HDPE, a material with, relative to other thermoplastics, a relatively low strain hardening slope and a very large draw ratio (~ 9). In order to systematically investigate the role that matrix strain hardening plays in the localization of deformation in rigid particle-modified polymers, simulations were conducted with the initial strain hardening modulus of the matrix, μ_{R}, magnified by factors of 5 ($\overline{\mu}_{\mathrm{R}} = 5$) and 10 ($\overline{\mu}_{\mathrm{R}} = 10$). Figure 6-14 depicts the result that increasing μ_{R} has on the uniaxial stress-strain response of the matrix.

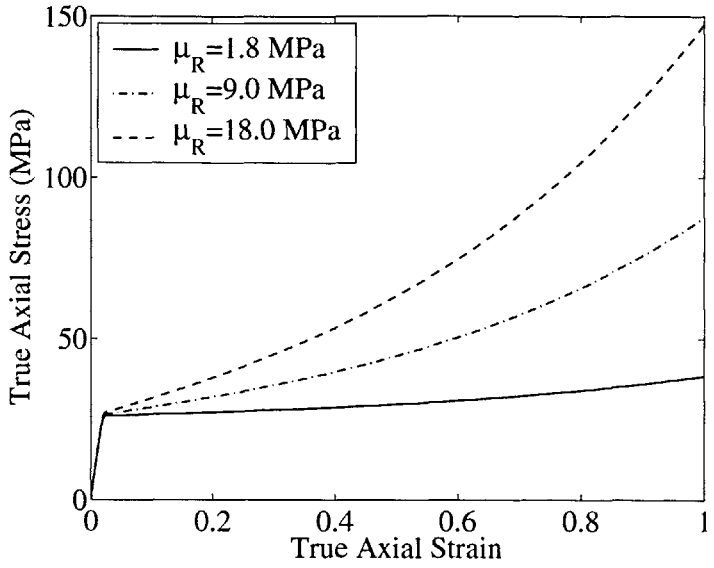

Figure 6-14: Matrix material ($f = 0$) constitutive response under uniaxial tension with increasing strain hardening modulus, μ_{R}.

Figure 6-15 shows that increasing the strain hardening modulus of the matrix causes the predictions of the SA and multi-particle RVE's at $f = 0.15$ and $X = 1.0$ to become nearly equivalent. The plots of macroscopic and cell volumetric strain in Figure 6-16 (compare to Figure 6-9b) show that, as $\overline{\mu}_{\mathrm{R}}$ increases, rather than localizing in cells 4-6, the deformation becomes spread uniformly amongst all of the cells. The contour plots of equivalent plastic shear strain rate in Figure 6-17 further elucidate the deformation mechanisms behind the macroscopic responses. With $\overline{\mu}_{\mathrm{R}} = 5$, at $\overline{E}_{zz} = 0.02$ and $\overline{E}_{zz} = 0.20$, the patterns of viscoplastic shearing are nearly identical to those for $\overline{\mu}_{\mathrm{R}} = 1$ (compare to Figure 6-10 a'-d'). At $\overline{E}_{zz} = 0.40$, localization in the lower cells (cells 4-6) is substantially weaker with $\overline{\mu}_{\mathrm{R}} = 5$ than it is with $\overline{\mu}_{\mathrm{R}} = 1$, and the upper cells (cells 1-3) are still actively deforming. By $\overline{E}_{zz} = .75$, the ligaments of the lower cells have hardened to a degree that the ligaments of the upper cells are now at least equally favorable to plastic flow, and cells 1-3 are shearing at rates equal to or exceeding those of cells 4-6. In Figure 6-16a, the volumetric strains of cells 1-3 initially lag behind those of cells 4-6, but, by $\overline{E}_{zz} = 1.0$, the cell volumetric strains are all approximately equal. With $\overline{\mu}_{\mathrm{R}} = 10$, there is no evidence of localization in either the cell volumetric responses of Figure 6-16b or the contours of viscoplastic shearing

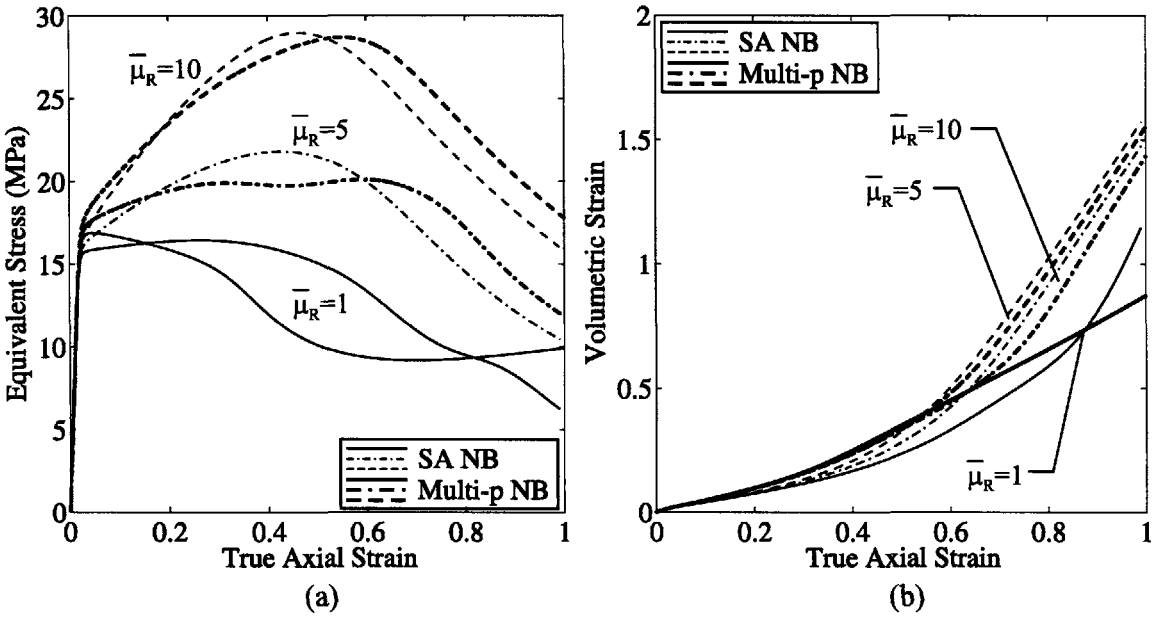

Figure 6-15: Macroscopic predictions of $f = 0.15$, multi-particle NB and SA-NB RVE's under triaxial loading, $X = 1.0$, with increasing normalized strain hardening modulus of the matrix, $\bar{\mu}_R$: (a) equivalent stress versus true axial strain, (b) volumetric strain versus true axial strain.

of Figure 6-17 a'-d'. Increasing the rate of strain hardening of the matrix reduces the tendency of the deformation to localize in certain cells, but, considering that many thermoplastics actually strain soften before they strain harden, localization will occur in numerous particle-modified polymers under these conditions.

6.2 Particle Clustering

Particle agglomeration or "clustering" is a common problem when stiff fillers are added to a polymer matrix. Poor particle dispersion has no significant effect on the elastic properties of a composite (Argon and Cohen [2]), but it often leads to brittle behavior under both uniaxial tension and highly triaxial loadings. In thermoplastics modified with mineral particles, Aronow [3], Thio et al. [71], and Wilbrink et al. [79] all showed brittle fracture to initiate at large clusters of particles. Microscopy revealed that the clusters generally remained intact and acted as supercritical flaws in a role similar to that of clustered carbide particles in high strength steels. Microscopy by

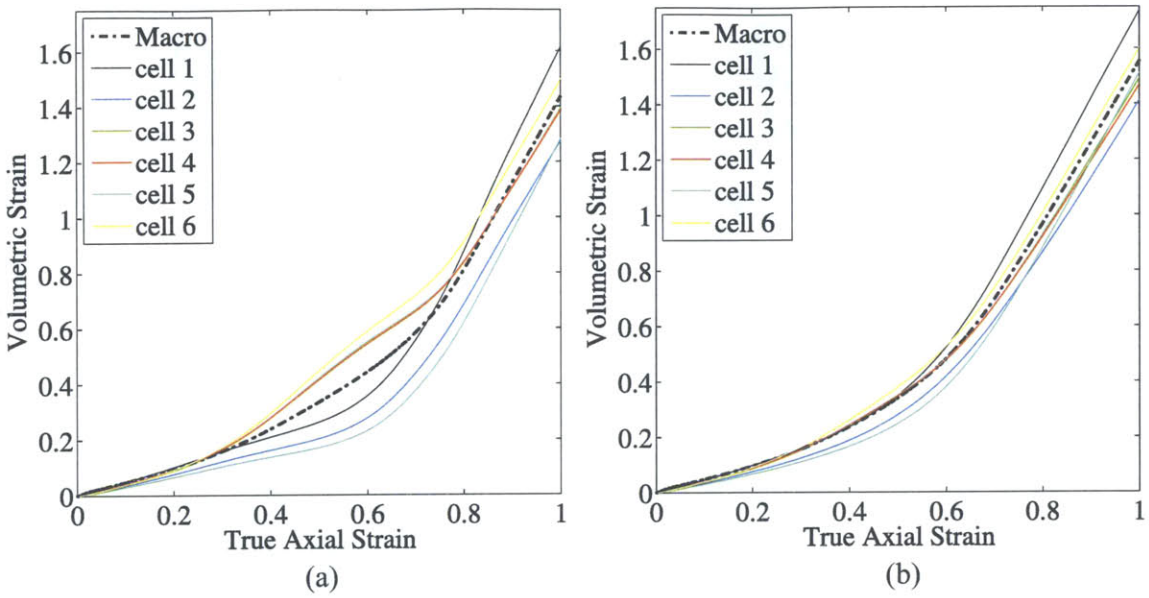

Figure 6-16: Macroscopic and cell volumetric strains of an $f = 0.15$, multi-particle RVE, with rigid particles with no bonding, under triaxial loading, $X = 1.0$: (a) $\overline{\mu}_{\mathrm{R}} = 5$, (b) $\overline{\mu}_{\mathrm{R}} = 10$.

Bartczak et al. [8] showed substantial particle agglomeration in the blends that the CC1-filled and CC2-filled HDPE of this study were meant to replicate. Despite the presumed presence of clusters, the material tested by Bartczak et al. and the material tested in this work were reasonably ductile in uniaxial tension and Izod impact tests at most volume fractions of particles. In this section, the effects of particle clustering on the large-strain tensile deformation of rigid particle-modified polymers are examined.

Figure 6-18 illustrates the types of multi-particle RVE's utilized in the clustering study. The RVE's consist of 2-8 particles with clusters as big as four particles. Within each cluster, the particles are constrained to displace and rotate as one. It should be noted that, in one respect, clustering has already been addressed. In Chapter 5 and the previous section, the responses of the SA and SHA RVE's were compared and contrasted. As noted in Chapter 5, the SHA-NB model simulates, in relation to the SA-NB model, weak porous layers alternating with stiff layers of pure matrix. The particles in the SHA RVE are "clustered" on planes aligned with the principal directions. The result is that the SHA-NB model predicts substantially more strain

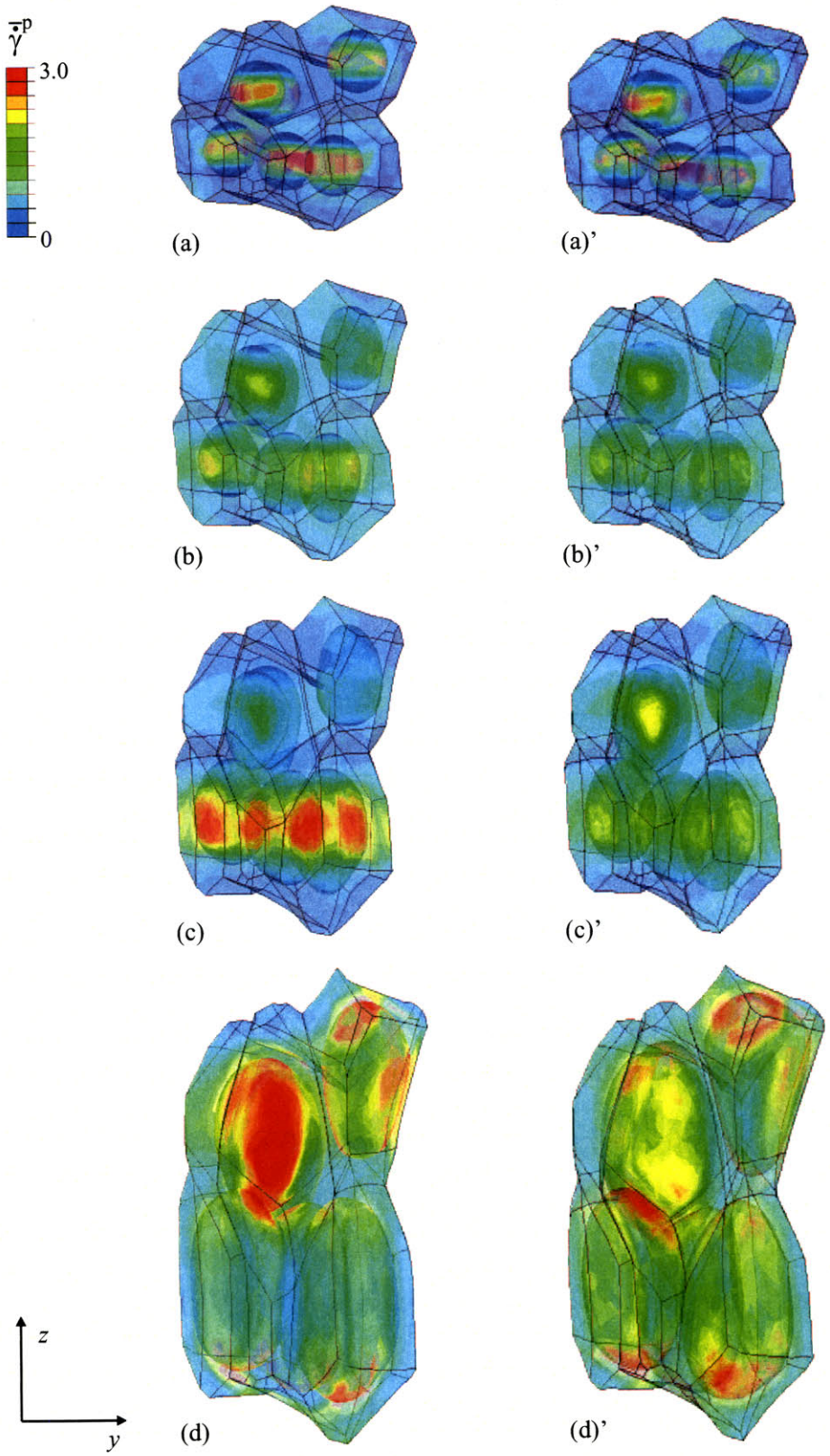

Figure 6-17: $f = 0.15$, 6-particle RVE with no bonding under triaxial loading, $X = 1.0$, with $\overline{\mu}_{\mathrm{R}} = 5$ (left) and $\overline{\mu}_{\mathrm{R}} = 10$ (right). Contour plots of normalized equivalent plastic shear strain rate, $\dot{\overline{\gamma}}^{\mathrm{P}}$, for increasing macroscopic axial strain, $\overline{E}_{zz}$: (a), (a′) $\overline{E}_{zz} = 0.02$; (b), (b′) $\overline{E}_{zz} = 0.20$; (c), (c′) $\overline{E}_{zz} = 0.40$; (d), (d′) $\overline{E}_{zz} = 0.75$.

softening at all triaxialities and higher levels of volumetric strain under uniaxial tension than the SA-NB model.

A comprehensive study of particle clustering would involve a multitude of particle distributions and RVE's with many particles. While advances in computational power may soon make this possible, at this time, resources dictated a more modest approach. In an effort to systematically investigate the ramifications of particle clustering, 2-particle RVE's were first considered. The 2-particle RVE's are based on a body-centered cubic (bcc) arrangement of particles and variations thereof. Perfectly dispersed RVE's ("bcc") were constructed by performing the tessellation procedure on particles placed at Cartesian coordinates (0.25, 0.25, 0.25) and (0.75, 0.75, 0.75) (Figure 6-18a). Clustering was simulated by moving the particles progressively closer together along the unit cube body diagonal until their center to center separation, c, was equal to the diameter of the particle (Figure 6-18b).

Figure 6-19 displays the macroscopic predictions of the 2-particle RVE's loaded in uniaxial tension in the z-direction (as defined in Figure 6-18) versus the predictions of 6-particle RVE's with randomly positioned particles at $f = 0.10$ and $f = 0.20$. The 2-particle bcc RVE's, with slightly lower yield strengths and higher rates of strain hardening than the 6-particle RVE's, behave almost identically to the SA RVE's (which, recall, are based on a tessellation of the body-centered tetragonal lattice). At $f = 0.10$, decreasing the particle spacing to $c = 2r$ in the 2-particle RVE causes only slightly less strain softening and a bit more dilatation to occur. Similar effects are apparent at $f = .20$ upon reducing the particle spacing to $c = 2.5r$. Decreasing the particle spacing at $f = 0.20$ to $c = 2r$, however, causes the macroscopic stress-strain prediction to soften substantially and the macroscopic volumetric strain prediction to more than double at $\overline{E}_{zz} = 1.0$.

Figure 6-20 shows the results of loading the 2-particle RVE's at $f = 0.20$ in uniaxial tension in directions normal and parallel to the unit cube body diagonal. The bcc RVE exhibits nearly isotropic behavior, but the clustered RVE plainly is anisotropic. When loaded in the direction parallel to the body diagonal, the clustered RVE exhibits a macroscopic response with significantly more strain hardening and

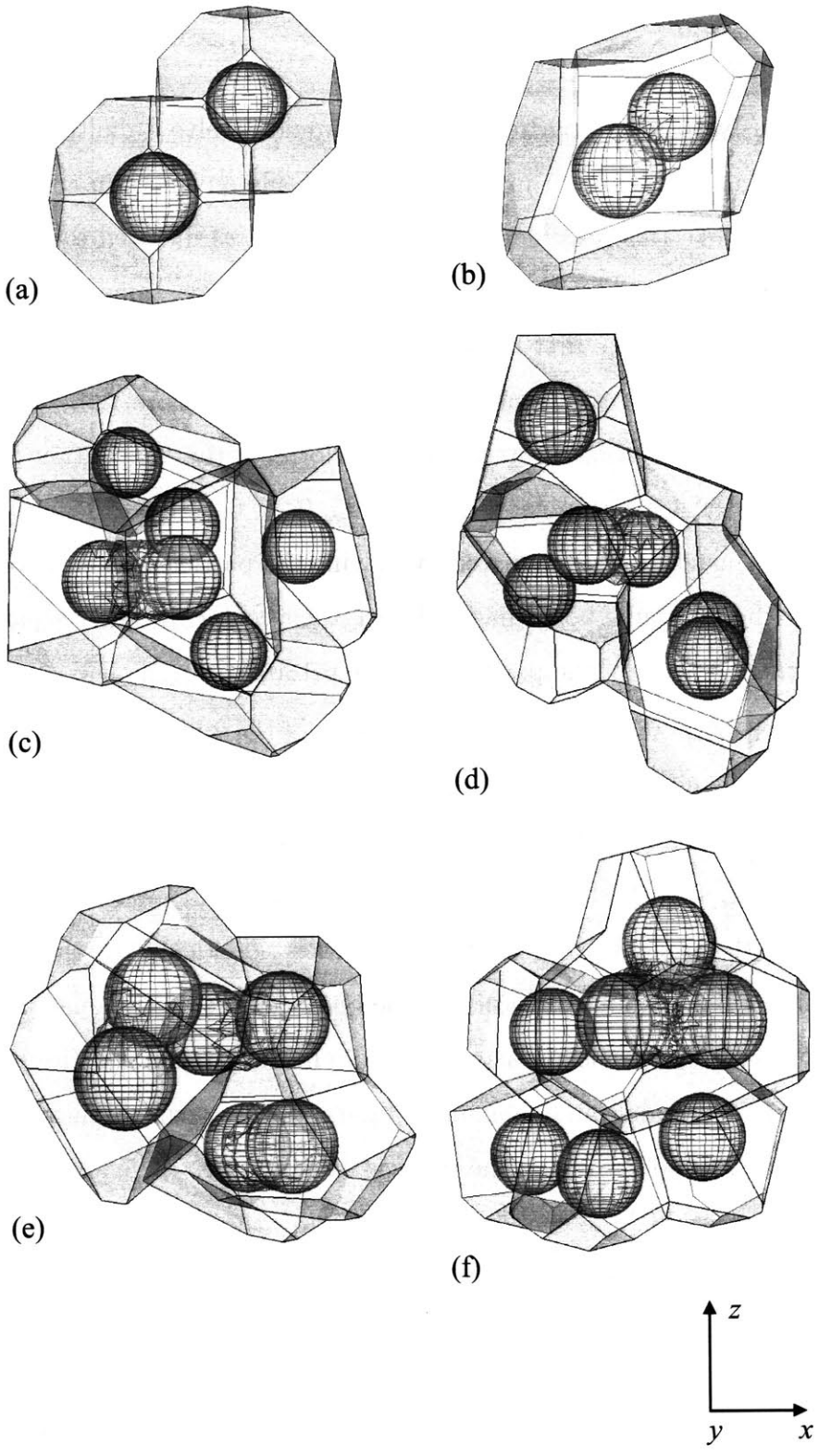

Figure 6-18: RVE's used in clustering study: (a) 2-particle bcc RVE, (b) 2-particle clustered RVE, (c) 6-particle RVE with 2-particle cluster #1, (d) 6-particle RVE with 2-particle cluster #2, (e) 6-particle RVE with three 2-particle clusters, (f) 8-particle RVE with a 4-particle cluster.

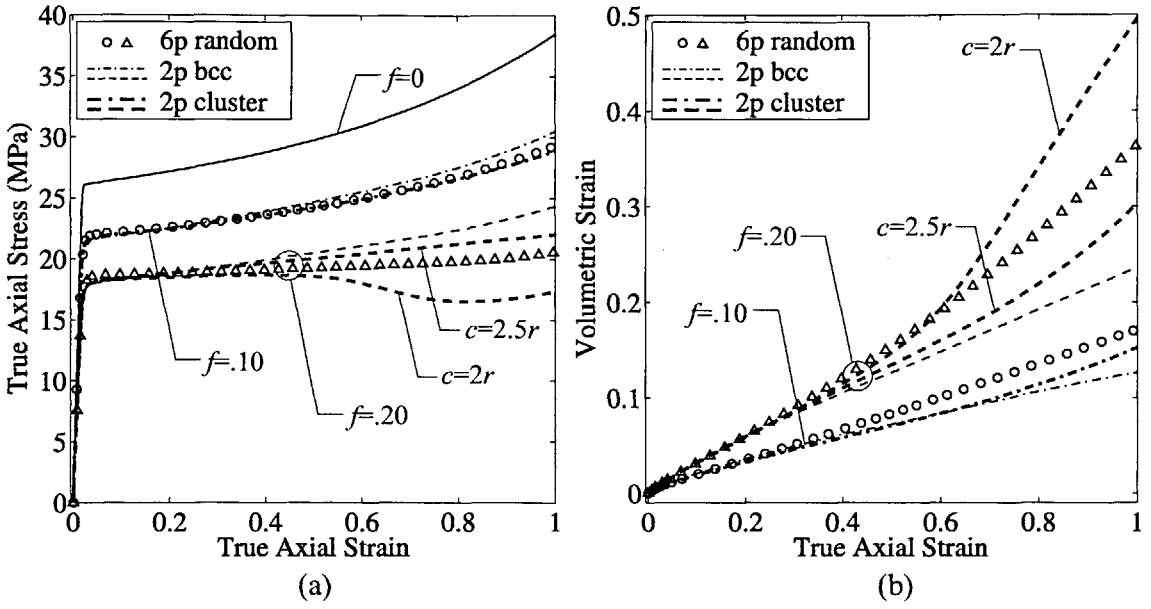

Figure 6-19: Macroscopic predictions of random 6-particle RVE's and 2-particle bcc-based RVE's, with rigid particles with no bonding, loaded in uniaxial tension in the z-direction: (a) true axial stress versus true axial strain, (b) volumetric strain versus true axial strain.

less volumetric strain than it does when loaded in the z-direction. With regards to cluster shape alone, loading the clustered RVE in the direction perpendicular to the body diagonal would seem to cause the most void growth, and, in turn, the softest stress-strain response. However, the projection of the RVE's periodic neighbor cells must be taken into account. In reference to the z-direction, the clustered RVE actually represents a stacked array of clusters, and hence the resemblance between its macroscopic response when loaded in this direction and the predictions of the SHA RVE. In reference to the rotated coordinate frame, the clusters are arranged in a two-dimensional staggered sense, and the RVE's response when loaded in this frame is similar to the predictions of the SA RVE. In a sense, this exercise has as much to do with particle shape as it does particle clustering, and the effects of cluster shape are apparent in Figure 6-20. The predictions of the clustered RVE loaded perpendicular to the body diagonal are over 10% softer and exhibit substantially more volumetric strain than the predictions when the RVE is loaded parallel to the body diagonal. Constrained to move as one, the particles in the clustered RVE's may be compared

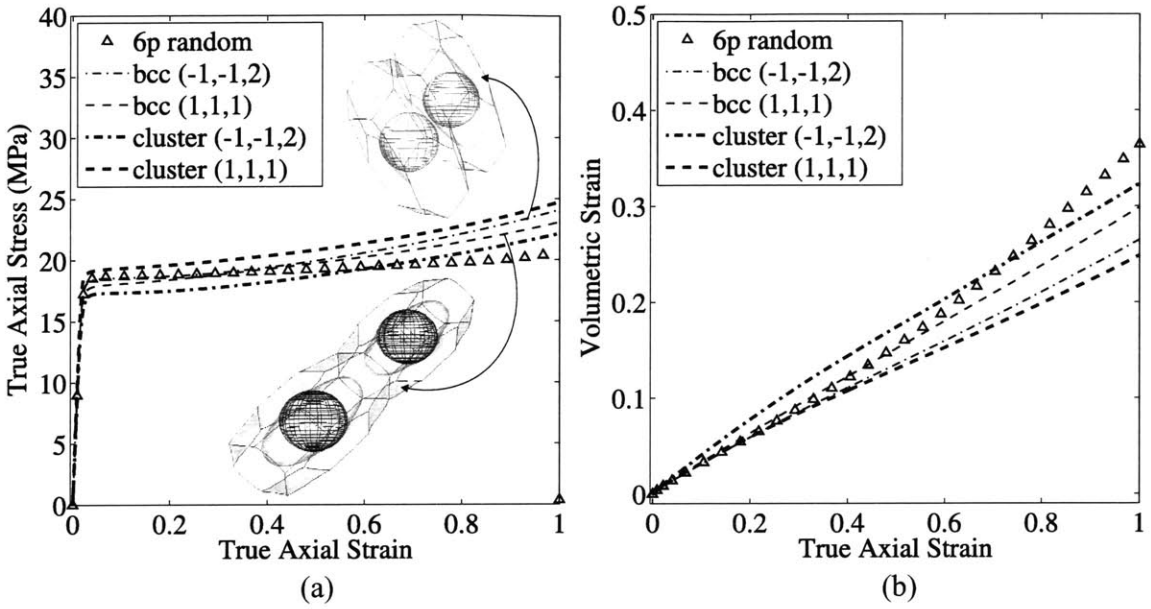

Figure 6-20: Macroscopic predictions of random 6-particle RVE with no bonding loaded in uniaxial tension and 2-particle bcc-based RVE's with no bonding loaded in uniaxial tension in directions normal $(-1/\sqrt{6}\mathbf{x} - 1/\sqrt{6}\mathbf{y} + 2/\sqrt{6}\mathbf{z})$ and parallel $(1/\sqrt{3}\mathbf{x} + 1/\sqrt{3}\mathbf{y} + 1/\sqrt{3}\mathbf{z})$ to the body diagonal of the unit cube: (a) true axial stress versus true axial strain, (b) volumetric strain versus true axial strain.

to short fibers or ellipsoids, but, interestingly, the response in the direction parallel to the body diagonal is virtually independent of whether or not the particles are bonded to each other.

In an effort to capture more accurately the effects of particle agglomeration, RVE's with more than two particles were constructed. The major issues addressed with these RVE's are uniformity of clustering and the size and shape of clusters.

Figure 6-21 depicts the result of adding a single 2-particle cluster oriented in the plane perpendicular to the loading direction (z, in this case) to an RVE containing six particles in total (Figure 6-18c). This RVE is meant to represent a blend where only a portion of the particles agglomerate. The positions of the four non-clustered particles as well as the orientation in the $x - y$ plane of the clustered particles were chosen at random for the $f = .20$ RVE. The $f = .10$ RVE was constructed by placing the four non-clustered particles at the same locations and the clustered particles along the same line as in the $f = .20$ RVE. The cluster has little impact on the macroscopic

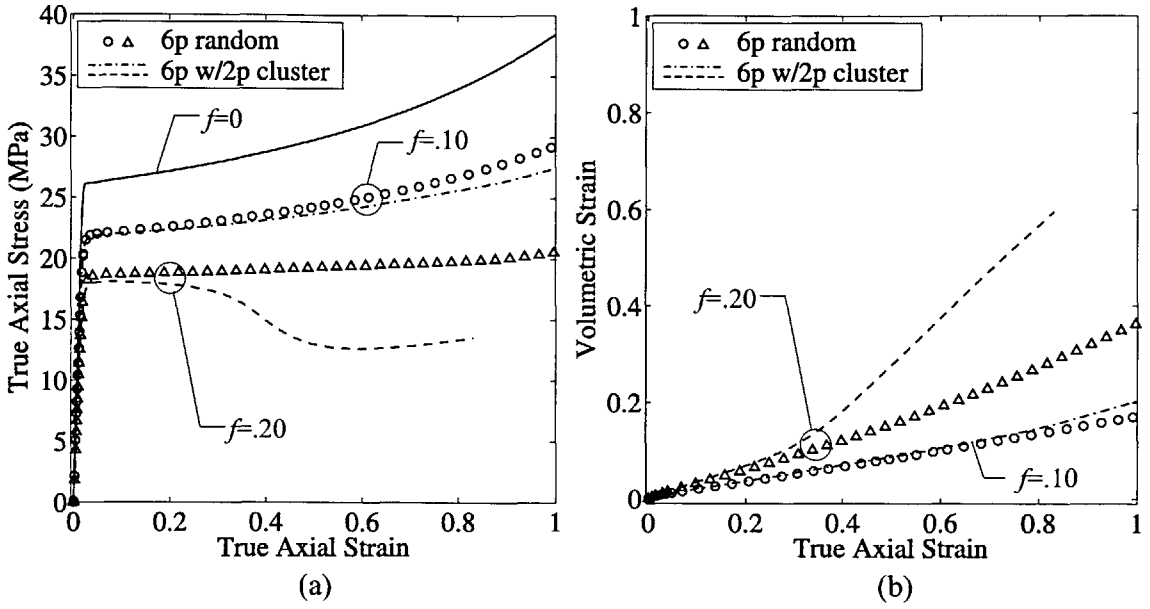

Figure 6-21: Macroscopic predictions of random 6-particle RVE's and 6-particle RVE's with a single 2-particle cluster #1 (Figure 6-18c), with rigid particles with no bonding, loaded in uniaxial tension: (a) true axial stress versus true axial strain, (b) volumetric strain versus true axial strain.

predictions at $f = .10$, but, at $f = 0.20$, the RVE with the cluster exhibits strain softening beginning at $\overline{E}_{zz} \approx 0.20$ and substantially more volumetric strain than the RVE with six randomly positioned particles. The contours of viscoplastic shearing in Figure 6-24 a-d show that, at $\overline{E}_{zz} = 0.20$, the deformation has begun to localize in the cells of the cluster and the two cells nearest to the z-plane of the cluster. A pattern of deformation previously observed only at higher levels of stress triaxiality develops. The ligaments at the center of the RVE neck, and large ellipsoidal cavities form around the particles. At $\overline{E}_{zz} = 0.75$, the deformation in the center ligaments has yet to stabilize.

In Figure 6-22, the effects of changing the strain hardening response of the matrix to that of the eight-chain model of rubber elasticity are shown. At $f = 0$ and at $f = 0.20$ with the 6-particle RVE with well dispersed particles, the existence of a matrix locking stretch does not increase the rate of strain hardening appreciably until $\overline{E}_{zz} \approx 0.75$. With the cluster, however, the predictions with the two types of matrix strain hardening diverge at $\overline{E}_{zz} \approx 0.40$. Macroscopic strain softening occurs in

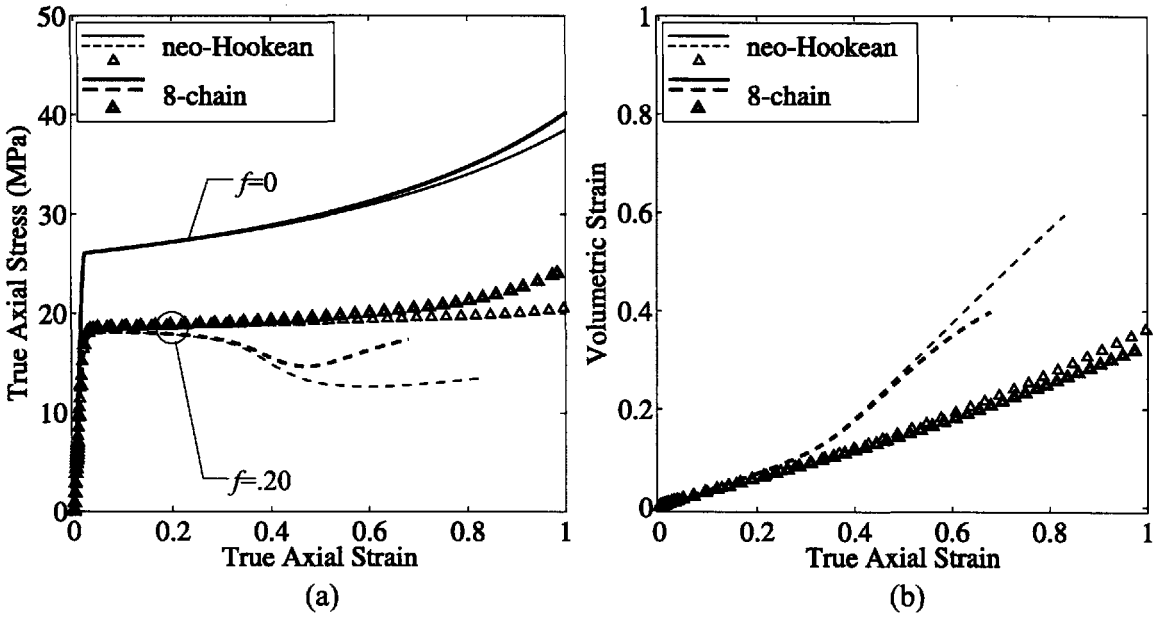

Figure 6-22: Effects of matrix strain hardening on the macroscopic predictions of the random 6-particle RVE and the 6-particle RVE with a single 2-particle cluster #1, with no bonding rigid particles at $f = 0.20$, under uniaxial tension: (a) true axial stress versus true axial strain, (b) volumetric strain versus true axial strain.

both cases, but the amount of strain softening is less and is followed by macroscopic strain hardening with the eight-chain version of the constitutive model. The rate of strain hardening in the necking ligaments increases rapidly as the locking stretch of the polymer is approached, causing the deformation to stabilize and draw at a smaller macroscopic axial strain.

Figure 6-23 displays the macroscopic predictions of the 6-particle RVE in Figure 6-18d. This RVE, like the previously presented RVE, has a single 2-particle cluster in the plane perpendicular to the loading direction (z again) amongst four randomly positioned particles. Unlike the preceding case, however, the presence of the cluster has virtually no effect on the macroscopic response at either $f = 0.10$ or $f = 0.20$. The contours of viscoplastic shearing for this 2-particle cluster RVE (#2) at $f = 0.20$ in Figure 6-24 a′-d′ show that the deformation does not localize and that all cells experience similar void growth. The difference between the two RVE's with 2-particle clusters is that the first RVE has more particles whose axial projections overlap than the second RVE. It appears from this admittedly small sample that non-

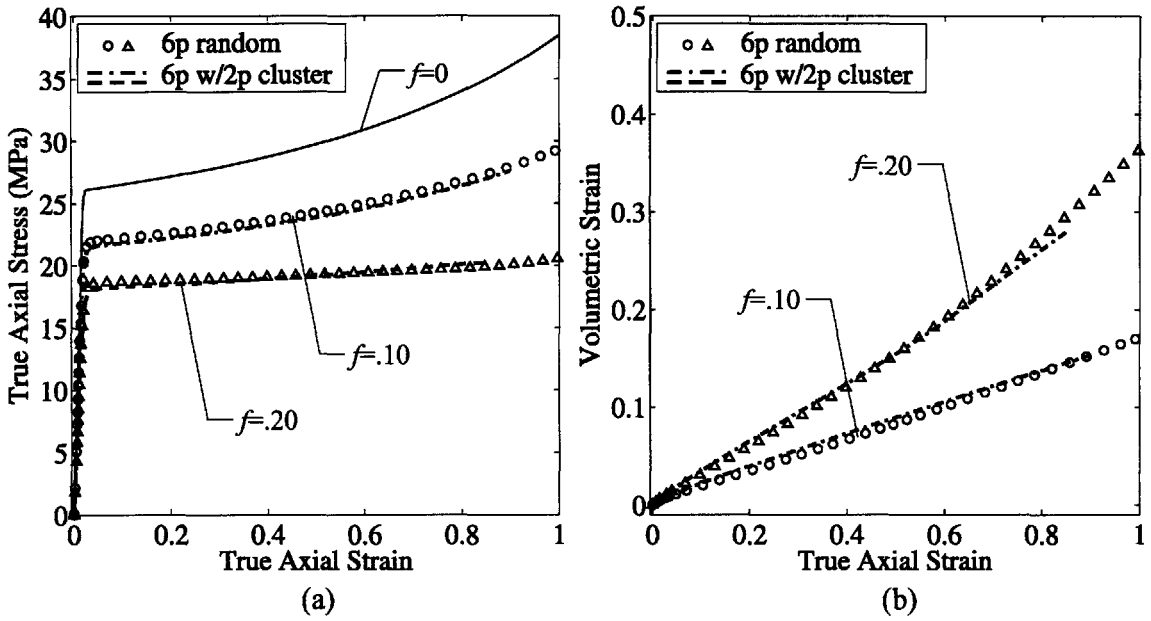

Figure 6-23: Macroscopic predictions of random 6-particle RVE's and 6-particle RVE's with a single 2-particle cluster #2 (Figure 6-18d), with rigid particles with no bonding, loaded in uniaxial tension: (a) true axial stress versus true axial strain, (b) volumetric strain versus true axial strain.

uniform clustering of particles *can*, under certain circumstances, trigger deformation at low triaxiality that would otherwise only occur at elevated levels of triaxiality. Furthermore, this suggests than an RVE with non-uniform clusters would be even more sensitive to triaxiality than an RVE with well dispersed particles.

Next, an RVE with uniform agglomeration is considered. The RVE in Figure 6-18e consists of three 2-particle clusters. The location and orientation of each cluster was chosen at random. The macroscopic predictions of this RVE under loading in the three principal directions show that the clustering has no consistent effect on the composite's response. In one direction, strain softening occurs, but, in the other two directions, the clustered RVE exhibits more strain hardening than the RVE with well dispersed individual particles. The mean of the three stress-strain responses is very similar to the prediction of the RVE with well dispersed individual particles. Similar results were found with an entirely different RVE with four 2-particle clusters. With an RVE composed of many more particles, the response presumably would be isotropic. In summary, on average, RVE's with well dispersed clusters of uniform size

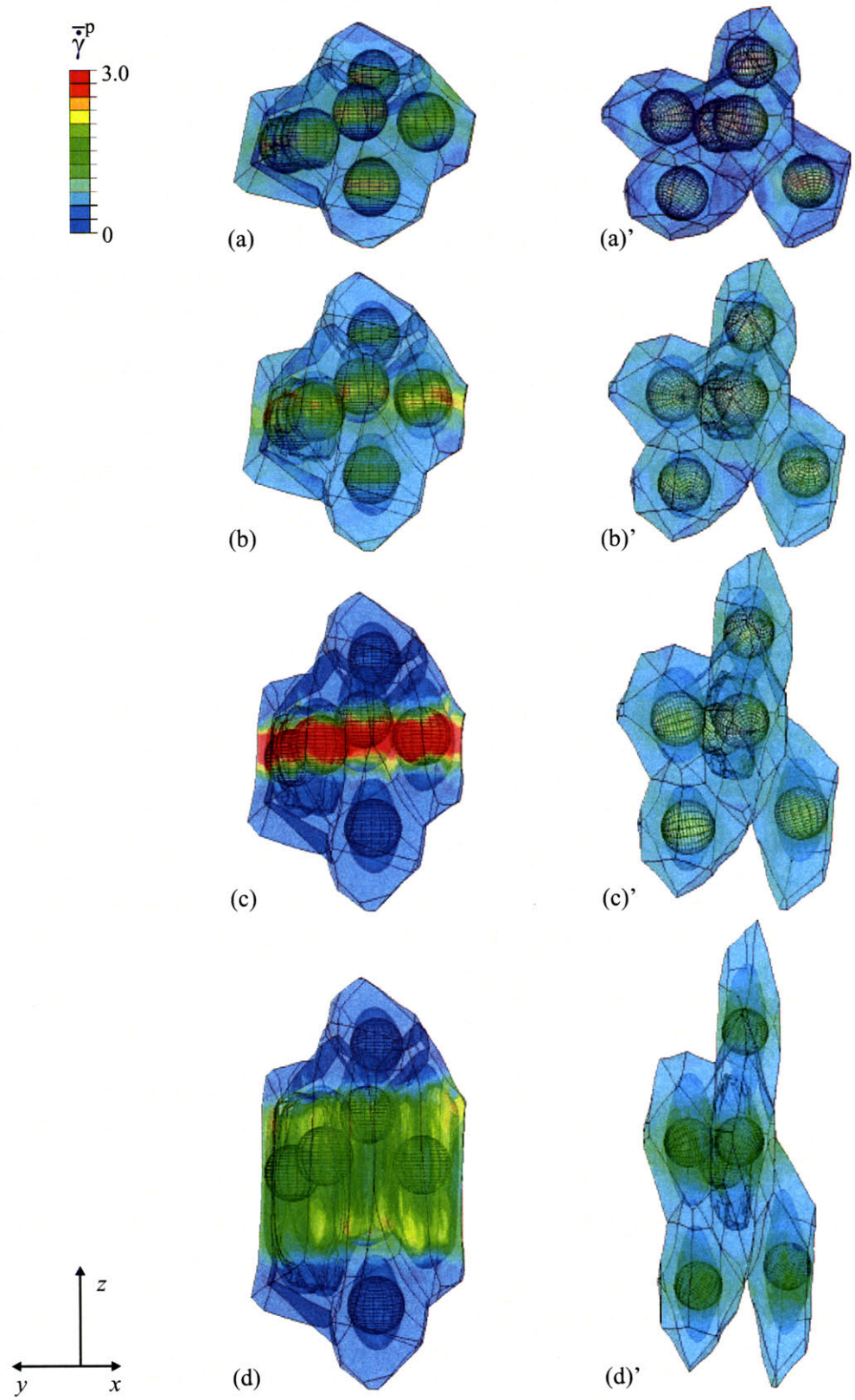

Figure 6-24: $f = 0.20$, 6-particle RVE's (#1 on the left, #2 on the right) with no bonding, each with a single 2-particle cluster, loaded in uniaxial tension. Contour plots of normalized equivalent plastic shear strain rate, $\dot{\overline{\gamma}}^p$, for increasing macroscopic axial strain, $\overline{E}_{zz}$: (a), (a′) $\overline{E}_{zz} = 0.02$; (b), (b′) $\overline{E}_{zz} = 0.20$; (c), (c′) $\overline{E}_{zz} = 0.40$; (d), (d′) $\overline{E}_{zz} = 0.75$.

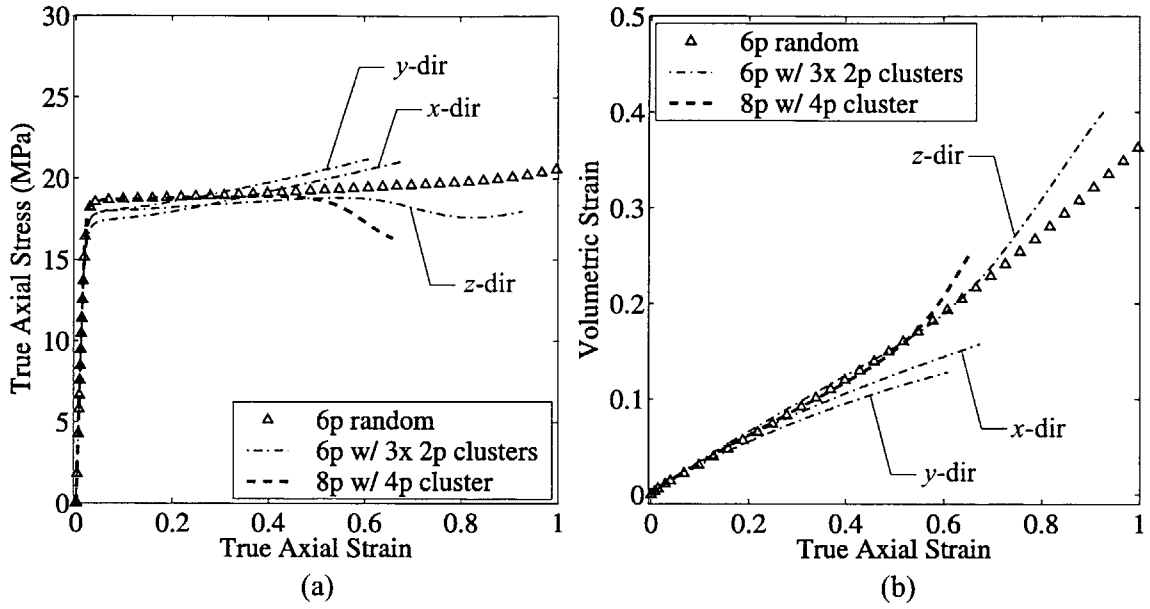

Figure 6-25: Macroscopic predictions of random 6-particle RVE, 6-particle RVE with three 2-particle clusters, and 8-particle RVE with a 4-particle cluster, with rigid particles with no bonding at $f = 0.20$, loaded in uniaxial tension: (a) true axial stress versus true axial strain, (b) volumetric strain versus true axial strain.

do not deform differently than RVE's with well dispersed individual particles.

If particle agglomeration is to have any significant impact on large-strain macroscopic deformation, it appears that non-uniformly sized clusters must be present. It also appears that "small" (i.e. two-particle) clusters do not consistently alter the response of an otherwise well dispersed RVE. Thus, in order to investigate the effects of larger clusters as well as more uniformly shaped clusters, the 8-particle RVE with a 4-particle cluster of Figure 6-18f was constructed. The macroscopic predictions of this RVE, loaded in uniaxial tension in the z-direction, are plotted in Figure 6-25. At strains less than $\overline{E}_{zz} \approx 0.50$, its response is nearly identical to that of the RVE with randomly positioned particles. At larger strains, however, strain softening occurs, and the slope of the volumetric strain response increases. The contours of viscoplastic shearing in Figure 6-26 show that the deformation has begun to localize in the z-plane of the cluster at $\overline{E}_{zz} \approx 0.50$, and, at $\overline{E}_{zz} \approx 0.65$, the interparticle ligaments are necking in a manner similar to that observed in RVE's with well dispersed particles at elevated triaxialities. This is further evidence that an RVE with non-uniform

clustering of particles would be even more sensitive to triaxiality than an RVE with well dispersed particles.

6.3 Conclusions

In this chapter, the effects of stress triaxiality and particle clustering on the large-strain deformation of rigid particle-modified polymers have been investigated. In single-particle RVE's, interparticle ligaments were shown to neck at decreasing macroscopic axial strains with increasing macroscopic stress triaxiality ratios. In multi-particle RVE's containing up to 10 particles, both elevated levels of triaxiality and clusters of irregular size were shown to induce the deformation to localize within a subset of the cells. Localization led to strain softening and an increase in volumetric strain. The extent of localization was shown to be inversely proportional to the strain hardening modulus of the matrix.

The multi-particle micromechanical models of this chapter may, in one sense, exaggerate the propensity of the deformation to localize. In each case, localization, whether due to triaxiality or clustering, occurs in one or two bands that span the entire RVE. Periodic constructions, the RVE's predict these bands to extend infinitely in the plane perpendicular to the direction of maximum applied stress. In a specimen or structure containing far more particles, the band(s) would likely encounter regions with a low local volume fraction of particles, and the deformation might be stymied and/or jump to other planes. Future work on this topic would involve performing simulations with RVE's comprised of an order of magnitude more particles.

On the other hand, localization took place too frequently for it to be purely an artifact of the RVE's. The deformation concentrated in a subset of the total number of cells in every multi-particle RVE, including those with a volume fraction of particles as small as 5% (the lowest f modeled) and those loaded with a stress triaxiality ratio as low as $X = 1/2$. Furthermore, as the triaxiality increases, particle dispersion becomes more important. In actual rigid particle-modified polymers, the spacing of particles is not restricted to $c \geq 2.5r$, and clusters of particles are known to exist. While the

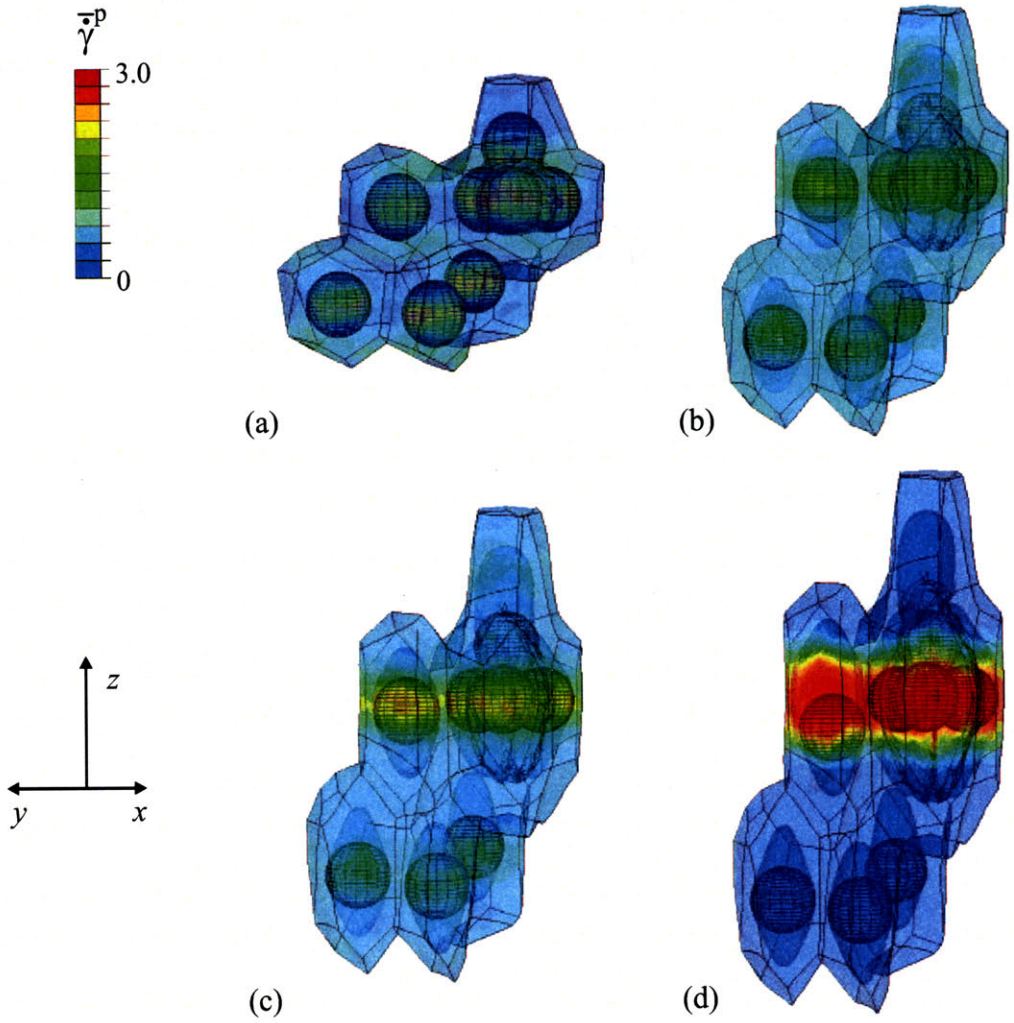

Figure 6-26: $f = 0.20$, 8-particle RVE with a 4-particle cluster, with rigid particles with no bonding, loaded in uniaxial tension. Contour plots of normalized equivalent plastic shear strain rate, $\dot{\overline{\gamma}}^p$, for increasing macroscopic axial strain, $\overline{E}_{zz}$: (a) $\overline{E}_{zz} = 0.02$, (b) $\overline{E}_{zz} = 0.40$, (c) $\overline{E}_{zz} = 0.50$, (d) $\overline{E}_{zz} = 0.65$.

boundary conditions on the RVE's may intensify the localization, the opposing effect of the artificially good dispersion of the RVE's with randomly positioned particles likely delays the onset of localization.

In a structural component, if particle agglomeration occurs at a crucial location or unequal settling of particles during molding results in regions of high filler content spanning the width of the part, premature failure is a very real concern. At the root of a notch or at a crack tip, unless the particles are perfectly dispersed, one would expect there to be at least regions where the deformation localizes. The high strains and, in turn, the high stresses experienced by the interparticle ligaments in these regions may cause fracture. In fact, it is not uncommon in an Izod impact test, for example, to see, on the fracture surface of a brittle specimen, a small area near the root of the notch which exhibits signs of plastic deformation. In these cases, the initiation of brittle fracture may actually be precipitated by a highly localized ductile fracture event. Toughness is best achieved, not through these isolated large strains, but via widespread, uniform dissipative plastic flow.

Chapter 7

Constitutive Modeling of Polymers with Perfectly Bonded Rigid Particles

In the final portion of the thesis, a constitutive model for rigid particle-modified polymers is presented. In this chapter, the component of the model which accounts for particles that do not debond is described. It was shown in Chapter 5 that polymer composites with perfectly bonded particles exhibit an increasing modulus, yield strength, and rate of strain hardening with increasing volume fraction of filler. The model, formulated within the framework of Boyce et al. [13], accounts for each of these features. The structure of the model is illustrated in one dimension in Figure 7-1. The bars over the stress tensors, in Figure 7-1 and throughout this and the next chapter, identify the tensors as macroscopic, continuum-level quantities as opposed to quantities associated with the individual phases of the polymer composite. The constitutive model is developed and verified by drawing comparison with the results of micromechanical simulations similar to those of the previous two chapters.

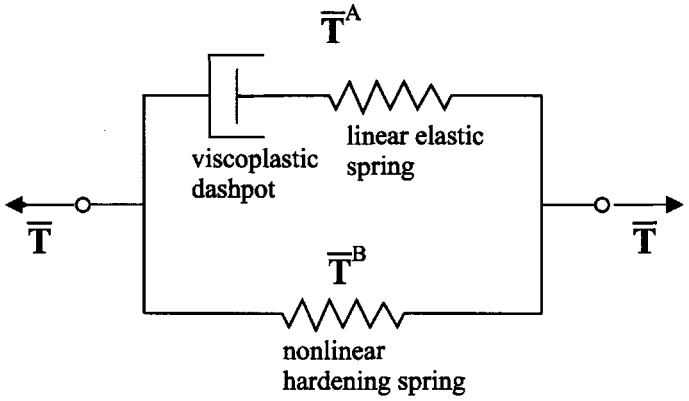

Figure 7-1: Schematic of the constitutive model for polymers with perfectly bonded rigid particles. $\overline{\mathbf{T}}^{A}$ and $\overline{\mathbf{T}}^{B}$ are the tensorial stress quantities which act on each leg in the three-dimensional implementation of the model.

7.1 Elasticity

The addition of perfectly bonded rigid particles increases the modulus of a polymer. The initial elastic resistance, $\overline{\mathbf{T}}^{A}$, is described by a fourth-order elasticity tensor derived from traditional multi-phase composite theory:

$$\overline{\mathbf{T}}^{A} = \frac{1}{\overline{J}^{e}} \overline{\mathscr{L}}^{e} \left[\overline{\mathbf{E}}^{e}\right], \tag{7.1}$$

with

$$\overline{\mathscr{L}}^{e} = 2\overline{\mu}\mathcal{I} + (\overline{\kappa} - 2/3\overline{\mu})\mathbf{1} \otimes \mathbf{1}, \tag{7.2}$$

where $\overline{\mu}$ and $\overline{\kappa}$, the effective shear modulus and bulk modulus, respectively, of the filled polymer, are functions of the properties and volume fractions of the individual phases. Anticipating Chapter 8, in which, with the introduction of debonded particles, there will be three distinct phases, we introduce notation slightly different from that of the previous chapters. The polymer matrix is termed the 0-th phase, with volume fraction c_0, and c_1 denotes the volume fraction of perfectly bonded particles. Assuming spherical particles and following Weng[78], whose analysis produces a result identical to the predictions of Mori and Tanaka [48], the effective elastic moduli

of the composite are taken to be

$$\overline{\kappa} = \kappa_0 + \frac{c_1\kappa_0}{\dfrac{3c_0\kappa_0}{3\kappa_0+4\mu_0} + \dfrac{\kappa_0}{\kappa_1-\kappa_0}} \tag{7.3}$$

and

$$\overline{\mu} = \mu_0 + \frac{c_1\mu_0}{\dfrac{6}{5}\dfrac{c_0(\kappa_0+2\mu_0)}{3\kappa_0+4\mu_0} + \dfrac{\mu_0}{\mu_1-\mu_0}}, \tag{7.4}$$

which, for $\mu_1 \gg \mu_0$ and $\kappa_1 \gg \kappa_0$, reduce to

$$\overline{\kappa} \approx \kappa_0 + \frac{c_1}{c_0}\left(\frac{3\kappa_0+4\mu_0}{3\kappa_0}\right)\kappa_0 \tag{7.5}$$

and

$$\overline{\mu} \approx \mu_0 + \frac{5c_1}{6c_0}\left(\frac{3\kappa_0+4\mu_0}{\kappa_0+2\mu_0}\right)\mu_0. \tag{7.6}$$

7.2 Viscoplastic Flow

The addition of perfectly bonded rigid particles elevates the yield strength of a polymer. The incompressible plastic flow in the dashpot in Figure 7-1 is derived from a plastic strain rate potential of the form

$$\hat{\Phi} = \frac{\sqrt{2}\dot{\nu}_0\overline{s}_0}{1/m+1}\left(\frac{\overline{\tau}^{\mathrm{A}}}{\overline{s}_0}\right)^{1/m+1}, \tag{7.7}$$

where $\dot{\nu}_0$ and m are the matrix constants defined in Chapter 4, $\overline{s}_0$ is the effective shear strength of the composite, and $\overline{\tau}^{\mathrm{A}}$ is the effective shear stress in network A of the composite.

There have been numerous theories and models developed to predict the effective properties of nonlinear composites. Nearly all overestimate the increase in flow stress exhibited with increasing volume fraction of perfectly bonded spherical fillers. Of the

models surveyed, Suquet's modified secant method [67] provides the best fit with the micromechanical modeling results of Chapter 5. Its derivation and the assumptions behind its application are briefly summarized below.

In all secant methods, the N-phase nonlinear composite is replaced by a linear comparison composite whose modulus at every point in the overall deformation is equal to the secant modulus of the nonlinear composite. The constitutive relation in each phase of the nonlinear composite is written

$$\mathbf{T}^{(r)}(\mathbf{x}) = \mathcal{L}_s{}^{(r)}(\mathbf{E}^{(r)})\mathbf{E}^{(r)}(\mathbf{x}), \tag{7.8}$$

where $\mathcal{L}_s{}^{(r)}(\mathbf{E}^{(r)})$ is the secant stiffness tensor in phase r. In the linear comparison composite, an "effective strain," $\mathbf{E}^{(r)}_{\text{eff}}$, is defined to approximate the main features of the strain field in phase r. The secant stiffness tensor of each phase in the linear comparison composite is thus taken to be independent of position at a given macroscopic strain, $\overline{\mathbf{E}}$:

$$\mathcal{L}^{(r)} \equiv \mathcal{L}_s{}^{(r)}(\mathbf{E}^{(r)}_{\text{eff}}). \tag{7.9}$$

The constitutive relation becomes

$$\mathbf{T}^{(r)} = \mathcal{L}^{(r)}\mathbf{E}^{(r)}_{\text{eff}}. \tag{7.10}$$

The effective strain in each phase is a function of the macroscopic strain and $\mathcal{L}^{(r)}|_{r=1,N}$. An appropriate linear predictive scheme is then used to compute the effective stiffness of the linear comparison composite,

$$\overline{\mathcal{L}} = \overline{\mathcal{L}}(c_r,\ \mathcal{L}^{(r)}|_{r=1,N}), \tag{7.11}$$

and the macroscopic constitutive law becomes

$$\overline{\mathbf{T}} = \overline{\mathcal{L}}\overline{\mathbf{E}}, \tag{7.12}$$

where $\overline{\mathcal{L}}$ depends on $\overline{\mathbf{E}}$ through $\mathbf{E}_{\text{eff}}^{(r)}$ and $\mathcal{L}^{(r)}$.

An effective strain measure that turns out to capture the nature of the strain distribution in many composites is the second-order moment (or root mean square) of the strain field,

$$\hat{E}_{\text{eq}}^{(r)} = \left\langle {E_{\text{eq}}}^2 \right\rangle_r^{1/2}, \tag{7.13}$$

where E_{eq} is the Mises equivalent strain and $\langle\ .\ \rangle_r$ indicates the spatial average over the volume of the r-th phase. This measure is more sensitive to variations in the strain field than the conventional mean strain, $\langle E_{\text{eq}} \rangle_r$, and thus simulates more accurately the effect that local concentrations of strain have on a composite's yield strength. From the result of Kreher [41] and Buryachenko [16], the second-order moment of the strain in the linear comparison composite is calculated from the overall stiffness of the composite:

$$\hat{E}_{\text{eq}}^{(r)} = \left(\frac{1}{3c_r} \overline{\mathbf{E}} \frac{\partial \overline{\mathcal{L}}}{\partial \mu_r} \overline{\mathbf{E}} \right)^{1/2}, \tag{7.14}$$

where $\mu_r = \dfrac{T_{\text{eq}}^{(r)}}{3\hat{E}_{\text{eq}}^{(r)}}$ is the secant shear modulus of phase r. Following Suquet [68], the rigid particle-modified polymer is approximated as a two-phase composite comprised of incompressible power-law materials with the same exponent, m, and yield strain, ϵ_{y}, but different yield strengths, $\sigma_{\text{y}}^{(r)}$:

$${T_{\text{eq}}}^{(0)} = \sigma_{\text{y}}^{(0)} \left(\frac{\hat{E}_{\text{eq}}^{(0)}}{\epsilon_{\text{y}}} \right)^m \tag{7.15}$$

and

$${T_{\text{eq}}}^{(1)} = \sigma_{\text{y}}^{(1)} \left(\frac{\hat{E}_{\text{eq}}^{(1)}}{\epsilon_{\text{y}}} \right)^m. \tag{7.16}$$

The problem thus reduces to a nonlinear scalar equation of the form

$$\frac{\hat{E}_{\mathrm{eq}}^{(1)}}{\hat{E}_{\mathrm{eq}}^{(0)}} = \left(\frac{c_0}{c_1} \frac{\frac{\partial \overline{\mu}}{\partial \mu_1}}{\frac{\partial \overline{\mu}}{\partial \mu_0}} \right)^{1/2}, \qquad \frac{\mu_1}{\mu_0} = \frac{\sigma_{\mathrm{y}}^{(1)}}{\sigma_{\mathrm{y}}^{(0)}} \left(\frac{\hat{E}_{\mathrm{eq}}^{(1)}}{\hat{E}_{\mathrm{eq}}^{(0)}} \right)^{m-1}. \tag{7.17}$$

Using the Hashin-Shtrikman [34] lower bound (for isotropic phases) form of the expression for $\overline{\mu}$, the energy balance,

$$\overline{\mu} \overline{E}_{\mathrm{eq}}{}^2 = c_0 \mu_0 \left(\hat{E}_{\mathrm{eq}}^{(0)} \right)^2 + c_1 \mu_1 \left(\hat{E}_{\mathrm{eq}}^{(1)} \right)^2, \tag{7.18}$$

and taking the particles to be rigid, $\hat{E}_{\mathrm{eq}}^{(1)} = E_{\mathrm{eq}}^{(1)} = 0$, the macroscopic deviatoric stress becomes

$$\overline{\mathbf{T}}' = \frac{2}{3} \frac{\overline{\sigma}_{\mathrm{y}}}{\epsilon_{\mathrm{y}}} \left(\frac{\overline{E}_{\mathrm{eq}}}{\epsilon_{\mathrm{y}}} \right) \overline{\mathbf{E}}', \tag{7.19}$$

with

$$\overline{\sigma}_{\mathrm{y}} = \sigma_{\mathrm{y}}^{(0)} \frac{\left(1 + \frac{3}{2} c_1\right)^{\frac{m+1}{2}}}{(1 - c_1)^m}. \tag{7.20}$$

The polymer matrix is approximated as rigid-plastic (m=0), and, in Equation 7.7, the effective shear strength of the reinforced polymer is taken to be

$$\overline{s}_0 = s_0 \left(1 + \frac{3}{2} c_1 \right)^{\frac{1}{2}}. \tag{7.21}$$

Analogous to Section 4.2.2, the incompressible plastic stretching is calculated as

$$\overline{\mathbf{D}}^{\mathrm{p}} = \frac{\partial \hat{\Phi}}{\partial \overline{\mathbf{T}}^{\mathrm{A}}} = \dot{\gamma}^p \mathbf{N}, \tag{7.22}$$

with the plastic shear strain rate given by

$$\dot{\gamma}^{\mathrm{p}} = \dot{\nu}_0 \left(\frac{\overline{\tau}^{\mathrm{A}}}{\overline{s}_0} \right)^{1/m}. \tag{7.23}$$

7.3 Strain Hardening

In order to capture the increase in rate of orientation hardening with the addition of rigid filler particles, a strategy of strain amplification was utilized. The concept of strain amplification has traditionally been used to predict the behavior of particle-filled elastomers. It was first introduced by Mullins and Tobin [49] who, for the case of uniaxial loading, amplified the axial stretch in the constitutive law of the matrix by a factor dependent on the volume fraction of filler. Bergstrom and Boyce [11] amplified the first invariant of the stretch, $I_1 = (\lambda_1^2 + \lambda_2^2 + \lambda_3^2)$, considered to be a reasonable scalar measure of the overall strain, and inserted it into the I_1-based strain energy density function of the matrix in place of I_1. The amplification factor,

$$X_S = \frac{\langle I_1 \rangle_0 - 3}{\overline{I}_1 - 3}, \tag{7.24}$$

where $\langle I_1 \rangle_0$ is the average I_1 in the matrix phase and $\overline{I}_1$ is the macroscopic I_1, was estimated from the Smallwood [62], Guth-Gold [30, 29], and Guth [29] composite modulus predictions. The Bergstrom-Boyce model accurately predicts to large strains the behavior of particle-filled elastomers under uniaxial and multiaxial stress states.

The methodology of Bergstrom and Boyce was used to calculate the stress in network B. The strain energy density function of network B of the composite is taken to be

$$\overline{W}_B = (1 - c_1) \langle W_B \rangle_0 , \tag{7.25}$$

where the average strain energy density of the matrix, $\langle W_B \rangle_0$, is evaluated via the amplification scheme. Amplification factors based on two strain measures were considered: $\langle I_1 \rangle_0$ and the second-order moment of the matrix I_1, $\langle {I_1}^2 \rangle_0^{1/2}$.

With a neo-Hookean matrix, in terms of $\langle I_1 \rangle_0$, the strain energy density function of network B becomes

$$\overline{W}_B = (1 - c_1) \left\{ \frac{\mu_R}{2} \left[\langle I_1 \rangle_0 - 3 \right] - \mu_R \ln \overline{J} + \frac{\overline{\kappa}_B}{2} \left[\overline{J} - 1 \right]^2 \right\}, \tag{7.26}$$

with

$$\langle I_1 \rangle_0 = X_S(\overline{I}_1 - 3) + 3, \tag{7.27}$$

where μ_R is the initial hardening modulus of the matrix, $\overline{J} = \det\overline{\mathbf{F}}$ $(= \overline{J}^e)$, and $\overline{\kappa}_B$ is the bulk modulus of network B. The stress in network B,

$$\overline{\mathbf{T}}_B = \frac{2}{\overline{J}}\frac{\partial \overline{W}_B}{\partial \overline{I}_1}\overline{\mathbf{B}} + \frac{\partial \overline{W}_B}{\partial \overline{J}}\mathbf{1}, \tag{7.28}$$

is then

$$\overline{\mathbf{T}}_B = (1 - c_1)\left\{\frac{\mu_R}{\overline{J}}\left[X_S\overline{\mathbf{B}} - \mathbf{1}\right] + \overline{\kappa}_B\left[\overline{J} - 1\right]\right\}, \tag{7.29}$$

where $\overline{\mathbf{B}} = \overline{\mathbf{F}}\overline{\mathbf{F}}^T$, and the bulk response is lumped entirely into network A, giving $\overline{\kappa}_B = 0$. Neglecting the (small) elastic strains, the initial tensile modulus of network B is $\overline{E} = X_S\,(1 - c_1)\,E_0$. Drawing comparison with the frequently cited Guth-Gold model, which predicts $\overline{E} = (1 + 2.5c_1 + 14.1c_1^2)\,E_0$ for a composite with well dispersed rigid spheres, the first candidate for amplification factor was analytically predicted to be

$$X_S = 1 + 3.5c_1 + 17.6{c_1}^2. \tag{7.30}$$

Single-particle and multi-particle micromechanical simulations were conducted with perfectly bonded (PB) rigid particles and a matrix constitutive response described by the parallel model of Boyce et al. [13] with neo-Hookean strain hardening. The average over the matrix phase of the first stretch invariant, $\langle I_1 \rangle_0$, was extracted from the simulations as a function of the applied macroscopic stretch, $\overline{I}_1$, and X_S was computed from Equation 7.24. Figure 7-2 displays the analytical predictions for X_S of Equation 7.30 together with the predictions for X_S of both staggered array (SA) and six-particle RVE's plotted versus the generalized strain measure $(\overline{I}_1/3)^{1/2}$. At each c_1, the results of at least three multi-particle simulations are shown. With

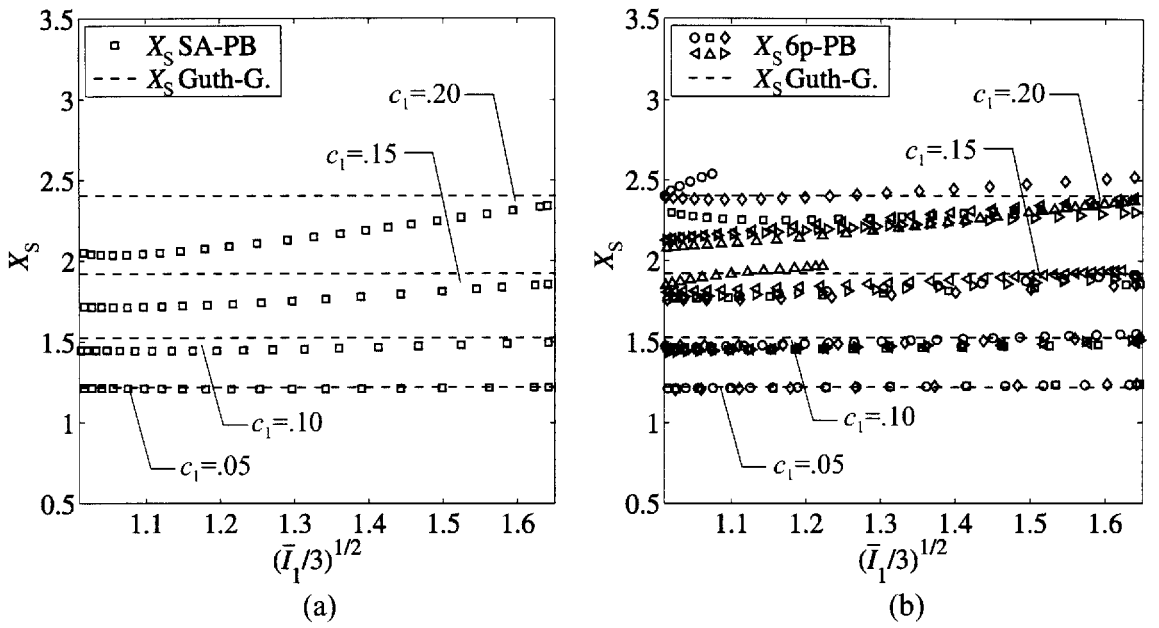

Figure 7-2: Mean strain amplification factors, $X_S = (\langle I_1 \rangle_0 - 3) / (\bar{I}_1 - 3)$, extracted from micromechanical models under uniaxial tension and, $X_S = 1 + 3.5c_1 + 17.6c_1^2$, used in the constitutive model: (a) Staggered array (SA) perfect bonding (PB) RVE's, (b) 6-particle PB RVE's.

the SA-PB RVE, the analytical predictions for X_S show good agreement with the micromechanical predictions at $c_1 = 0.05$ and $c_1 = 0.10$ but fall substantially short of the micromechanical results at the higher volume fractions of filler. The mean multi-particle RVE predictions are very similar to the predictions of the SA RVE at the two lower volume fractions of filler, but, agreeing fairly well with the analytical predictions, the multi-particle RVE predictions exceed those of the SA RVE at $c_1 = 0.15$ and $c_1 = 0.20$. Moving from the perfect dispersion of the SA RVE to the more realistic (but good) dispersion of the multi-particle RVE's has the effect, as Guth [29] predicted, of increasing the degree of strain amplification. X_S of Equation 7.30 is thus taken to provide an acceptable representation of the $\langle I_1 \rangle_0$-based strain amplification factor.

In terms of $\langle I_1^2 \rangle_0^{1/2}$, the root mean square of the first stretch invariant of the

matrix, the strain energy density function of network B becomes

$$\overline{W}_{\mathrm{B}} = (1-c_1)\left\{\frac{\mu_{\mathrm{R}}}{2}\left[\left\langle {I_1}^2\right\rangle_0^{1/2} - 3\right]\right] - \mu_{\mathrm{R}}\ln\overline{J} + \frac{\overline{\kappa}_{\mathrm{B}}}{2}\left[\overline{J}-1\right]^2\right\}, \tag{7.31}$$

with

$$\left\langle {I_1}^2\right\rangle_0^{1/2} = \hat{X}_{\mathrm{S}}\left(\overline{I}_1 - 3\right) + 3, \tag{7.32}$$

and the stress in network B, with $\overline{\kappa}_{\mathrm{B}} = 0$, is

$$\overline{\mathbf{T}}_{\mathrm{B}} = (1-c_1)\left\{\frac{\mu_{\mathrm{R}}}{\overline{J}}\left[\left(\hat{X}_{\mathrm{S}} + (\overline{I}_1 - 3)\frac{\partial \hat{X}_{\mathrm{S}}}{\partial \overline{I}_1}\right)\overline{\mathbf{B}} - \mathbf{1}\right] + \overline{\kappa}_{\mathrm{B}}\left[\overline{J}-1\right]\right\}. \tag{7.33}$$

Analogous to the second-order moment of the strain presented in the previous section, $\hat{X}_{\mathrm{S}}$ gives more weight to heterogeneous strain fields than X_{S}.

Figure 7-3 shows the values of $\hat{X}_{\mathrm{S}}$ extracted from the micromechanical simulations. Initially, with both types of RVE, $\hat{X}_{\mathrm{S}}$ is approximately equal to X_S. As $(\overline{I}_1/3)^{1/2}$ increases, however, the micromechanical predictions of $\hat{X}_{\mathrm{S}}$ increase at an approximately linear rate. The rate of increase is proportional to the volume fraction of filler, an indication that the strain field becomes less uniform with increasing c_1. The slopes of the SA and multi-particle RVE predictions are approximately equal. For use in the constitutive model, an analytical expression for $\hat{X}_{\mathrm{S}}$ was fit to the mean multi-particle RVE predictions. Plotted in Figure 7-3, it takes the form

$$\hat{X}_{\mathrm{S}} = X_{\mathrm{S}} + 53.8c_1^2\left[\left(\overline{I}_1/3\right)^{1/2} - 1\right]. \tag{7.34}$$

The analytical prediction of X_{S} should be a general result for in its derivation no assumptions were made about the matrix other than that it is much softer than the particles. In order to validate this assertion and demonstrate the applicability of $\hat{X}_{\mathrm{S}}$ in the form of Equation 7.34 to other matrix behaviors, the effect of increasing the initial hardening modulus of the matrix, μ_{R}, on X_{S} and $\hat{X}_{\mathrm{S}}$ is shown in Figure 7-4 for a $c_1 = 0.15$, six-particle RVE loaded in uniaxial tension. Increasing μ_{R} has virtually

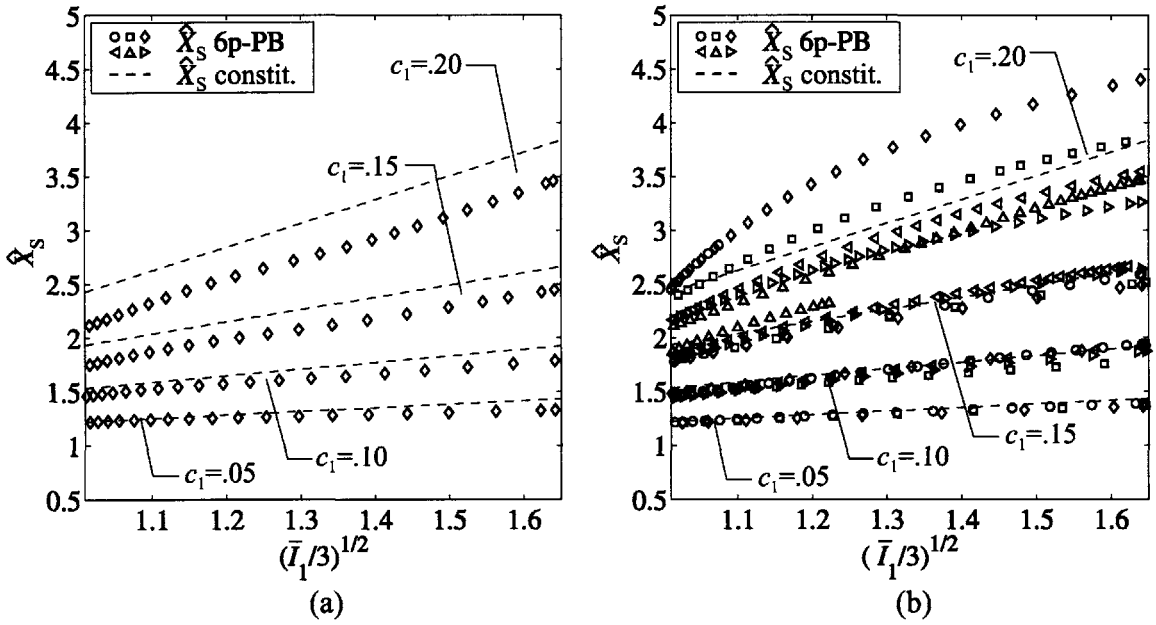

Figure 7-3: Second-order strain amplification factors, $\hat{X}_S = \left(\langle I_1^2\rangle_0^{1/2} - 3\right) / \left(\bar{I}_1 - 3\right)$, extracted from micromechanical models under uniaxial tension and, $\hat{X}_S = X_S + 53.8c_1^2\left[\left(\bar{I}_1/3\right)^{1/2} - 1\right]$, used in the constitutive model: (a) SA-PB RVE's, (b) 6-particle PB RVE's.

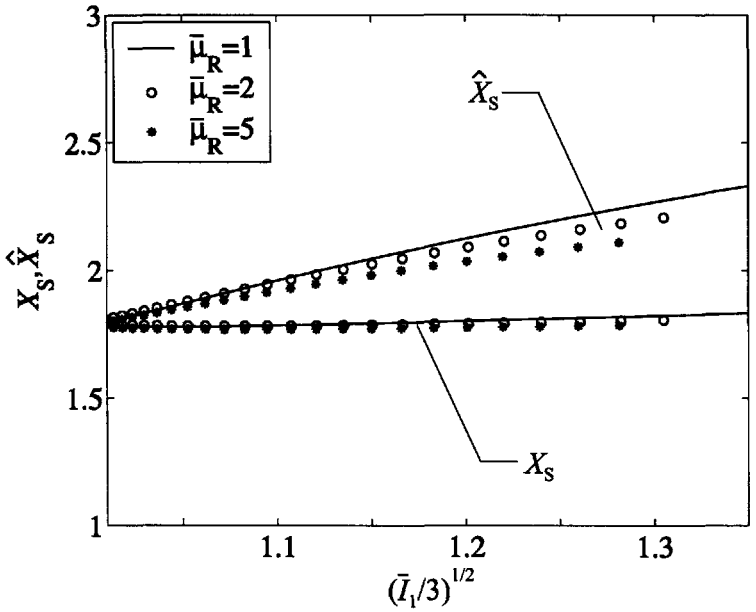

Figure 7-4: Strain amplification factors extracted from $c_1 = 0.15$, 6-particle RVE's under uniaxial tension as a function of the normalized initial hardening modulus of the matrix, $\overline{\mu}_R$.

no effect on X_S but does decrease $\hat{X}_S$ slightly. As shown in Section ??, for the case of particles without bonding, elevating the rate of matrix strain hardening causes the deformation to be increasingly homogeneous. $\hat{X}_S$ is thus a weak function of the matrix behavior but is still a reasonably general expression.

7.4 Results

The predictions of the constitutive model with $\overline{T}_B$ defined in terms of X_S (Equation 7.29) are plotted versus the median predictions of the multi-particle RVE's for the case of uniaxial tension in Figure 7-5. The constitutive model predictions show excellent agreement with the modulus and yield strength predictions of the micromechanical simulations. The constitutive model rate of strain hardening, however, becomes increasingly deficient as the strain and volume fraction of filler increase.

The predictions of the constitutive model with $\overline{T}_B$ defined in terms of $\hat{X}_S$ (Equation 7.33) are plotted versus the median predictions of the multi-particle RVE's for

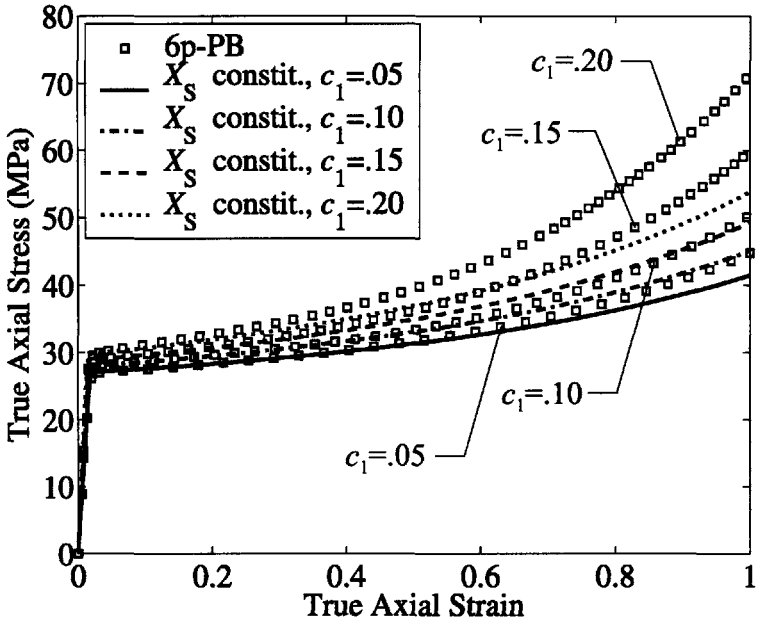

Figure 7-5: X_S-amplification constitutive model predictions versus 6-particle PB RVE macroscopic predictions for uniaxial tension: macroscopic true axial stress versus true axial strain.

the case of uniaxial tension in Figure 7-6. In this form, the constitutive model exhibits excellent agreement with the micromechanical simulations at all strains and volume fractions of filler. Clearly, this is the more accurate model. By emphasizing the heterogeneity of the strain field, it provides a representation of the state of deformation in the matrix superior to that of the model based on the mean matrix I_1. Figures 7-7 and 7-8 illustrate that the $\hat{X}_S$-amplification constitutive model is also highly accurate under triaxial states of stress and plane strain tension, respectively.

Figure 7-9 demonstrates the validity of applying the $\hat{X}_S$-amplification constitutive model to polymers with higher rates of strain hardening. As μ_R increases, the constitutive model predictions exceed those of the multi-particle RVE's by increasing amounts, but the agreement is still impressive.

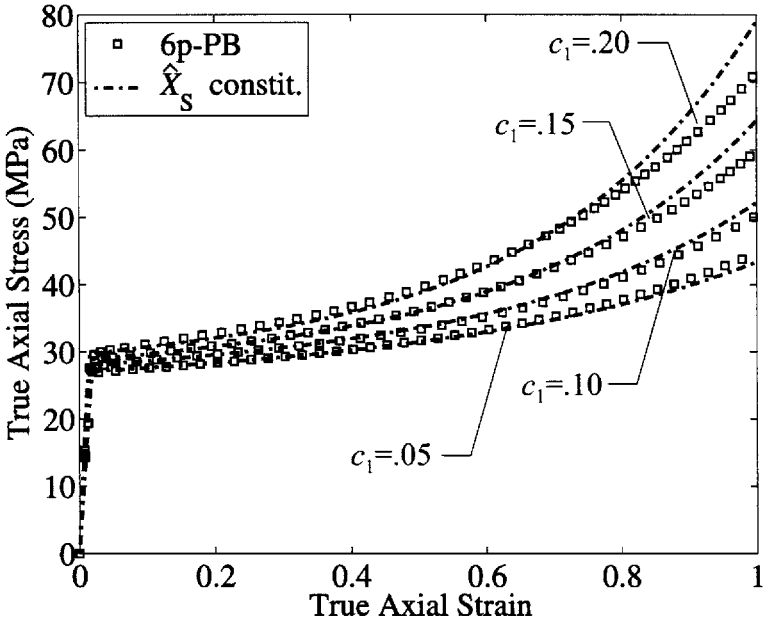

Figure 7-6: $\hat{X}_S$-amplification constitutive model predictions versus 6-particle PB RVE macroscopic predictions for uniaxial tension: macroscopic true axial stress versus true axial strain.

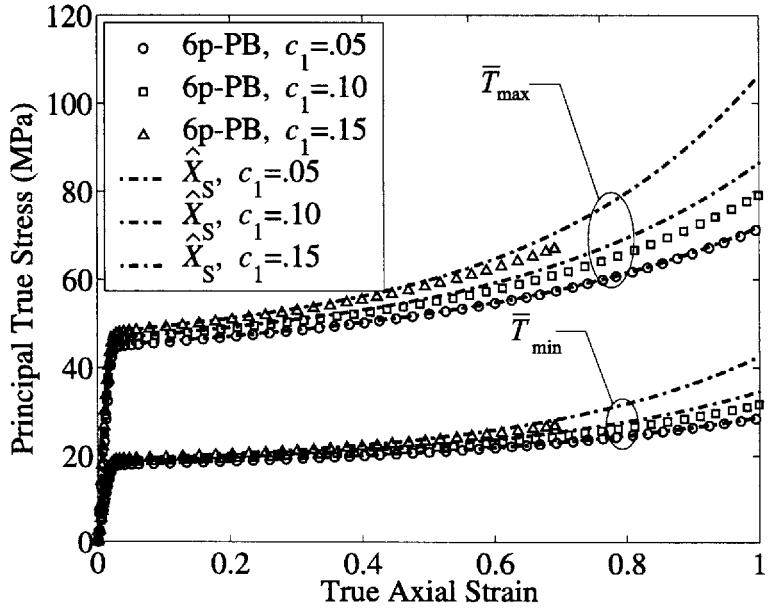

Figure 7-7: $\hat{X}_S$-amplification constitutive model predictions versus 6-particle PB RVE macroscopic predictions for axisymmetric triaxial tension, $X = 1.0$: macroscopic principal true stress versus true axial strain.

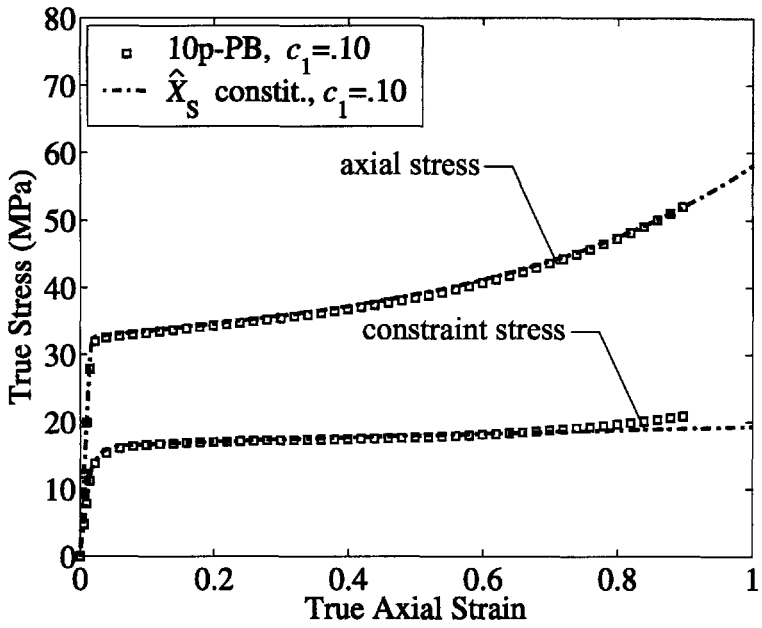

Figure 7-8: $\hat{X}_S$-amplification constitutive model predictions versus 10-particle PB RVE macroscopic predictions at $c_1 = 0.10$ for plane strain tension: macroscopic principal true stress versus true axial strain.

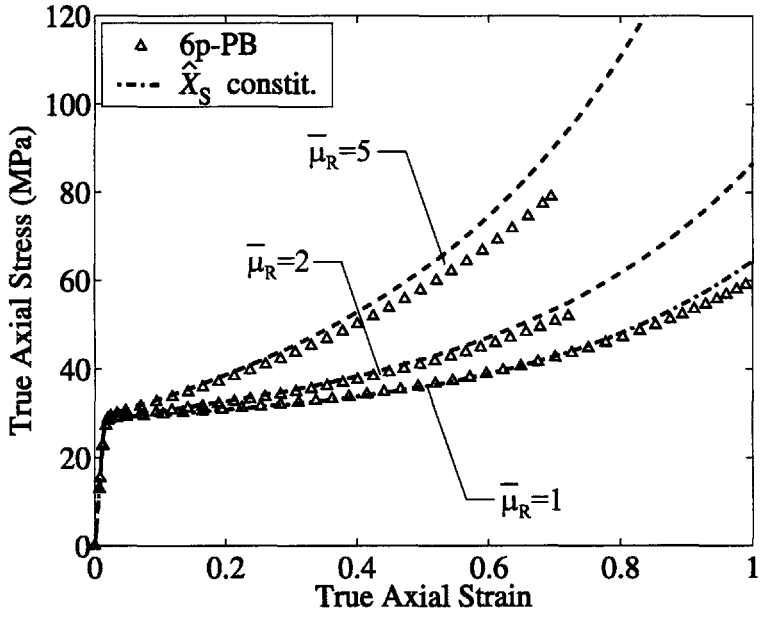

Figure 7-9: $\hat{X}_S$-amplification constitutive model predictions versus 6-particle PB RVE macroscopic predictions as a function of the normalized initial hardening modulus of the matrix, $\bar{\mu}_R$ for uniaxial tension at $c_1 = 0.15$: macroscopic true axial stress versus true axial strain.

7.5 Conclusions

The $\hat{X}_S$-amplification model accurately predicts the major aspects of the deformation of a polymer modified with perfectly bonded rigid particles. By utilizing second-order moments of the strain fields, it is able to capture the sizeable effects that local concentrations of deformation have on the macroscopic behavior of the composite. Furthermore, it is accurate under both uniaxial and multiaxial states of stress, and, only faintly dependent on the matrix rate of strain hardening, it is relevant to the behavior of many ductile polymers containing approximately spherical, well-dispersed rigid particles that do not debond.

Chapter 8

Constitutive Modeling of Polymers with Debonding Rigid Particles

In the penultimate chapter of this thesis, a constitutive model for the tensile loading ($X > 1/3$) of polymers modified with potentially debonding rigid particles is presented. The CC-filled HDPE experiments of Chapter 3 and the micromechanical simulations of Chapters 5 and 6 dictate the features of deformation which must be accounted for. Relative to both the unfilled polymer and the polymer with perfectly bonded rigid particles, a polymer with debonded rigid particles exhibits:

- a decrease in elastic stiffness
- a decrease in flow stress
- a reduction in rate of strain hardening
- an increase in volumetric strain due to void growth around the particles

The model is implemented as an approximate extension of the model for polymers with perfectly bonded rigid particles presented in the previous chapter. When the particles do not debond, the predictions of the two models are virtually identical.

When particle debonding occurs, the polymer composite may consist of up to three phases: matrix (phase-0), perfectly bonded particles (phase-1), and debonded particles (phase-2). As depicted in Figure 8-2, the volume fraction of each phase,

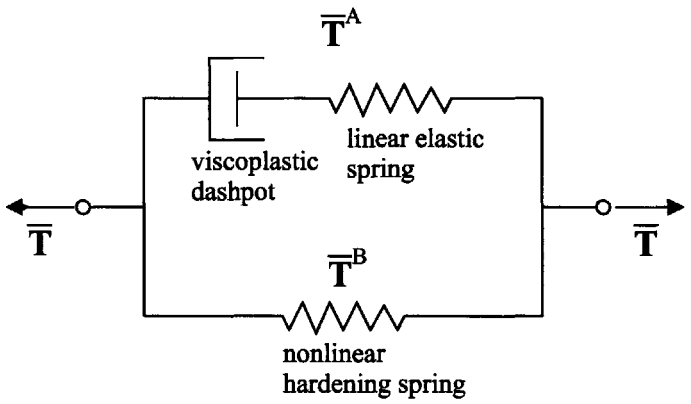

Figure 8-1: Schematic of the constitutive model for polymers with potentially debonding rigid particles. $\overline{\mathbf{T}}^A$ and $\overline{\mathbf{T}}^B$ are the tensorial stress quantities which act on each leg in the three-dimensional implementation of the model.

relative to the initial volume of the composite, is denoted respectively, by c_0, c_1, and c_2. In the constitutive model, all or a portion of the particles may be specified as initially debonded, or they may debond during the deformation. The initial volume fraction of particles, whether debonded or perfectly bonded, is denoted f_0. An additional variable which will be frequently cited in this chapter is the fraction of debonded particles, $c_d \equiv c_2/(1 - f_0)$.

The overlying structure of the model, identical to that of the model for polymers with perfectly bonded rigid particles, is illustrated in Figure 8-1. As in the preceding chapter, the bars over the tensors identify them as macroscopic quantities representative of the composite as a whole.

8.1 Elasticity

The SA micromechanical predictions of Sections 5.3.1 and 6.1.1 show that, under uniaxial tension, once debonding initiates at the pole of the particle, it quickly progresses around the majority of the surface of the particle. As illustrated in Figure 6-7b, increasing the macroscopic stress triaxiality ratio, X, hastens the debonding process. Furthermore, the multi-particle micromechanical models of Section 5.3.1, lacking the perfect symmetry and thus artificial constraint at the particle equator of the SA

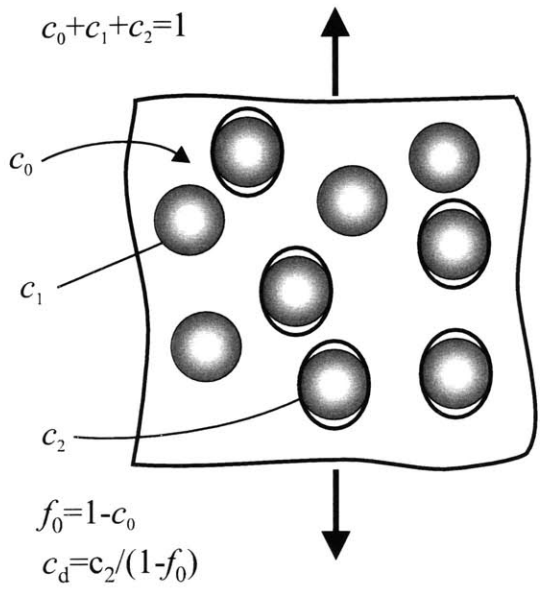

Figure 8-2: Definition of phase volume fractions, c_r, and the fraction of debonded particles, c_d.

RVE, exhibit nearly instantaneous, complete debonding. Taken together, these observations are sufficient reason to treat a debonded particle as *completely* debonded once the debonding criterion is met. Thus, the three-phase composite is isotropic, and the initial elastic resistance, $\overline{\mathbf{T}}^{\mathrm{A}}$, is described by a fourth-order elasticity tensor derived from classic multi-phase composite analysis:

$$\overline{\mathbf{T}}^{\mathrm{A}} = \frac{1}{\overline{J}^{\mathrm{e}}} \overline{\mathscr{L}}^{\mathrm{e}} \left[\overline{\mathbf{E}}^{\mathrm{e}} \right], \tag{8.1}$$

with

$$\overline{\mathscr{L}}^{e} = 2\overline{\mu}\mathcal{I} + (\overline{\kappa} - 2/3\overline{\mu})\mathbf{1} \otimes \mathbf{1}, \tag{8.2}$$

where $\overline{\mu}$ and $\overline{\kappa}$, the effective shear modulus and bulk modulus, respectively, of the filled polymer, are functions of the properties and volume fractions of the individual phases.

For a given matrix material, the bulk response of a composite with voids is identical to that of a composite with debonded particles. Assuming spherical particles and

following Weng [78], who utilizes Eshelby's [24] equivalent inclusion method, Hill's [37] stress concentration tensor, and the Mori and Tanaka [48] concept of average matrix stress, the effective bulk modulus of a composite with perfectly bonded rigid particles and voids is predicted to be

$$\overline{\kappa} = \kappa_0 + \frac{a}{1 - \alpha_0 a}\kappa_0, \tag{8.3}$$

where

$$a = \frac{c_1 (\kappa_1 - \kappa_0)}{\alpha_0 (\kappa_1 - \kappa_0) + \kappa_0} - \frac{c_2}{(1 - \alpha_0)} \quad \text{and} \quad \alpha_0 = \frac{3\kappa_0}{3\kappa_0 + 4\mu_0}. \tag{8.4}$$

For $\frac{\kappa_1}{\kappa_0} \gg 1$,

$$a \approx \frac{c_1}{\alpha_0} - \frac{c_2}{(1 - \alpha_0)}. \tag{8.5}$$

The corresponding solution for the effective shear modulus is

$$\overline{\mu} = \mu_0 + \frac{b}{1 - \beta_0 b}\mu_0, \tag{8.6}$$

where, for $\frac{\mu_1}{\mu_0} \gg 1$,

$$b \approx \frac{c_1}{\beta_0} - \frac{c_2}{(1 - \beta_0)} \quad \text{and} \quad \beta_0 = \frac{6}{5}\frac{\kappa_0 + 2\mu_0}{3\kappa_0 + 4\mu_0}. \tag{8.7}$$

Subject to types of loading other than hydrostatic tension, however, a polymer with voids and the same polymer with debonded particles deform differently. Under uniaxial tension, for example, debonded rigid particles impede contraction in the two lateral directions and, as witnessed in the micromechanical simulations of Chapter 5 (see Tables 5.1 and 5.2), degrade, relative to the homopolymer, the elastic modulus slightly less than voids. The effect of the debonded particles must be accounted for when determining the second independent elastic constant. In an analysis similar to that of Weng, but in component form, Mochida et al. [47] subject an infinite composite

body containing perfectly bonded rigid particles and debonded rigid particles to a state of uniaxial tension in the 3-direction. Utilizing $T_{33}^{(2)} = 0$, $E_{11}^{(1)} = 0$, $E_{22}^{(1)} = 0$, and the form of the strain energy derived by Taya and Chou [70], the effective Young's modulus of a composite with perfectly bonded and debonded rigid particles is found to be

$$\overline{E} = \frac{1}{1 + c_1 \eta_p^{III} + c_2 \eta_3} E_0, \tag{8.8}$$

where η_p^{III} and η_3, given in Appendix B3 of Reference [47], are functions of the volume fractions and properties of the individual phases. $\overline{\mu}$ is trivially calculated from Equations 8.3 and 8.8.

Figure 8-3 shows the constitutive model elastic predictions compared with the elastic predictions of multi-particle RVE's for the case of uniaxial tension. In Figure 8-3a, the constitutive model with Equations 8.3 and 8.8 accurately captures the enhancement in effective modulus when the particles are all perfectly bonded ("PB", $c_d = 0$) and the degradation in effective modulus when the particles are all initially debonded ("NB", $c_d = 1$). The analytical (using Equations 8.3 and 8.6) and micromechanical predictions for a composite containing voids are also given. It is apparent that Equation 8.8 provides a significantly more accurate representation of the degradation in modulus due to debonded rigid particles than Equation 8.6. In Figure 8-3b, the effective Poisson's ratios of the constitutive model show excellent agreement with those of the micromechanical models for the PB case but only fair agreement for the NB case. The NB constitutive model predictions, however, exhibit the correct trend and significantly better agreement with the NB micromechanical predictions than the analytical expression derived for voids.

Figure 8-4 displays the effective modulus predictions of the constitutive model as a function of the fraction of debonded particles, c_d, at three initial volume fractions of filler, f_0. The constitutive model predicts a nearly monotonic decrease in effective modulus with increasing c_d at each f_0.

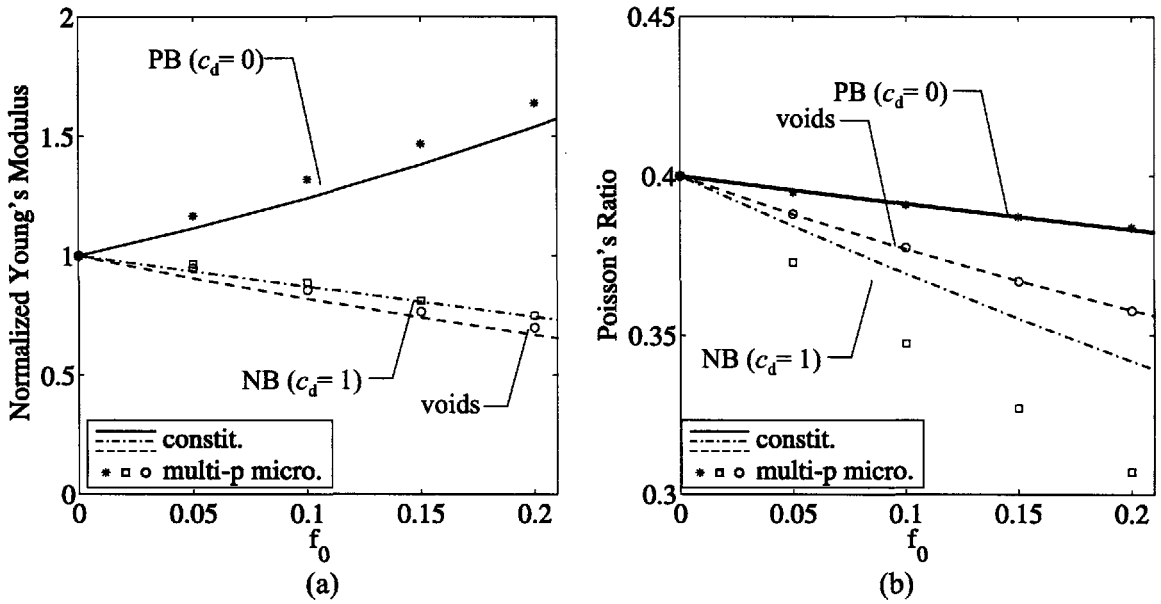

Figure 8-3: Elastic properties predicted by the constitutive and micromechanical models under uniaxial tension: (a) normalized effective Young's modulus, $\overline{E}/E_0$; (b) effective Poisson's ratio, $\overline{\nu}$.

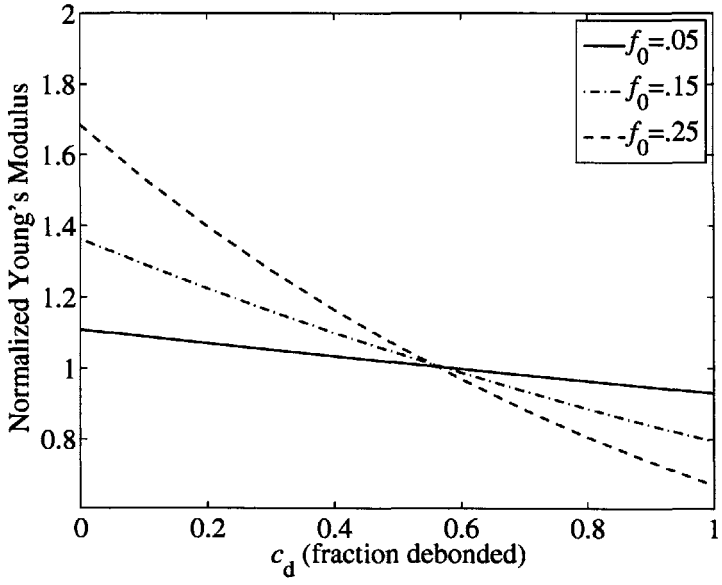

Figure 8-4: Normalized effective Young's modulus, $\overline{E}/E_0$, as a function of the volume fraction of debonded particles, c_d, at $f_0 = 0.05$, $f_0 = 0.15$, and $f_0 = 0.25$.

8.2 Viscoplastic Flow

The flow rule must be reformulated to reflect the reduction in flow stress due to debonded particles and the increase in volume due to void growth around debonded particles. A strategy developed to model porous metals and ceramics and used recently by Danielsson et al. [21] to model rubber-filled polycarbonate was found to meet these criteria.

Over the past several decades, a number of authors have proposed models to represent the behavior of power-law materials containing voids. For a dilute concentration of spherical voids in a non-hardening power-law matrix, Duva and Hutchinson [23] suggested a macroscopic plastic strain rate potential function of the form

$$\overline{\Phi} = F\left(X, f, m\right) \Phi\left(\overline{\tau}, m\right), \tag{8.9}$$

where X is the macroscopic stress triaxiality ratio, f is the current porosity, m is the strain rate sensitivity parameter of the matrix, and Φ is the plastic potential of the matrix. F represents the amplification of plastic flow due to the voids. The macroscopic plastic stretching for a porous material becomes

$$\overline{\mathbf{D}}^{\mathrm{p}} = \frac{\partial \overline{\Phi}}{\partial \overline{\mathbf{T}}} = \sqrt{\frac{2}{3}} \dot{\nu}_0 \left[\frac{3}{2} \left(F - \frac{F' X}{1/m + 1} \right) \frac{\operatorname{dev} \overline{\mathbf{T}}}{\sqrt{3}\, \overline{\tau}} + \frac{F'}{3\left(1/m + 1\right)} \mathbf{1} \right] \left(\frac{\overline{\tau}}{s_0} \right)^{1/m}, \tag{8.10}$$

where the prime denotes the derivative with respect to X. In order for $\overline{\Phi}$ to be convex, F must satisfy the condition (Rodin and Parks [60])

$$F F'' - \frac{1}{m+1} F'^2 > 0. \tag{8.11}$$

In successfully extending this formalism to materials with non-dilute porosity, various authors, including Duva and Crow [22], Haghi and Anand [33], Sofronis and McMeeking [66], and Michel and Suquet [46] have suggested convex functions F of

the form

$$F = A_1 + \left(A_2 X^2 + A_3\right)^{\frac{1/m+1}{2}}, \tag{8.12}$$

where $A_i = \hat{A}_i\left(f, m\right)$. F essentially interpolates between the behaviors at $X = 0$ and $X \to \infty$.

In the application of this framework to polymers containing debonded rigid particles, a debonded particle is considered to be a void. The current porosity f is due to the volume of the debonded particles themselves plus the ensuing void growth that occurs at the debonded particles' surfaces. For the general case, when an arbitrary fraction of the particles have debonded, the composite is conceptualized as a material with a volume fraction of voids f embedded in a matrix with a volume fraction of perfectly bonded particles $c_1/(1-c_2)$. The plastic potential is therefore taken to be

$$\overline{\Phi} = F\left(X^{\mathrm{A}}, f, m\right)\hat{\Phi}\left(\overline{\tau}^{\mathrm{A}}, m\right), \tag{8.13}$$

where $X^{\mathrm{A}} = \dfrac{\overline{T}^{\mathrm{A}}_{\mathrm{m}}}{\overline{T}^{\mathrm{A}}_{\mathrm{eq}}}$ is the stress triaxiality ratio of the stress in network A, the stress driving plastic flow, and $\hat{\Phi}$ is the plastic potential (Equation 7.7) of a polymer containing a volume fraction of perfectly bonded rigid particles $c_1/(1-c_2)$. The flow rule becomes

$$\overline{\mathbf{D}}^{\mathrm{p}} = \frac{\partial\overline{\Phi}}{\partial\overline{\mathbf{T}}^{\mathrm{A}}} = \sqrt{\frac{2}{3}}\dot{\nu}_0\left[\frac{3}{2}\left(F - \frac{F'X^{\mathrm{A}}}{1/m+1}\right)\frac{\operatorname{dev}\overline{\mathbf{T}}^{\mathrm{A}}}{\sqrt{3}\,\overline{\tau}^{\mathrm{A}}}, + \frac{F'}{3\left(1/m+1\right)}\mathbf{1}\right]\left(\frac{\overline{\tau}^{\mathrm{A}}}{\overline{s}_0}\right)^{1/m} \tag{8.14}$$

with, due to the plastic incompressibility of the matrix, the evolution equation for f given by

$$\dot{f} = \left(1 - f - \frac{c_1}{\overline{J}^{\mathrm{p}}}\right)\operatorname{tr}\overline{\mathbf{D}}^{\mathrm{p}}, \tag{8.15}$$

where $\overline{J}^{\mathrm{p}}$ is the plastic volume change. An interpolation function F of the form of Equation 8.12 was assumed. Following Haghi and Anand, A_1 was set to unity. A_2 and

A_3 were determined from the results of multi-particle micromechanical simulations with debonded rigid particles.

Figure 8.17a presents, as a function of f, the macroscopic mean stress predictions of six-particle RVE's with debonded rigid particles when loaded in hydrostatic tension. The matrix constitutive behavior is specified by the parallel model of Boyce et al. [13] with neo-Hookean strain hardening. It is apparent, presumably due to the voids around the debonded particles remaining approximately spherical, that the hydrostatic response of the RVE's is predominantly a function of f and only weakly dependent on f_0. Following the aforementioned authors, A_2 was assumed to be a function solely of f and m. Under hydrostatic loading, $(X,\ X^{\mathrm{A}}) \rightarrow \infty$, the macroscopic volumetric plastic strain rate, $\overline{\dot{E}}^{\mathrm{p}}_{\mathrm{h}} = \dfrac{\partial \overline{\Phi}}{\partial \overline{T}^{\mathrm{A}}_{\mathrm{m}}}$ $(= \mathrm{tr}\ \overline{\mathbf{D}}^{\mathrm{p}})$, predicted by the constitutive model is given by

$$\overline{\dot{E}}^{\mathrm{p}}_{\mathrm{h}} = \sqrt{\frac{2}{3}}\dot{\nu}_0 A_2^{(1/m+1)/2}\left(\frac{\overline{T}^{\mathrm{A}}_{\mathrm{m}}}{\sqrt{3}\ \overline{s}_0}\right)^{1/m}. \tag{8.16}$$

The preceding authors chose

$$A_2 = \frac{9}{4}\left(\frac{m}{f^{-m}-1}\right)^{2/(1+m)} \tag{8.17}$$

such that Equation 8.16 reproduces the analytical solution for the volumetric strain rate of a thick-walled, hollow sphere of isotropic, incompressible, power-law viscoplastic material, subject to external hydrostatic loading. The analytical prediction is plotted in Figure 8.17b and shows reasonable agreement with the macroscopic mean stresses at initial yield exhibited by the multi-particle RVE's. Also plotted in Figure 8.17b is an alternative expression for A_2:

$$A_2 = \frac{1}{1-f^2}\left(7.5f - 22.1f^2 + 66.5f^3\right), \tag{8.18}$$

determined via a least-squares fit to the micromechanical predictions. While the analytical solution has the advantage of being valid for arbitrary strain rate sensitivities,

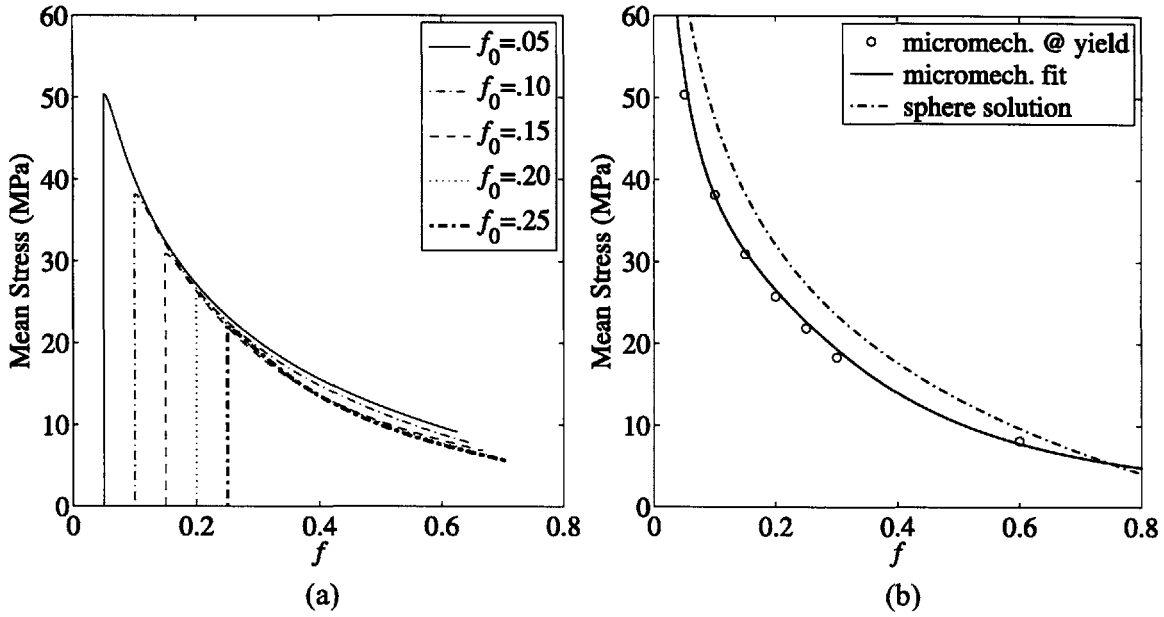

Figure 8-5: Determining A_2: (a) macroscopic mean stress predictions of multi-particle RVE's with debonded rigid particles under hydrostatic tension as a function of current void volume fraction, f; (b) constitutive model predictions using Equations 8.17 and 8.18 versus micromechanical predictions at macroscopic yield.

Equation 8.18 is used in the constitutive model due to its superior accuracy.

As the macroscopic stress triaxiality ratio decreases, the validity of assuming that the viscoplastic flow is a function only of f and the properties of the matrix is not obvious. As observed in the micromechanical modeling results of Chapters 5 and 6, at $X = 1/3$, the voids around debonded particles may take decidedly non-spherical shapes. Thus, the interpolation function F of a composite deformed at low to intermediate stress triaxiality ratio to a current porosity "f^{I}," would presumably differ from F of a composite with $f_0 = f^{\mathrm{I}}$ subject to an identical stress triaxiality ratio. Extraction of the macroscopic volumetric strain rate and the macroscopic equivalent plastic strain rate, $\dot{\bar{E}}^{\mathrm{p}}_{\mathrm{eq}} = \dfrac{\partial \bar{\Phi}}{\partial \bar{T}^{\mathrm{A}}_{\mathrm{eq}}}$, as function of f, from multi-particle micromechanical simulations show this f_0 dependency to exist, but the effect is surprisingly small, and it largely disappears at $X \geq 1$. All revealed in the micromechanical modeling results of Chapters 5 and 6, the causes are threefold:

1. The lateral compressive constraint of the particle limits the aspect ratios of the

voids.

2. Particle interactions cause lateral void expansion, in some cases even under uniaxial tension, further limiting the aspect ratios of the voids.

3. Plastic flow localizes within the axial interparticle ligaments while the material at the poles of the particles remains in the elastic regime, and the "effective" void volume fraction becomes greater than the actual f.

For these reasons, in addition to the attraction of its simplicity, the assumption was made that F is entirely a function of f and m.

Following Haghi and Anand and Sofronis and McMeeking, the function A_2 was fit to the initial macroscopic equivalent plastic strain rates, $\dot{\overline{E}}^{\mathrm{p}}_{\mathrm{eq}}$, exhibited by micromechanical models under purely deviatoric axisymmetric states of stress (e.g. $\overline{T}_{33} > \overline{T}_{11} = \overline{T}_{22}$). For arbitrary, finite X,

$$\dot{\overline{E}}^{\mathrm{p}}_{\mathrm{eq}} = \sqrt{\frac{2}{3}}\dot{\nu}_0 \left(-\frac{F'X}{1/m+1} + F \right) \left(\frac{\overline{\tau}^{\mathrm{A}}}{\overline{s}_0} \right), \tag{8.19}$$

and, for $X = 0$, the equivalent plastic strain rate of the composite, normalized by the equivalent plastic strain rate of the unfilled polymer, is

$$F\left(X=0\right) = \frac{\dot{\overline{E}}^{\mathrm{p}}_{\mathrm{eq}}}{\sqrt{\frac{2}{3}}\dot{\nu}_0 \left(\frac{\overline{\tau}^{\mathrm{A}}}{\overline{s}_0} \right)^{1/m}} \equiv F_0. \tag{8.20}$$

The initial F_0 for multi-particle micromechanical simulations with debonded rigid particles at various f_0 are plotted in Figure 8-6. Using the m-dependency of Haghi and Anand, a good fit to the micromechanical data, with the constraint that $F_0 \to \infty$ for $f_0 \to 1$, was found with

$$F_0 = \left(\frac{1 + 2.57f + 4.12f^2}{1 - f^2} \right)^{1/2m}. \tag{8.21}$$

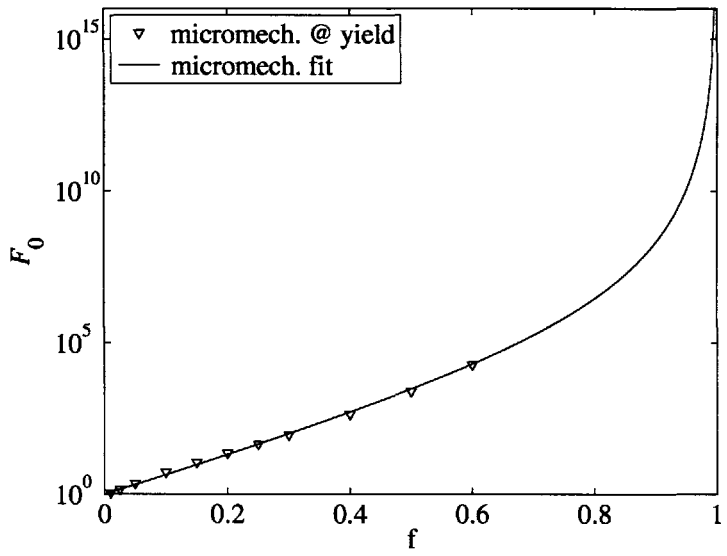

Figure 8-6: Fit of function F_0 to the macroscopic equivalent plastic strain rates, $\overline{\dot{E}}^{\mathrm{p}}_{\mathrm{eq}}$, of multi-particle RVE's with debonded rigid particles at initial yield.

Trivially,

$$A_3 = (F_0 - 1)^{2/(1/m+1)} . \tag{8.22}$$

It is noted that $F \rightarrow 1$ for $f \rightarrow 0$, resulting in the recovery of the plastic potential of the neat polymer.

8.3 Strain Hardening

The macroscopic stress predictions of micromechanical models show that voids and debonded particles have virtually identical effects on orientation strain hardening. The solution of Danielsson et al. [20] for the strain energy density function of an initially spherical void in a concentric neo-Hookean matrix subjected to a macroscopic state of stretch, $\overline{I}_1$, is thus used to model network B. When the particles are all

debonded ($c_2 = f_0$, $c_d = 1$), the strain energy density function of network B is simply

$$\overline{W}_B = \frac{\mu_R}{2}\left\{\overline{I}_1\left(2 - \frac{1}{\overline{J}^p} - \frac{c_2 + 2\left(\overline{J}^p - 1\right)}{\left(\overline{J}^p\right)^{2/3}\eta^{1/3}}\right) - 3\left(1 - c_2\right)\right\}, \tag{8.23}$$

where $\eta \equiv \left(1 + \left(\overline{J}^p - 1\right)/c_2\right)$, and, as it is throughout this section, the approximation $\overline{F} \approx \overline{F}^p$ is made.

For the general case, either due to debonding during the deformation or initial conditions $0 < {c_d}^0 < 1$, the fraction of debonded particles may vary from $c_d = 0$ to $c_d = 1$. Extending the physical conceptualization of Section 8.2, the strain hardening is specified by the analytical solution for a porous polymer with an applied macroscopic stretch state amplified by the current volume fraction of perfectly bonded particles, $c_1/\overline{J}^p$. The strain energy density function of network B becomes

$$\hat{\overline{W}}_B = \left(1 - \frac{c_1}{\overline{J}^p}\right)\frac{\mu_R}{2}\left\{\hat{\overline{I}}_1^p\left(2 - \frac{1}{\overline{J}^p} - \frac{c_2 + 2\left(\overline{J}^p - 1\right)}{\left(\overline{J}^p\right)^{2/3}\eta^{1/3}}\right) - 3\left(1 - c_2\right)\right\}, \tag{8.24}$$

where, from Section 7.3, $\hat{\overline{I}}_1^p = \hat{X}_s(\overline{I}_1^p - 3) + 3$, with

$$\hat{X}_S = 1 + 3.5\left(\frac{c_1}{\overline{J}^p}\right) + 17.6\left(\frac{c_1}{\overline{J}^p}\right)^2 + 53.8\left(\frac{c_1}{\overline{J}^p}\right)^2\left[\left(\overline{I}_1^p/3\right)^{1/2} - 1\right]. \tag{8.25}$$

The stress in network B is

$$\overline{\mathbf{T}}^B = \frac{2}{\overline{J}^p}\frac{\partial \hat{\overline{W}}_B}{\partial \overline{I}_1^p}\overline{\mathbf{B}}^p + \frac{\partial \hat{\overline{W}}_B}{\partial \overline{J}^p}\mathbf{1}, \tag{8.26}$$

and the derivatives of the strain energy density function are given by

$$\frac{\partial \hat{\overline{W}}_B}{\partial \overline{I}_1^p} = \left(1 - \frac{c_1}{\overline{J}^p}\right)\frac{\mu_R}{2}\left(\hat{X}_s + \frac{\partial \hat{X}_s}{\partial \overline{I}_1^p}\left(\overline{I}_1^p - 3\right)\right)\left\{2 - \frac{1}{\overline{J}^p} - \frac{c_2 + 2\left(\overline{J}^p - 1\right)}{\left(\overline{J}^p\right)^{2/3}\eta^{1/3}}\right\} \tag{8.27}$$

and

$$\frac{\partial \hat{\overline{W}}_{\mathrm{B}}}{\partial \overline{J}^{\mathrm{p}}} = \left(1 - \frac{c_1}{\overline{J}^{\mathrm{p}}}\right) \frac{\mu_{\mathrm{R}} \hat{\bar{I}}_1^{\mathrm{p}}}{2} \left\{ \frac{1}{\left(\overline{J}^{\mathrm{p}}\right)^2} - \frac{1}{3\left(\overline{J}^{\mathrm{p}}\right)^{2/3} \eta^{1/3}} \left(\frac{4}{\overline{J}^{\mathrm{p}}} \left(1 - \frac{c_2}{2}\right) + \frac{1}{\eta} \right) \right\}$$
$$+ \left(1 - \frac{c_1}{\overline{J}^{\mathrm{p}}}\right) \frac{\mu_{\mathrm{R}}}{2} \frac{\partial \hat{X}_{\mathrm{s}}}{\partial \overline{J}^{\mathrm{p}}} \left(\bar{I}_1^{\mathrm{p}} - 3\right) \left\{ 2 - \frac{1}{\overline{J}^{\mathrm{p}}} - \frac{c_2 + 2\left(\overline{J}^{\mathrm{p}} - 1\right)}{\left(\overline{J}^{\mathrm{p}}\right)^{2/3} \eta^{1/3}} \right\}$$
$$+ \frac{c_1}{\left(\overline{J}^{\mathrm{p}}\right)^2} \left\{ \frac{\hat{\overline{W}}_{\mathrm{B}}}{1 - c_1/\overline{J}^{\mathrm{p}}} \right\}. \tag{8.28}$$

It is noted that, with the approximation $\overline{F} \approx \overline{F}^{\mathrm{p}}$, the constitutive model for polymers with debonding rigid particles does not reduce precisely to the model of the homopolymer for $f_0 \to 0$ or to the model for polymers with perfectly bonded rigid particles for $f_0 \neq 0$, $c_{\mathrm{d}} \to 1$. This approximation could have been made in the strain hardening components of the models of the previous chapters with no significant impact on their predictions.

8.4 Debonding Criterion

With a framework in place to describe the major aspects of the deformation of a rigid particle-modified polymer for arbitrary f_0 and c_{d}, all that remains is to specify the debonding criterion. Following Tohgo and Chou [72] and Zhao and Weng [82], debonding is taken to be controlled by the average stress in the perfectly bonded particles, $\hat{\mathbf{T}}^{(1)}$. It is common, as observed in the experiments on CC-filled HDPE of Chapter 3 and by many other investigators studying mineral-filled thermoplastics (Bartczak et al. [8], Thio et al. [71], Wilbrink et al. [79], etc.), for hard particles to debond completely by the time of pervasive matrix yielding. For this case, a linear analysis of the type utilized in Section 8.1 provides a straightforward approximate expression for the average stress in the particles as a function of the macroscopic stress. Once the matrix yields, however, as Hill [37] discovered in the context of polycrystal plasticity, the constraint power of the matrix decreases, and the stress in the particles decreases relative to the macroscopic stress.

In an effort to understand and account for the effect of matrix nonlinearity on debonding, an admittedly simplistic method, similar to that of Tandon and Weng [69], is adopted. In the method of Mori and Tanaka [48], these authors replaced the elastic modulus of the matrix, E_0, with the secant modulus of the matrix,

$$E_0^{\mathrm{s}} = \frac{\hat{T}_{\mathrm{eq}}^{(0)}}{\hat{E}_{\mathrm{eq}}^{(0)}}, \tag{8.29}$$

where $\hat{T}_{\mathrm{eq}}^{(0)}$ and $\hat{E}_{\mathrm{eq}}^{(0)}$ are the average equivalent stress and average equivalent strain, respectively, in the matrix. For $\frac{\kappa_1}{\kappa_0} \gg 1$, with debonded particles approximated as voids, the Mori-Tanaka method predicts the average stress in the matrix to be

$$\hat{\mathbf{T}}^{(0)} \approx \frac{1}{(1+(1-\beta_0^{\mathrm{s}})\, b^{\mathrm{s}})} \mathrm{dev}\, \overline{\mathbf{T}} + \frac{1}{(1+(1-\alpha_0^{\mathrm{s}})\, a^{\mathrm{s}})} \overline{T}_{\mathrm{m}}\, \mathbf{I}, \tag{8.30}$$

and the average stress in the perfectly bonded particles to be

$$\hat{\mathbf{T}}^{(1)} \approx \frac{1}{\beta_0^{\mathrm{s}}\,(1+(1-\beta_0^{\mathrm{s}})\, b^{\mathrm{s}})} \mathrm{dev}\, \overline{\mathbf{T}} + \frac{1}{\alpha_0^{\mathrm{s}}\,(1+(1-\alpha_0^{\mathrm{s}})\, a^{\mathrm{s}})} \overline{T}_{\mathrm{m}}\, \mathbf{I}, \tag{8.31}$$

with

$$\alpha_0^{\mathrm{s}} = \frac{3\kappa_0^{\mathrm{s}}}{3\kappa_0^{\mathrm{s}} + 4\mu_0^{\mathrm{s}}}, \quad \beta_0^{\mathrm{s}} = \frac{6}{5}\frac{\kappa_0^{\mathrm{s}} + 2\mu_0^{\mathrm{s}}}{3\kappa_0^{\mathrm{s}} + 4\mu_0^{\mathrm{s}}} \tag{8.32}$$

and

$$a^{\mathrm{s}} \approx \frac{c_1}{\overline{J}^{\mathrm{p}} \alpha_0^{\mathrm{s}}} - \frac{f}{(1-\alpha_0^{\mathrm{s}})}, \quad b^{\mathrm{s}} \approx \frac{c_1}{\overline{J}^{\mathrm{p}} \beta_0^{\mathrm{s}}} - \frac{f}{(1-\beta_0^{\mathrm{s}})}. \tag{8.33}$$

Due to the plastic incompressibility of the matrix, $\kappa_0^{\mathrm{s}} = \kappa_0$. The "secant" Poisson's ratio is therefore given by

$$\nu_0^{\mathrm{s}} = \frac{1}{2} - \left(\frac{1}{2} - \nu_0\right) \frac{E_o^{\mathrm{s}}}{E_0}, \tag{8.34}$$

and the secant shear modulus is calculated as

$$\mu_0^{\mathrm{s}} = \frac{E_0^{\mathrm{s}}}{2\left(1+\nu_0^{\mathrm{s}}\right)}. \tag{8.35}$$

Prior to matrix yielding, $E_0^{\mathrm{s}} = E_0$, and Equations 8.30-8.35 reduce to their linear counterparts.

Calculating E_0^{s} entails several assumptions. The average stress in the matrix is computed similarly to Haghi and Anand [33] via the dissipated power expression,

$$\overline{\mathbf{T}}^{\mathrm{A}} \cdot \overline{\mathbf{D}}^{\mathrm{p}} = \left(1 - f - \frac{c_1}{\overline{J}^{\mathrm{p}}}\right) \sqrt{2}\tau^{\mathrm{A}}\dot{\gamma}^{\mathrm{p}}, \tag{8.36}$$

where τ^{A} is the effective shear stress in network A of the matrix and $\dot{\gamma}^{\mathrm{p}}$ is the effective plastic shear strain rate in the matrix. The secant modulus is calculated solely from the stress driving plastic flow. It will be shown below that $\hat{\mathbf{T}}^{(1)}$ is only sensitive to the choice of E_0^{s} at strains where the stress due to strain hardening is not appreciable. Using, $\overline{\mathbf{T}}^{\mathrm{A}} \cdot \overline{\mathbf{D}}^{\mathrm{p}} = (1/m+1)\,\overline{\Phi}$,

$$\hat{T}_{\mathrm{eq}}^{(0)} \approx \sqrt{3}\tau^{\mathrm{A}} = \frac{s_0}{\overline{s}_0}\left(\frac{\overline{s}_0}{s_0}\frac{F}{\left(1 - f - \frac{c_1}{\overline{J}^{\mathrm{p}}}\right)}\right)^{1/(1/m+1)} \overline{T}_{\mathrm{eq}}^{\mathrm{A}}. \tag{8.37}$$

The average strain in the matrix is estimated to be

$$\hat{E}_{\mathrm{eq}}^{(0)} \approx \frac{\overline{J}^{\mathrm{p}}}{\overline{J}^{\mathrm{p}} - c_1}\overline{E}_{\mathrm{eq}}, \tag{8.38}$$

where

$$\overline{E}_{\mathrm{eq}} \equiv \sqrt{\frac{2}{3}\overline{\mathbf{E}}' \cdot \overline{\mathbf{E}}'}. \tag{8.39}$$

Micromechanical simulations with debonded and perfectly bonded rigid particles prove Equation 8.38 to be an excellent approximation.

Figure 8-7 illustrates the allocation of stress predicted by Equations 8.30 and 8.31 for uniaxial tension of a linear elastic material modified with a range of volume

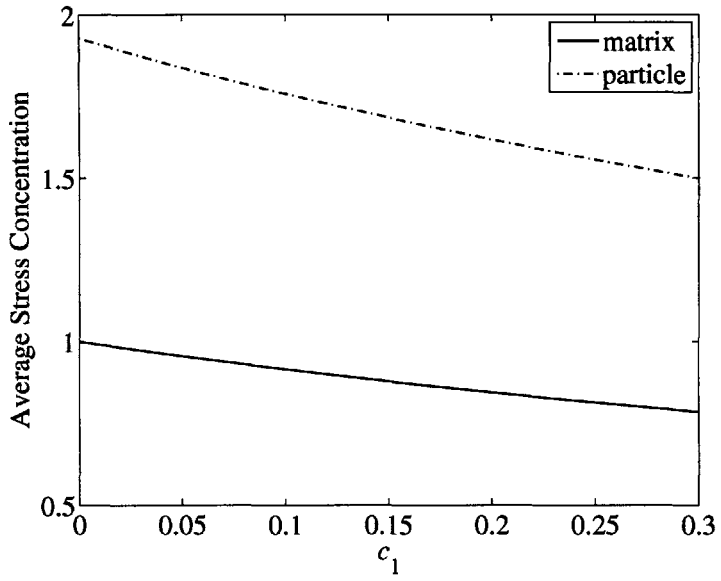

Figure 8-7: Normalized maximum average stress in the matrix, $\hat{T}^{(0)}_{\max}/\overline{T}_{\max}$, and perfectly bonded particles, $\hat{T}^{(1)}_{\max}/\overline{T}_{\max}$, predicted by linear composite theory ($E^s_0 = E_0$) for uniaxial tension.

fractions of perfectly bonded rigid particles. The average stress in the particles is predicted to be on the order of twice as high as the average stress in the matrix. As the volume fraction of filler increases, the maximum average stress concentration in the particles, $\dfrac{\hat{T}^{(1)}_{\max}}{\overline{T}_{\max}}$, decreases significantly.

In order to determine the relationship between $\hat{\mathbf{T}}^{(1)}$ and the macroscopic stress at which debonding occurs, a series of micromechanical simulations were conducted with a linear elastic matrix with the elastic properties of neat HDPE. The micromechanical simulations of Chapter 5 showed that, with the maximum macroscopic principal stress in the vertical direction, debonding always initiates at the poles of the particles. It is near the poles of the particles that the maximum principal stress in the matrix is found. Therefore, in the simulations, the stress in the matrix at the surfaces of the particles at locations that intersect with the direction(s) of maximum macroscopic principal stress was monitored. It is or is very close to the maximum principal stress in the matrix and is hence denoted as "$T^{(0)}_{\max}$." The results, normalized by the maximum macroscopic axial stress predicted by the RVE, $\overline{T}_{\max}$, for single-particle RVE's at three volume fractions of perfectly bonded particles and three types of loading are

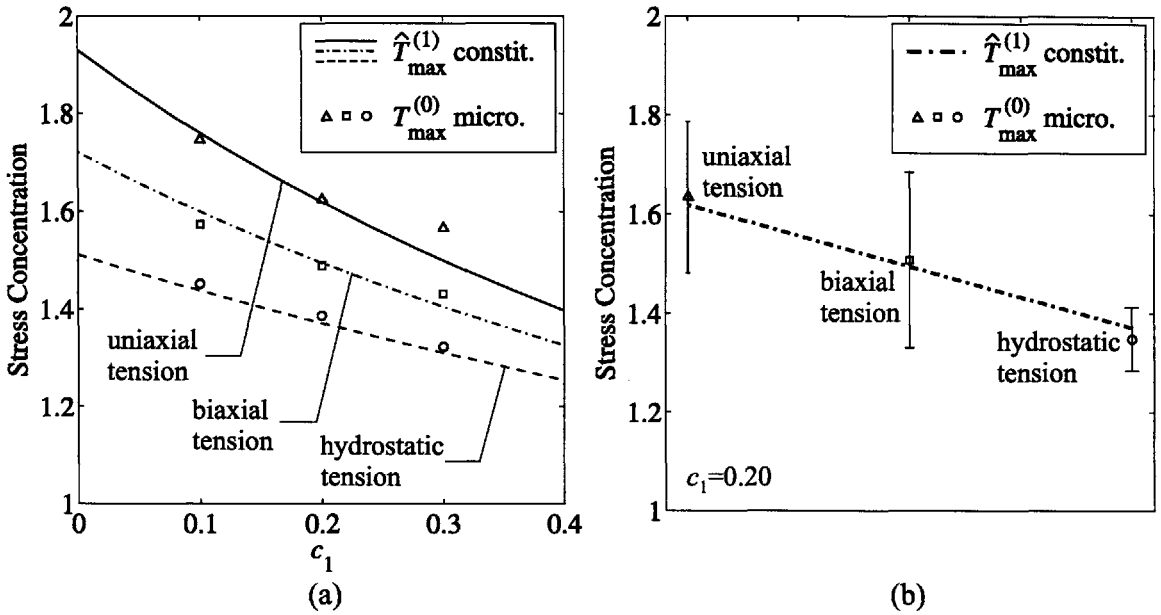

Figure 8-8: Comparison of the normalized maximum average stress in the perfectly bonded particles, $\hat{T}^{(1)}_{max}/\overline{T}_{max}$, predicted by the linear composite theory, and the normalized maximum stress in the matrix, $T^{(0)}_{max}/\overline{T}_{max}$, predicted by micromechanical models for various loadings: (a) single-particle RVE's with linear elastic matrix, (b) multi-particle RVE with linear elastic matrix and $c_1 = f_0 = 0.20$ (mean of the stresses at the poles over all cells of the RVE).

plotted in Figure 8-8a. $\hat{\mathbf{T}}^{(1)}$ is shown to be an exceptional predictor of the stress in the matrix at the particle surface. In Figure 8-8b, the analogous quantities are plotted for a five-particle RVE with $c_1 = f_0 = 0.20$. In this case, the stresses at the two poles of each particle are averaged over all of the cells. The total length of each error bar corresponds to two standard deviations. While there is significant variation amongst the individual cells, the average stress at the poles of the particles shows excellent agreement with the predictions of the linear composite analysis for the average stress in the particles. Figure 8-9 displays the predictions of the five-particle RVE and linear composite model for uniaxial tension at $f_0 = 0.20$ with varying fractions of debonded particles. Each data point corresponds to three different combinations of debonded particles. As the fraction of debonded particles increases, the stress concentration at the perfectly bonded particles increases. The predictions of the linear composite model for the average stress in the perfectly bonded particles are

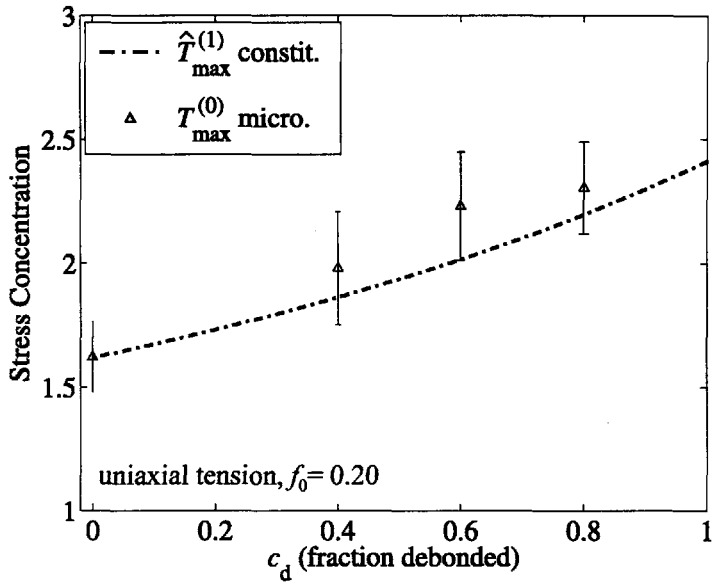

Figure 8-9: Comparison of the normalized maximum average stress in the perfectly bonded particles, $\hat{T}^{(1)}_{max}/\overline{T}_{max}$, predicted by the linear composite theory, and the maximum stress in the matrix, $T^{(0)}_{max}/\overline{T}_{max}$ (mean of the stresses at the poles over all cells of the RVE), predicted by multi-particle RVE's as a function of the volume fraction of debonded particles, c_d.

in reasonable agreement with the stresses found in the matrix at the poles of the particles. Therefore, for an arbitrary state of macroscopic stress, it is concluded that the maximum principal stress in the particle, $\hat{T}^{(1)}_{max}$, is an acceptable representation of the maximum stress at the matrix-particle interface. Debonding is designated to occur when $\hat{T}^{(1)}_{max}$ reaches a critical value.

In order to assess the effect of matrix yielding on debonding, the stress at the poles of the particles was monitored, as a function of macroscopic strain, in a multi-particle RVE with the viscoplastic, strain hardening matrix. In Figure 8-10a, the micromechanical predictions for $c_1 = f_0 = 0.20$ are plotted at three macroscopic stress triaxiality ratios. At the macroscopic axial strain corresponding to the onset of local yielding, there is a drop in the stress concentration factor. Yield occurs first where the stress is highest and, thereafter, until macroscopic yield of the composite, the stress concentration at the particle decreases. On average, the actual *stress* at the particles does not fall. The predictions of the secant form of Equation 8.31 are also

given in Figure 8-10a. The nonlinear composite analysis does not predict a decrease in stress concentration at $X = 1/3$, but, although the drop in stress concentration is underestimated, the model does show the proper trend at $X = 1.0$ and $X = 2.0$. Figure 8-10b displays the micromechanical predictions for the stress concentration at the particles that remain perfectly bonded in a composite with $f_0 = 0.20$ and $c_d = 0.40$. Both the elastic stress concentration and the magnitude of the reduction in stress concentration accompanying matrix yield increase with increasing c_d. After macroscopic yield of the composite, the stress concentration increases slowly with increasing axial strain. The nonlinear composite analysis in this case as well fails to predict accurately the sudden drop in stress concentration, but it does predict the increase in stress concentration as the porosity increases and the current volume fraction of perfectly bonded particles, $c_1/\overline{J}^p$, decreases. In the plastic regime, $\hat{T}^{(1)}_{max}$ clearly increasingly overestimates the stress at the particle-matrix interface as the porosity increases. The debonding criterion based on $\hat{T}^{(1)}_{max}$ therefore exaggerates the propensity of particles to debond subsequent to yielding.

It was shown in the micromechanical modeling of Section 5.3.1 that, in order to reproduce the experimentally measured stress-strain behavior of CC-filled HDPE, debonding must take place over a range of macroscopic stresses/strains. As such, in the constitutive model, the cumulative fraction of debonded particles is specified by a Weibull distribution (Tohgo and Chou [72], Zhao and Weng[82]) as a function of the maximum principal stress in the particles:

$$c_d = 1 - \exp\left[-\left(\frac{\hat{T}^{(1)}_{max}}{S_0}\right)^{m_0}\right], \tag{8.40}$$

where S_0 and m_0 are the scale factor and the shape factor, respectively. Debonding is irreversible and is not allowed in compression. Figure 8-11 illustrates the form of c_d for three different shape factors at a constant scale factor. Increasing m_0 reduces the range of particle stresses over which debonding occurs. S_0 is proportional to the strength of the interface. The average interface stress ($\hat{T}^{(1)}_{max}$) at which the particles

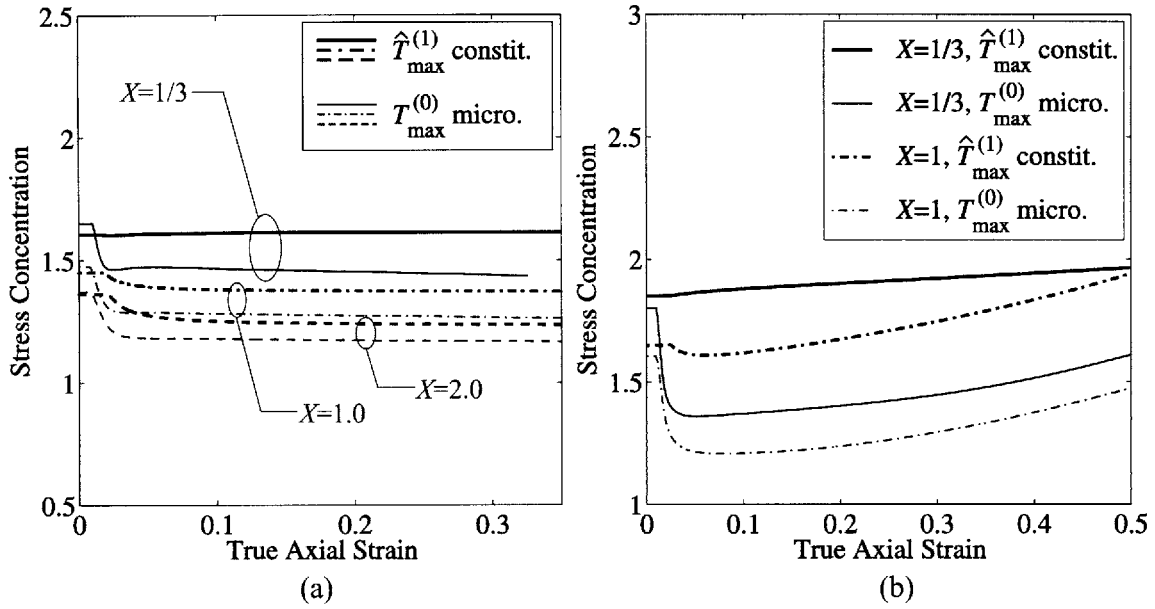

Figure 8-10: Comparison of the normalized maximum average stress in the perfectly bonded particles, $\hat{T}^{(1)}_{\max}/\overline{T}_{\max}$, predicted by the nonlinear composite theory and the maximum stress in the matrix of multi-particle RVE's, $T^{(0)}_{\max}/\overline{T}_{\max}$ (mean of the stresses at the poles over all cells of the RVE), as a function of macroscopic axial strain for various loadings: (a) $f_0 = 0.20$ with $c_d = 0$, (b) $f_0 = 0.20$ with $c_d = 0.40$.

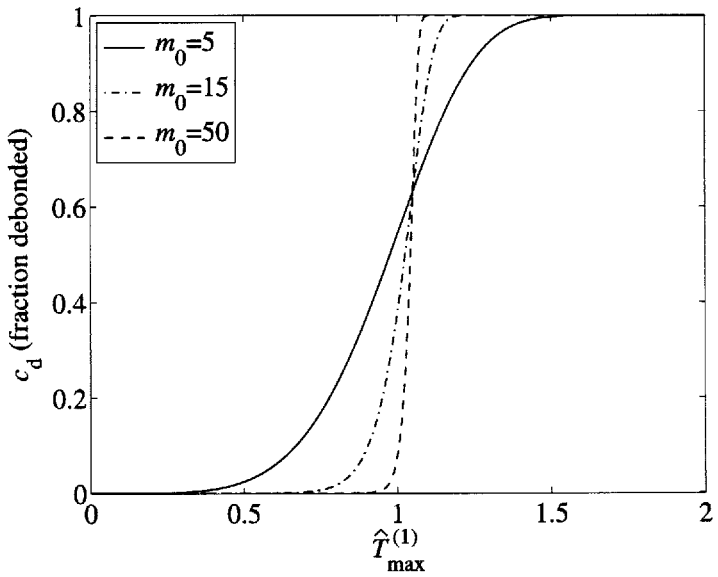

Figure 8-11: Distributed debonding function at several shape factors, m_0, for a fixed scale factor, $S_0 = 1.05$.

debond is

$$\hat{T}_{\mathrm{d}}^{(1)} = S_0 \Gamma \left(1 + \frac{1}{m_0}\right), \tag{8.41}$$

where $\Gamma(\cdot)$ is the Gamma function.

8.5 Results

No bonding

First, the performance of the constitutive model is evaluated with no initial bonding ("NB") between the particles and the matrix. The predictions of the constitutive model are compared with the macroscopic predictions of SA RVE's and the median macroscopic predictions of multi-particle RVE's. In the micromechanical models, the matrix constitutive behavior is specified by the parallel model of Boyce et al. [13] with neo-Hookean strain hardening.

Figure 8-12 displays the constitutive and multi-particle micromechanical predictions for the case of hydrostatic tension. The flow stress of the constitutive model is in excellent agreement with that of the micromechanical models to large volumetric strains.

Figure 8-13 a,b shows the constitutive and multi-particle micromechanical predictions for loading in uniaxial tension. The yield strengths of the constitutive model exhibit excellent agreement with those of the micromechanical models. The constitutive model flow stress and volumetric strain predictions as a function of axial strain are also in relatively good agreement with the predictions of the micromechanical models. There is a not insignificant discrepancy, however, between the constitutive and micromechanical stress-strain predictions at $f_0 = 0.05$ and $f_0 = 0.15$. The error is due to failing to account for the effect of non-symmetric void shapes in the plastic potential and assuming that, aside from the properties of the matrix, the viscoplastic behavior is a function solely of the current porosity, f. At the lower volume fractions of particles, the consequence is a too soft stress-strain response at intermediate to

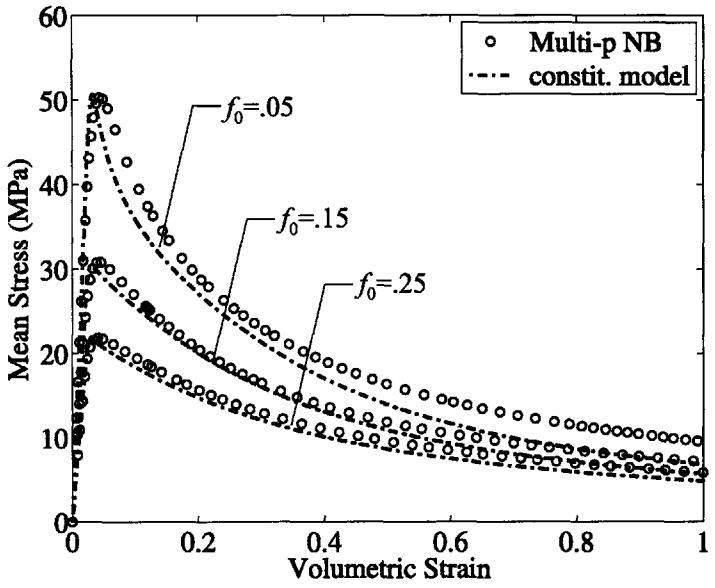

Figure 8-12: Constitutive and multi-particle RVE predictions with no initial bonding ("NB") between the particles and the matrix for the case of hydrostatic tension: hydrostatic stress versus volumetric strain.

large axial strains. As f_0 increases further, the micromechanical models show particle interactions to become prevalent at decreasing macroscopic strains, resulting in more symmetric void shapes and a closer correspondence, irrespective of f_0, between f and the viscoplastic strain rates $\dot{\overline{E}}_{\mathrm{h}}$ and $\dot{\overline{E}}_{\mathrm{eq}}$.

Analogous plots for the case of equi-biaxial tension are given in Figure 8-13 c,d. Overall, the constitutive model predictions show relatively good agreement with the micromechanical predictions in terms of both stress and volumetric strain. The constitutive model does exhibit lower flow stresses and greater volumetric strains than the micromechanical models due largely to the void shape effects discussed in the previous paragraph. As in the case of uniaxial tension, and for the same reasons, the error becomes smaller as f_0 increases.

Figure 8-15 shows the predictions for macroscopic stress triaxiality ratios $X = 1.0$ and $X = 2.0$. As in the elevated triaxiality study of Chapter 6, the macroscopic principal state of stress is such that there is a single major stress and two minor stresses. We recall from Chapter 6 that, due to bands of localized deformation spanning the entire multi-particle RVE's, it is not clear whether single-particle or multi-particle

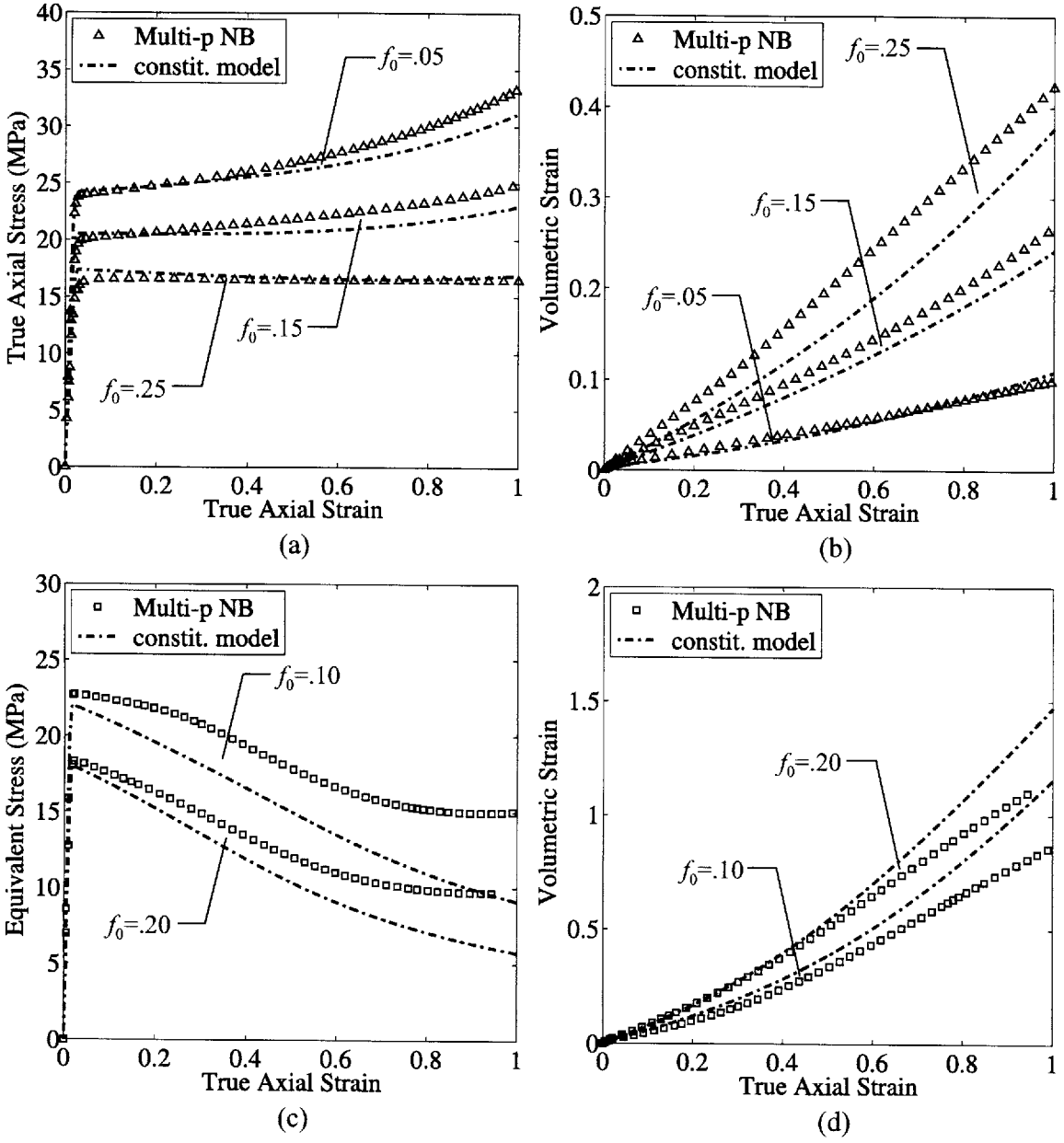

Figure 8-13: Constitutive model and multi-particle RVE predictions with no initial bonding ("NB") between the particles and the matrix as a function of $c_2 = f_0$: (a), (b) uniaxial tension; (c), (d) biaxial tension.

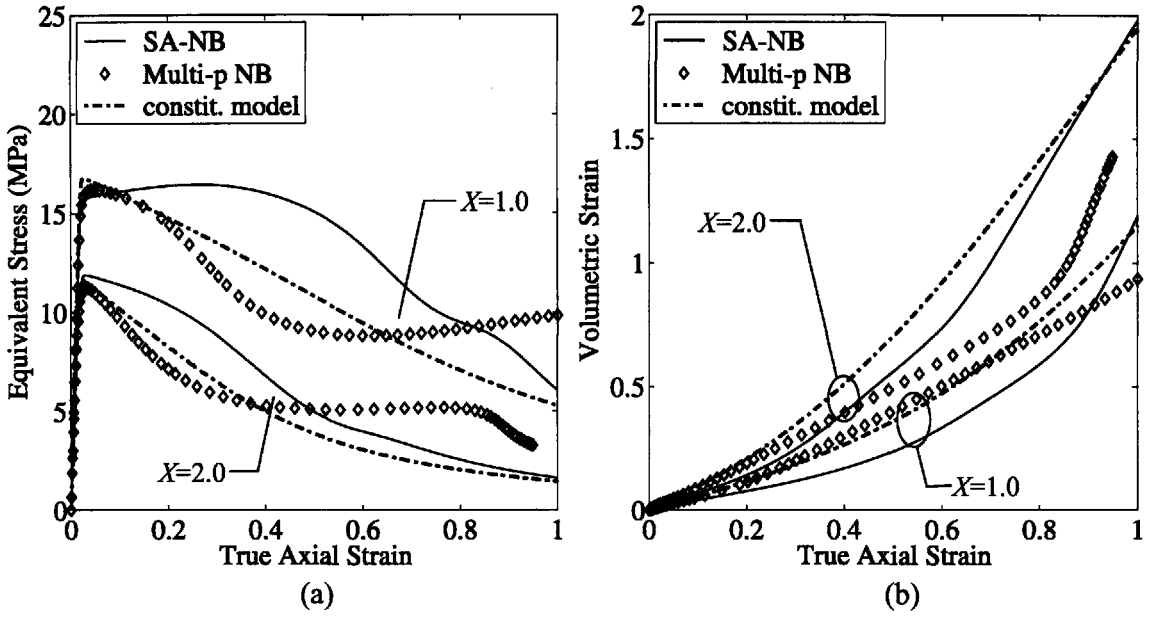

Figure 8-14: Constitutive model and multi-particle RVE predictions for cases of elevated triaxiality loading with no initial bonding ("NB") between the particles and the matrix and $c_2 = f_0 = 0.15$.

RVE's offer a more realistic representation of a material subject to an elevated triaxiality ratio. Therefore, the predictions of both the SA and multi-particle RVE's are plotted in Figure 8-15. In terms of both macroscopic stress and volumetric strain, the constitutive model predictions exhibit excellent agreement with the multi-particle predictions until the deformation localizes to certain cells ($\overline{E}_{zz} \approx 0.20$ at $X = 1.0$, $\overline{E}_{zz} \approx 0.10$ at $X = 2.0$.) After localization, as discussed in Chapter 6, the multi-particle RVE is no longer representative of the continuum material. While the SA RVE is unable to capture the effects of a heterogeneous arrangement of particles, it remains a true representative volume element, and, at large strains, the constitutive model predictions show reasonable agreement with the SA RVE predictions.

It was also shown in Chapter 6 that increasing the rate of strain hardening of the matrix suppresses the tendency of deformation to localize both within certain cells of a multi-particle RVE and within the interparticle ligament(s) of SA and multi-particle RVE's. In Figure 8-15, the constitutive model, SA RVE, and multi-particle RVE predictions are compared at $f_0 = 0.15$ with the initial rate of matrix strain hardening

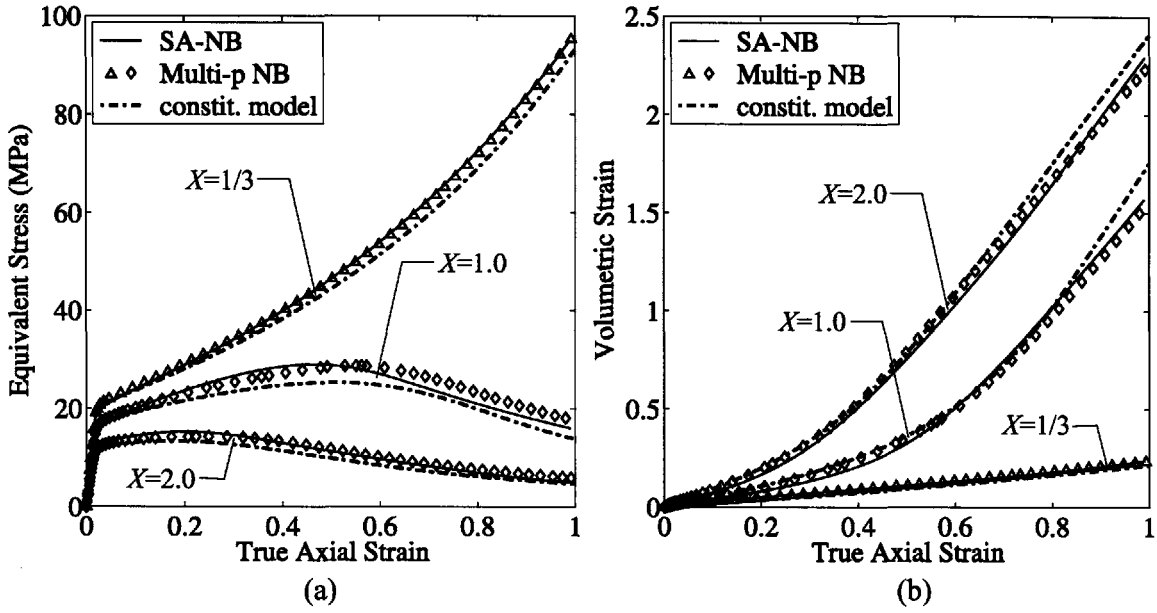

Figure 8-15: Constitutive model and multi-particle RVE predictions for a matrix with normalized initial hardening modulus $\overline{\mu}_{\mathrm{R}} = 10$, no initial bonding between the particles and the matrix, and $c_2 = f_0 = 0.15$.

increased an order of magnitude to $\overline{\mu}_{\mathrm{R}} = 10$. The SA-NB and multi-particle predictions coalesce, and the constitutive model predicts the micromechanical behavior very well at all three stress triaxiality ratios. With the viscoplastic behavior specified by the single parameter f, the constitutive model cannot predict exactly the occurrence nor the effect of localization within interparticle ligaments of the type portrayed in Figures 6-3 and 6-4, for example. Therefore, as the rate of strain hardening of the matrix increases, the constitutive model becomes more accurate

Debonding

Here, the performance of the constitutive model is assessed under conditions of evolutionary debonding and initial partial debonding. The predictions of the constitutive model are compared with the macroscopic predictions of SA RVE's and typical multi-particle RVE's. In the micromechanical models, the matrix constitutive behavior is specified as either linear elastic with the properties of neat HDPE or viscoplastic, strain hardening by the model of Boyce et al.

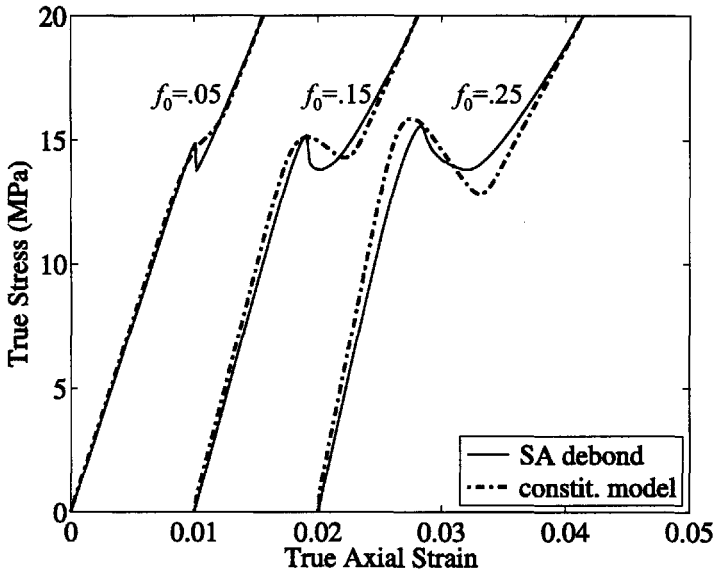

Figure 8-16: Linear elastic constitutive model predictions (m_0=15, $S_0 = 29.5$) versus SA-debond RVE predictions for uniaxial tension at $f_0 = 0.05$, $f_0 = 0.15$, and $f_0 = 0.25$.

Figure 8-16 displays the predictions of the constitutive model compared with the predictions of SA-debond RVE's for the case of uniaxial tension and a linear elastic matrix. In the micromechanical models, the interface properties were set identically to those in Chapter 6: $\sigma_{\max} = 15.0$ MPa and $\delta_n = \delta_t = 0.0025r$. The debonding parameters in the constitutive model were set at $m_0 = 15$ and $S_0 = 29.5$ MPa in order to match the macroscopic debonding stress of the SA-debond RVE at $f_0 = 0.15$. The constitutive model predicts reasonably well the moduli before and after debonding as well as the increase in macroscopic debonding stress with increasing f_0. Furthermore, the constitutive model also predicts the increase in magnitude, with increasing f_0, of the drop in macroscopic stress that occurs when the particles shed the majority of their load bearing capacity.

Figure 8-17 presents the constitutive model predictions versus the SA-debond predictions as a function of macroscopic stress triaxiality ratio for $f_0 = 0.15$ and a linear elastic matrix. The constitutive model provides an excellent prediction of the decrease in macroscopic equivalent stress required to cause debonding with increasing X. The pre-debonding and post-debonding moduli as well as the elastic volumetric strain are

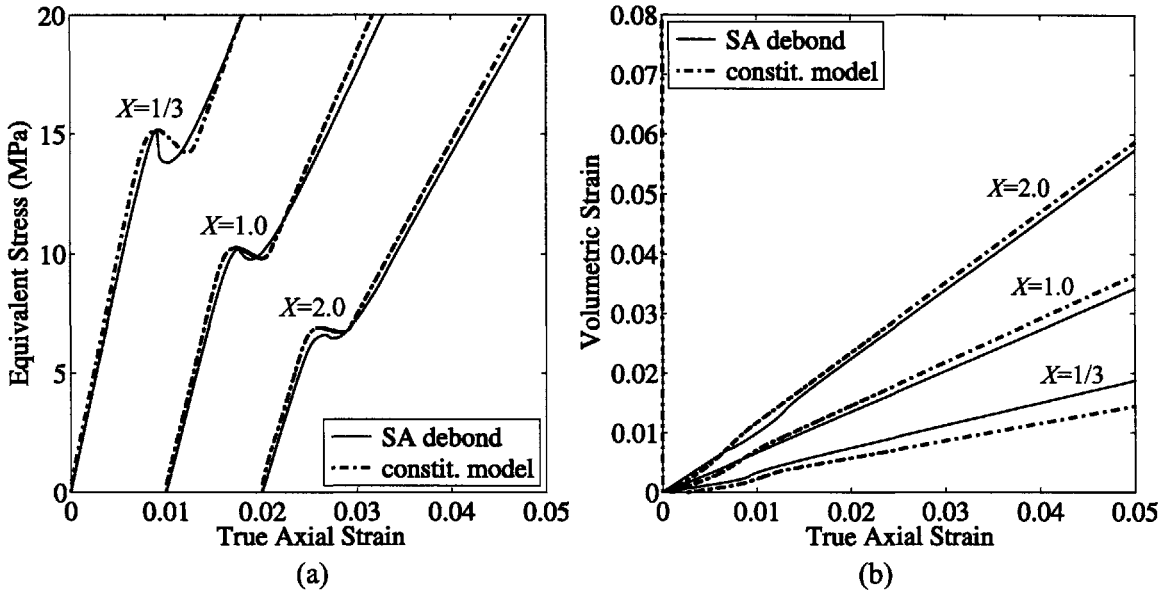

Figure 8-17: Linear elastic constitutive model predictions (m_0=15, $S_0 = 29.5$) versus SA-debond RVE predictions as a function of macroscopic stress triaxiality ratio, X, at $f_0 = 0.15$: (a) macroscopic equivalent stress versus macroscopic true axial strain, (b) macroscopic volumetric strain versus true axial strain.

predicted accurately. In addition, Figure 8-18 illustrates that the constitutive model also predicts the increase in macroscopic principal stress required to cause debonding with increasing X.

In a single-particle RVE, "all" of the particles debond at once, and the result is the jog in the stress-strain curve. In order to replicate this abrupt type of debonding, a relatively high shape factor, m_0, was specified in the constitutive model. However, no jog is apparent in the experimental stress-strain curves of CC-filled HDPE due, as shown in the multi-particle micromechanical modeling of Section 5.3.1, to the distributed nature of debonding in an actual material. In order to evaluate the constitutive model under these more realistic conditions, multi-particle simulations were conducted with the distributed debonding properties of Section 5.3.1 and the viscoplastic, strain hardening matrix. The results of the micromechanical simulations and the predictions of the constitutive model with $m_0 = 5$ and $S_0 = 34$ are plotted in Figure 8-19 for the case of uniaxial tension. Good agreement is seen in both the stress-strain behavior and the fraction of debonded particles as a function of macro-

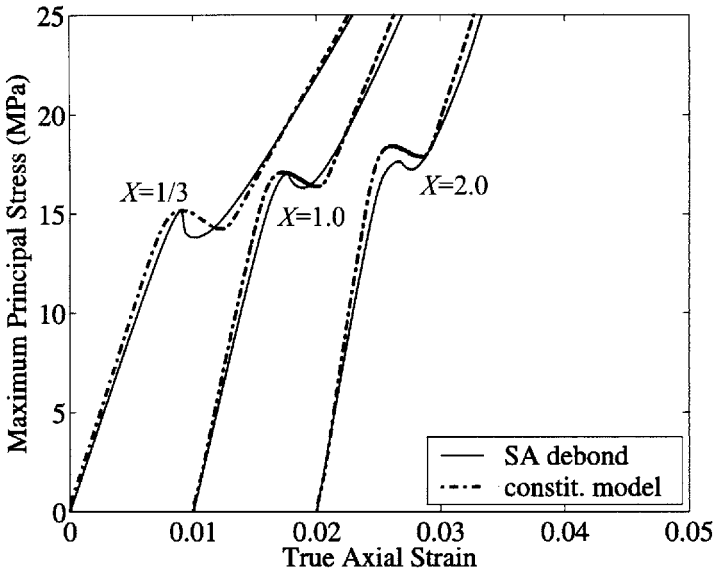

Figure 8-18: Linear elastic constitutive model predictions (m_0=15, $S_0 = 29.5$) versus SA-debond RVE predictions as a function of macroscopic stress triaxiality ratio, X, at $f_0 = 0.15$: maximum macroscopic principal stress versus macroscopic true axial strain

scopic axial strain. The constitutive and micromechanical models both predict 100% debonding prior to macroscopic yield.

In the development and processing of particle-modified composites, systematically altering interface properties is a difficult task. The effect on macroscopic behavior of a whole spectrum of interface properties may be evaluated conveniently with the constitutive model. For example, in Figure 8-20, the interface strength, a property commonly tailored via surface treatment of the particles, is varied. The prediction for uniaxial tension at $f_0 = 0.15$ with the interface properties utilized above ($m_0 = 5$, $S_0 = 34$) is the reference. Decreasing S_0, directly proportional to the average interface strength via Equation 8.41, by 50% causes the particles to debond at smaller macroscopic axial stresses/strains. Increasing S_0 by 50% delays debonding to larger macroscopic axial stresses and strains and also prevents approximately half of the particles from debonding, resulting in a 20% stronger composite. The shape factor at constant interface strength $\hat{T}_{\mathrm{d}}^{(1)}$ is varied in Figure 8-21. Adjusting m_0 corresponds, in an actual material, to varying the range of particle size or the type of

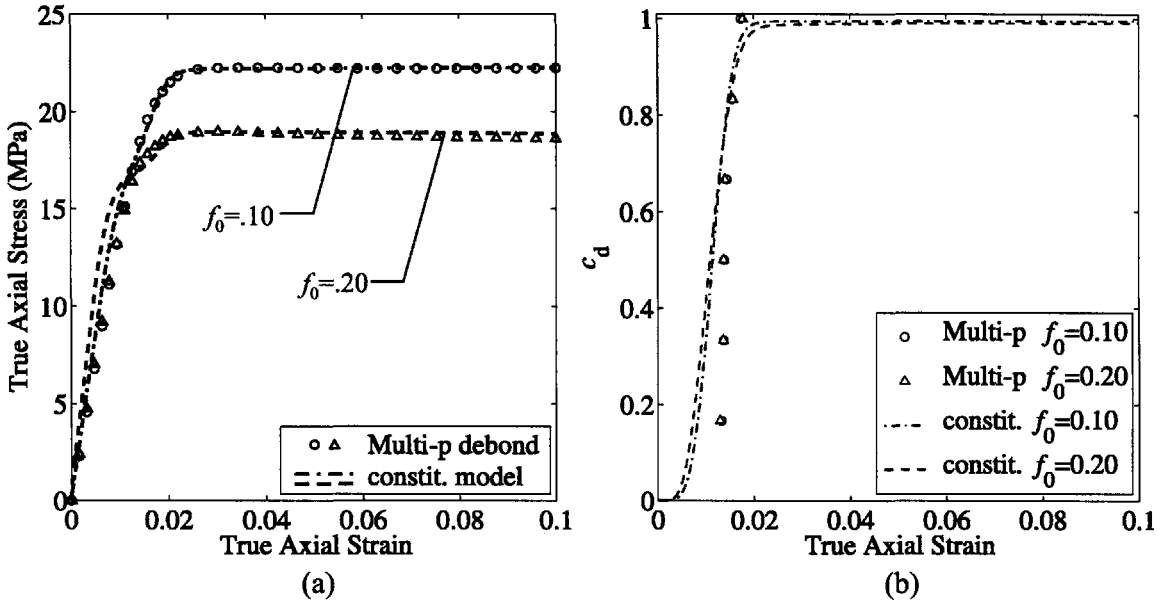

Figure 8-19: Constitutive model predictions ($m_0 = 5$, $S_0 = 34$) versus multi-particle RVE debonding predictions for uniaxial tension at $f_0 = 0.10$ and $f_0 = 0.20$: (a) macroscopic true axial stress versus true axial strain, (b) fraction of debonded particles, c_d, versus macroscopic true axial strain.

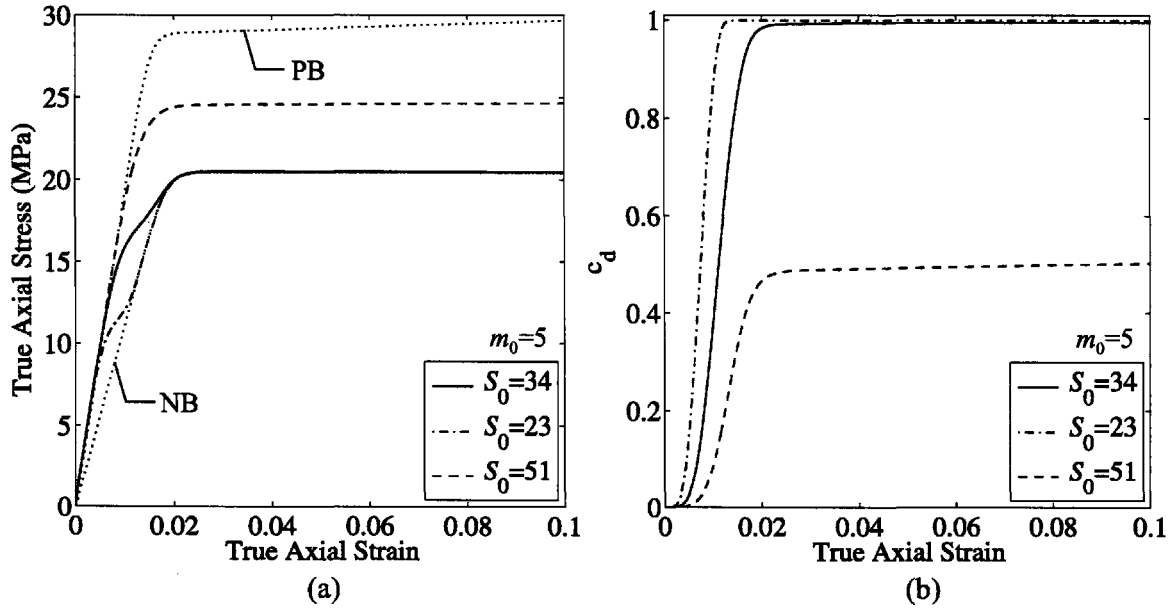

Figure 8-20: Constitutive model predictions as a function of debonding scale factor, S_0, for uniaxial tension at $f_0 = 0.15$: (a) macroscopic true axial stress versus true axial strain, (b) fraction of debonded particles, c_d, versus true axial strain.

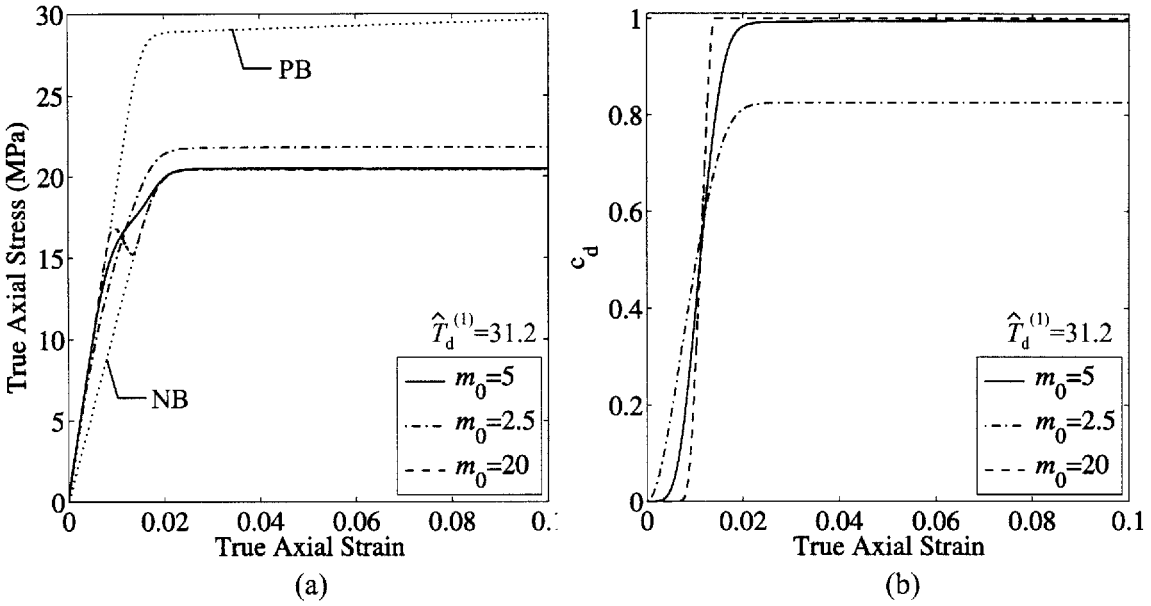

Figure 8-21: Constitutive model predictions as a function of debonding shape factor, m_0, for uniaxial tension at $f_0 = 0.15$: (a) macroscopic true axial stress versus true axial strain, (b) fraction of debonded particles, c_d, versus true axial strain.

surface treatment within a given blend. The reference properties are again $m_0 = 5$, $S_0 = 34$. Quadrupling the shape factor to $m_0 = 20$ delays the onset of debonding and causes debonding to happen over a narrower range of macroscopic stresses/strains. The stress-strain curve exhibits a sudden drop, reminiscent of the linear elastic predictions, as the majority of the load bearing capacity of the particles is lost almost instantaneously. Halving the shape factor to $m_0 = 2.5$ causes debonding to begin at the onset of deformation but also increases the range of stresses/strains over which debonding occurs. The result is a reduced elastic modulus and incomplete debonding which elevates the flow stress of the composite.

It is noted that, in the plastic regime, the debonding criterion of Section 8.4 becomes increasingly inaccurate as the fraction of debonded particles increases . The constitutive model is therefore most appropriate under the following conditions:

1. All of the debonding occurs at or before macroscopic yield of the composite (but completed debonding is not required).

2. Debonding does not initiate until the plastic regime, and the debonding that

takes place occurs over a narrow range of macroscopic stress/strains.

In the plastic regime, if $c_d > 0$, the constitutive model overestimates the stress at the particle-matrix interface and may therefore predict additional debonding prematurely. Practically speaking, most, if not all, mineral-filled thermoplastic polymers exhibit complete debonding by the time of macroscopic yield.

Finally, the ability of the constitutive model to represent the behavior of a composite with a mixed population of particles is demonstrated. In Figure 8-22, for uniaxial tension, the predictions of the constitutive model are compared with the macroscopic predictions of multi-particle RVE's at several fractions of initially debonded particles, c_d^0. During the deformation, c_d remains constant at $c_d = c_d^0$. Generally very good agreement is seen in terms of both stress and volumetric strain at each f_0 and c_d, validating the large-strain conceptual framework of the constitutive model.

8.6 Conclusions

A constitutive model for the large-strain elasto-viscoplastic deformation of polymers with potentially debonding rigid particles has been shown to predict accurately the macroscopic responses of micromechanical models over a range of volume fractions of particles and types of loading. The model as presented is valid only for polymers with the strain rate sensitivity of HDPE but, with additional fitting of function A_2 in the plastic potential, could be made applicable to polymers of arbitrary m. The debonding criterion of the model is not valid under all circumstances, but the modular form of the model would allow simple insertion of a more sophisticated debonding criterion.

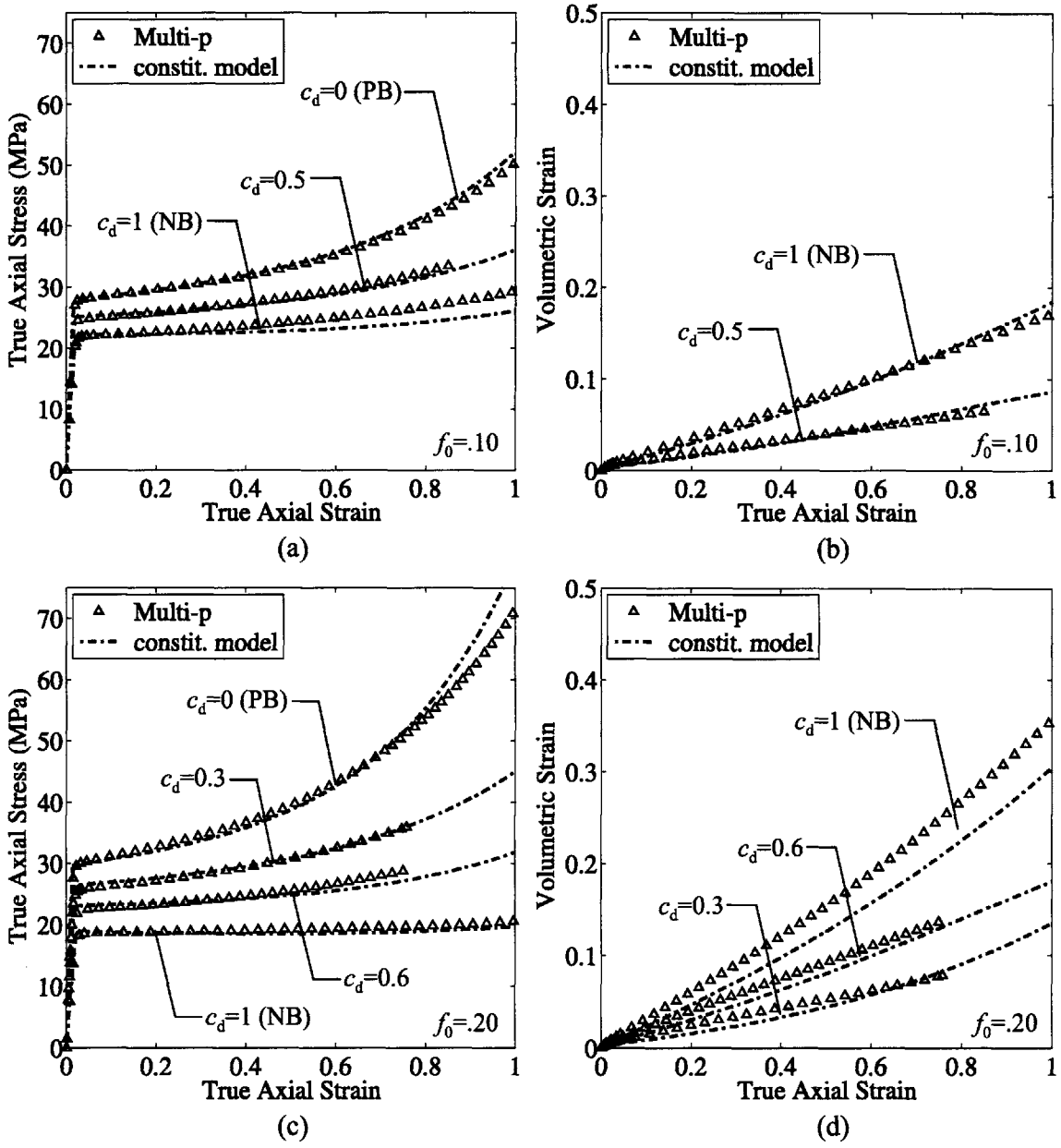

Figure 8-22: Constitutive model and multi-particle RVE predictions as a function of the fraction of debonded particles, $c_d = c_d^0$: (a), (b) $f_0 = 0.10$; (c), (d) $f_0 = 0.20$.

Chapter 9

Conclusion

9.1 Summary

A framework of experimental and numerical tools has been developed through which to investigate the deformation of particle-modified polymers.

The experimental techniques presented in Chapters 2 and 3 allowed characterization of several polymers to large tensile strains. True stress-true strain response, volumetric strain response, and full-field contours of strain were measured for uniaxial tension of neat and particle-modified polymers. Specifically, the following was found:

- Rubber particles decrease the elastic modulus of a polymer; $CaCO_3$ particles increase the elastic modulus of a polymer.
- Rubber and $CaCO_3$ particles decrease the yield strength of a polymer; $CaCO_3$ particles provide slightly more reinforcement than rubber particles.
- Rubber and $CaCO_3$ particles decrease the strain hardening slope; $CaCO_3$ particles have an effect much larger than that of rubber particles.
- Rubber particles do not cavitate in PC or HDPE under uniaxial tension.
- $CaCO_3$ particles debond prior to macroscopic yield in HDPE; the debonding strength is inversely proportional to the size of the particles.

- Rubber particles diffuse the neck that forms in the specimens during uniaxial tension of PC and HDPE; in HDPE, $CaCO_3$ particles have a similar effect at large strains but the opposite effect at small strains.

In Chapter 5, finite element-based micromechanical models were developed to represent the deformation of particle-modified HDPE under uniaxial tension. The accuracy of the various models was evaluated by drawing comparisons with the experimental data. The following was shown:

- Rubber particles that do not cavitate provide negligible reinforcement to the matrix; $CaCO_3$ particles contribute significant reinforcement only up to the point of debonding.

- Debonding of $CaCO_3$ particles occurs over a range of macroscopic stresses/strains. This is the primary reason that the yield strengths of $CaCO_3$-filled HDPE are superior to those of rubber-filled HDPE.

- In all cases, a composite with randomly dispersed particles exhibits a higher yield strength than a composite with perfect dispersion. With a heterogeneous spatial distribution of particles, sections of the matrix are shielded or constrained, and plasticity does not simultaneously span every interparticle ligament as it does when the particles are homogeneously distributed.

- With cavitated or debonded particles, a composite with random dispersion exhibits more volumetric strain, and less strain hardening than a composite with perfect dispersion. Particles that are close to one another on appropriate planes cause the deformation to localize sooner than it would if the particles were uniformly spaced.

- By limiting dilatation, rubber particles that do not cavitate and voids cause substantially more strain hardening than $CaCO_3$ particles.

In Chapter 6, the micromechanical models of rigid particle-modified polymers were extended to simulate more complex states of stress and clustering of particles. It was

found that localization of deformation, both within the ligaments of an individual cell and within a subset of an array of cells, occurs at a decreasing macroscopic axial strain with increasing stress triaxiality ratio and with increasing volume fraction of debonded rigid particles. Raising the strain hardening modulus of the matrix suppressed both types of localization. It was also shown that clustering of particles can trigger localization of deformation under uniaxial tension that is only observed at elevated stress triaxiality ratios when the particles are well dispersed. Thus it was postulated that localization becomes more likely to occur as the dispersion of the particles worsens. This theory offers a possible explanation for why toughening with mineral particles is more difficult to achieve than toughening with rubber particles. In a tough polymer composite, the deformation occurs, not in isolated, highly localized events, but through extensive, pervasive plastic flow. It is via this more uniform mode of deformation that the most energy is dissipated. Rubber particles are well known to toughen many thermoplastics, but the enhancement in toughness observed in some polymers, such as PC and Nylon, has proven difficult to duplicate with mineral particles. Rubber particles separate out from the melt, and are therefore far less prone to aggregate than mineral particles. In addition, it was shown experimentally that, in uniaxial tension, mineral particles debond much more easily than rubber particles cavitate. If some or all of the rubber particles do not cavitate, localization would likely be further suppressed. Rubber particles were observed not to cavitate at all under uniaxial tension, but, at elevated stress triaxiality ratios, the increased levels of hydrostatic tension in the matrix presumably cause some of the particles to cavitate. However, once particles begin to cavitate, the negative pressure in the matrix is somewhat relieved, and it becomes more difficult for the remaining (intact) particles to cavitate.

The findings of the experiments and micromechanical simulations were utilized to develop, calibrate, and verify a constitutive model for polymers with potentially debonding rigid particles. It was discovered that, when particles are perfectly bonded, for the purpose of predicting both yield strength and strain hardening slope, second order moments of the strain field provide an accurate scalar representation of the het-

erogeneous state of strain in the matrix. When particles debond, the plastic stretching is well modeled as a function solely of the current porosity f. The constitutive model was shown to be accurate to large strains for various loadings, volume fractions of particles, matrix strain hardening moduli, and states of debonding. It may be implemented into finite element models in order to simulate components or structures and also allows infinite tailoring of interface properties.

9.2 Future Work

This work has raised many interesting questions, and there are numerous opportunities for future investigation.

The experimental techniques are readily transferable to virtually any material system. In addition to the capabilities presented in Chapters 2 and 3, the characterization of the full-field deformation state of materials under loadings other than uniaxial tension is possible. Examples include tension and bend tests on notched specimens. Contours of strain around notches would provide insight into the effects of stress triaxiality and toughening mechanisms.

Localization, both on the scale of individual interparticle ligaments and within a subset of the total number of cells of an RVE, was shown to be suppressed as the hardening modulus of the matrix increases. HDPE, an exceptionally ductile polymers, has a very low initial hardening modulus and is therefore particularly susceptible to localization. Nevertheless, HDPE and similarly ductile polypropylene have been successfully toughened with mineral fillers whereas analogous toughening of PC and Nylon, polymers with strain hardening moduli significantly greater than those of HDPE and polypropylene, has not been accomplished. Aside from yield strength, the major difference between these two groups of polymers is that HDPE and polypropylene exhibit little or no post-yield strain softening, but PC and Nylon both strain soften substantially after macroscopic yield before they strain harden. Strain softening would presumably intensify localization, and it would be informative to perform micromechanical simulations at elevate stress triaxialities with a matrix that initially

strain softens.

An additional area to explore with micromechanical simulations is the cavitation of rubber particles under triaxial states of stress. By specifying in multi-particle simulations a criterion for particle cavitation, such as that utilized by Baumann [10] in single particle RVE's, the likelihood and extent of particle cavitation as a function of macroscopic stress triaxiality ratio could be evaluated. The hypothesis that the failure of some particles to cavitate may prevent or reduce localization could thus be explored.

A number of extensions could be made to the constitutive model without sacrificing much of its simplicity. When some or all of the particles are perfectly bonded, the strain hardening response is a function of the strain amplification factor, $\hat{X}_{\mathrm{S}}$. As shown in Chapter 7, $\hat{X}_{\mathrm{S}}$ is slightly dependent on the strain hardening modulus of the matrix (μ_{R}). With further micromechanical modeling and fitting, a functional form for $\hat{X}_{\mathrm{S}}$ that includes the dependence on μ_{R} could be derived. Furthermore, when some or all the particles are debonded, the viscoplastic stretching is dependent on the strain rate sensitivity of the matrix. The form of the viscoplastic potential function $\overline{\Phi}$ was derived for a matrix with the strain rate sensitivity (m) of HDPE. Additional micromechanical modeling and fitting as a function of m would enable the model to capture this dependence as well. Finally, the applicability of the constitutive model could be extended to polymers that exhibit post-yield strain softening by following Haghi and Anand [33], who take the matrix shear strength, s, to evolve according to the plastic strain rate in the matrix.

The constitutive model has potential uses in addition to those cited in the previous section. It is desirable to have the capability to predict localization of deformation from the macroscopic stress-strain response of a composite. Analyzing the stability of the stress-strain predictions of the constitutive model via constructions such as a compressible Considère type analysis might enable assessment of a material's vulnerability to localization. In addition, in conjunction with experiments and micromechanical simulations, the constitutive model would play a major role in a multi-scale fracture analysis such as that performed by Danielsson [18]. Brittle and ductile fracture crite-

ria determined from such an analysis could then be incorporated into the constitutive model.

Appendix A

Experimental Error Analysis

There are sources of error in the data acquisition, image correlation, and strain calculation procedures. The error can be separated into noise and systematic components.

A simple test was performed to assess the noise levels in the data acquisition and image correlation procedures. A neat PC tensile specimen was tested with an image resolution of 37.5 pixels/mm and an image acquisition rate of 1 Hz. Before starting the test, a reference image was taken and then 100 additional images were acquired. The specimen was then deformed at a constant nominal strain rate of $.005\,s^{-1}$ to a crosshead displacement (estimated from prior tests) corresponding to a true axial strain, E_{yy}, of approximately 0.10, and the test was stopped. The image acquisition process was halted for two minutes, and then 100 images were acquired while the specimen was still stationary. The sequence was repeated at strain increments of 0.10 until a maximum strain of approximately 0.50 had been reached. In order to assess the accuracy of the local strain calculation, the images were then analyzed with a subset size of 75 pixels at the lateral center of the specimen at the axial location where necking initiated. As described in Section 2.2.3, E_{yy} was calculated from the raw displacement gradient data via Equation 2.6. The very first image acquired was the reference image for all calculations. For the 100 undeformed images, the mean "apparent" strain was $4\,\mu\epsilon$ with a range of $229\,\mu\epsilon$ and a standard deviation of $40\,\mu\epsilon$. The baseline accuracy of the local strain measurement is thus on the order of $\pm 100\,\mu\epsilon$. At each subsequent strain, a similar analysis was conducted on the 100 "fixed" images.

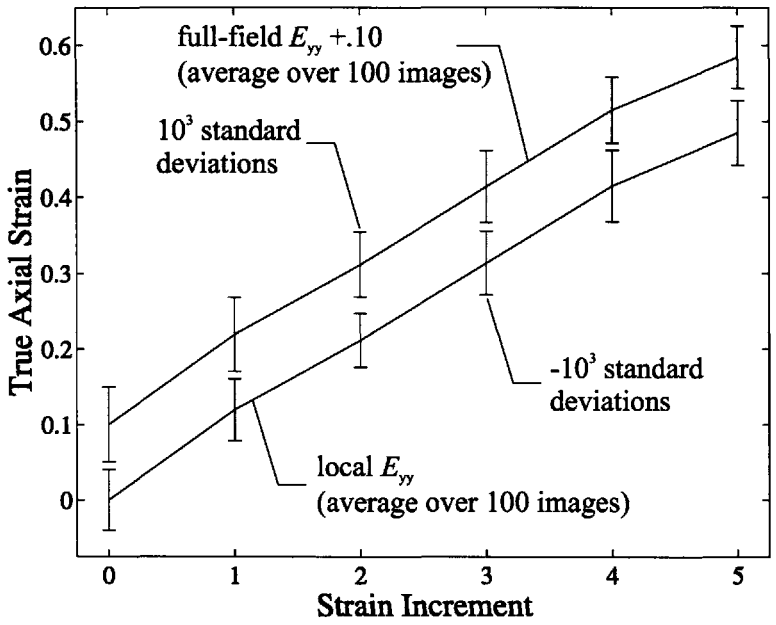

Figure A-1: True axial strain, E_{yy}, measured with the local and full-field techniques as a function of strain. For clarity, the full-field E_{yy} is shifted by .10, and the standard deviations are scaled by 10^3.

Due to elastic unloading near the grip regions of the specimen, the strain increased slightly at the point of interest over the course of each set of 100 images. A second-order polynomial was therefore fit to the data at each strain increment, and the range and standard deviation were defined in reference to the polynomial approximation. The range and standard deviation varied from 166 $\mu\epsilon$ to 276 $\mu\epsilon$ and 34 $\mu\epsilon$ to 47 $\mu\epsilon$, respectively, and were not a function of strain. Furthermore, in order to assess the accuracy of the full-field strain calculation as well, the procedure was repeated at a step size of two over a 21 pixel $\times$ 21 pixel subset centered on the point described above. Following the algorithm of Section 2.2.3, the displacement gradient at the center of the subset, and in turn the strain, was calculated by fitting quadratic polynomials to the u and v displacements of the resulting 11 $\times$ 11 grid. As shown in Figure A-1, the average axial strains (the maximum difference is 340 $\mu\epsilon$) and level of noise measured with the full-field technique are virtually identical to those measured with the local technique.

While the error due to noise is not a function of the strain, it is a strong function

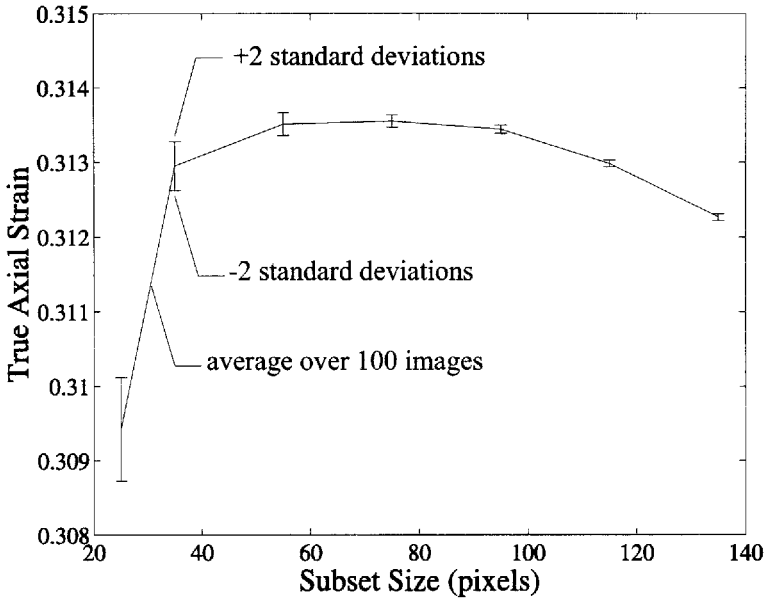

Figure A-2: True axial strain, E_{yy}, as a function of correlation subset size.

of the subset size. Figure A-2 plots the average axial strain and noise level measured with the local technique as a function of correlation subset size at strain increment 3. The image-to-image variability decreases dramatically and the strain approaches a constant value as the subset size increases. At subset sizes greater than 100 pixels, however, the strain begins to decrease indicating that the subset size is too large to capture the strain gradient in the specimen. The subset size of 75 pixels used in all subsequent analyses was thus chosen as a satisfactory compromise between random error and detail lost due to over-smoothing of the data.

The most significant source of systematic error is the "out-of-plane" error, e, due to the Poisson contraction of the specimen. As the specimen contracts in x and z directions, the representation of the specimen at the camera sensor becomes smaller. In a coordinate system located at the image center, any point p appears to be at p'. In the y-direction, for example,

$$p_y{}' \approx \frac{F_o}{F_o + dF} \times p_y, \tag{A.1}$$

where F_o is the initial distance between the center of the camera lens and the specimen

surface (1.0 m) and dF is the out-of-plane displacement. Considering purely axial deformation and approximating the displacement field as linear over the subset, the actual true axial strain can be written as

$$E_{yy} = \ln\left(\frac{{p_y}^{\text{top}} - {p_y}^{\text{bot}}}{S-1}\right), \tag{A.2}$$

where S is the correlation subset size in the case of the local strain calculation and the grid subset size in the case of the full-field strain calculation, and ${p_y}^{\text{top}}$ and ${p_y}^{\text{bot}}$ are the locations of the top and bottom, respectively, of the subset. Similarly, the apparent true axial strain is

$$E_{yy}{}' = \ln\left(\frac{{p_y}^{\text{top}'} - {p_y}^{\text{bot}'}}{S-1}\right). \tag{A.3}$$

Calculating dF as a function of axial strain by assuming a Poisson's ratio of 0.5, the maximum out-of-plane error is estimated to be 3.5×10^{-3} of the actual value. The maximum error, e, for each strain component from the front and side views is summarized in Table A.1.

Table A.1: Maximum out-of-plane strain errors, e, expressed as a fraction of the corresponding actual strain value.

	E_{yy} (front)	E_{xx} (front)	E_{yy} (side)	E_{xx} (side)
e	-0.7×10^{-3}	1.4×10^{-3}	-1.7×10^{-3}	3.5×10^{-3}

There are also sources of systematic error due solely to the correlation algorithm itself. In Eq. 2.3, analytical expressions are developed to represent the discrete matrix of gray level values in each deformed subset. In order to achieve sub-pixel displacement accuracy, I_2 is constructed by evaluating the analytic intensity patterns or "interpolation functions" at non-integer locations. Schreier et al. [32] have shown that the form of interpolator used in this study, quintic B-spline interpolation, together with a speckle pattern exhibiting a uniform distribution of gray-values, reduces the systematic error (termed interpolation bias) to a level far below that of the measured noise. Systematic error may also arise if the shape functions $u(x, y)$ and $v(x, y)$ which

approximate the displacement field are under-matched. Schreier et al [31] also have shown this error to be insignificant when the shape functions are able to represent accurately the displacement field over the subset and an appropriate speckle pattern is used. For this reason, quadratic shape functions (as opposed to linear) and a relatively small subset size were used in this study.

The total error for a given normal strain component is thus approximated as the random error plus the systematic error due to out-of-plane motion. It takes the form

$$\text{error}(\mu\epsilon) \approx \pm 100 + eE \times 10^6, \tag{A.4}$$

where E is the appropriate actual strain. The measured strains are clearly very accurate, and the error is significant only at strains similar in magnitude to that of the noise.

Appendix B

Finite Element Model of Polycarbonate Uniaxial Tension Test

Since shear banding occurs during the axial tension test, the entire specimen, including the grip sections, was modeled with 2400 elements of ABAQUS type C3D20. The mesh is shown in Fig. B-1a, and the boundary conditions are illustrated in Figure B-1b. An Instron 5582 load frame with self-aligning manual grips was used in the experiments. With this set-up, the bottom grip is fixed while the top grip is free to rotate about a double pin joint 32 cm above the top grip. In the simulation, therefore, the boundary conditions on the 3-faces of the bottom grip were such that all but the upper-most two rows of nodes were fixed in all three directions. All three degrees of freedom on all but the bottom-most two rows of nodes on the 3-faces of the top grip were tied to a single node at the center of the top grip. A rigid beam element of type CONN3D2 was defined between that node and a node 32 cm away in the 2-direction. The top, or driver node, was fixed in the 1-direction and 3-direction. The driver node was displaced at a constant rate of .095 mm/s in the 2-direction. The macroscopic load, P, was obtained from the reaction force in the 2-direction at the driver node.

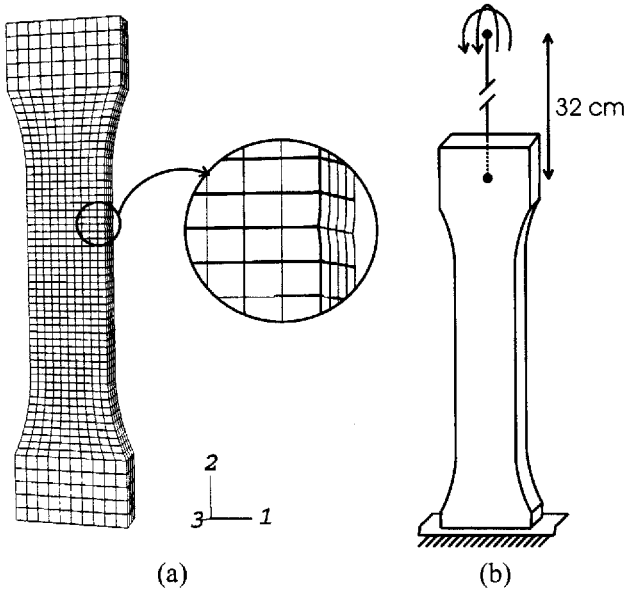

Figure B-1: (a) Tensile bar finite element mesh with close-up of defect, (b) finite element model boundary conditions.

Appendix C

Predicting Effective Composite Moduli

The theory of Mori and Tanaka [48] has been widely used to calculate the effective properties of composites. For the case of spherical elastic inclusions in an elastic matrix, the bulk and shear moduli, as expressed by Wang et al. [77] , are respectively given by

$$\kappa_{\text{blend}} = \kappa_{\text{m}} + f\frac{\kappa_{\text{m}}(\kappa_{\text{p}} - \kappa_{\text{m}})}{(1-f)\alpha(\kappa_{\text{p}} - \kappa_{\text{m}}) + \kappa_{\text{m}}} \tag{C.1}$$

and

$$\mu_{\text{blend}} = \mu_{\text{m}} + f\frac{\mu_{\text{m}}(\mu_{\text{p}} - \mu_{\text{m}})}{(1-f)\beta(\mu_{\text{p}} - \mu_{\text{m}}) + \mu_{\text{m}}}, \tag{C.2}$$

where subscripts "m" and "p" denote properties of the matrix and particle, respectively. The parameters α and β are given by

$$\alpha = \frac{1}{3}\left(\frac{1+\nu}{1-\nu}\right) \tag{C.3}$$

and

$$\beta = \frac{2}{15}\left(\frac{4-5\nu}{1-\nu}\right). \tag{C.4}$$

where ν is the Poisson's ratio of the matrix. For polycarbonate, κ_m and μ_m are calculated as 3520 MPa and 819 MPa, respectively, from the properties in Table 2.2 and the theory of elasticity. For the rubber particles, κ_p is taken as 2000 MPa and, since $\mu_p \ll \mu_m$, Eq. C.3 can be simplified to

$$\mu_{blend} = \mu_m\left(1 - \frac{f}{1-\beta(1-f)}\right). \tag{C.5}$$

The Poisson's ratio and tensile modulus of the polycarbonate blends, E_{blend}, are calculated from Eq.'s C.1 and C.5 and the theory of elasticity.

Bibliography

[1] A. S. Argon. A theory for the low-temperature plastic deformation of glassy polymers. *Philos. Mag.*, 28:839–865, 1973.

[2] A. S. Argon and R. E. Cohen. Toughenability of polymers. *Polymer*, 44:6013–6032, 2003.

[3] R. L. Aronow. *Toughenability of amorphous polymer/mineral filler composites.* PhD thesis, Massachusetts Institute of Technology, 2006.

[4] E. M. Arruda and M. C. Boyce. Evolution of plastic anisotropy in amorphous polymers during finite straining. *Int. J. Plasticity*, 9(6):697–720, 1993.

[5] E. M. Arruda and M. C. Boyce. A three-dimensional constitutive model for the large stretch behavior of rubber elastic materials. *J. Mech. Phys. Solids*, 41(2):389–412, 1993.

[6] H. H. Bailey, F. W. Blackwell, C. L. Lowery, and J. A. Ratkovic. USAF Rand Report R-2057/1-PR. Technical report, 1976.

[7] Z. Bartczak, A. S. Argon, R. E. Cohen, and M. Weinberg. Toughness mechanism in semi-crystalline polymer blends: I. High-density polyethylene toughened with rubbers. *Polymer*, 40:2331–2346, 1999.

[8] Z. Bartczak, A. S. Argon, R. E. Cohen, and M. Weinberg. Toughness mechanism in semi-crystalline polymer blends: II. High-density polyethylene toughened with calcium carbonate filler particles. *Polymer*, 40:2347–2365, 1999.

[9] Z. Bartczak, R. E. Cohen, and A. S. Argon. Evolution of the crystalline texture of high-density polyethylene during uniaxial compression. *Macromolecules*, 25:4692–4704, 1992.

[10] U. D. Baumann. The role of particle cavitation in the toughening of polymers. Master's thesis, Massachusetts Institute of Technology, 1998.

[11] J. S. Bergström and M. C. Boyce. Mechanical behavior of particle filled elastomers. *Rubber Chem. Technol.*, 72(4):633–656, 1999.

[12] M. C. Boyce, D. M. Parks, and A. S. Argon. Large inelastic deformation of glassy polymers. Part 1: Rate dependent constitutive model. *Mech. Mater.*, 7(1):15–33, 1988.

[13] M. C. Boyce, S. Socrate, and P. G. Llana. Constitutive model for the finite deformation stress-strain behavior of poly(ethylene terephthalate) above the glass transition. *Polymer*, 41:2183–2201, 2000.

[14] M. C. Boyce, G. G. Weber, and D. M. Parks. On the kinematics of finite strain plasticity. *J. Mech. Phys. Solids*, 37(5):647–665, 1989.

[15] G. Buisson and K. Ravi-Chandar. On the constitutive behavior of polycarbonate under large deformation. *Polymer*, 31:2071–2076, 1989.

[16] V. A. Buryachenko. The overall elastoplastic behavior of multiphase materials with isotropic components. *Acta Mech.*, 119:93–117, 1996.

[17] V. P. Chacko, R. J. Farris, and F. E. Karasz. Tensile properties of $CaCO_3$-filled polyethylenes. *J. App. Poly. Sci.*, 28:2701–2713, 1983.

[18] M. Danielsson. *Micromechanics, macromechanics and constitutive modeling of the elasto-viscoplastic deformation of rubber-toughened glassy polymers.* PhD thesis, Massachusetts Institute of Technology, 2003.

[19] M. Danielsson, D. M. Parks, and M. C. Boyce. Three-dimensional micromechanical modeling of voided polymeric materials. *J. Mech. Phys. Solids*, 50(2):351–379, 2002.

[20] M. Danielsson, D. M. Parks, and M. C. Boyce. Constitutive modeling of porous hyperelastic materials. *Mech. Mater.*, 36:347–358, 2004.

[21] M. Danielsson, D. M. Parks, and M. C. Boyce. Micromechanics, macromechanics and constitutive modeling of the elasto-viscoplastic deformation of rubber-toughened glassy polymers. *Submitted to J. Mech. Phys. Solids for publication.*, 2006.

[22] J. M. Duva and P. D. Crow. Analysis of consolidation of reinforced materials by power-law creep. *Mech. Mater.*, 17:25–32, 1994.

[23] J. M. Duva and J. W. Hutchinson. Constitutive potentials for dilutely voided non-linear materials. *Mech. Mater.*, 3:41–54, 1984.

[24] J. D. Eshelby. The determination of the elastic field of an ellipsoidal inclusion, and related problems. *Proc. Roy. Soc. A*, 241:376–396, 1957.

[25] J. M. Gloaguen and J. Lefebvre. Plastic deformation behaviour of thermoplastic/clay nanocomposites. *Polymer*, 42:5841–5847, 2001.

[26] A. A. Griffith. The phenomenon of rupture and flow in solids. *Philos. Trans. A*, 221:163–198, 1920.

[27] C. G'Sell, J. M. Hiver, and A. Dahoun. Experimental characterization of deformation damage in solid polymers under tension, and its interrelation with necking. *Int. J. Solids Struct.*, 39:3857–3872, 2002.

[28] C. G'Sell and J. J. Jonas. Determination of the plastic behaviour of solid polymers at constant true strain rate. *J. Mater. Sci.*, 14:583–591, 1979.

[29] E. Guth. Theory of filler reinforcement. *J. Appl. Phys.*, 16:20–25, 1945.

[30] E. Guth and O. Gold. On the hydrodynamical theory of the viscosity of suspensions. *Phys. Rev.*, 53:322, 1938.

[31] M. A. Sutton H. W. Schreier. Systematic errors in digital image correlation due to undermatched subset shape functions. *Exp. Mech.*, 42:303–310, 2002.

[32] M. A. Sutton H. W. Schreier, J. R. Braasch. Systematic errors in digital image correlation caused by intensity interpolation. *Opt. Eng.*, 39:2915–2921, 2000.

[33] M. Haghi and L. Anand. A constitutive model for isotropic, porous elasto-viscoplastic metals. *Mech. Mater.*, 13:37–53, 1992.

[34] Z. Hashin and S. Shtrikman. A variational approach to the theory of the elastic behavior of multiphase materials. *J. Mech. Phys. Solids*, 11:127–140, 1963.

[35] R. N. Haward and G. Thackray. The use of a mathematical model to describe isothermal stress-strain curves in glassy thermoplastics. *Proc. Roy. Soc. A*, 302:453–472, 1968.

[36] A. R. Haynes and P. D. Coates. Semi-automated image analysis of the true tensile drawing behaviour of polymers to large strains. *J. Mat. Sci.*, 31:1843–1855, 1996.

[37] R. Hill. A self-consistent mechanics of composite materials. *J. Mech. Phys. Solids*, 13:213–222, 1965.

[38] R. Hiss, S. Hobeika, C. Lynn, and G. Strobl. Network stretching, slip processes, and fragmentation of crystallites during uniaxial drawing of polyethylene and related copolymers. A comparative study. *Macromolecules*, 32:4390–4403, 19999.

[39] M. D. Johnson. Deformation and fracture of polycarbonate and rubber-modified polycarbonate under controlled temperature, deformation rate, and notch stress triaxiality. Master's thesis, Massachusetts Institute of Technology, 2001.

[40] R. Kraus, W. Wilke, A. Zhuk, I. Luzinov, S. Minko, and A. Voronov. Investigation of debonding processes in particle-filled polymer materials by acoustic

emission. Part I. Acoustic emission and debonding stress. *J. Mat. Sci.*, 32:4397–4403, 1997.

[41] W. Kreher. Residual stresses and stored elastic energy of composites and polycrystals. *J. Mech. Phys. Solids*, 38:115–128, 1990.

[42] F. Laraba-Abbes, P. Ienny, and R. Piques. A new 'tailor-made' methodology for the mechanical behaviour analysis of rubber-like materials. 1. Kinematics measurements using digital speckle extensometry. *Polymer*, 44:807–820, 2003.

[43] A. Lazzeri, Y. S. Thio, and R. E. Cohen. Volumetric strain measurements on $CaCO_3$/polypropylene particulate composites: The effect of particle size. *J. Appl. Polym. Sci.*, 91:925–935, 2004.

[44] L. Lin and A. S. Argon. Structure and plastic deformation of polyethylene. *J. Mat. Sci.*, 29:294–323, 1994.

[45] A. Meddad and B. Fisa. Stress-strain behavior and tensile dilatometry of glass bead-filled polypropylene and polyamide 6. *J. App. Poly. Sci.*, 64(4):653–665, 1997.

[46] J. C. Michel and P. Suquet. The constitutive law of non-linear viscous and porous materials. *J. Mech. Phys. Solids*, 40(4):783–812, 1992.

[47] T. Mochida, M. Taya, and M. Obata. Effect of damaged particles on the stiffness of a particle/metal matrix composite. *JSME Int. J.*, 34:187–191, 1991.

[48] T. Mori and K. Tanaka. Average stress in matrix and average elastic energy of materials with misfitting inclusions. *Acta. Metall.*, 21:571–574, 1973.

[49] L. Mullins and N. R. Tobin. Stress softening in rubber vulcanizates. Part I. Use of a strain amplification factor to describe the elastic behavior of filler-reinforced vulcanized rubber. *J. Appl. Polym. Sci.*, 9:2993–3009, 1965.

[50] O. K. Muratoglu, A. S. Argon, R. E. Cohen, and M. Weinberg. Microstructural processes of fracture of rubber-modified polycarbonate. *Polymer*, 36:4771–4786, 1995.

[51] S. Nazarenko, S. Bensason, A. Hiltner, and E. Baer. The effects of temperature and pressure on necking of polycarbonate. *Polymer*, 35:3883–3391, 1994.

[52] A. Needleman. Continuum model for void nucleation by inclusion debonding. *J. App. Mech.*, 54:525–531, 1987.

[53] M. Nichols, C. Webb, C. Willingham, and B. Henry. *The Graduate*, 1967.

[54] D. M. Parks and S. Ahzi. Polycrystalline plastic deformation and texture evolution for crystals lacking five independent slip systems. *J. Mech. Phys. Solids*, 38:701–724, 1990.

[55] A. Peterlin. A molecular model of drawing polyethylene and polypropylene. *J. Mat. Sci.*, 6:409–508, 1971.

[56] M. Psarski, A. S. Argon, and R. E. Cohen. Private communication. 2001.

[57] B. Pukanszky. Effect of interfacial interactions on the deformation and failure properties of PP/$CaCO_3$ composites. *New Polymeric Mater.*, 3:205–217, 1992.

[58] B. Pukanszky and F. H. J. Maurer. Composition dependence of the fracture toughness of heterogeneous polymer systems. *Polymer*, 36:1617–1625, 1995.

[59] B. Pukanszky, M. van Es, F. H. J. Maurer, and G. Voros. Micromechanical deformations in particulate filled thermoplastics: Volume strain measurements. *J. Mat. Sci.*, 29:2350–2358, 1994.

[60] G. Rodin and D. M. Parks. On consistency relations in nonlinear fracture mechanics. *J. Appl. Mech.*, 53:834–838, 1986.

[61] D. C. Roux, J. J. Cooper-White, G. H. McKinley, and V. Tirtaatmadja. Drop impact of newtonian and elastic fluids. *Phys. Fluids*, 15:S12, 2003.

[62] H. M. Smallwood. Limiting law of the reinforcement of rubber. *J. Appl. Phys.*, 15:758–766, 1944.

[63] R. J. M. Smit, W. A. M. Brekelmans, and H. E. H. Meijer. Prediction of the large-strain mechanical response of heterogeneous polymer systems: Local and global deformation behaviour of a representative volume element of voided polycarbonate. *J. Mech. Phys. Solids*, 47(2):201–221, 1999.

[64] S. Socrate. *Mechanics of microvoid nucleation and growth in high-strength metastable austenite steels.* PhD thesis, Massachusetts Institute of Technology, 1995.

[65] S. Socrate and M. C. Boyce. Micromechanics of toughened polycarbonate. *J. Mech. Phys. Solids*, 48(2):233–273, 2000.

[66] P. Sofronis and R. M. McMeeking. Creep of a power-law material containing spherical voids. *J. Appl. Mech.*, 59:S88–S95, 1992.

[67] P. Suquet. Overall properties of nonlinear composites: A modified secant moduli theory and its link with ponte castaneda's nonlinear variational procedure. *C.R. Acad. Sc. Paris*, 320:563–571, 1995.

[68] P. Suquet. *Continuum Micromechanics.* Springer-Verlag Wein New York, 1997.

[69] G. P. Tandon and G. J. Weng. A theory of particle-reinforced plasticity. *Trans. ASME*, 55:126–338, 1988.

[70] M. Taya and T. W. Chou. On two kinds of ellipsoidal inhomogeneities in an infinite elastic body: An application to a hybrid composite. *Int. J. Solids Struct.*, 17:553–563, 1981.

[71] Y. S. Thio, A. S. Argon, R. E. Cohen, and M. Weinberg. Toughening of isotactic polypropylene with $CaCO_3$ particles. *Polymer*, 43:3661–3674, 2002.

[72] K. Tohgo and T. W. Chou. Incremental theory of particulate-reinforced composites including debonding damage. *JSME Int. J.*, 39:389–397, 1996.

[73] V. Tvergaard. On localization in ductile materials containing spherical voids. *Int. J. Fracture*, 18(4):237–252, 1982.

[74] P. A. Tzika, M. C. Boyce, and D. M. Parks. Micromechanics of deformation in particle-toughened polyamides. *J. Mech. Phys. Solids*, 48(9):1893–1929, 2000.

[75] E. A. A. van Hartingsveldt and J.J. van Aartsen. Interfacial debonding in polyamide-6/glass bead composites. *Polymer*, 30:1984–1991, 1989.

[76] P. Vollenberg, D. Heikens, and H. C. B. Ladan. Experimental determination of thermal and adhesion stress in particle filled thermoplasts. *Polym. Compos.*, 9:382–388, 1988.

[77] X. Wang, K. Xiao, L. Ye, Y. Mai, C. H. Wang, and L.R. Francis Rose. Modelling mechanical properties of core-shell rubber-modified epoxies. *Acta Mater.*, 48:579–586, 2000.

[78] G. J. Weng. Some elastic properties of reinforced solids, with special reference to isotropic ones containing spherical inclusions. *Int. J. Engng Sci.*, 22:845–856, 1984.

[79] M. W. L. Wilbrink, A. S. Argon, R. E. Cohen, and M. Weinberg. Toughenability of nylon-6 with $CaCO_3$ filler particles: New findings and general principles. *Polymer*, 42:10155–10180, 2001.

[80] X. P. Xu and A. Needleman. Numerical simulations of fast crack growth in brittle solids. *J. Mech. Phys. Solids*, 42:1397–1434, 1994.

[81] A. F. Yee. The yield and deformation behaviour of some polycarbonate blends. *J. Mater. Sci.*, 12:757–765, 1977.

[82] Y. H. Zhao and G. J. Weng. Plasticity of a two-phase composite with partially debonded inclusions. *Int. J. Plasticity*, 12:781–804, 1996.